ASSESSMENT OF WIND TURBINE FOUNDATION RESPONSE USING FIELD INSTRUMENTATION AND DYNAMIC LABORATORY TESTING OF UNSATURATED SITE SOIL

by

CHRISTOPHER ENOS

A thesis submitted in partial fulfillment of the requirements for the degree of

MASTER OF SCIENCE

(CIVIL AND ENVIRONMENTAL ENGINEERING)

At the

UNIVERSITY OF WISCONSIN-MADISON

2018

ASSESSMENT OF WIND TURBINE FOUNDATION RESPONSE USING FIELD INSTRUMENTATION AND DYNAMIC LABORATORY TESTING OF UNSATURATED SITE SOIL

Approved

James M. Tinjum, Associate Professor

Date: 5/11/2018

EXECUTIVE SUMMARY

Wind turbine generator (WTG) foundations undergo continuous, dynamic loading conditions that make their design unique and complex. Though many foundation alternatives exist for WTG's, the most common design is a shallow, octagonal, gravity-based footing. Two utility-scale (≥ 1.5 MW) WTG's in the Midwest were outfitted with foundation and tower instrumentation to monitor *in situ* loads. Furthermore, undisturbed soil samples were taken at the site and tested with resonant column and cyclic triaxial devices that were retrofitted with suction-saturation control capabilities. This thesis focuses on the analysis and interpretation of field instrumentation data and laboratory results to assess current WTG foundation design practices.

For field instrumentation, nine pressure gauges (PG's) and ten soil deformation gauges (SG's) were placed under the foundation to measure the distribution of contact pressure and vertical soil deformation. At Site A, four thermal dissipation sensors (TDS's) were installed in the soil below the footing to measure fluctuations in water content. In addition, six sets of full-bridge strain gauges were placed on the WTG tower at two elevations to measure the tower loading (i.e. wind induced moment and tower vibration). Finally, three MEMS accelerometers were installed on the foundation pedestal to measure foundation tilt.

Regarding laboratory testing, a Hardin-type resonant column and load-controlled cyclic triaxial apparatus were outfitted with suction-saturation control capabilities. New bottom platens for each were machined with a hole for a high air entry (HAE) ceramic disc to control the flow of water in and out of the specimens. Using the axis translation technique, the soil suction could be controlled by increasing the air pressure relative to the pore water pressure. Four conditions were tested: 0 kPa (saturated), 25 kPa, 50 kPa, and 100 kPa soil suction. To supplement the data, soil water characteristic curves (SWCC's) were developed to relate the soil suction and soil saturation.

Soil suction (i.e. saturation) is known to impact the stiffness of the soil. Stiffness is a crucial soil property in the design of a WTG foundation, as it controls the response of the structure to the dynamic loads imparted by the oscillating tower. Previous analysis of these WTG sites has indicated that the foundation is out-performing its expected stiffness response. One hypothesis is that the soil, being unsaturated, is stiffer than

engineers might assume based on assumptions for saturated soil. By understanding the soil's response to varying saturation, implications to the foundation design and performance can be drawn.

Tower moment and shear force were found to be correlated with wind speed, with magnitudes within expected design values. Furthermore, the moment along the predominant wind direction (PWD) was found to spike when the wind direction coincided with the PWD. When overturning moment was compared to the soil deformation and vertical pressure, the three mirrored each other extremely well, indicating a predictable, consistent load transfer. The overturning moment and pressure along the PWD also proved to have a nearly linear relationship. When normalized to the static, zero wind-load vertical pressure, the pressure responses at the two sites were nearly identical. The windward and leeward pressure gauges also nearly perfectly mirrored each other, indicating that the windward uplift was roughly balanced by the leeward pressure spike. Finally, the harmonic analysis of the tower and soil pressure response revealed that the amplitude of the cyclic moment was about an order of magnitude less than the overall overturning moment, and that the cyclic pressure amplitude was nearly two orders of magnitude less than the static pressure.

The application of matric suction to the two approaches proved to be effective overall in affecting the stiffness response. A clear trend of increasing shear modulus with increasing soil suction was present. Moreover, this increase existed at all strain magnitudes measured, though the effect was most pronounced at low strain. At a soil suction of 100 kPa, the value of G_0 more than doubled in many specimens. The method worked better with the resonant column, as it is non-destructive, so the suction could be progressively increased without changing the specimen out. Thus, the results of the resonant column are likely more representative of the true response of a soil to changes in saturation, whereas the cyclic triaxial method requires a new specimen for each suction level, adding in the variability of soil properties along the profile. Furthermore, the variation in response across the site was significant, with $G_{0,sat}$ varying from 43 to 76 MPa. Based on the boring logs, the site subsurface was reported as very uniform. The use of undisturbed soil, however, showed that, though the site appeared uniform, the laboratory tested soil stiffness distribution did not necessarily follow the same trend.

Using the data from one of the thermal dissipation sensors, TDS-1, the in situ water content (Θ) directly below the footing could be assessed. The sensors revealed a clear seasonal trend, where moisture content reaches a peak of 0.4531 in November. The minimum recorded value occurred in minimum of 0.4515 in August. Since the void ratio where the sensors were placed is unknown, assumptions from measurements at other site locations were made. Assuming the maximum measured Θ corresponds to the saturated condition, the stiffness within the range of measured saturation levels ranged from approximately 43 MPa to 115 MPa for specimens tested at a confining stress of 70 kPa, approximately the confining stress at TDS-1.

Overall, the results of this study can apply in a few key ways. First is through understanding of the impacts of soil suction on the stiffness. A shallow foundation situated 10 m above the water table, for example, would theoretically feel roughly 100 kPa of suction at its base, which could more than double the stiffness. Furthermore, this increase in soil stiffness could be compounded by a two-orders-of-magnitude decrease in shear strain, which would double the reduced shear modulus for this soil type. Altogether, these observations could result in a reduction in the required radius for rotational stiffness to the point where it no longer controls the overall design.

ACKNOWLEDGEMENTS

I would like to dedicate this thesis to Vreni Pigorsch. I am forever grateful to you for spending two of the last three years driving back-and-forth between Minneapolis and Madison and giving me your unconditional love and support throughout this process. I couldn’t have done it without you!

I would like to offer my most sincere gratitude to my advisors Dr. James Tinjum and Dr. Dante Fratta. Their vigor for excellence, passion for their work, and love for their students was a privilege to be a part of, and I cannot thank them enough for all they have done for me.

A very special thanks to my family: my parents, Jack and Barbara, for their endless love, support, and encouragement through my graduate school journey, and my brothers, Dan and Sean, for always being there to provide some much needed laughs and supporting me throughout my studies. Words can’t describe my gratitude to you all. I couldn’t have done it without you. I also owe tremendous gratitude to the Pigorsch family. Their hospitality, kindness, and generosity meant so much to me throughout my time at UW-Madison.

My sincere gratitude towards the UW-Madison faculty and students for making my seven years here as an undergraduate and graduate student so special. Thanks to Alex Michaud, Mehmet Yilmaz, Adam McDaniel, Nick Jordan, Brent Teske, Mike Zimmerman, Idil Deniz Akin, Bharat Natarajan, and the rest of the office for helping and supporting me through my graduate studies. Thanks to Ken Baker, Bryan Dunn, Tom Klister, Bryce Nelson, Dillon O’Brien, Sam Orke, Jared Peroutky and Josh Peterson for the last seven years and for making my time at UW unforgettable. Special thanks to Dr. Jose Pincheira for serving on my M.S. defense committee and Xiaodong Wang for his willingness to provide top-tier technical assistance whenever needed.

Additionally, thanks to the UW COE Machine Shop for helping teach me to build my equipment and being so patient with me, as well as Mott Corp. for supplying the porous sintered steel discs for my lab equipment *pro bono*. Finally, I would like to thank the US National Science Foundation (Grant No. 1238963) and US Department of Energy for funding the field instrumentation.

Table of Contents

1. INTRODUCTION

Wind energy is the fastest growing source of renewable energy in the US. Wind turbines generated 5.6% of US electricity in 2016 and accounted for 41% of the added power capacity (AWEA 2017; EIA 2017). Growth in wind energy production is supported by increases in the number, capacity, and average electrical energy produced by wind turbine generators (WTGs). This trend is predicted to continue for the foreseeable future, and the anticipated rated capacity of WTGs is expected to reach 5 MW by the end of the decade (Fig. 1).

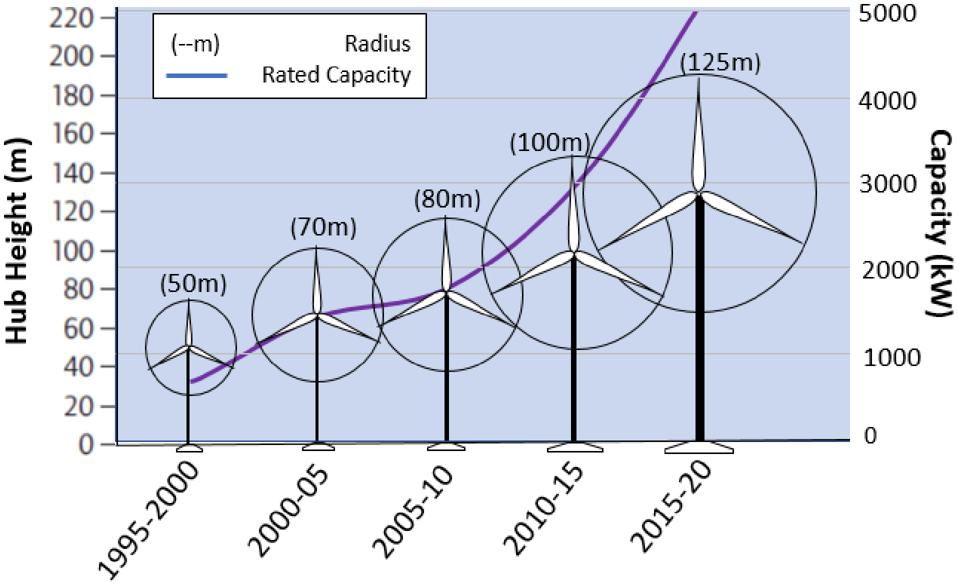

Figure 1-1: Increase in hub height and rated turbine capacity (adapted from IPCC 2012).

Shallow, on-shore WTG systems are typically supported on massive, octagonal, gravity-based foundations. As WTGs increase in size, their foundations will need to accommodate greater overturning moments and satisfy tighter rotational stiffness requirements without becoming over-conservative, costly (Fig 1-2), or needlessly increasing the environmental life-cycle footprint of WTG systems. However, the current state-of-practice uses parameters and assumptions borrowed from shallow foundation design

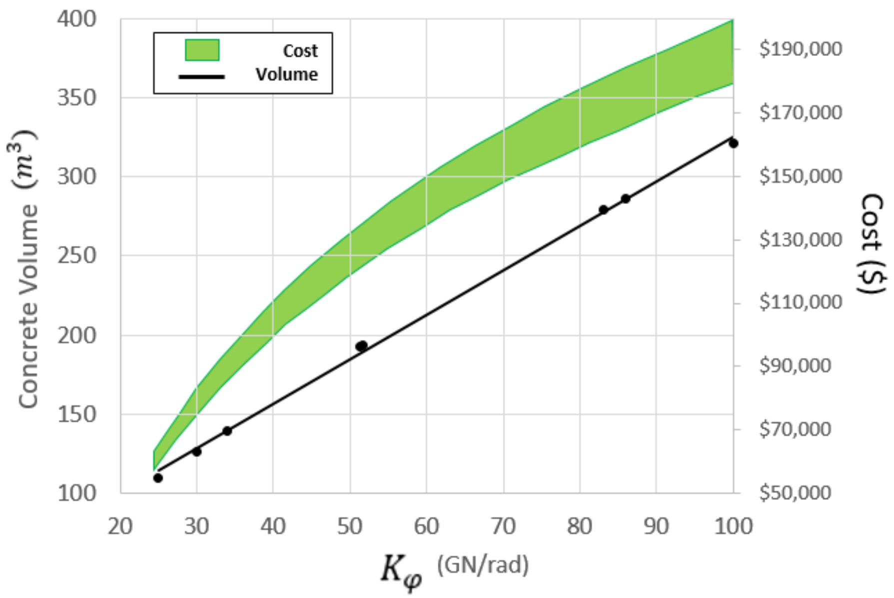

Figure 1-2: WTG foundation cost-volume relationships. K_ϕ represents the rotational stiffness parameter, which increases as the WTG size increases.

analogies and methodologies, which have not been scientifically validated for application in large-scale, dynamically loaded WTG foundations (Ntambakwa 2009). The continued growth and innovation of WTG foundation design, such as the use of cast-on-site concrete towers, will place even more extreme loads on the foundation (Lockwood et al. 2016), pushing design into territory beyond which mechanistically based, field-validated science has kept pace. WTG foundations are designed to transmit moderate vertical and large, highly variable horizontal forces and overturning moments to the soil (Tinjum and Christensen 2010; Tinjum and Lang 2012). These unique loading conditions cause non-uniform pressure distribution and soil deformations that vary spatially and temporally with wind direction and speed (Yilmaz 2014). As WTG towers continue to grow taller and swept rotor areas increase, the foundation design must keep paced with the continually increasing demand.

Current design approaches vastly simplify design calculations, as the contact pressure and soil deformation distributions beneath WTG foundations are poorly understood due to a lack of research and robust measurement. These simplified approaches do not consider the effect of dynamic loads that are dominant in WTG foundations nor the relative distribution of soil stiffness both in the foundation concrete and soils. Improvement of design approaches for dynamically loaded foundations, such as WTG foundations, requires knowledge of cyclic stress-strain mechanisms, as well as an understanding of the in situ soil response to dynamic loading (Vucetic and Dobry 1991).

The dynamic response of the foundation and WTG structural elements are intimately tied to one another. For example, in the manufacturer-supplied Load Document, a minimum foundation rotational stiffness is prescribed for each turbine. This value is essential for estimation of the WTG tower's response to dynamic loading and is dependent on the structure's natural frequency (DNV/Risø 2002). Madaschi et al. (2016) measured the foundation and tower response to controlled loading and found that the stiffness of the foundation was approximately 10 times that of the base joint, where the WTG tower meets the concrete foundation. Furthermore, the base joint was found to be another order of magnitude stiffer than the tower itself, indicating that the vibration was driven by the tower rather than the foundation system, and that the effects of the foundation on the system's overall stiffness are negligible (Madaschi et al. 2016). Such a stark difference in foundation versus tower stiffness suggests an over-designed foundation. In addition, Yilmaz (2014) found that the in situ static soil strain present beneath two instrumented WTG's was one to two orders of magnitude less than the value that industry guidance suggests, 0.1%. Such a decrease in assumed soil strain would yield a substantially larger assumed shear modulus, potentially resulting in a smaller foundation size, similarly pointing to an over-conservative foundation design.

The purpose of this thesis is to characterize the dynamic response of a WTG system through foundation instrumentation and dynamic laboratory testing of site soil specimens, as well as interpret these results as they pertain to WTG foundation design practices.

2. BACKGROUND

2.1. WTG Foundation Types

When designing a foundation for a wind turbine generator, the engineer has several options to choose from based on site conditions and cost. Typical to foundation design, these types are generally categorized as either shallow or deep foundation systems. Foundation size and type often vary within a given wind farm site, however, limiting the number of unique designs allows for greater economies of scale and overall construction efficiency.

Where surface soil conditions are generally strong, shallow foundations can be used to support the WTG. Shallow-type foundations typically used are: octagonal gravity-based, short pier, rock socketed, and rock anchored. Where soil near the surface may not be suitable for significant load bearing, deep foundations can be used, which typically include: mono-piles, pile and cap, and the patented Patrick and Henderson Tensionless Pier. In addition to altering foundation type and geometry, ground improvement techniques can be used by the engineer on the foundation subgrade to add strength to otherwise unsatisfactory soil below shallow foundation systems. Specific ground improvement options are discussed in more detail later.

2.1.1. Shallow Octagonal

Foundations of the shallow, octagonal variety are the most commonly utilized in on-shore WTG construction (Tinjum & Christensen, 2010). As the name suggests, these foundations are octagonal in shape due to ease of construction compared to circular footings. This shape allows the footing to disperse the static and dynamic horizontal and vertical forces through the underlying soil due to wind loads in all 360^o. These footings rely on sheer mass, size, and soil overburden to stabilize the WTG, requiring a substantial amount of concrete and steel rebar reinforcement, and are accordingly expensive. Foundations such as these are composed of approximately 140-500 m^3 of concrete and 125 to 360 kN of steel reinforcement, resulting in costs of \$100,000 to upwards of \$250,000 (Tinjum & Lang, 2012). Approximate dimensions are illustrated in Figure 2-1 below.

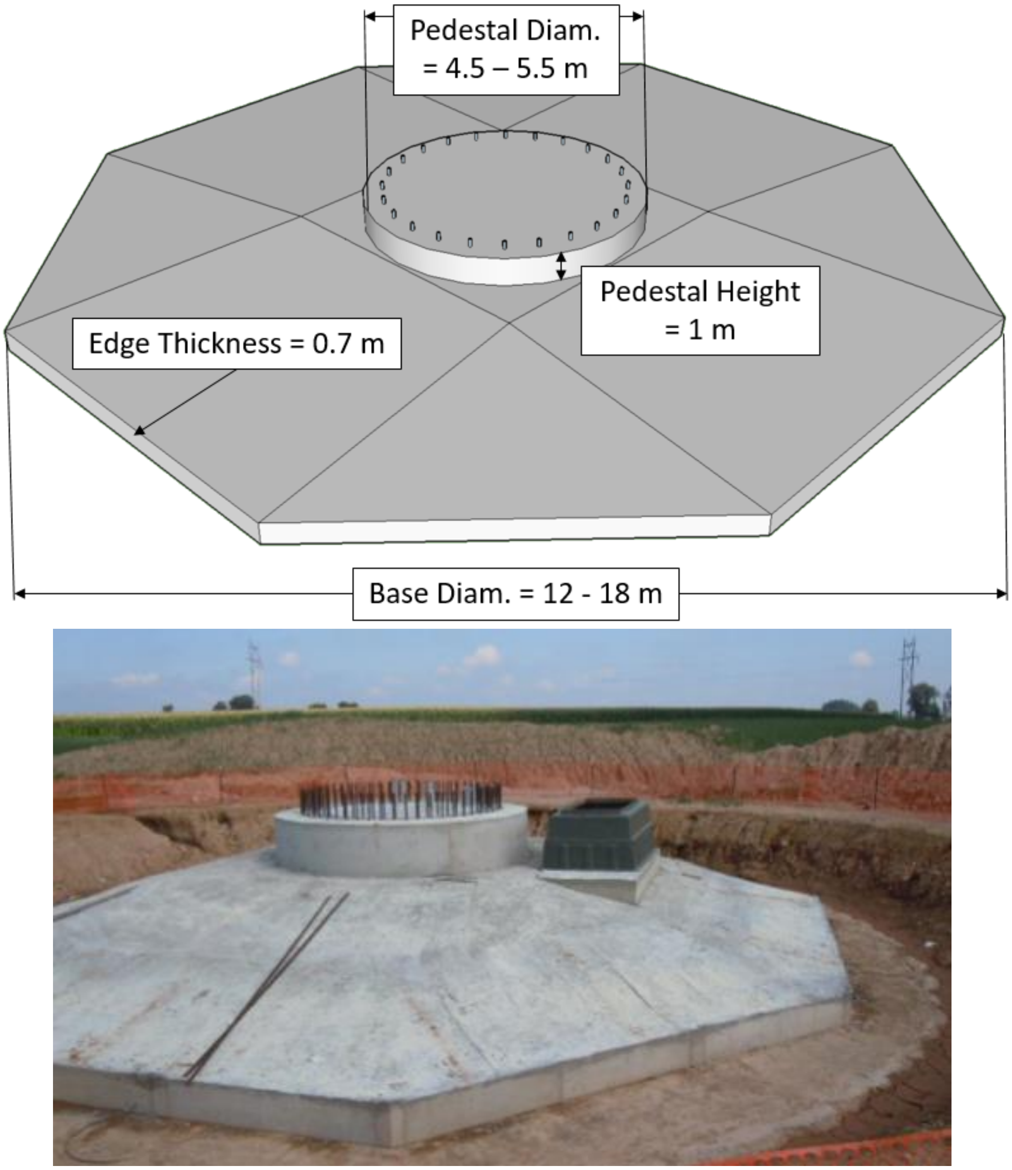

Figure 2-1: (a) Typical dimensions of a WTG shallow octagonal foundation and (b) construction of a shallow octagonal foundation.

2.1.2. Short Pier, Rock-Socketed Piers, & Rock Anchor

Where the surficial soil is relatively weak, but lies over a layer of strong soil or rock, alternative measures can be taken to a simple shallow foundation. Short piers, rock-socketed piers, and rock anchors can be placed below the footing base into the usable layer, using primarily end bearing and tensioned steel grouted into bedrock, as well as some side wall friction to bear the load (Morgan & Ntambakwa, 2008).

Though these are still classified as shallow foundations, the primary mechanism is similar to that of deep foundations, where loads are transmitted below the surface soil into more competent layers.

2.1.3.Deep Pile

Where surficial soil conditions are not viable for a shallow foundation, deep foundation systems, such as deep pile and cap foundations and monopiles, can be employed. Long piles are placed deep below the surface by either the drilling of a shaft or by driving the piles. Depending on type of soil and depth to bedrock or extremely strong soil, piles can rely primarily on end bearing, side wall friction, lateral earth pressure, or combinations of the three (see – Figure 2-2). For loading conditions, such as extreme wind loads, that may cause uplift on an area of a foundation, side wall friction and weight of the piles act against the uplift force, as opposed to shallow foundations that would have to rely on mass and overburden to overcome such forces.

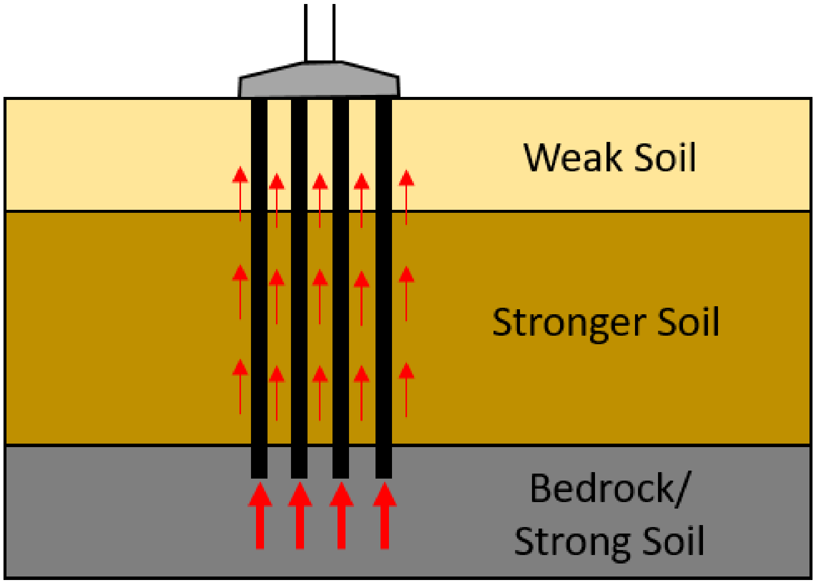

Figure 2-2: Diagram of typical deep pile system and resistance forces (in red)

An example of a commonly used deep foundation is the patented Patrick and Henderson (P&H) Tensionless Pier. This foundation can be employed for site conditions where sufficiently strong soil or bedrock is located relatively close to the surface, and is composed of a singular, wide, hollow pier, where the space between two concentric cylinders of corrugated metal are filled with concrete. Post-tensioned bolts maintain a compressive force on the concrete during extreme wind events causing uplift. The interior of the concrete-filled cylinder is filled with excavated soil. Total diameter is typically 4.5 to 5.5 m, and depth typically ranges between 8 and 12 m. These foundations can result in cost savings; however, large grout volumes and soil caving can nullify these savings (Tinjum & Christensen, 2010). A diagram of a P&H Tensionless Pier can be seen in Figure 2-3.

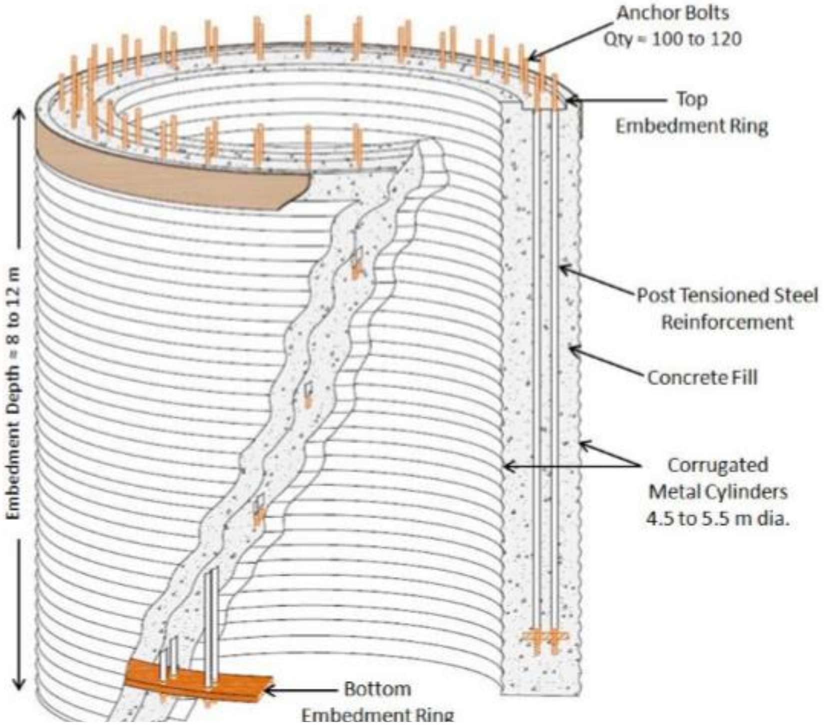

Figure 2-3: Patented Patrick & Henderson Tensionless Pier (Lang 2012)

2.1.4. Soil Improvement

In addition to the above foundation type options, ground improvement techniques can strengthen the underlying soil enough to allow a simple octagonal gravity foundation. Soil improvement techniques general fall into two categories: ground reinforcement and compaction. Vibratory compaction densifies the soil by essentially repeatedly dropping a weight onto the soil (Holtz et al. 1986). To reduce future settlement potential, applying a known load well in advance of construction consolidates the soil, minimizing the possible change in void ratio.

If the depth of poor soil is shallow enough, it can simply be excavated and replaced with a more suitable material, such as coarse stone, compacted granular fill, and lean mix concrete, among others. The cost of this technique, which includes excavation, hauling, and new material, however, can become quite high as the amount of material needed increases.

2.2. WTG Geotechnics

2.2.1.Foundation Forces & Load Document

WTG structures undergo a unique and complex loading conditions that change both spatially and temporally with the direction and speed of the wind (Yilmaz 2014). Specifically, WTG’s experience high horizontal forces and moments around the base (Fig. 2-4), resulting in an eccentric vertical load and giving rise to a number of unique failure modes that must be accounted for, such as overturning, sliding, and rotational stiffness.

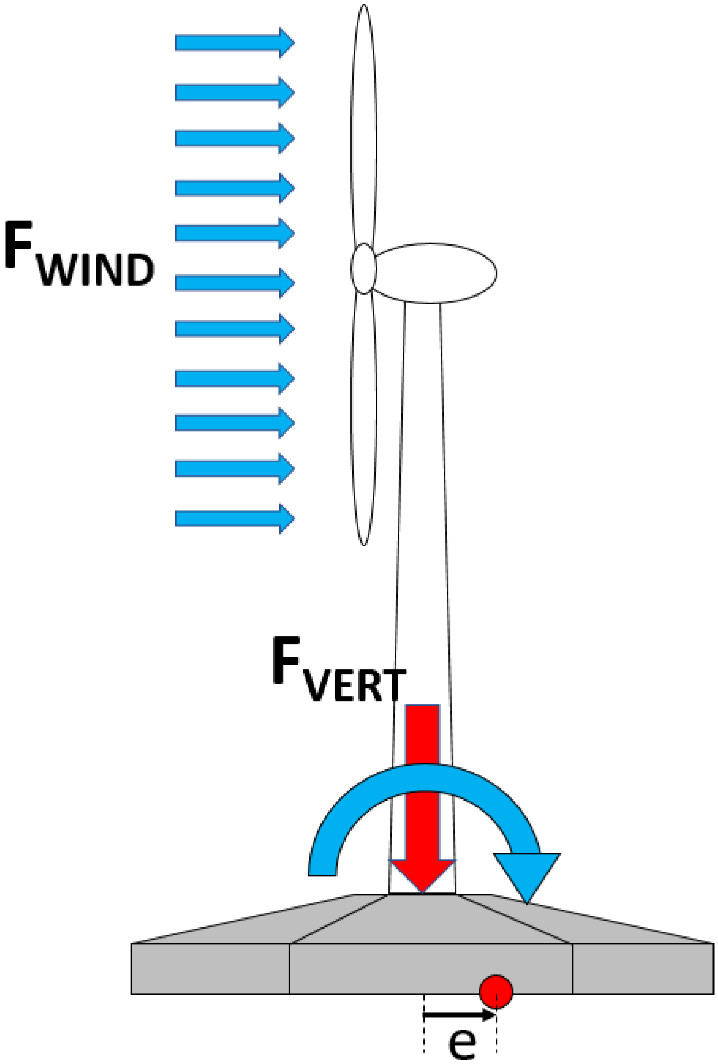

Figure 2-4: Simplified loading conditions for a WTG foundation.

The engineer is supplied with a Load Document by the turbine manufacturer, which, when combined with site conditions, establishes the forces the foundation must be capable of supporting. Typically included with the load document is information regarding: the approach to determining WTG loads, minimum rotational stiffness (GNm/rad), natural frequency, fatigue loads/cycles, turbine coordinate system, and scope/purpose. Vertical load (F_z), horizontal loads (F_x, F_y, F_{xy}), and moments (M_x, M_y, M_{xy}) are given for foundation loads, as well as allowable settlement (overall and differential) and extreme load factors based on 50-year extreme wind gusts (IEC-61400 2005). Site conditions to be considered are detailed in the geotechnical report (discussed later), codes and regulations regarding safety, serviceability, environmental impact, and design loads, owner requirements/needs, and operation/maintenance requirements outlined in the agreement between the owner and power purchaser. A detailed analysis of the full scope of requirements and conditions will yield the controlling design loads.

2.2.2. Geotechnical Investigation and Report

The key component to a thorough and accurate WTG geotechnical design is the site investigation and geotechnical report. Through a combination of field and laboratory testing, the subsurface conditions of the soil and bedrock can be logged, quantified, and analyzed for use by the engineer in their foundation design recommendations. The geotechnical report should communicate these results in a clear, concise, and effective manner.

Samples of the soil are commonly taken via split spoon, Shelby tube, rock coring, and grab sampling. *In situ* measurements can be made by methods such as wave propagation (i.e. geophysical) techniques, cone penetration tests (CPT) and, where coarse-grained material exists, standard penetration tests (SPT). Typical laboratory tests include: unit weight, moisture content, Atterberg limits, unconfined compressive strength, consolidation testing, thermal resistivity, and electrical resistivity (Tinjum & Christensen 2010; Tinjum & Lang 2012). At least one investigation per turbine location is needed for proper site characterization, and may include borings or CPT, as well as periodic investigations for other structures such as access roads and substations.

2.2.3. Design Path

Standard WTG foundation design procedure is illustrated in Figure 2-5 below. The process begins with acquisition of the Load document and geotechnical report, which will allow the engineer to develop a preliminary design. This preliminary design then must go through a series of design checks to identify possible modes of failure. Once the dimensions have been reworked and optimized to pass these checks, structural design of the foundation, including concrete, steel reinforcement, anchor bolts, and embedment plates. Finally, field quality control during construction assures proper installation and execution of the design.

2.2.4. Preliminary Design

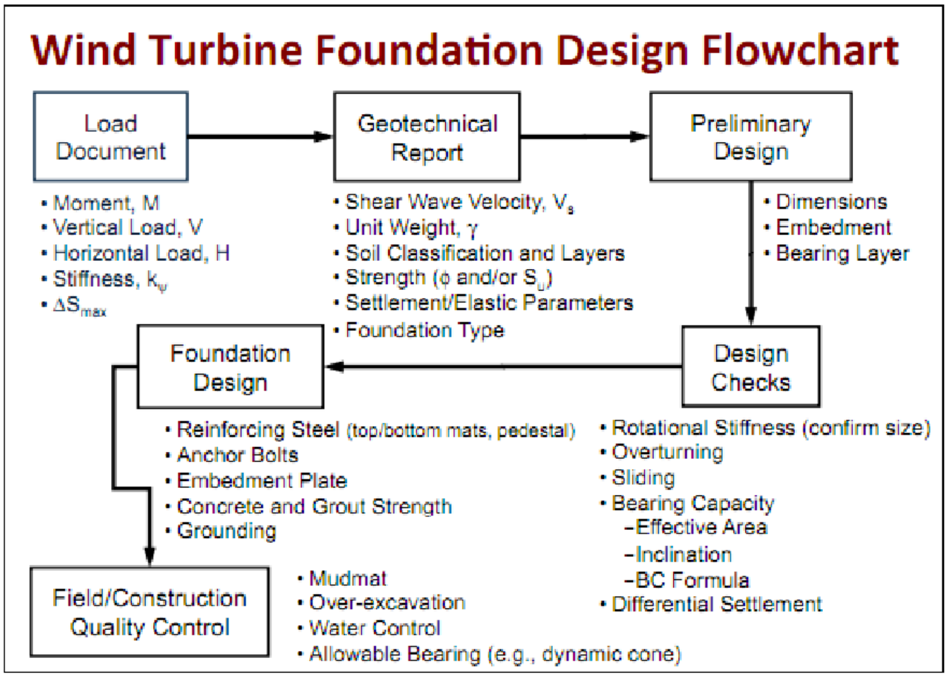

Figure 2-5: WTG foundation design path (Lang 2012).

Once the load document, geotechnical report, and other miscellaneous design requirements have been assembled, the engineer can put together a preliminary design. Included in this design is are estimates based on experience and past projects of foundation type, dimensions, and embedment depth. Since the design will have to go through a series of design calculation checks, it is not vital to pick accurate dimensions during this phase, though accuracy will reduce time spent going through repetitions of design checks. The process is iterated until a sufficiently supportive foundation design is created. Although this process applies to any foundation type, this thesis focuses on the design process for shallow, octagonal, gravity-based foundation systems only.

2.2.5. Design Checks

As discussed previously, each design iteration must pass a series of design check calculations to ensure the foundation will properly resist failure. Secondarily, the design checks will reveal whether the design is overly-conservative (i.e. overly expensive), and can be reduced in size. In total, five design checks are necessary for proper evaluation: overturning, rotational stiffness, bearing capacity, sliding, and settlement (Tinjum & Christensen 2010). Typically, the controlling parameters are rotational stiffness, overturning, and bearing capacity (Lang 2012).

2.2.5.1. Overturning

Overturning failure occurs when the wind-induced moment about the WTG foundation overcomes the resisting moment, resulting in a catastrophic event in which the entire WTG structure tips over. It is generally one of the first checks performed, as it often controls the design in soil with a relatively high shear modulus, and of the variables that influence overturning, it is most affected by depth to water table, especially in cases where the water table is high (Lang 2012). Overturning is a relatively simple statics problem, where the applied force (wind, mechanical movement of WTG structures, etc.) must be balanced by the resistive forces (structure weight, soil overburden, foundation geometry, etc.). If the applied moment about the base of the structure is larger than the moment from the resistive forces, the turbine is at risk of overturning. The first step in the design check is gathering all relevant forces and factors that affect these forces. These forces and factors include: forces from the load document, foundation dimensions, embedment depth, concrete and soil properties, and volume of concrete. With these, the engineer must calculate the weight of both the concrete foundation itself and *compacted* soil backfill. Typical soil unit weights can be found below in Table 2-1.

Once all relevant forces are established, the resisting moment must be calculated, which includes: the weight of concrete, weight of soil backfill, and the vertical load of the WTG structure. Being that overturning would occur over the edge of the foundation, the moment arm for these forces is the foundation radius. Keep in mind that in cases where the water table is above the foundation base, one must account for the buoyancy of the structure in this component of the design check. The equation for resisting moment is as follows:

Table 2-1: Typical soil unit weights (kN/m^3) (Budhu 2007)

Soil Type	γ_{sat}	γ_{dry}
Gravel	20 - 22	15 - 17
Sand	18 - 20	13 - 16
Silt	18 - 20	14 - 18
Clay	16 - 22	14 - 21

$$M_{res} = (F_V + W_{soil} + W_{conc}) * r \qquad [2\text{-}1]$$

$Where$:

$M_{res} = Total\ resisting\ moment$

$F_V = Vertical\ turbine\ load$

$W_{soil} = Weight\ of\ soil\ backfill$

$W_{conc} = Weight\ of\ concrete\ foundation$

$r = Foundation\ radius$

Following this calculation, the opposing side of the free-body-diagram must be calculated. The applied moment consists of the overturning moment about the base combined with the horizontal force (both found in the load document) multiplied by the embedment depth. The extreme wind condition is to be used, as this is the most relevant condition to a sudden, catastrophic failure. The equation for applied moment is as follows:

$$M_{App} = M_{xy} + F_{xy} d_e \tag{2-2}$$

$Where:$

$M_{App} = Total\ applied\ moment$

$F_{xy} = Horizontal\ force\ felt\ at\ base\ of\ tower$

$d_e = Embedment\ depth$

The factor of safety can be calculated by dividing the resisting moment by the extreme applied moment. The factor of safety must be at least 1.5 for a foundation to pass this design check (Morgan & Ntambakwa 2008). If the design fails, increasing the foundation radius will increase the resisting moment by both lengthening the moment arm and adding to the concrete and soil backfill volumes.

2.2.5.2. Horizontal & Vertical Stress Distribution

Predicting the stress distribution under a WTG foundation is paramount to a thorough and sound design. The vertical and horizontal distributions control the stress and strain imparted on the soil. Due to

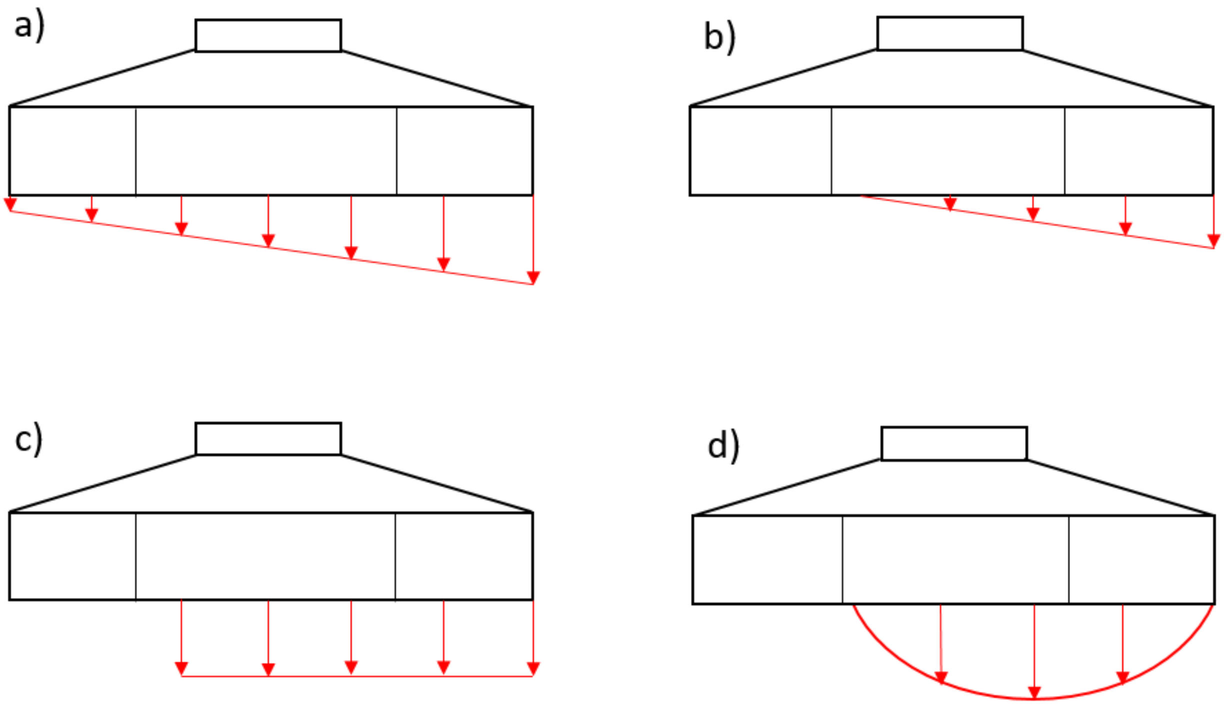

Figure 2-6: Stress distributions for eccentrically loaded WTG foundations: (a) linear along entire diameter, (b) triangular along effective bearing area (Czerniak 1969), (c) uniform along effective bearing area, and (d) circular along effective bearing area (DNV/Risø 2002).

the unique horizontal forces acting on a WTG, the vertical load acts eccentrically to the center of the footing. This eccentricity must be considered when calculating, for example, bearing capacity. Many methods for simplification exist, with each having their own strengths and weaknesses. Figure 2-6 illustrates four such distributions. In Figure 2-6a, the stress varies linearly along the entire diameter of the footing, with peak pressure occurring at the edge. Figure 2-6b utilizes an "effective bearing area", where the pressure is assumed to vary linearly along a given area of the footing. Similarly, Figures 2-6 c-d represent this bearing area, but with a uniform (c) and circular (d) distribution.

The eccentricity can be calculated according to the following formula:

$$e = \frac{M_{App}}{F_{V,extreme}} \qquad [2\text{-}3]$$

$Where$:

$M_{App} = Extreme\ applied\ moment$

$F_{V,extreme} = Total\ extreme\ vertical\ load$

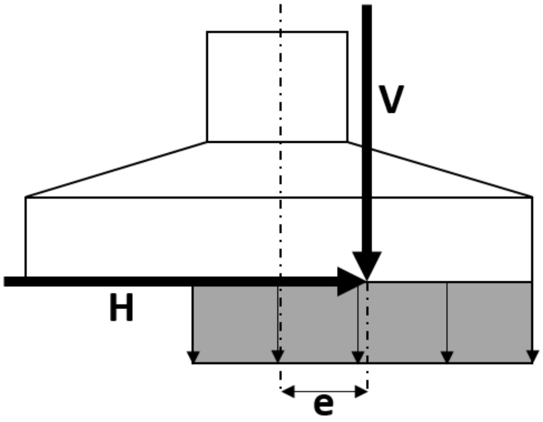

Figure 2-7: Eccentricity of a WTG foundation (from DNV/Risø 2002)

The components of the vertical force in addition to the WTG self-weight are the foundation weight and soil overburden. The applied extreme moment is calculated as in Equation 2-2. Figure 2-7 from DNV/Risø (2002) illustrates the phenomenon, where the load center occurs at the intersection of the vertical (V) and horizontal (H) forces. The distance from the footing center to the load center is the eccentricity.

DNV/Risø (2002) calls this ellipse the effective foundation area, with its center coinciding with the center of the load. Though WTG shallow foundations are typically octagonally-shaped, they can be simplified to a circle that fits perfectly inside the octagon (Fig. 2-8). For such a foundation, the foundation effective area is defined as:

$$A_{eff} = 2\left(R^2 \cos^{-1}\left(\frac{e}{R}\right) - e\sqrt{R^2 - e^2}\right) \qquad [2\text{-}4]$$

$Where$:

$R = Foundation\ radius$

$e = Load\ eccentricity$

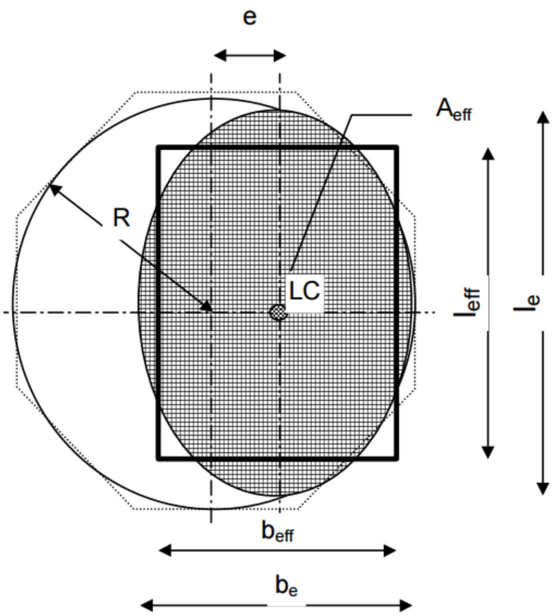

Figure 2-8: Effective foundation area (DNV/Risø 2002)

Following calculation of the effective area, the ellipse shape can be converted to a rectangular shape for use in conventional bearing capacity calculations. The length, l_{eff}, and width, b_{eff}, represent the dimensions of the rectangle, which is overlaid on the ellipse in Figure 2-8 above. The following equations are used to calculate these values:

$$l_{eff} = \sqrt{A_{eff}\left(\frac{l_e}{b_e}\right)} \qquad [2\text{-}5] \qquad\qquad b_{eff} = \frac{l_{eff}}{l_e} b_e \qquad [2\text{-}6]$$

$Where$:

$$b_e = Width\ of\ ellipse = 2(R - e) \qquad [2\text{-}7]$$

$$l_e = Length\ of\ ellipse = 2R\sqrt{1-\left(1-\frac{b}{2R}\right)^2} \quad [2\text{-}8]$$

$b = Width\ of\ foundation$

$A_{eff} = Foundation\ effective\ area$

Efforts have been made to accurately measure the horizontal stress distribution and examine the effects of varying wind loads. Adekunte et al. (2009) buried four pressure cells beneath a WTG foundation and found that the magnitude of pressure greatly depended on wind speed and direction. They also found that the magnitudes of stress were well below design predictions. Yilmaz (2014) found similar results with the nine pressure sensors placed below a WTG foundation at two sites in the Midwest. Furthermore, the instrument data pointed to a non-uniformity in stress distribution, contradicting the assumptions made in the simplification process outline earlier in this section.

Boussinesq pioneered the derivation of vertical stress distributions in an elastic half-space (EHS) due to an applied point load at the surface. His work was later refined to solutions for several geometric shapes, including strip footings, rectangles, and circles (Coduto 2010). As referenced previously, though shallow WTG foundations are typically octagonal, a circle is typically used as an approximation, as it is easier to find solutions for and mimics the overall shape quite well. Nathan Mortimore Newmark developed equations for these distributions and produced isoline contour charts for the induced stress, where each point along a given contour line represents the same influence factor. The contours take a “bulb” shape due to the increasing dissipation with depth (see – Figure 2-9).

The charts are independent of units and scale, as the distribution depends only on depths proportional to the foundation dimensions. For a given layer in consolidation calculation, one must find the associated depth fraction on the chart and use the contour the point falls on as the influence factor.

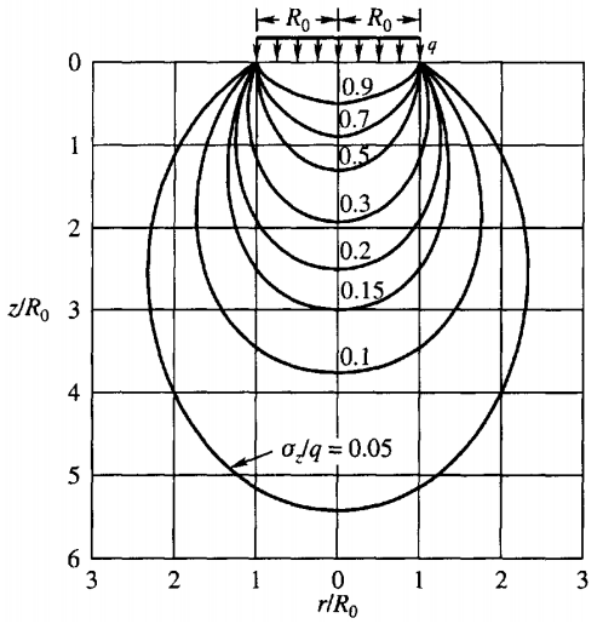

Figure 2-9: Boussinesq stress distribution contour chart for a uniformly loaded circular foundation (Murthy 2003)

The simplified solution for circular shaped footings is as follows:

$$\Delta\sigma_z = \left[1 - \left(\frac{1}{1+\left(\frac{B}{2z_f}\right)^2}\right)^{1.5}\right](q - \sigma'_{zD}) \qquad [2\text{-}9]$$

$Where$:

$B = Foundation\ diameter$

$q = Applied\ bearing\ pressure$

$z_f = Depth\ below\ soil - structure\ interface$

$\sigma'_{zD} = Vertical\ effective\ stress\ at\ depth\ D$

2.2.5.3. Bearing Capacity

The next design check is to compare the allowable bearing capacity of the soil versus the applied bearing pressure of the structure. Bearing capacity quantifies the ability of the soil to resist loading. Ultimately, the allowable bearing capacity must be greater than the applied bearing pressure to prevent foundation failure. Factors that influence the applied bearing pressure are: foundation geometry, vertical load, eccentricity due to the applied moment, and the method in which the pressure distribution is determined. Though previous research has shown the distribution to be non-uniform (Yilmaz 2014), DNV/Risø (2002) outlines the standard design process summarized in this section, and begins by simplifying the pressure distribution to a uniform load over a reduced ellipse-shaped area eccentric to the foundation center.

Once this simplification is complete, bearing capacity can be calculated using standard procedures, considering both drained and undrained conditions. For drained conditions, one can apply the following formula to a horizontal footing, as obtained in Equations 2-5 and 2-6.

$$q_d = \frac{1}{2}\gamma' b_{eff} N_\gamma s_\gamma i_\gamma + p'_o N_q s_q i_q + c_d N_c s_c i_c \qquad [2\text{-}10]$$

$Where$:

$q_d = Design\ bearing\ capacity$

$\gamma' = Saturated\ unit\ weight\ of\ soil$

$b_{eff} = Effective\ rectangle\ width$

$p'_o = Effective\ overburden\ stress$

$c_d = Undrained\ shear\ strength$

$N_\gamma, N_q, N_c = Bearing\ capacity\ factors$

$s_\gamma, s_q, s_c = Shape\ factors$

$i_\gamma, i_q, i_c = Inclination\ factors$

The three components of the above equation are based on weight (γ), overburden (q), and undrained shear strength (c), respectively. The numerous factors, where applicable, for bearing capacity, shape, and inclination can be found with a multitude of charts and equations. Equations for many of the factors for drained conditions can be found below:

$$\emptyset_d = \arctan\left(\frac{tan\emptyset}{\gamma_c}\right) \qquad [2\text{-}11]$$

Bearing Capacity Factors

$$N_q = e^{\pi tan\emptyset_d}\left(\frac{1+sin\emptyset_d}{1-sin\emptyset_d}\right) \qquad [2\text{-}12]$$

$$N_c = \left(N_q - 1\right)cot\emptyset_d \qquad [2\text{-}13]$$

$N_\gamma = \frac{1}{4}\left((N_q - 1)cos\emptyset_d\right)^{\frac{3}{2}}$ [2-14] $N_\gamma = \frac{3}{2}(N_q - 1)tan\emptyset_d$ [2-15]

Shape Factors

$$s_\gamma = 1 - 0.4\frac{b_{eff}}{l_{eff}} \quad [2\text{-}16]$$

$$s_c = s_q = 1 + 0.2\frac{b_{eff}}{l_{eff}} \quad [2\text{-}17]$$

Inclination Factors

$$i_q = i_c = \left(1 - \frac{H_d}{V_d + A_{eff}c_d cot\emptyset_d}\right)^2 \quad [2\text{-}18]$$

$$i_\gamma = i_q^2 \quad [2\text{-}19]$$

An analysis must also be run for undrained conditions, where the pore pressure is not able to immediately able to dissipate, and instead takes on all of the load immediately upon loading (assuming a Skempton's coefficient of 1). During such conditions, it is assumed the friction angle, $\emptyset$, goes to 0^o. The governing equation for drained conditions and its factors are as follows:

$$q_d = c_{ud} * N_c^o * s_c^o * i_c^o + p_o \quad [2\text{-}20]$$

$Where$:

$$c_{ud} = \frac{c}{\gamma_c} \quad [2\text{-}21]$$

$$N_c^o = \pi + 2 \quad [2\text{-}22]$$

$$s_c^o = s_c \quad [2\text{-}23]$$

$$i_c^o = 0.5 + 0.5\sqrt{1 - \frac{H}{A_{eff}c_{ud}}} \quad [2\text{-}24]$$

Once both analyses have been completed, the controlling parameter is the smallest value (i.e. the bearing capacity of the soil is taken to be the weakest between the drained and undrained conditions). The allowable bearing capacity ultimately must satisfy a factor of safety of 2.26. Similar to the overturning analysis, the factor of safety is obtained by simply dividing the dividing the allowable bearing capacity by the applied bearing pressure.

$FS = \frac{q_{all}}{q_u} \geq 2.26$ [2-25]

$Where$:

$q_{all} = Allowable\ bearing\ capacity$

$q_u = Applied\ bearing\ pressure$

2.2.5.4. Rotational Stiffness

The stiffness of a WTG foundation is analogous to a spring's stiffness. Following Hooke's Law, as the load increases, so does the deflection. The stiffness coefficient is generally denoted as 'k'. The spring coefficient of the foundation system depends on the strength and stiffness of both the concrete footing and underlying soil. Hooke's Law of Elasticity is calculated using the formula below:

$F = -k\Delta x$ [2-25]

$Where$:

$F = Applied\ force$

$k = Spring\ coefficient$

$\Delta x = Total\ displacement\ of\ the\ spring\ from\ rest$

There are four modes of stiffness in a WTG foundation: vertical, horizontal, torsional, and rotational, denoted K_V, K_H, K_T, and K_φ, respectively. Vertical stiffness describes the stiffness in a linear upward-downward direction, much like the classic spring system discussed above. Horizontal stiffness describes the translational response to forces in the x-y axis. Torsional stiffness controls the response of the WTG in a "twisting" motion about the vertical axis. Rotational stiffness describes the soil's response to overturning moments, with the tower rotating about the x or y axis. Of the four modes, rotational stiffness is almost always the controlling design parameter, and often controls the overall design when constructed on soil with a shear modulus below 29 MPa (Lang 2012). Using Hooke's Law, the spring constant for rotational stiffness quantifies the rate the WTG system will rotate due to a given applied moment.

$M = K_\varphi \theta$ [2-26]

$Where$:

$M = Applied\ moment$

$K_\varphi = Rotational\ spring\ constant$

$\theta = Rotational\ displacement\ (in\ radians)$

As stated, rotational stiffness is of particular interest to WTG foundation design. Sometimes referred to as “rocking stiffness”, rotational stiffness is a concept derived from Hooke’s Law of Elasticity. As the WTG rocks back and forth during operation, it imparts a cyclic load into the foundation soil. Calculations of rotational stiffness are centered on the shear modulus and derivations of elastic half-space (EHS) theory. An EHS is a highly idealized medium that is assumed to be perfectly elastic, homogenous, isotropic, and semi-infinite. Boussinesq (1885) first provided a closed-form solution to stress distributions below a point load above an EHS, which became the basis for further derivations of stress distributions below various shapes. Borowicka (1943) developed Boussinesq’s theory for application to rocking motion of a circular foundation, which was given in more modern terms by Richart et al. (1970). The equation for rotational stiffness follows:

$$K_\varphi = \frac{8GR^3}{3(1-v)} = \frac{M}{\theta} \qquad [2\text{-}27]$$

$Where$:

$G = Shear\ modulus$

$R = Foundation\ radius$

$v = Poisson's\ ratio$

$M = Applied\ Moment$

$\theta = Foundation\ rotation\ (radians)$

When designing the footing, the engineer must match the minimum rotational stiffness given in the load document. With K_φ known, the engineer must then apply a shear modulus and Poisson's ratio representative of the soil medium. Typically, the Poisson's ratio is estimated based on soil type and information gathered from the geotechnical report. Table 2-2 (Bowles 1982) outlines typical values for a variety of soil types.

Table 2-2: Typical values of Poisson's Ratio (Bowles, 1982)

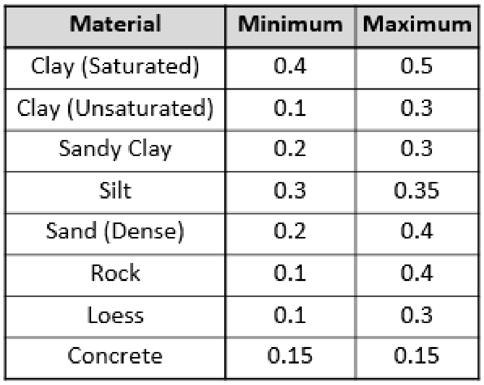

Material	Minimum	Maximum
Clay (Saturated)	0.4	0.5
Clay (Unsaturated)	0.1	0.3
Sandy Clay	0.2	0.3
Silt	0.3	0.35
Sand (Dense)	0.2	0.4
Rock	0.1	0.4
Loess	0.1	0.3
Concrete	0.15	0.15

DNV/Risø (2002) supplies a multitude of empirical methods for determining the shear modulus, G. In practice, however, G is most commonly found via measurement of the shear wave velocity by cone penetration testing (CPT), seismic testing, or surface geophysical testing (Tinjum & Christensen 2010). Using Equation 2-28 (Araya et al. 1979), the maximum shear modulus can be derived. For reference, typical shear wave velocities are given in Table 2-3 (Tinjum & Christensen 2010).

$$G_o = \rho V_s^2 \qquad [2\text{-}28]$$

$Where$:

$\rho = Density\ of\ medium$

$V_s = Shear\ wave\ velocity$

Table 2-3: Typical shear wave velocities (Tinjum & Christensen 2010)

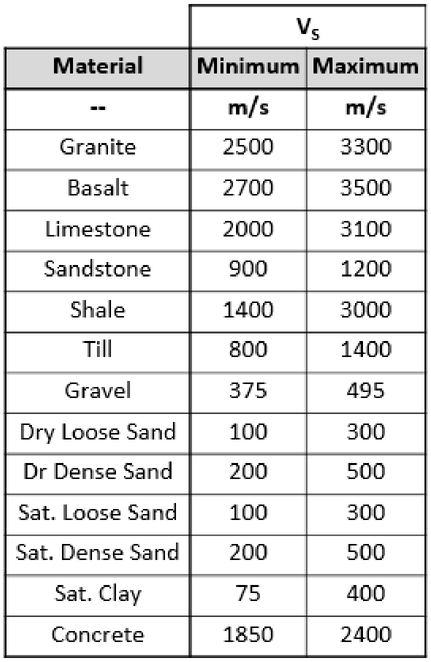

	V_S	
Material	**Minimum**	**Maximum**
--	**m/s**	**m/s**
Granite	2500	3300
Basalt	2700	3500
Limestone	2000	3100
Sandstone	900	1200
Shale	1400	3000
Till	800	1400
Gravel	375	495
Dry Loose Sand	100	300
Dr Dense Sand	200	500
Sat. Loose Sand	100	300
Sat. Dense Sand	200	500
Sat. Clay	75	400
Concrete	1850	2400

In reality, the conditions in which the relationship was derived are unrealistic. *In situ*, the foundation is embedded beneath the surface over multiple layers of soil and/or bedrock. DNV/Risø (2002) gives correction terms for depth to bedrock (Elsabee 1977), stratification (Hadjian & Luco 1977), and embedment above bedrock (Kausel 1972). Figure 2-10 summarizes the modes of stiffness and their respective corrections. The corrections are empirical relationships derived from the results of finite element models. Though they have thus far been conservatively adequate, further field and finite element validation of these formulas with respect to WTG foundations has remained relatively untouched. As these formulas are, again, empirically derived and based on EHS theory, they represent highly specific, idealized conditions and are not mechanistically correct.

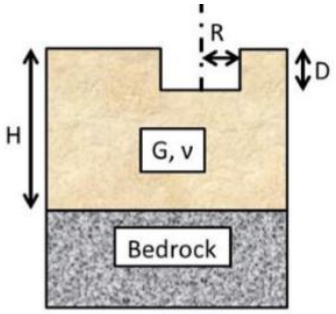

Range of Validity:

$D/R < 2$ and $D/H < 1/2$

Mode of Motion	Foundation Stiffness
Vertical	$K_V = \frac{4GR}{1-\nu}(1+1.28\frac{R}{H})(1+\frac{D}{2R})(1+(0.85-0.28\frac{D}{R})\frac{D/H}{1-D/H})$
Horizontal	$K_H = \frac{8GR}{1-\nu}(1+\frac{R}{2H})(1+\frac{2}{3}\frac{D}{R})(1+\frac{5}{4}\frac{D}{H})$
Rocking	$K_R = \frac{8GR^3}{3(1-\nu)}(1+\frac{R}{6H})(1+2\frac{D}{R})(1+0.7\frac{D}{H})$
Torsion	$K_T = \frac{16GR^3}{3}(1+\frac{8D}{3R})$

	On stratum over bedrock	On stratum over half-space
	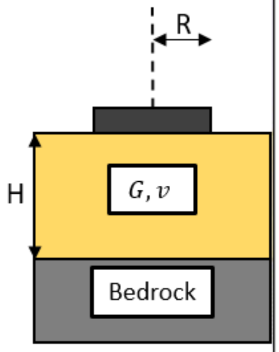	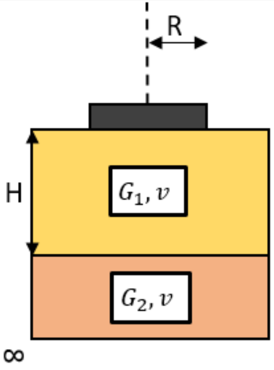
Mode of motion	Foundation stiffness	Foundation stiffness
Vertical	$K_V = \frac{4GR}{1-\nu}(1+1.28\frac{R}{H})$	$K_V = \frac{4G_1R}{1-\nu_1}\frac{1+1.28\frac{R}{H}}{1+1.28\frac{R}{H}\frac{G_1}{G_2}}$; $1 \le H/R \le 5$
Horizontal	$K_H = \frac{4GR}{1-\nu}(1+1.28\frac{R}{H})$	$K_H = \frac{8G_1R}{1-\nu_1}\frac{1+\frac{R}{2H}}{1+\frac{R}{2H}\frac{G_1}{G_2}}$; $1 \le H/R \le 4$
Rocking	$K_R = \frac{8GR^3}{3(1-\nu)}(1+\frac{R}{6H})$	$K_R = \frac{8G_1R^3}{3(1-\nu_1)}\frac{1+\frac{R}{6H}}{1+\frac{R}{6H}\frac{G_1}{G_2}}$; $0.75 \le H/R \le 2$
Torsion	$K_T = \frac{16GR^3}{3}$	Not given

Figure 2-10: Corrections for embedment above bedrock (top), depth to bedrock (bottom left), and depth to 2nd stratum (bottom right) (DNV/Risø, 2002)

Accurate determination of the shear modulus is key to correctly calculating foundation stiffness.

As discussed previously, G_o is frequently found using the shear wave velocity (see – Equation 2-28). At small strain (<0.001%), inter-particle forces play the dominant role in the soil's dynamic response and the shear modulus remains relatively constant (Vucetic & Dobry 1991; Diaz-Rodriguez & Lopez-Molina 2008). At larger levels of strain (>0.001%), however, relative slippage of particles degrades the soil fabric, resulting in a re-structuring of the soil skeleton and non-linear reduction of the shear modulus (Santamarina et al. 2001; Santamarina 2003; Cho et al. 2006; Diaz-Rodriguez & Lopez-Molina 2008). This reduction in shear modulus is quantified in a shear modulus reduction curve (SMRC) (Figure 2-11).

The shape of this curve is influenced by many properties of the soil, including particle size distribution, plasticity index, matric suction (ψ), and void ratio (Wu et al. 1984; Stanislav 2004; Biglari & Ashayeri 2011; Khosravi et al. 2016). Beyond the actual shape of the curve, the magnitude of shear strain determines the G most suitable for design use. According to DNV/Risø (2002), the recommended strain for WTG loading is 0.1%, resulting in a reduction coefficient of roughly 0.2 to 0.72. Though engineers in practice use this assumption, field experimentation has yielded a maximum *in situ* strain of 0.006% in stiff clays, suggesting that current industry practice uses overly-conservative strains for this type of soil (Yilmaz 2014), warranting further field study to develop validated, accurate assumptions. A slight decrease in

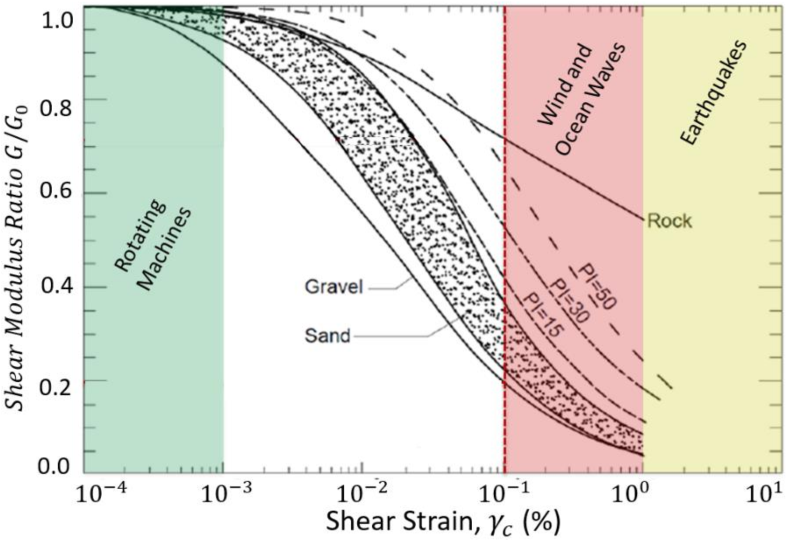

Figure 2-11: Shear modulus reduction curve variation based on soil type/plasticity index (after Sykora et al. 1992 and Vucetic & Dobry 1991) and typical strains (DNV/Risø 2002).

assumed shear strain could have potentially large ramifications to the reduced shear modulus, which directly influences foundation size.

Finally, revisiting Equation 2-26, the maximum foundation rotation can be calculated. Knowing the rotational stiffness spring coefficient and applied overturning moment, θ in radians can be calculated by rearranging the equation:

$$\theta = \frac{M}{K_{\varphi}} \qquad [2\text{-}29]$$

$Where$:

$M = Applied\ overturning\ moment$

$K_{\varphi} = Foundation\ rotational\ stiffness$

2.2.5.5. Sliding

Due to the large magnitude of horizontal forces acting on the WTG, precautions must be taken to prevent horizontal translation, or sliding, across the soil-structure interface. Similar to classic friction calculations, the total vertical force multiplied by a friction coefficient yields a resisting frictional force. If this force is larger than the applied horizontal force, the structure will remain in place. To pass this design check, the factor of safety must meet a minimum of 1.5.

Friction Coefficient

$$\mu = tan\delta \qquad [2\text{-}30]$$

$Where$:

$\delta = Friction\ angle\ between\ soil\ and\ structure$

Frictional Force

$$F_f = \mu(W_{conc} + W_{soil} + F_V) \qquad [2\text{-}13]$$

$Where$:

$W_{conc} = Weight\ of\ concrete\ foundation$

$W_{soil} = Weight\ of\ soil\ backfill$

$F_V = Vertical\ load\ of\ WTG\ structure$

$\mu = Friction\ coefficient$

Factor of Safety

$$FS_{sliding} = \frac{F_f}{F_H} \geq 1.5 \qquad [2\text{-}32]$$

$Where$:

$F_f = Frictional\ resisting\ force$

$F_H = Applied\ horizontal\ force$

2.2.5.6. Settlement

Similar to other types of shallow foundations, WTG's undergo immediate elastic settlement, primary consolidation, and secondary compression due to the vertical load of the system. Relative to larger structures, WTG bearing pressures tend to be low, typically between 50 and 75 kPa. According to Tinjum & Christensen (2010), WTG constructed above adequately strong/stiff soil will settle no more than 2.5 cm. WTG foundations also experience cyclic loading due to WTG tower rocking. This cyclic load can cause an accumulation of plastic strains, and, with the existence of a predominant wind direction, can unevenly distribute this dynamic settlement to one side of the foundation, resulting in a differential settlement/inclination. Current design guidance gives no formal methodology or means to estimate this type of settlement, and does not supply criteria for failure, leaving the engineer to use past experience to guide their design process. Analysis of strain accumulation effect below WTG loads will be one of the main focuses of this thesis.

Immediate settlement is a result of the elastic properties of soil upon loading. In fine-grained soil, this component is generally small compared to time-dependent settlement, however, in coarse-grained soil, immediate settlement is the dominant settlement mechanism due to the rapid dissipation of pore pressures. Immediate settlement of fine-grained soil can be calculated according to the following equation (Gazetas *et al*. 1985):

$$S_i = C_s q B \left(\frac{1-v^2}{E_u}\right) \qquad [2\text{-}33]$$

$Where$:

$C_s = Shape\ \&\ rigidity\ factor$

$q = Applied\ surface\ load$

$B = Foundation\ characteristic\ dimension$

$v = Pisson's\ ratio$

$E_u = Young's\ Modulus$

In coarse grained soil, the totality of settlement must be captured in immediate settlement calculations. Unlike fine grained soil, relatively undisturbed samples are almost impossible to capture for laboratory testing. As a result, alternative methods must be used to infer the soil properties, such as SPT or CPT testing. A commonly used methodology is the Schmertmann (1970) approach. Based on assumptions of an elastic half-space (see – Sec. 2.2.5.3), this approach uses both material properties and empirically derived correction factors to determine settlement:

$$S_i = C_1 C_2 \Delta \mathrm{p} \sum_{i=1}^{n} \left(\frac{I_z}{E}\right)_i \Delta z_i \qquad [2\text{-}34]$$

$Where$:

$C_1, C_2 = Correction\ factors$

$\Delta p = Net\ footing\ pressure$

$I_z = Influence\ factor$

$E = Young's\ Modulus$

$\Delta z = Layer\ thickness$

And:

$$C_1 = 1 - 0.5\left(\frac{\sigma' m}{\Delta p}\right) \geq 0.5 \qquad [2\text{-}35] \qquad\qquad C_2 = 1 + 0.2\log\left(\frac{t}{0.1}\right) \qquad [2\text{-}36]$$

$\sigma' = Effective\ stress\ at\ depth$

$m = Depth\ of\ layer$

$t = Time\ since\ load\ application$

Schmertmann also provides a method for determining strain influence factor, I_z, where the maximum influence factor of 0.6 occurs at a depth equal to half of the foundation width (i.e. $\frac{z}{B} = 0.5$). The influence factor diagram given below includes distributions for plane strain and axisymmetric conditions.

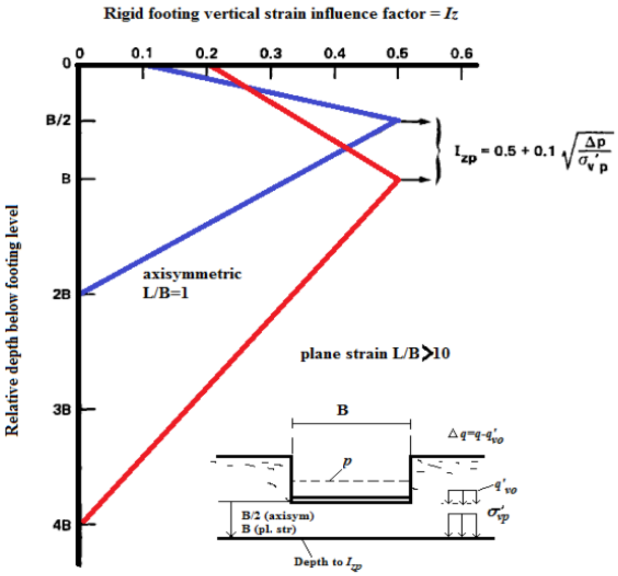

Figure 2-12: Influence factor diagram for plane strain and axisymmetry (after Schmertmann 1978)

Fine-grained soil, on the other hand, settles slowly over time in a process called “consolidation settlement”, where water is squeezed out of the pores, reducing the overall volume of the soil, resulting in a vertical displacement of the foundation. The low permeability of fine-grained soils restricts flow of water and results in initially undrained conditions, as opposed to coarse-grained soils, such as sands, where the pores are relatively large and allow much easier drainage of water. When a load is applied to the soil, assumed to be saturated, the pore water takes on the load, which, over time, forces the water out of the pore space until hydrostatic equilibrium is again reached.

The most common approach to predicting consolidation settlement was developed by Karl Terzaghi, where laboratory testing yields parameters to be used in combination with soil conditions and properties (Coduto *et al.* 2010). The two parameters of interest are the compression index, C_c, and recompression index, C_r (see – Figure 2-13). The use of each of these indices depends on the induced stress and the soil's stress history, quantified by the over-consolidation ratio (OCR).

$$OCR = \frac{\sigma'_{zc}}{\sigma'_{zo}} \qquad [2\text{-}37]$$

$Where$:

$\sigma'_{zc} = Preconsolidation\ stress$

$\sigma'_{zo} = Overburden\ effective\ stress$

When the OCR is less than 1.0, the soil in question has not experienced a stress greater than the current stress level, and is referred to as "normally consolidated". In cases where the OCR is greater than 1.0, the soil has experienced a vertical stress greater than what currently exists, and is referred to as "over consolidated". Due to past soil skeleton restructuring, these types of soil consolidate at a slower rate than normally consolidated soil. This leads to three possible scenarios for consolidation settlement calculation: (1) normally consolidated soil (2) over-consolidated where the induced stress is smaller than pre-

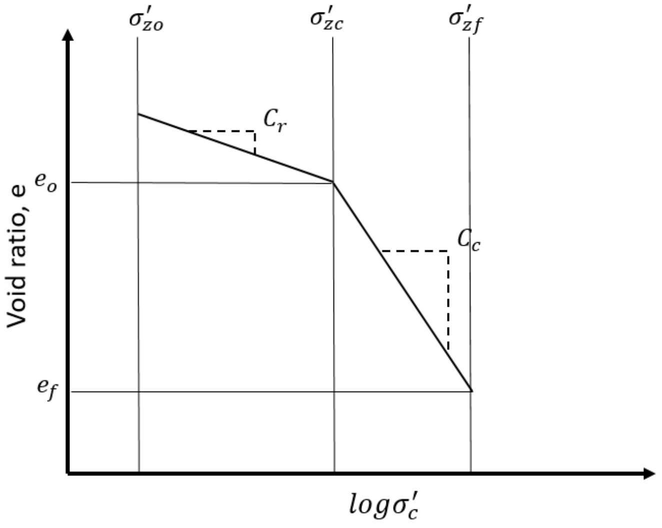

Figure 2-13: One dimensional compression lab results

consolidation stress and (3) over-consolidated soil where the induced stress is larger than pre-consolidation stress.

Each of these scenarios requires a unique equation, though the same C_c and C_r apply to each. The soil should first be broken up into layers whose thickness should be uniform, logical, and small enough to attain good resolution, but thick enough so that calculation time is not excessive. The consolidation for each layer should then be summed to estimate total settlement. Shallow, octagonal WTG foundations are assumed perfectly rigid, thus requiring the inclusion of a rigidity factor, r, of 0.85 (Coduto 2010). The three equations are outlined below:

Normally Consolidated:

$$\sigma'_{vo} \geq \sigma'_p \qquad s_c = r \sum \frac{C_c}{1+e_o} H log\left(\frac{\sigma'_{vf}}{\sigma'_{vo}}\right) \qquad [2\text{-}38]$$

Overconsolidated:

$$\sigma'_{vf} < \sigma'_p \qquad s_c = r \sum \frac{C_r}{1+e_o} H log\left(\frac{\sigma'_{vf}}{\sigma'_{vo}}\right) \qquad [2\text{-}39]$$

Overconsolidated:

$$\sigma'_{vo} < \sigma'_p < \sigma'_{vf} \qquad s_c = r \sum \left[\frac{C_r}{1+e_o} H log\left(\frac{\sigma'_p}{\sigma'_{vo}}\right) + \frac{C_c}{1+e_o} H log\left(\frac{\sigma'_{vf}}{\sigma'_p}\right)\right] \qquad [2\text{-}40]$$

$Where$:

$s_c = Consolidation\ settlement$

$r = Rigitiy\ factor$

$C_c = Compression\ index$

$C_r = Recompression\ index$

$H = Layer\ thickness$

$\sigma'_p = Effective\ preconsolidation\ stress$

$\sigma'_{vo} = Effective\ overburden\ stress$

$\sigma'_{vf} = Effective\ induced\ stress$

$e_o = Initial\ void\ ratio$

Beyond the compression indices, the most significant factors affecting the total settlement are the magnitude and propagation of induced stress. As soil dissipates applied loads, the stress felt a distance below the surface will not be equal to the stress at the surface. Calculation of the induced stress at a given depth begins by calculation of the initial effective stress, followed by addition of the applied load and reduction by an influence factor.

Initial Effective Stress:

$$\sigma'_{zo} = \sum_{i=1}^{n} \gamma_i H_i - \mu \qquad [2\text{-}41]$$

$Where$:

$\gamma_i = Unit\ weight\ of\ i^{th}\ layer$

$H_i = Thickness\ of\ i^{th}\ layer$

$\mu = Pore\ water\ pressure$

Final Effective Stress:

$$\sigma'_{vf} = \sigma'_{zo} + \Delta\sigma_z \qquad [2\text{-}42]$$

$Where$:

$\sigma'_{zo} = Initial\ effective\ stress\ at\ midpoint\ of\ layer$

$\Delta\sigma_z = Induced\ stress\ at\ midpoint\ of\ layer$

Induced Effective Stress:

$$\Delta\sigma'_z = I_\sigma(q - \sigma'_{zD}) \qquad [2\text{-}43]$$

$Where$:

$I_\sigma = Influence\ factor$

$q = Applied\ pressure\ at\ soil - structure\ interface$

$\sigma'_{zD} = Effective\ stress\ at\ depth\ D$

2.3 Dynamic Soil Properties

Classic soil mechanics problems revolve around assumptions of static conditions, however, in reality, many geotechnical problems involve dynamic loading conditions, such as earthquake engineering, machine foundations, and railway design. Soils are generally considered to fall under an elasto-plastic model (Budhu 2007), where soil exhibits deformation properties elastically and plastically. The stress-strain relationship of soil becomes non-linear as strain increases, and eventually reaches a threshold where it begins to develop non-recoverable plastic strain (Lade 1977; Porter 1946; Wood 1991).

As discussed in section 1.2.1, WTG foundations experience spatially and temporally variable loads. In addition to loads changing with the speed and direction of the wind (Yilmaz 2014), the WTG tower constantly oscillates/vibrates, imparting a dynamic, cyclic load onto the soil. The soil's response to such forces is determined by two parameters: shear modulus (G) and damping (D). The shear modulus is a ratio of the shear stress and shear strain. The material damping quantifies the soil's ability to dissipate the energy from applied loading (Prakash 1981). In a "backbone curve" (Fig. 2-14), which plots shear strain vs shear stress, the initial shear modulus is equal to the small-strain slope of the curve.

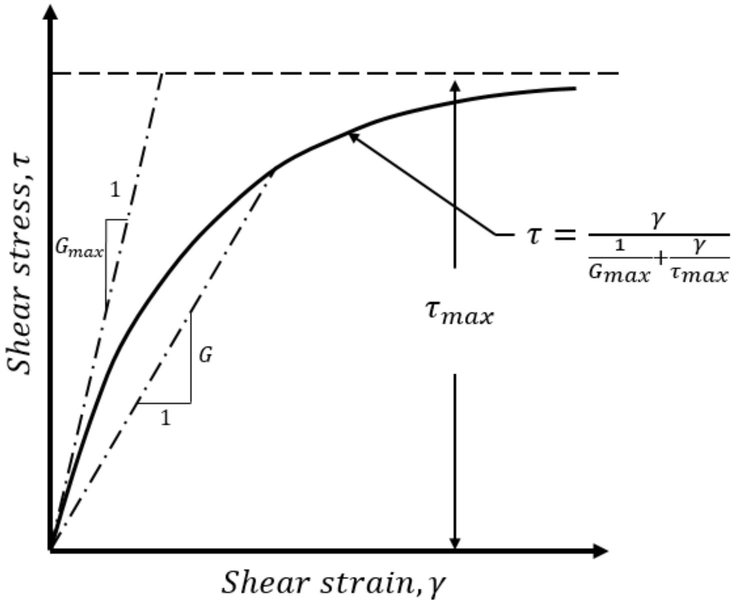

Figure 2-14: Backbone curve for shear moduli (from Hardin & Drnevich 1972)

A soil may also be characterized by its secant or tangent shear modulus, depending on the stress applied. Secant modulus is found by calculating the slope of a line between two points on the curve, whereas the tangent modulus is calculated by finding the slope of a line tangent to a point on the curve (Hardin & Drnevich 1972). The initial shear modulus is a possible example of a tangent modulus (Fig. 2-14). The reduced shear modulus used in rotational stiffness calculations (see – Section 1.2.5.3) is an example of a secant shear modulus in practice.

2.3.1 Elastic Wave Propagation in Soils

Fundamental to soil dynamics is the propagation of waves, as any force imparted on/in a soil medium will travel through the soil at an amplitude and speed dependent on the soil's material properties. Two types of waves, longitudinal and shear, are used to determine small-strain elastic properties of soils. Laboratory methods to determine such dynamic properties involve the use of cylindrical rods of soil of a finite-length, such as in the *Resonant Column* and *Cyclic Triaxial* methods, discussed later in Section 2.3. The fundamental equation governing wave propagation in an elastic medium is known as the "wave equation" and is as follows:

$$\frac{\partial^2 u}{\partial t^2} = v^2 \frac{\partial^2 u}{\partial x^2} \qquad [2\text{-}45]$$

$Where$:

$u = Displacement\ in\ the\ x\ direction$

$t = Time$

$v = Wave\ Velocity$

This equation is a fundamental equation of mechanics and can be applied to many physical systems experiencing vibration, such as rods in longitudinal and torsional motion (Richart *et al*. 1970). The resonant column approach, the focus of Chapter 1 (Sec. 5) of this thesis, utilizes torsional motion to determine the shear wave velocity and strain amplitude to produce a shear modulus reduction curve for a given soil specimen (see – Section 2.2.5.3). The use of a cyclic triaxial apparatus utilizes longitudinal/axial motion to impart a load into the soil specimen, and is used in Chapter 2 of this thesis to measure dynamic strain accumulation.

2.3.2 Shear Modulus & Damping

The response of soil to applied loading is often modelled as a vibrating spring-dashpot system, where the spring and dashpot are characterized by the shear modulus, G, and material damping, D, respectively (Richart *et al.* 1970). Figure 2-15 illustrates the system using a classic spring and viscous damper (i.e. dashpot).

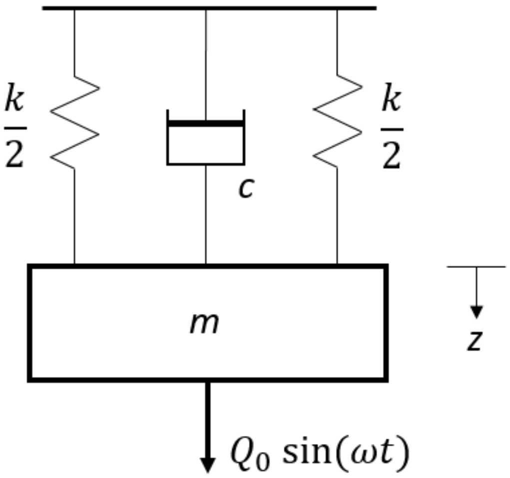

Figure 2-15: Simple spring-dashpot system undergoing forced vibration (from Richart et al. 1970)

Though this model uses an idealized viscous damping dashpot for mathematical simplification, the model is generally satisfactory and valid for real-world systems (Richart *et al.* 1970). The forces in this system balance according to the following equation:

$$m\ddot{z} + c\dot{z} + kz = Q_o sin\omega t \quad [2\text{-}46]$$

$Where$:

$m = System\ mass$

$c = Damping\ coefficient$

$k = Spring\ constant$

$z = Vertical\ displacement$

$\dot{z} = Vertical\ velocity$

$\ddot{z} = Vertical\ acceleration$

$Q_o = Force\ amplitude$

$\omega = Circular\ frequency$

$t = Time$

In this model, G is represented by the spring constant. The shear modulus describes the soil's stress-strain relationship with respect to forces perpendicular to axial loads (see – Figure 2-16), where a higher shear modulus means a larger force is required to apply an equivalent strain.

Shear strain

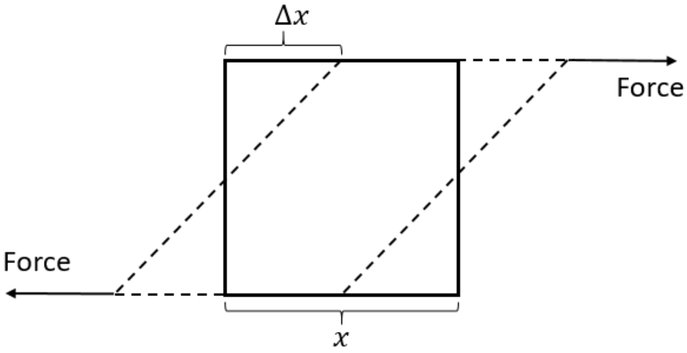

Figure 2-16: Illustration of an element's shear response to shear forces.

$$\gamma = \frac{\Delta x}{x} \qquad [2\text{-}47]$$

$Where$:

$\Delta x = Deformation\ in\ the\ x - direction$

$x = Original\ element\ length$

Shear Modulus

$$G = \frac{\tau}{\gamma} \qquad [2\text{-}48]$$

$Where$:

$\tau = Shear\ stress$

Shear modulus can be calculated via the shear wave velocity as in Equation 2-28 or, if the Young's modulus and Poisson's ratio are known, via the following relationship:

$$G = \frac{E}{2(1+v)} \qquad [2\text{-}49]$$

$Where$:

$E = Young's\ modulus$

$v = Poisson's\ ratio$

Shear modulus is a function of many soil parameters, including soil type, water content, void ratio, effective stress, and shear strain. As void ratio is directly tied to material density, the shear modulus decreases as void ratio increases. Similarly, as water content/saturation decrease, shear modulus increases due to the strengthening effects of matric suction (Lu & Likos 2004). As described in Sec. 2.2.5.4, the shear modulus deteriorates as the cyclic shear strain amplitude increases. Furthermore, as effective stress increases, so does the shear modulus (Kramer 1996).

Though WTG design check calculations do not explicitly take into account material damping, it is still an important soil property that affects its dynamic response, as it describes the soil's ability to dissipate mechanical energy. When an excitation is applied and then removed, material damping controls how quickly the amplitude of vibration decreases to zero. Damping is described by the viscous damping coefficient, C, which is defined as follows (Prakash 1981):

$$C = \frac{F_d}{\dot{z}} \qquad [2\text{-}50]$$

Where:

$\dot{z} = Velocity$

$F_v = Damping\ force$

There exists a special case of damping called critical damping, which results in the most rapid approach to zero amplitude for a system (Prakash 1981). It is defined as follows:

$$c_c = 2m\omega_n \qquad [2\text{-}51]$$

Where:

$m = Mass$

$\omega_n = Natural\ frequency$

However, damping is commonly given as a number known as the damping ratio, D, which is a ratio of the actual damping to critical damping (Prakash 1981). Two methods exist for determining the damping ratio of a vibrating system, such as a soil in a resonant column device: logarithmic decrement and half-power bandwidth.

The logarithmic decrement method measures the decay of the amplitude of a signal for a freely vibrating system, and can be calculated by the following equation:

$$D = \frac{1}{2\pi} \ln\left(\frac{x_1}{x_2}\right) \tag{2-52}$$

Where:

$x_1 = Amplitude\ of initial\ vibration$

$x_2 = Amplitude\ of\ successive\ vibration$

For a system under a constant excitation force with varying frequencies, the half-power bandwidth method can be used, which utilizes a plot of frequency vs. amplitude. The “half power” component refers to the point on the resonance curve where the response signal is at half the power of the maximum, or resonant mode. This occurs when the amplitude is 0.707 times the peak amplitude on either side of the curve. The damping ratio can be calculated as follows:

$$D = \frac{1}{2}\frac{f_2 - f_1}{f_n} \tag{2-53}$$

Where:

$f_n = Natural\ frequency$

$f_1 = Frequency\ of\ half\ power\ (f_1 < f_n)$

$f_2 = Frequency\ of\ half - power\ (f_2 > f_n)$

2.4 Measurement Techniques

2.4.1 Resonant Column

The resonant column apparatus is used to measure dynamic soil response at low strain levels (<0.01%) in a non-destructive manner (Drnevich *et al*. 1978), utilizing torsional motion to impart shear waves into the soil. By propagating a “sweep” of a range of frequencies, the resonant frequency of the system can be determined by measuring the peak amplitude response of the soil. The resonant frequency can then be used to calculate the shear modulus of the soil using the theory of elastic wave propagation (Richart *et al.* 1970). First developed by Ishimoto & Iida (1937), the concept has been applied in various iterations and developments, with the most common being the Hardin type and Stokoe type, which apply unique boundary conditions to achieve desired results.

The Hardin type utilizes a *fixed-free* boundary condition, where the bottom of the specimen is fixed to a bottom platen, while the top of the cylinder is attached to a top platen and heavy, freely rotating oscillator controlled by a magnet-coil system. The high mass of the oscillator is necessary to apply sufficient shear strain to the specimen, and must be counterbalanced to control deviatoric stress (Richart *et al.* 1970). In this study, a Hardin-type resonant column is used, with the operation and components described in further detail later in this thesis. The Stokoe type utilizes a *free-free* or *fixed-free* condition to apply sufficient shear strain. Stokoe type resonant columns have the advantage over Hardin types in that they can apply a larger torque and are generally easier to assemble and operate. As shown in Figure 2-17, the bottom of the specimen is, again, fixed to the bottom platen, while the top is connected to a top platen that is rotated by a magnet-coil system that is *fixed* to the resonant column apparatus. Stokoe's method, after extended refinement and development, was adopted as a testing standard by ASTM (ASTM 4015-07).

2.4.2 Bender Elements

Similarly, bender elements testing utilizes measurement of shear waves in a soil specimen. This method uses two small piezoelectric elements inserted into either end of a specimen to simulate small cyclic strains ($<10^{-5}$) in a material, such as soil. When two piezoelectric elements are excited with an alternating voltage, a bending motion is induced. This bending motion sends waves through the soil specimen, which in turn apply an alternating bending force to the second piezoelectric element, which creates a voltage reading that can be recorded and monitored. The shear wave velocity can then be determined by calculating the time delay in signal from one bender element to the other. Using the shear modulus and specimen density, the shear modulus can then be determined for the soil.

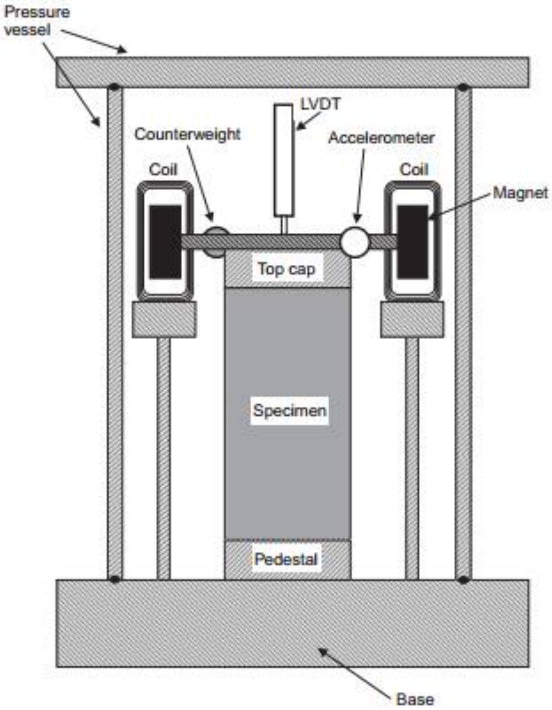

Figure 2-17: Stokoe-type resonant column schematic (Clayton et al. 2009)

2.4.3 Cyclic Triaxial

Given that resonant column and bender elements methods cannot accurately induce and measure large strains, the cyclic triaxial apparatus is most frequently used to measure the shear modulus as such strains.

The setup is similar to a conventional triaxial test, where a cylindrical soil specimen within a rubber membrane is placed between a top and bottom platen. The bottom platen is fixed, while the top platen is free to move up and down. A confining pressure can be applied to the cell chamber to control the net or effective stress of the specimen. A cyclic axial stress is then applied to the specimen at a rate of typically 0.1-1 Hz. Using recorded axial stress and strain measurements, a Young's modulus can be calculated for the cylinder, which, using Poisson's ratio, can be converted to a shear modulus.

2.3. Unsaturated Soils

2.3.1. Soil Suction

Due to the influences of several phenomena, soil that is in an unsaturated state (i.e. <100% saturation) will experience a negative pore pressure effect, creating tension within the soil (Fredlund & Raharjdo 2012). In other words, a suction force will exist within the soil skeleton. According to Lu and Likos (2002), soil suction is defined as the "thermodynamic potential of soil pore water relative to a reference potential of free water," where free water refers to water that does not have a dissolved solute, mixture of phases (e.g. air and water), or external forces beyond gravity. Lu and Likos (2002) outline three dominant phenomena that impact the soil suction: capillarity, osmotic effects, and short-range adsorption effects. Capillary effects arise from the curved air-water interface, where the surface tension of water imparts a tensile force, pulling the soil particles together. Osmotic suction is the consequence of a change in chemical concentrations of a dissolved solute, which will induce a spatial gradient within the soil, thus increasing the pore water's potential. Short-range adsorption effects are products of electrical fields and van der Waals forces between particles.

2.3.2. Soil-Water Retention Curve

The soil water characteristic curve (SWCC) describes the relationship between soil suction and saturation (or water content) for a given soil (Lu & Likos 2002). Typically plotted with the logarithm of soil suction, the shape of the curve varies considerably for different soils. General shapes for sands, silts,

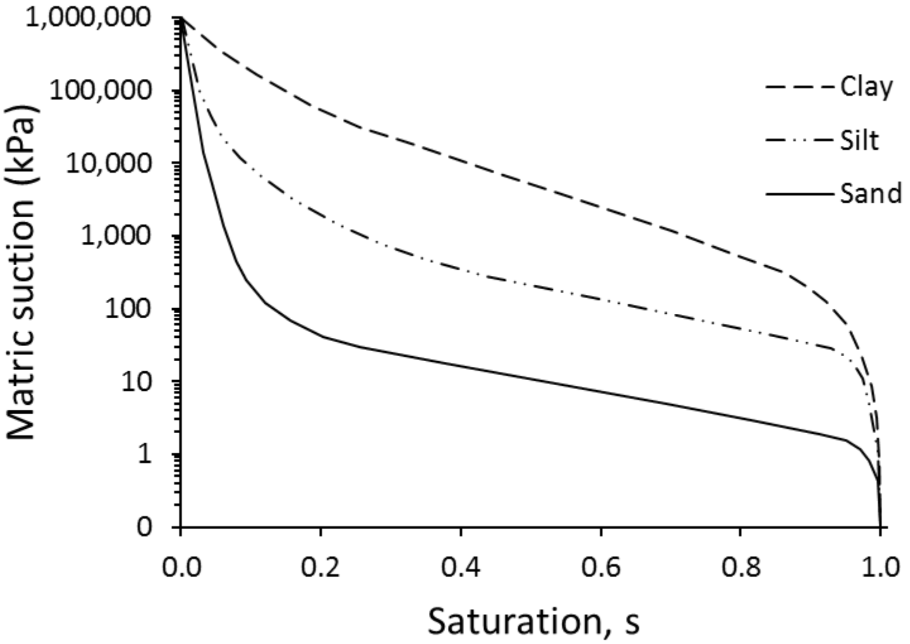

Figure 2-18: Typical SWCC curves for various soil types (from Lu & Likos 2002).

and clays can be seen in Fig. 2-18. The primary influencing factors on shape include pore size distribution, grain size distribution, density, organic content, and minerology (Lu & Likos 2002).

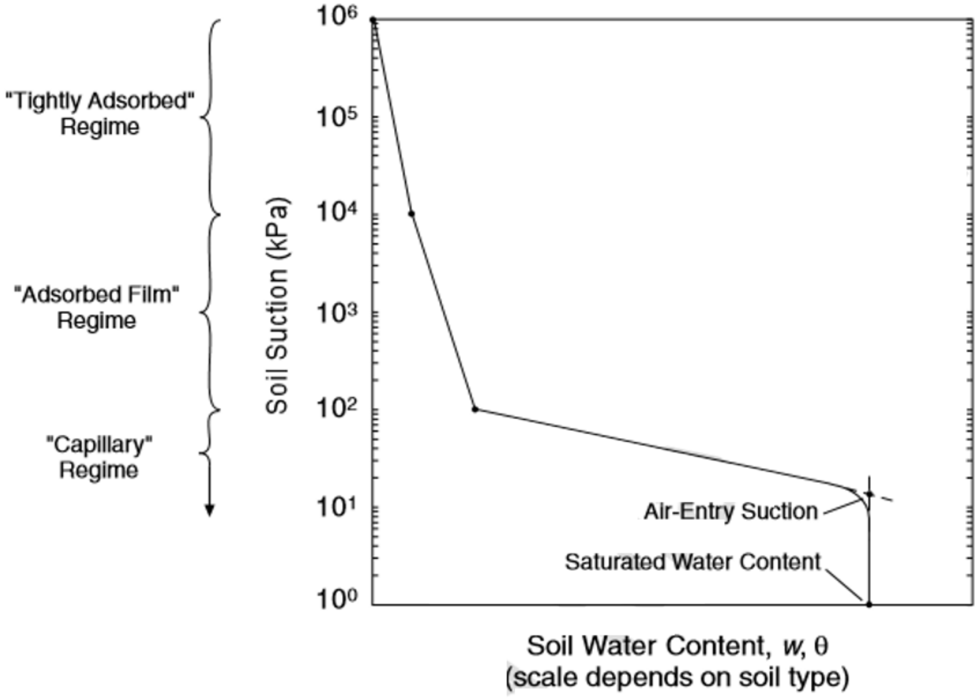

Figure 2-19: Suction regimes of a soil illustrated on a SWCC (Lu & Likos 2002).

Three suction regimes exist within an unsaturated soil: the capillary regime, adsorbed film regime, and tightly adsorbed regime (Fig. 2-19). Within the capillary regime, the controlling mechanism for pore water retention is the pore and grain size distribution and lies in the relatively low suction portion of a SWCC. The curve then transitions at higher suctions into the adsorbed film regime, characterized by a thin layer of water surrounding the particle surfaces, which is controlled by short-range interactions, such as electrical fields, van der Waals, and cation exchange. Finally, the tightly adsorbed region is dominated by molecular bonding, such as hydrogen bonding between water and the polarized particle surfaces (Lu & Likos 2002).

2.3.3.Impact on Stiffness

Several studies have examined the effects of saturation on the maximum (i.e. small strain) shear modulus, G_0, with a suction-controlled resonant column test via the axis translation technique, including Hoyos *et al*. (2015), Khosravi *et al*. (2016), Biglari *et al*. (2010), and Mancuso *et al* (2002), among others. Khosravi and McCartney (2011) examined the effects of suction control on both a drainage and imbibition path with a resonant column by using a flow pump to induce a positive/negative water pressure through the bottom platen in lieu of a positive air pressure through the top platen. In these studies, a decrease in saturation was found to increase the small strain shear modulus (G_0). Additionally, sparser, separate studies have been conducted on the intermediate to large strain response of unsaturated soils tested with a cyclic triaxial apparatus, including those by Biglari *et al*. (2011), Ng & Xu (2012), and Ghayoomi *et al* (2017), among others. Again, a decrease in saturation was found to yield an increase in G at each Υ_c tested.

Several studies have developed SMRC's using the combined results of resonant column and cyclic triaxial testing without suction-saturation control (Hardin *et al*. 1994; Cavallaro and Grasso 2006; El Mohtar *et* al. 2013; and Savidis *et* al. 1993). Dong *et al*. (2018) did measure G on unsaturated soils at both small strain (G_0) and at specimen failure (i.e. large strain), the study did not measure the response at any intermediate strains, instead fitting an SMRC model to the two measured points. Though numerous studies have examined the dynamic response of unsaturated soils, no study was found that combined the results of resonant column and cyclic triaxial tests to develop a shear modulus reduction curve (SMRC) with soil suction control. Such a dearth of research prohibits robust characterization of the highly non-linear portion of the SMRC, where slight changes in slope and curvature could yield significant variation in the shear modulus an engineer would use in practice.

Characterizing the complete SMRC is crucial for proper design of structures such as wind turbine foundations, which are subjected to eccentric, dynamic loads due to strong wind-derived thrust that impart a highly variable cyclic stress into the underlying soil. However, in wind turbine foundation design, engineers in practice commonly assume a uniform shear modulus based on a singular assumed Υ_c of 10^{-3} (DNV/Risø 2002). Likewise, ASCE/AWEA (2011) instructs engineers to assume a reasonable magnitude of Υ_c, but gives no guidance on how to estimate this and instead directs engineers back to DNV/Risø (2002). The soil supporting the foundation, however, experiences non-uniform conditions with depth, including effective stress, saturation, and stratigraphy, that can impact the magnitude of cyclic strain. Yilmaz (2014) found that soil strain dissipated rapidly with depth, suggesting that a singular assumed cyclic strain value may not necessarily be applicable to the foundation soil. Moreover, the study showed that operating strain values were much smaller than the assumed 0.1%, placing the shear strain within the highly non-linear portion of the SMRC. Thus, characterization of the shear modulus degradation over a full range of strains is critical to the sound design of dynamically loaded structures such as WTG foundation.

Fig. 2-20 shows the results of several studies that examined the effects of matric suction on soil shear modulus. Fig. 2-20a summarizes some typical results from Hoyos *et al*. (2015), Khosravi and McCartney (2011) and Khosravi *et al*. (2016), who measured the small strain shear modulus, G_0, with suction-controlled resonant column devices at varying confining stresses and matric suctions. Though the small to intermediate strain component of the SMRC is not given, the results for G_0 clearly show a general stiffening of the soil with increasing matric suction. Furthermore, in Fig. 2-20b, Biglari *et al* (2011) and Ng and Xu (2012) produced the intermediate to large strain component of a SMRC with suction-controlled cyclic triaxial devices, yielding a similar stiffening trend. Though studies on suction controlled resonant column and cyclic triaxial devices are relatively sparse, the studies that do exist universally point to increasing stiffness as saturation decreases. Though this revelation could potentially be useful for engineers, a thorough investigation of the effects of soil suction on a wider scope of strains in a SMRC will not only provide a more robust tool for problems in soil dynamics, but will help deepen understanding of the response of dynamically loaded unsaturated soils.

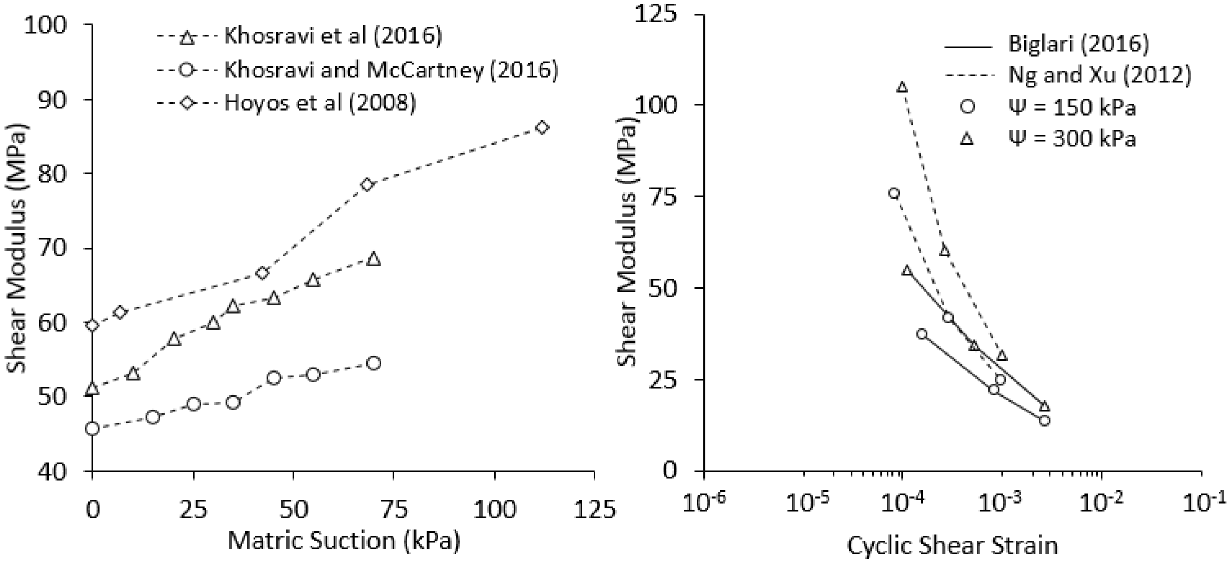

Figure 2-20: Shear modulus trends developed for: (a) Initial shear moduli, G_0, at varying matric suction levels via the resonant column method (Hoyos et al. 2015; Khosravi and McCartney 2016; Khosravi et al. 2016); (b) intermediate to large strain shear modulus degradation curves developed for kaolinite at two matric suctions via the cyclic triaxial method from (Biglari et al. 2011; Ng and Xu 2012.

3. MATERIALS AND METHODS

The soil samples and field data were taken from two WTG sites in the Midwest instrumented prior to and during foundation construction. The sensors and their layout were designed to monitor the dynamic response of the foundation soil and WTG tower to wind events. Most critical are the sensors measuring soil pressure and strain distribution. Both sites were instrumented with identical equipment, save for a few extra sensors at one site, with the orientation differing depending on predominant wind direction. Using undisturbed soil samples taken post-construction, dynamic lab testing via a resonant column and cyclic triaxial apparatus was performed to characterize the soil for design calculations.

3.1. Site A

Site A is home to a 1.65 MW Vestas V82 wind turbine, which has an 82m diameter, corresponding to a 5,821 m^2 swept area. Operating nominally at 14.4 revolutions per minute, the turbine cuts-in at about 3.5 m/s and cuts-out at about 20 m/s. According to the power production and power coefficient curves (Fig. 3-2), The highest efficiency energy production occurs at 13.5 m/s, which means that beyond 13.5 m/s, the turbine cannot produce more energy, while under 13.5 m/s maximum power production does not occur.

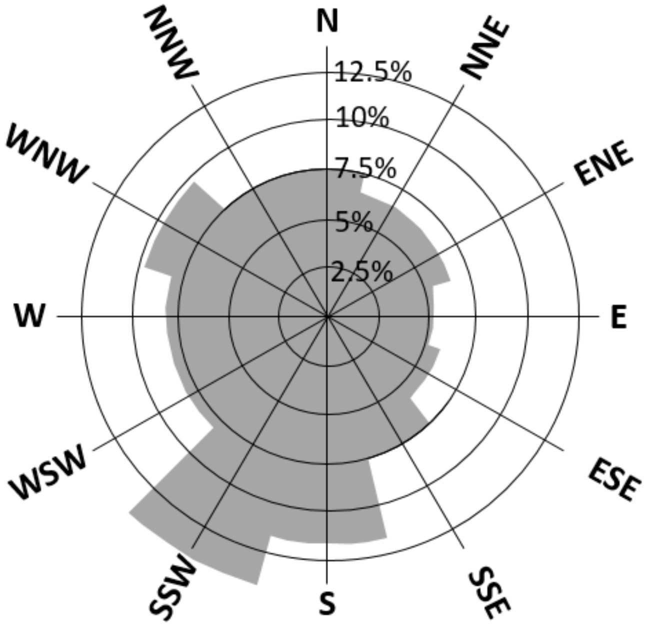

Figure 3-1: Wind Rose for Site A

Figure 3-1 shows the wind rose for the site, developed using data obtained from a meteorological tower and validated with data from an airport close to the site. The predominant wind was determined to come from the SSW, where the strongest and most frequent winds came from.

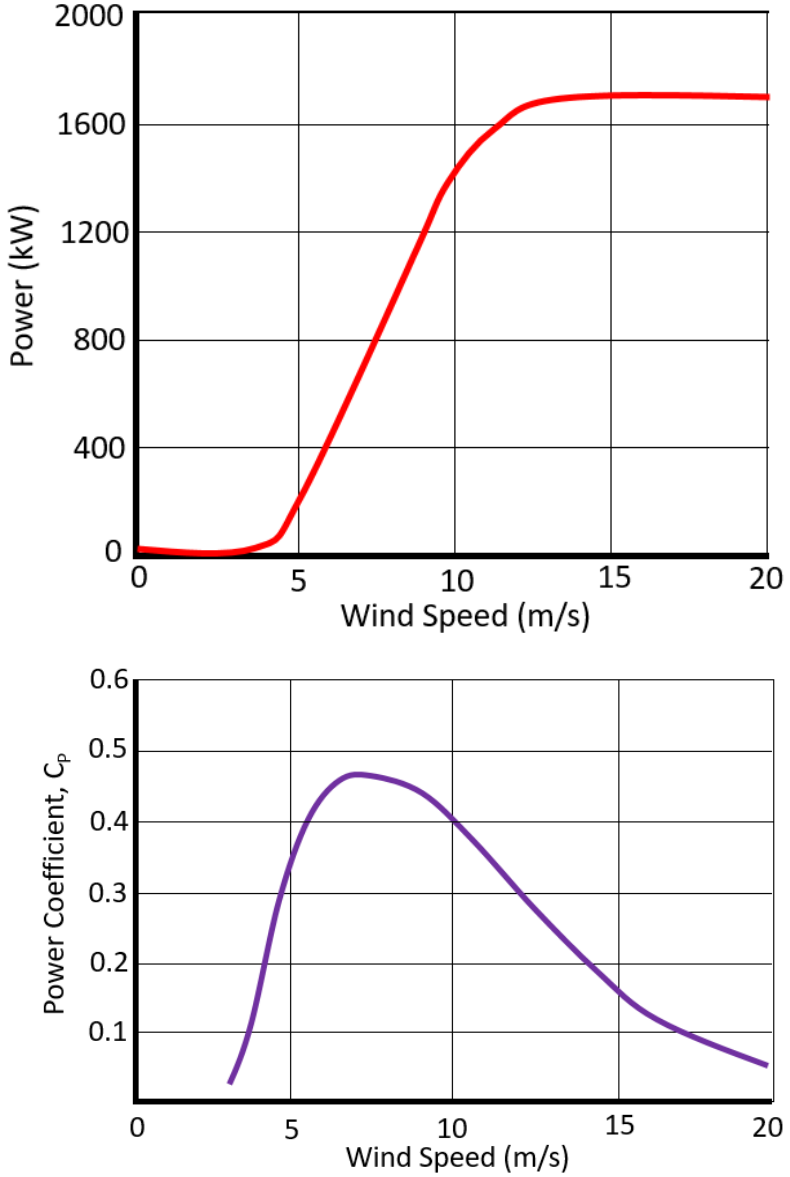

Figure 3-2: Vestas V82 curves for (a) Power Production and (b) Power Coefficient

5.1.1 Soil Conditions and Geotechnical Design

Prior to construction, two boreholes at 7.62m and 15.24m depth, with standard penetration tests (SPT) were performed to assess site soil conditions and collect samples for testing. Additionally, four Shelby tubes were advanced to obtain “undisturbed” soil samples.

To classify both the disturbed and undisturbed soil samples via the Unified Soil Classification System (USCS), Atterberg and grain size distribution (GSD) analyses were performed in accordance with ASTM standards. The GSD’s were developed using a sieve analysis (ASTM D6913-04) and hydrometer testing (ASTM D422-63). Atterberg testing produced values for the plastic limit (PL) and liquid limit (LL) (ASTM D4318). The results indicated that the soil was predominantly fine-grained, with a P200 of roughly 73% at shallow depth and 93% at the deeper points. The shallow soil had a PL of 13% and LL of 34%, with deeper soil having a lower values of 11% and 27%, respectively. Additionally, pocket penetrometer testing for unconfined compressive strength yielded results of 431+ kPa, the maximum value the instrument can measure. Lab results can be found in Appendix A. USCS (ASTM D2487-11) analysis classified the shallow soil as a stiff lean clay with sand (CL) and the deeper soil as a stiff lean clay (CL).

The turbine is founded on a shallow, octagonal, gravity-based footing. The foundation diameter is 16.46m, with the footing embedded 2.69m below ground surface. The entire foundation contains 241 m^3 of concrete and 29 metric tonnes of steel. Full details regarding foundation geometry can be found in Appendix A. Regarding foundation design calculations, the safety factors for overturning, sliding, and bearing capacity were 1.5, 1.5, and 5.0, respectively. According to the Load Document, the unfactored extreme moment, vertical force, and horizontal force at the tower base were 49,603 kN m, 730 kN, and 2340 kN, respectively.

3.2. Site B

At Site B, two Vensys V82 1.5 MW turbines were constructed, with one foundation being instrumented. Vensys V82 turbines are direct drive, meaning permanent magnets are used to generate electricity rather than a traditional gearbox. The power curve (Fig 3-3) outlines the turbine power generation at various wind speeds.

There was no meteorological tower installed to collect wind data, so wind data from a nearby airport was used to estimate wind speeds and directions at the site. Though the most likely winds come from the NNE, a westerly wind is more likely when considering the range from WNW to SSW (Fig. 3-4). Thus, the predominant wind direction was determined to be W for instrumentation purposes.

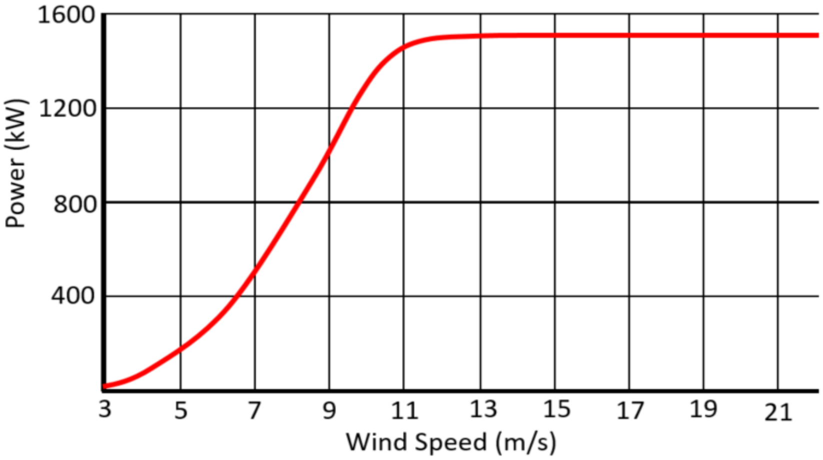

Figure 3-3: Power curve for Site B Vensys V82 turbine

3.2.1. Soil Conditions and Geotechnical Design

The soil profile for Site B was similar to the profile of Site A. Three site borings were advanced prior to construction to a depth of 15.2m. A SPT was performed every 0.76m until a depth of 6.1m, at which point the test was performed every 1.52m. The vast majority of soil below embedment depth was a lean clay (CL) or silty clay (ML-CL) according to USCS standards. The soil was generally stiff to very stiff,

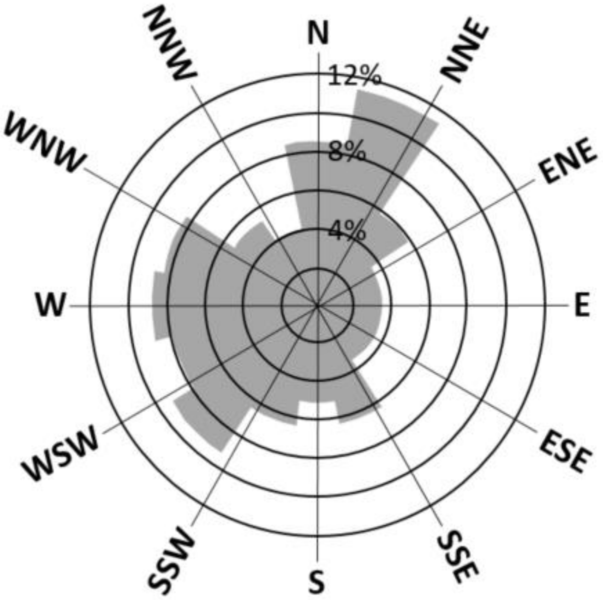

Figure 3-4: Site B wind rose

with thin layers of softer soil existing periodically throughout the profile. Again, Shelby tube samples were extracted for "undisturbed" specimens.

Lab testing yielded a PL of 11% and a LL of 23%. Wet density of the soil was measured as 2.225 g/cm^3 and dry density as 1.89 g/cm^3, yielding a water content of approximately 12%. Furthermore, pocket penetrometer readings yielded unconfined compressive strength values between 72 kPa and 431+ kPa. Complete geotechnical investigation data, including boring logs and lab testing performed by researchers previous to this study, can be found in Appendix B.

Like Site A, the turbine is constructed atop a shallow, octagonal, gravity based foundation with a diameter of 15.85m. Total embedment is 3.05m. Regarding foundation design calculations, the safety factors for overturning, sliding, and bearing capacity were 1.5, 1.5, and 5.0, respectively. According to the Load Document, the unfactored extreme moment, vertical force, and horizontal force at the tower base were 47,736 kN m, 667.4 kN, and 2269.1 kN, respectively. Further geometric design information can be found in Appendix B.

3.3. Site Instrumentation

The two selected sites were instrumented with a variety of sensors to measure the foundation system's load transfer mechanisms and response to operational loads. Specifically, the sensors measure the horizontal pressure distribution, vertical and horizontal soil deformation distribution, tower moment, soil moisture, and foundation tilt. The instrumentation was placed both prior to construction and after tower assembly, depending on the instrument. The sensor distribution was identical for each site, however, the orientation of each setup was designed to take advantage of predominant wind direction. The following sections will describe each sensor and their placement in further detail.

3.3.1.Pressure Gauges

Nine total Geokon Model 3500 Contact Earth Pressure Cells (PG) were spread along the base of the foundation. Five were placed along the predominant wind direction, with two placed 6.1m from center, two placed 2.85m from center, and one at the footing center. Additionally, two sensors were placed on the leeward side at both a 70^{o} and -70^{o} offset from the predominant wind direction for a total of four lateral PG's (Fig 3-6).

The pressure cells consist of two flat steel plates welded together with hydraulic fluid separating them in between (Fig 3-5). As pressure outside the cell increases (i.e. eccentric loading caused by overturning moment), the pressure increases in the hydraulic fluid. This pressure is then converted to an electrical signal within the sensor and sent to a datalogger. Gauge factors for data reduction (Appendix C) were supplied by the manufacturer, and initial readings taken as a baseline for data analysis.

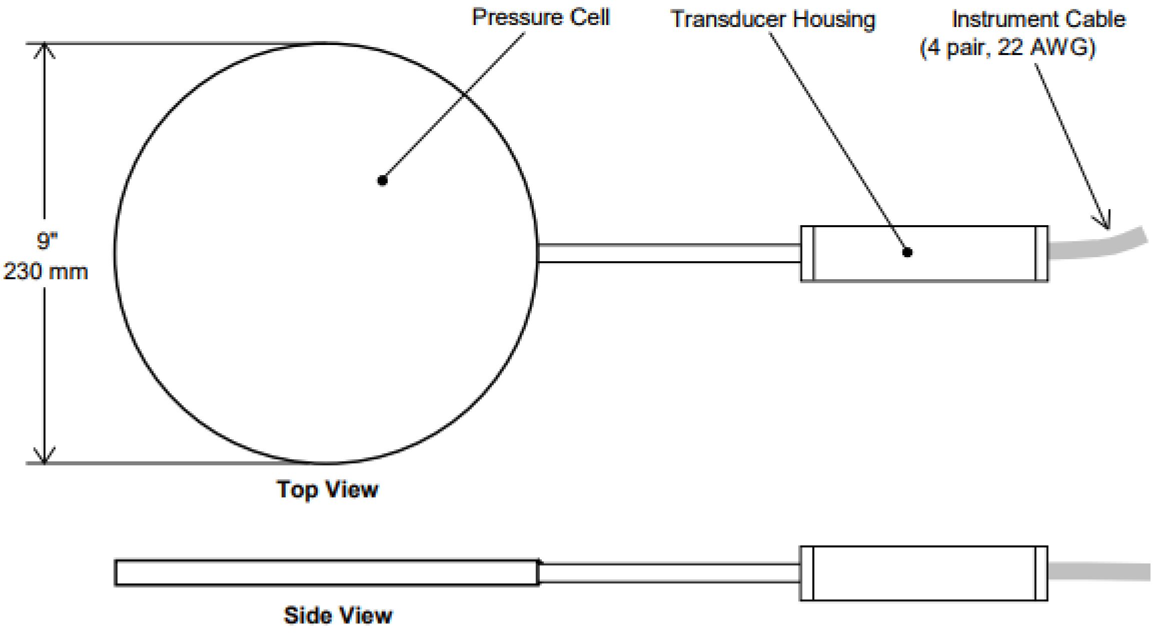

Figure 3-5: Geokon 3500 Pressure Cell

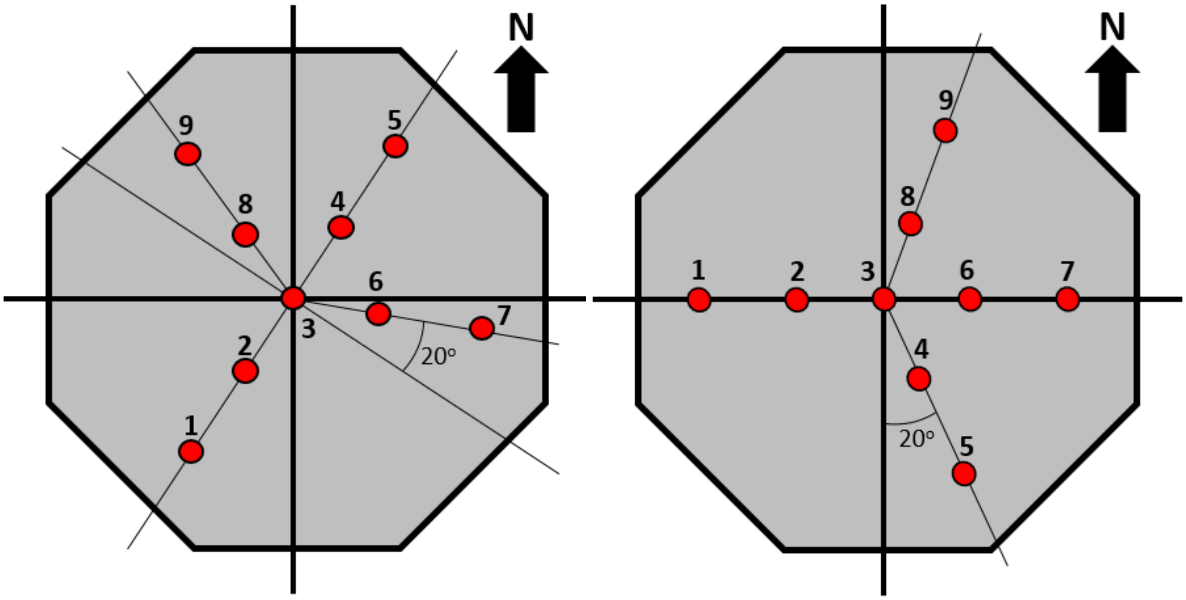

Figure 3-6: PG layout for Site A (left) and Site B (right)

There are, however, potential accuracy concerns with pressure cells such as this. In order for the PG to measure accurately, the medium that is used to envelop the PG must be of equal stiffness to the medium in which the PG is embedded. If the stiffnesses do not match a pressure redistribution phenomenon called “bridging” can occur. In this case, the PG’s are embedded in a stiff lean clay, but are enveloped by a thin (~2 cm on each side) pocket of Quikrete© all-purpose sand. Practically, it is nearly impossible to match a natural material’s stiffness with a compacted fill of a totally different material, so pressure redistribution is likely to be observed. Depending on the relative stiffness of the PG and sand pocket, the measured values may be greater or lesser than the actual value. If the PG system is less stiff than the soil, the stress will redirect around the cell, causing an under-reporting of pressure. Conversely, if the PG is *stiffer* than the soil, the stress will redirect into the cell, causing an over-reporting of pressure.

3.3.2.Soil Deformation Gauges

Ten Geokon 4430 Vibrating Wire Deformation Meters (SG) were placed below the surface to measure the change in vertical soil strain with depth and along the wind profile. Similar to the PG’s, the majority of SG’s (eight total) were placed along the predominant wind direction, with one additional SG placed on each side perpendicular to the predominant wind direction. Of the eight along the predominant wind axis, one was placed 4.12m on the windward side from center, three were stacked under the center, and four were stacked 4.12m on the windward side from center. The two perpendicular SG’s were also placed 4.12m from center. The layout is illustrated in Figures 3-7 and 3-8.

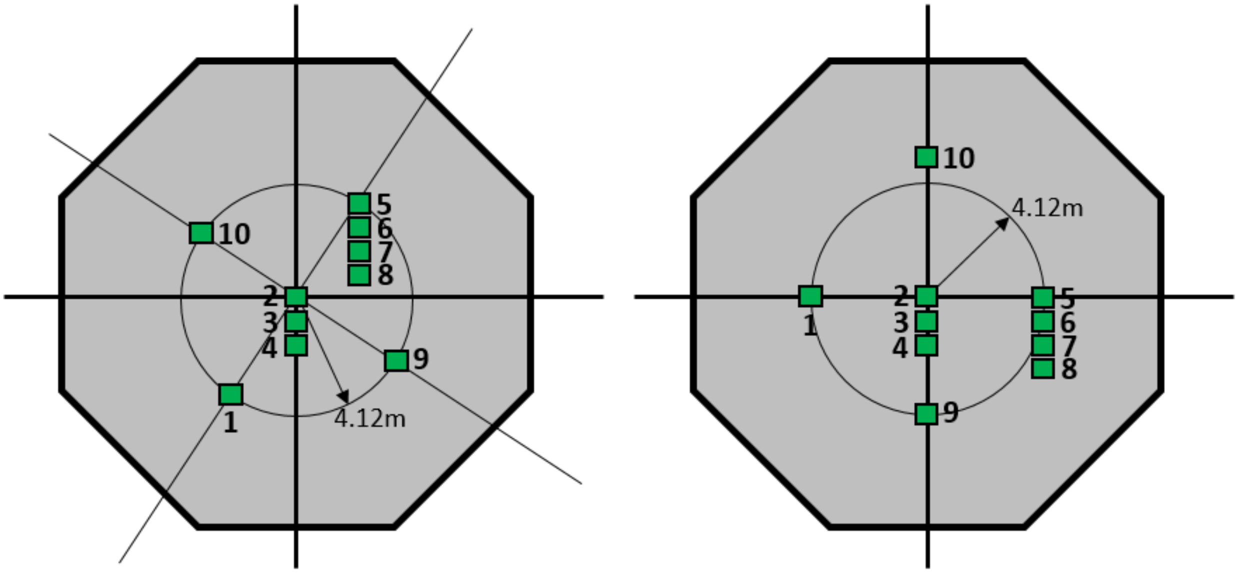

Figure 3-7: SG layout for Site A (left) and Site B (right).

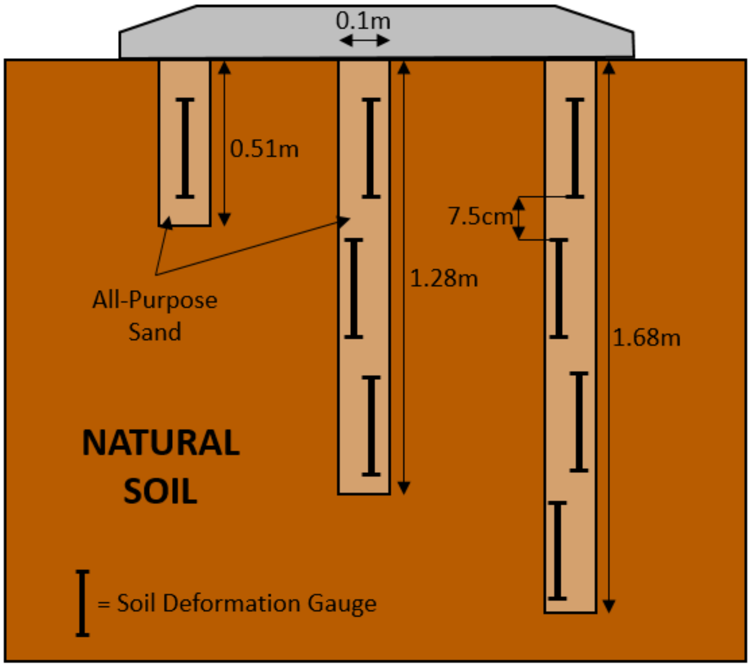

Figure 3-8: Vertical layout of SG's 1 through 8 (not to scale).

The SG's operate via a movable shaft that deforms with the surrounding soil. As this shaft moves, a music wire within the sensor experiences a varying tension. This tension is then related to a resonant vibration frequency, which is measured and converted to a voltage, which then transmits to the datalogger. The maximum displacement is 12.5 mm of the total length of 300 mm, corresponding to a strain of approximately 4.17%. The gauges were placed in vertical boreholes and filled with Quikrete all-purpose sand compacted with concrete vibrators. Initial readings, gage factors, and temperature are listed in Appendix C.

3.3.3. Thermal Dissipation Sensors

To monitor water content in the foundation soil, thermal dissipation sensors (TDS) were installed. Only Site A was outfitted with four total TDS's at three locations. These sensors take advantage of the variable thermal conductivity of a medium with moisture throughout. By calibrating the sensor with site soils of known water content (Appendix C), the thermal conductivity of the *in situ* soil can be correlated with a water content. The layout of the sensors can be seen below in Figure 3-9. TD-1 and TD-3 are at a depth of 610 mm, TD-2 is buried at 660 mm, and TD-4 embedded at 510 mm depth.

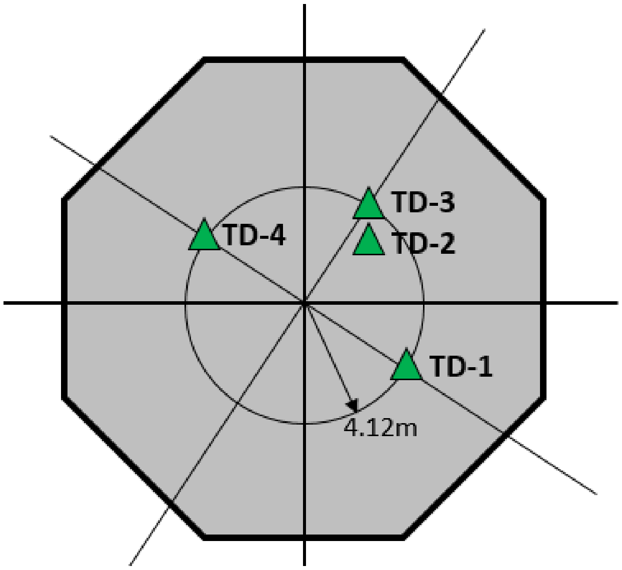

Figure 3-9: Layout of the thermal dissipation sensors beneath the foundation.

3.3.4. Tower Strain Gauges

Due to the immense horizontal forces on the WTG tower, a moment is induced about the base. To measure this moment, two sets of three optical full bridge strain gauges were placed along the interior wall of the tower. The two sets are offset by 1m in the vertical direction to allow calculation of equivalent tower moment and subsequently shear force. Within each set, the three strain gauges were placed at the same height at a 120^{o} separation around the tower wall (Fig 3-10).

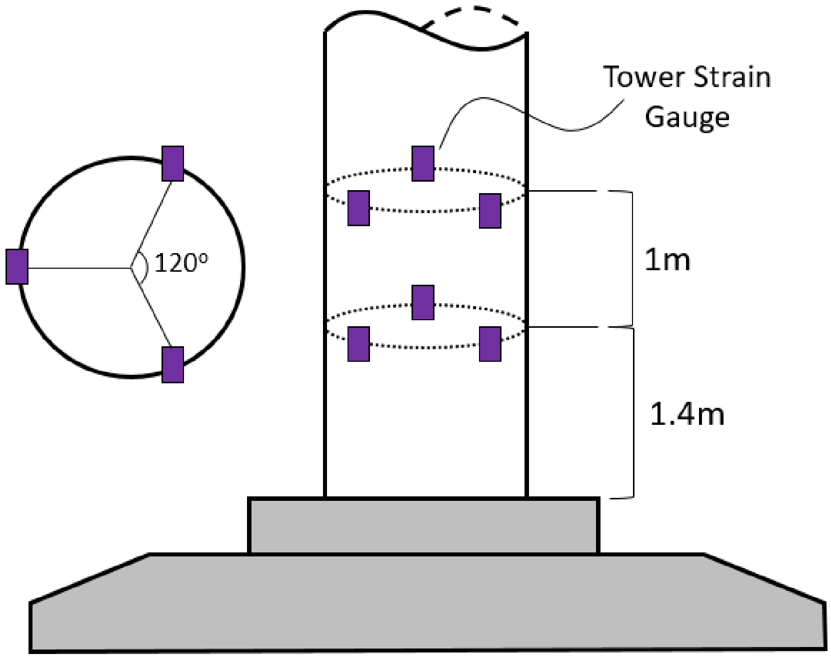

Figure 3-10: Tower strain gauge layout.

The tower can be modelled as a hollow cylinder using the tower dimensions, allowing analysis of the dynamic forces that develop and transfer into the foundation and underlying soil. Using bending moment equations, the strain can be converted into an equivalent moment. Additionally, the difference in moment between the two sets of strain gauges can be used to calculate the shear force, a key parameter in the tower design. At Site A, a pair of strain gauges is set on the west side of the tower, while at Site B, a pair is set up at the north side, with the other two pairs 120^{o} offset at both sites.

3.3.5. Micro-electro-mechanical (MEMS) Accelerometers

Finally, micro-electro-mechanical systems (MEMS) accelerometers were installed at Site A to measure changes in foundation tilt due to operational loading. Placed directly beneath the tower strain gauges at a 120° separation, the MEMS detect acceleration at three separate locations, allowing analysis for different incipient wind directions. MEMS layout can be seen in Figure 3-11.

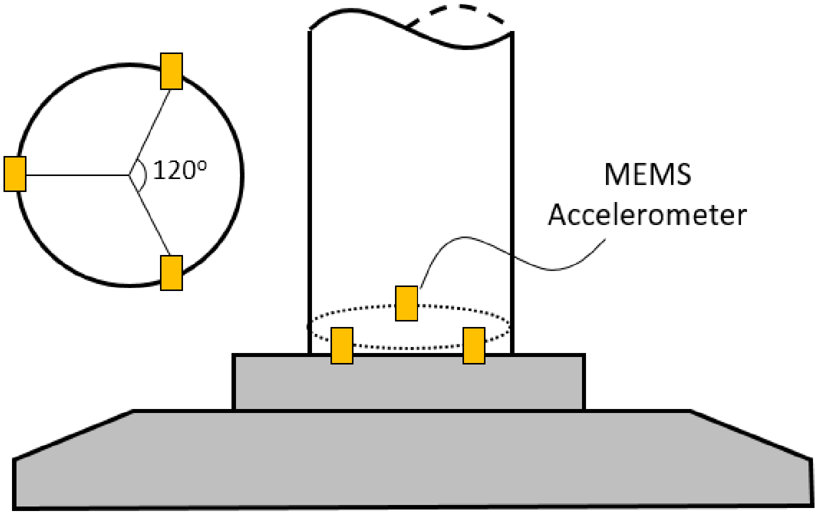

Figure 3-11: MEMS accelerometer layout.

3.4. Resonant Column System

The resonant column has been in use since the 1930's to measure the dynamic properties of soil and rocks, with several versions (see – Sec. 2.2.8.1) developed over that timespan (Richart *et al.* 1970). For the purposes of this study, a Hardin-type fixed-free system is used, with the bottom of the specimen being fixed and the top free to rotate, as illustrated in Figure 3-12. The top mass is driven by oscillating electromagnetic coils powered by a signal generator. The specimens must be cylindrical in shape, and though hollow specimens are viable for use, this study used solid samples for ease of operation. Specimen response is then measured via an accelerometer attached to the oscillator.

The outputs of a resonant column test are resonant frequency and strain amplitude. The resonant frequency can be converted to a shear wave velocity, which is then used to calculate the specimen's shear modulus. The accelerometer signal amplitude is then converted into a displacement and then strain, allowing the user to plot strain vs. shear modulus to develop a shear modulus reduction curve (SMRC). A range of likely frequencies is swept for each input voltage, and the response recorded, with the peak accelerometer output indicating the resonant frequency. Additionally, damping may be calculated from the output data. The response of each specimen is dependent on properties such as density, water content, void ratio, confining pressure, and plasticity index, among others.

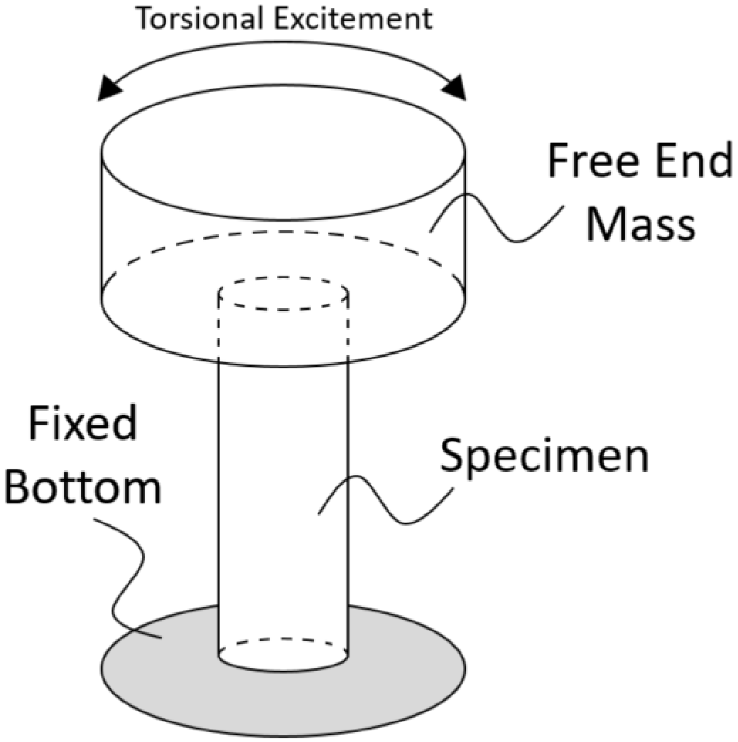

Figure 3-12: Schematic of general resonant column system.

3.4.1. Wave Propagation

Resonant column testing hinges on one-dimensional wave propagation theory in rods of finite length. Richart et al. (1970) give the following equation for a shear wave through a rod:

$$\frac{\partial}{\partial x}\left(GI_p\Delta x\frac{\partial\theta}{\partial x}\right)=\rho I_p\Delta x\frac{\partial^2\theta}{\partial t^2} \qquad [3\text{-}1]$$

Where:

$G = Shear\ Modulus$

$I_p = Rotational\ moment\ of\ inertia$

$\theta = Angular\ rotation$

$\rho = Soil\ density$

The left side of the equation represents the applied torque, while the right side represents the rotational inertia, assuming a linear elastic response. Due to this assumption, only *small strain* response can be measured with this testing method. When incorporating boundary conditions and rod length, the following trigonometric series can be used as a solution to wave propagation through a rod, where *u* is the displacement in the x-direction:

$$u = U(C_1 \cos(\omega_n t) + C_2 \sin(\omega_n t)) \qquad [3\text{-}2]$$

Where:

$\omega_n = Angular\ frequency\ of\ the\ natural\ mode\ of\ vibration$

$U = Displacement\ amplitude$

$C_1, C_2 = Constants$

Equation 3-2 solves for the displaced shape of a vibrating bar in a natural mode (Richart et al. 1970). When combined with Equation 3-1, the following solution for displacement amplitude can be derived:

$$U = C_3 \cos\left(\frac{\omega_n x}{v_C}\right) + C_4 \sin\left(\frac{\omega_n x}{v_C}\right) \qquad [3\text{-}3]$$

Where:

$V_s = Shear\ wave\ velocity$

$C_3, C_4 = Constants$

In the case of a fixed-free boundary condition, this equation can be re-written as:

$$U = C_3 \sin\left(\frac{\omega_n x}{V_s}\right) + C_4 \sin\left(\frac{n\pi x}{V_s}\right) \qquad [3\text{-}4]$$

Where:

$n = 1, 3, 5, \dots$

However, one must account for the oscillator that drives the "free" end of the rod. The oscillator has a certain mass, which nullifies the assumption of a "free" end, so its rotational inertia must be compensated for in the calculation of the resonant frequency. Given from Equation 3-1, the applied torque is equal to the rotational inertia of the oscillator. If $\frac{\partial^2\theta}{\partial t^2}$ can be determined from the accelerometer output, all that is needed is the oscillator's polar moment of inertia:

$$T = \frac{\partial\theta}{\partial x} G I_p = -I_0 \frac{\partial^2\theta}{\partial t^2} \qquad [3\text{-}5]$$

Which yields the following when combined with Equations 3-4 and 3-2:

$$\frac{I}{I_0} = \frac{\omega_n l}{V_s} \tan\left(\frac{\omega_n l}{V_s}\right) \qquad [3\text{-}6]$$

Where:

$I = Rotational\ moment\ of\ inertia\ of\ the\ soil$

$I_0 = Rotational\ moment\ of\ inertia\ of\ the\ oscillator$

$l = Length\ of\ the\ soil\ rod$

Ultimately, with the rod length and both moments of inertia known, all that is needed to determine the shear wave velocity, and thus the shear modulus, is the resonant frequency, ω_n.

3.4.2. Torsional Shear Strain

The shear strain due to torsional excitation in a rod is non uniform and varies with distance from the axis of rotation. The strain increases from zero at the center to a maximum at the edge at each vertical increment. Additionally, the angle of rotation increases from zero at the fixed end of the rod to a maximum at the top attached to the free end, illustrated in Figure 3-13.

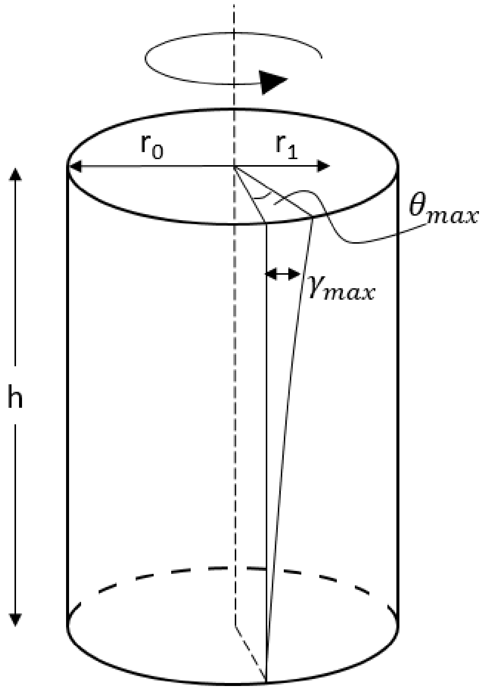

Figure 3-13: Schematic of torsional shear strain in a rod.

The definition of shear strain is as follows:

$$\gamma = \frac{r\theta}{h} \qquad [3\text{-}7]$$

Where:

$r = Radius\ of\ rod$

$\theta = Angle\ of\ rotation$

$h = Rod\ height$

Since the shear strain varies with distance from the center, it must be accounted for when determining the strain of the overall system. Based on ASTM 4015-07, the strain can be simplified as an average for solid (i.e. not hollow) specimens, as were used in this study:

$$\gamma_{avg} = \frac{\gamma_{max}}{2.5} \qquad [3\text{-}8]$$

Additional information and background regarding shear strain can be found in Section 2.2.7.

3.5. Cyclic Triaxial System

The cyclic triaxial test is used to measure the secant modulus and damping of a soil cylinder at the intermediate to high strain range via cyclic axial loading. When combined with the results of the resonant column, a SMRC for the full scale of strains can be developed. The testing was performed based on the setup and procedure found in ASTM D3999.

3.5.1.Test Parameters

This particular apparatus is load controlled, though a strain controlled setup is also possible. The loading is applied in a sinusoidal pattern, with pore pressure monitored to examine potential effects of liquefaction. The results taken by the computer should include vertical deformation, load, power pressure, and time. Using the time series of deformation and load, a hysteresis loop (Fig. 3-14) can be created, from which the shear modulus, cyclic strain, and damping can be determined.

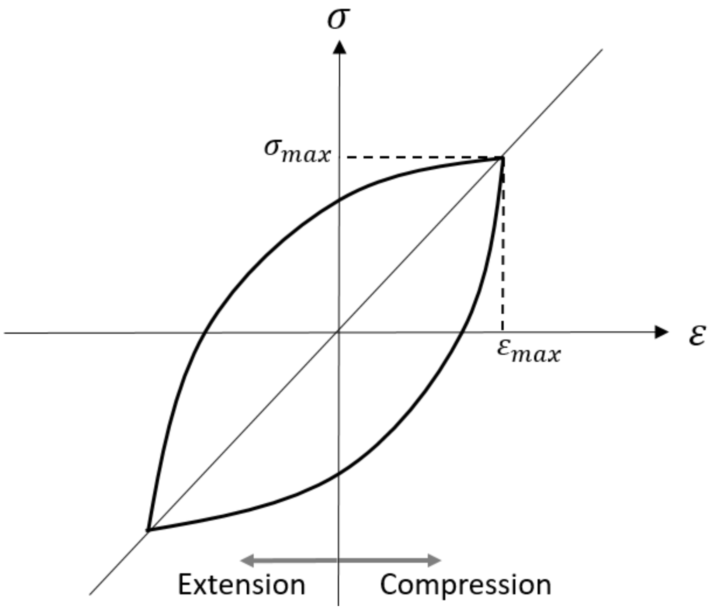

Figure 3-14: Idealized hysteresis loop.

There are two modes of loading for cyclic triaxial testing: one-way and two-way (Fig 3-15). In two-way loading, the sine wave straddles zero load, providing both compression and extension. In one-way loading, however, the specimen is under constant positive (compressive) load. For the purposes of this study, one-way loading was used, as the soil specimen cannot be “extended”, causing the load piston to lift off of the specimen upon negative loading and impact the specimen when positive load was induced. In order to have the minimum stress equal to zero, the load was offset by an amount equal to the signal amplitude

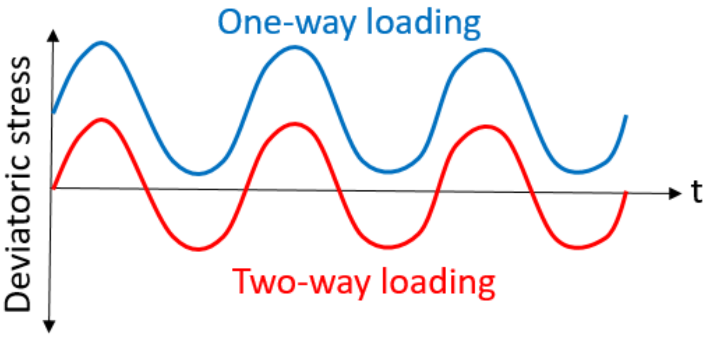

Figure 3-15: One vs. two-way loading

4. TESTING METHODOLOGY

The following sections describe in detail the components, operation, and resulting data reduction for both the resonant column and cyclic triaxial devices. The procedures, equipment, and calculations were done in accordance with ASTM standards, and may differ slightly for other setups for the same tests.

4.1. Resonant Column

4.1.1. Components of testing system

As discussed previously, the apparatus used for this study was a Hardin-type resonant column modified to perform suction-controlled tests. The output data is received from an accelerometer affixed to the oscillator atop the specimen. The soil specimen itself is approximately 57mm in length and 38mm in diameter, with a rubber membrane enclosing the specimen for confining stress application. The specimen is excited from the top via the heavy oscillator, which is powered by an electromagnetic motor with four coils symmetrically placed around the bottom of the oscillator. Using wave propagation theory (see – Sec. 3.4.1.), the shear modulus and shear strain can be calculated, and the damping of the soil estimated. A schematic of the resonant column system can be seen in Figures 4-1 and 4-2.

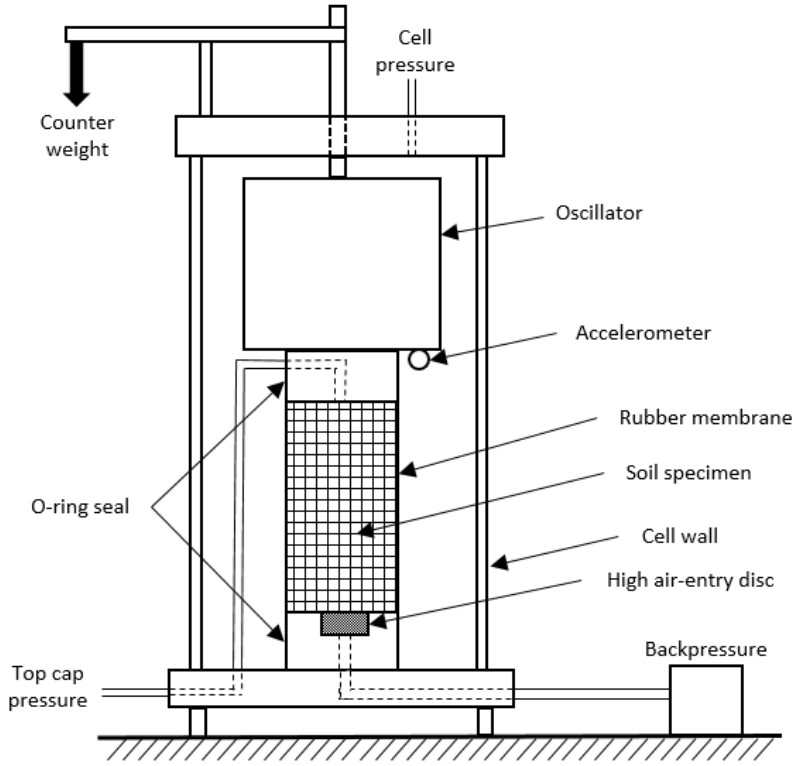

Figure 4-1: Resonant Column cell schematic

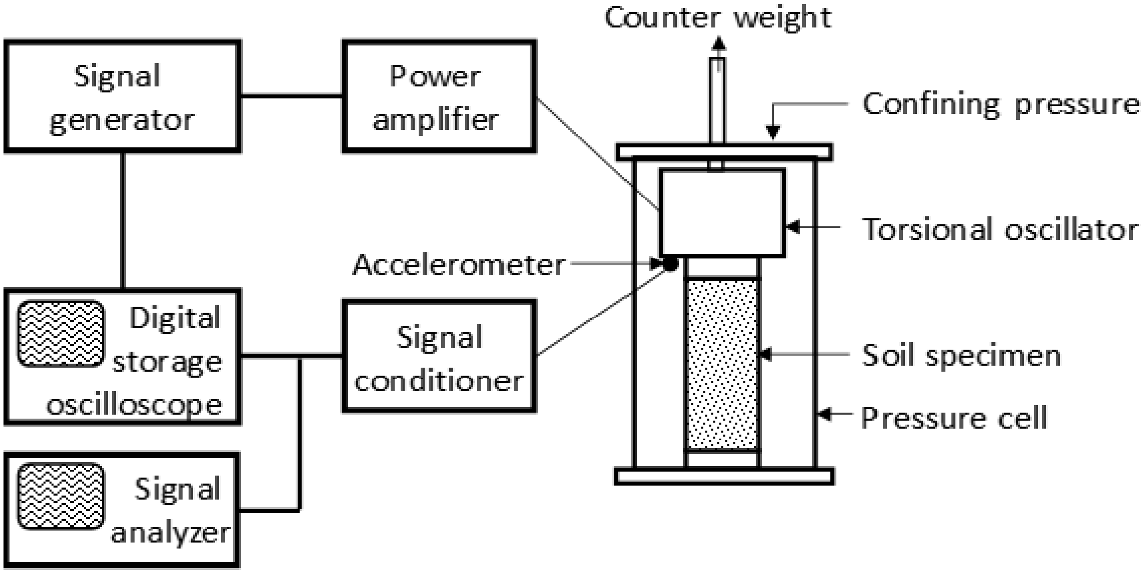

Figure 4-2: Resonant Column cell, control, and data acquisition schematic.

4.1.1.1. Main Cell

The main cell of the resonant column is where the actual testing takes place, and is comprised of several key components: the pedestal and cap, oscillator, accelerometer, cell wall, counterweight, and metal frame (Fig. 4-1). The frame is made of metal to ensure a system that is much stiffer than the material tested, as well as ensuring that the system's resonant frequency does not interfere with the specimen's resonant frequency. The thick cell wall ensures that the confining stress (max 700 kPa) applied does not leak, allowing control of the soil's effective/net stress. Contained within the cell is the soil specimen itself, capped on both ends by a metal pedestal and cap. The bottom pedestal contains a high air entry disc to allow passage of water, but not air, up to 300 kPa. The top cap contains a sintered metal disc used to evenly distribute air pressure to the top of the specimen. By controlling the air pressure on top and water pressure on the bottom, the saturation can be controlled in the specimen. Additionally, the contact surface for the cap and pedestal are roughened to ensure proper coupling with the soil.

Connected to the top cap is the oscillator and electromagnetic motor. The purpose of the heavy oscillator is to apply sufficient torque to induce the desired strain levels. The electromagnetic motor is controlled by a signal generator, which outputs a sine wave voltage signal at the desired frequency. An accelerometer is attached to the bottom of the oscillator. The accelerometer sends a voltage signal based on movement of a piezocrystal within it. Finally, the oscillator, which weighs 8.2g, must be counterbalanced to limit deviatoric stress on the specimen. When setting up the test, however, a pneumatic frame must be set up beneath the oscillator until the counterweight can be assembled

4.1.1.2. Signal Generator

To produce excitation in the coils driving the electromagnetic motor, an Agilent 33220A 20 MHz Function/Arbitrary Waveform Generator (Fig. 4-3) was used. Several signal options are available with this device, including sine, square, ramp, pulse, and noise. For the purposes of this study, a sine signal was chosen, as directed by the ASTM standard. Signals ranging from 0 to 20 MHz can be used, as well as amplitudes from 6 mV_{RMS} to 7.3 V_{RMS}. The frequency can be controlled manually or set to "sweep" through a set range. To find the resonant frequency of the specimens, the sweep function was used through a range of likely frequencies. The frequency corresponding to resonance would produce the largest response amplitude in the accelerometer, which would be the peak value on the response curve. The noise function may also be used to find the resonant frequency, where the signal, at a set amplitude, randomly changes frequency. However, the response was clearer when sweeping, so the noise function was ultimately not used.

Figure 4-3: Agilent 33220A Waveform Generator.

4.1.1.3. Amplifiers

Due to the relatively small input from the signal generator and output voltage from the accelerometer, amplifiers were used to better measure/control the input and response. For the excitation signal, an HP 6824A DC Power Supply Amplifier (Fig. 4-4a) was used to condition and amplify the signal. For the accelerometer output, a Columbia Research Laboratory Model 4102 Charge Amplifier (Fig. 4-4b) was used. Confirmation of the amplification level was used by measuring the output of the amplifier versus the output of the signal generator with the digital oscilloscope. This confirmation was performed throughout the study to ensure the amplification had not drifted or been changed over time.

Figure 4-4: Signal conditioner (left) and power amplifier (right).

4.1.1.4. Spectrum Analyzer

To plot the response curve for the accelerometer, a, HP 3582A Spectrum Analyzer (Fig. 4-5) was used. The device was set to plot in the frequency domain, with the amplitude of the signal plotted on the y-axis, from which the resonant frequency and amplitude were recorded. The resolution, range, and sensitivity can be controlled via the control panel on the right of the screen. The spectrum analyzer can measure voltages ranging from 1 μV to 40 V. As the signal analyzer sweeps through a range of frequencies, the spectrum analyzer, using a Fourier transform, records peak voltage at each frequency. Several sweeps are needed to fully develop the plot, as the sampling frequency cannot capture each frequency with only one pass.

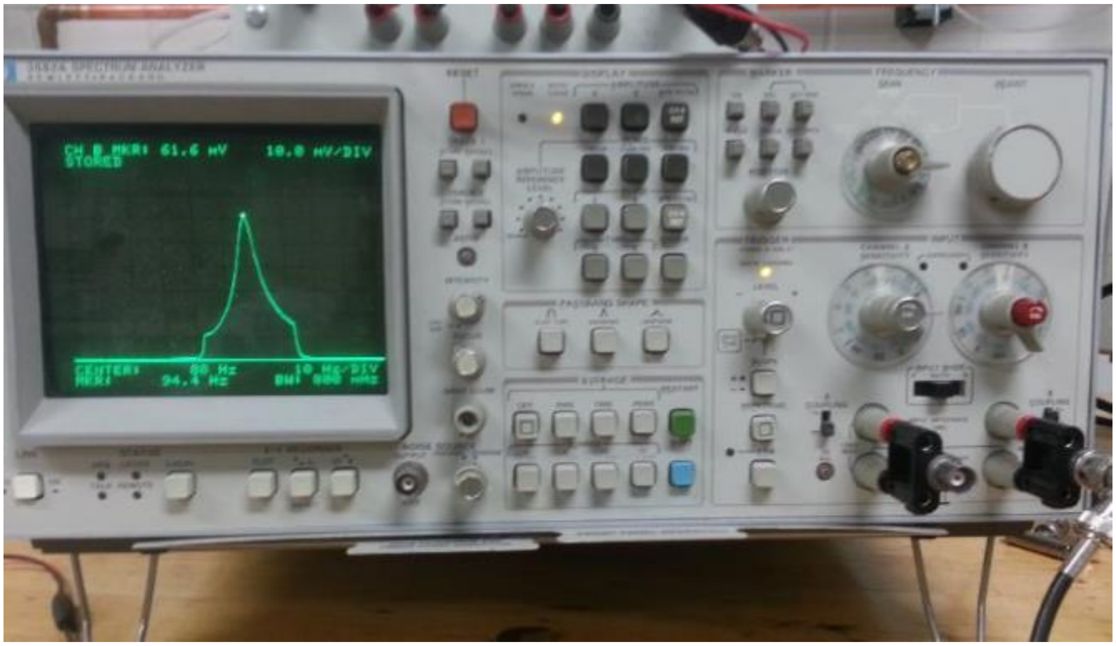

Figure 4-5: Spectrum analyzer.

4.1.1.5. Digital Oscilloscope

A digital oscilloscope was used to analyze the input and output signals for the accelerometer, oscillator, and both amplifiers. The electrical signal appears as a time series on the display, with the horizontal and vertical scales able to be altered to avoid clipping. Additionally, the oscilloscope can measure various properties of the signal, such as frequency and amplitude. This function was primarily used to periodically validate the spectrum analyzer output and visualize the frequency sweep and signal generator amplitude. The oscilloscope can is pictured below in Figure 4-6.

Figure 4-6: Digital oscilloscope.

4.1.2.System Calibration

Calibration of the system required two main components: apparatus resonant frequency and the rotational inertia of the oscillator. First, the resonant frequency of the apparatus was found by essentially running a test without a sample present. Using the counterbalance, the oscillator was suspended inside the chamber, and a range of frequencies swept, resulting in a peak amplitude at 24 Hz. Thus, the resonant frequency of the system was determined to be 24 Hz.

Second, the rotational inertia of the oscillator had to be determined to properly calculate the soil's resonant frequency. The following equation can be used to relate resonant frequency and rotational inertia:

$$J = \frac{k}{(2\pi f)^2} \quad [4\text{-}1]$$

$Where;$

$J = Rotational\ moment\ of\ inertia$

$k = Torsional\ stiffness$

$f = Resonant\ frequency$

Due to the complicated shape of the oscillator and varying densities of the components' materials, numerical calculation of the rotational moment of inertia is impractical. However, Equation 4-1 can be solved by measuring the resonant frequency of a material with a known stiffness. In this study, three PVC rods of varying diameter and constant shear modulus (1 GPa) were used as calibration rods. The shear modulus used for the PVC is an approximation, and if a more accurate value is needed, the calibration rods themselves must be calibrated. The equation that relates the resonant frequency of a known specimen to the rotational inertia of the oscillator is as follows:

$$J_{Osc} = \frac{\pi d^4 G}{32l} \qquad [4\text{-}2]$$

$Where$:

$G = Shear\ modulus\ of\ specimen$

$l = Length\ of\ specimen$

$d = diameter\ of\ specimen$

The procedure begins with installing the PVC rod in the chamber in place of the pedestal and soil. The signal generator was then set to sweep through a range of likely frequencies, with the peak amplitude representing the resonant mode. Then, using Equation 4-2, the oscillator's rotational inertia could be determined. Table 4-1 summarizes the results. Figure 4-7 illustrates the results for each calibration rod, as well as results from the same calibration process performed in 2014.

Column	**Diameter**	**Length**	**Resonant Frequency**	**Torsional Stiffness**	**Rotational Inertia**
--	**mm**	**mm**	**Hz**	**N·m**	**kg·m^2**
Large	35.1	129.1	206	1154.2	0.000698
Medium	24.8	129.1	109	287.7	0.000645
Small	15.0	129.1	47	38.5	0.000597

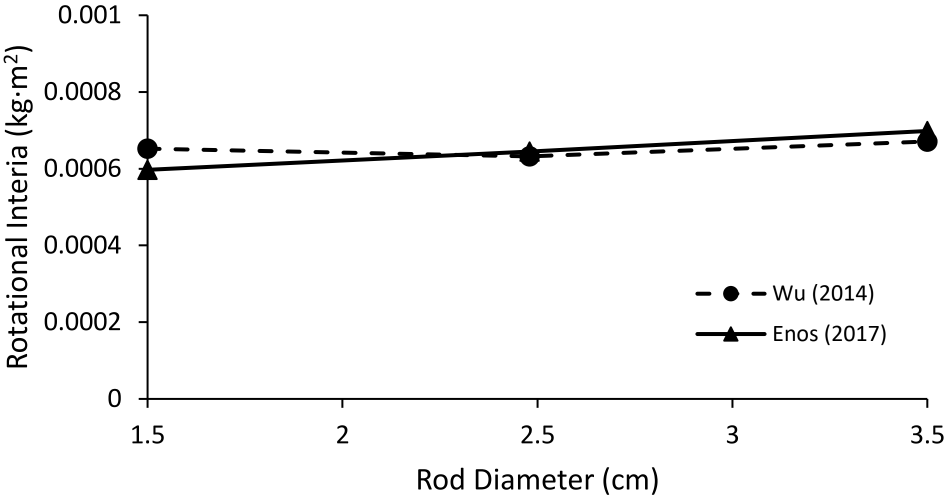

Figure 4-7: Oscillator rotational inertia calibration results

The calibration rods yielded very similar results, averaging out to about 0.000647 kg·m^2., with the deviation of the minimum and maximum values being within 8% of the average. Furthermore, the measured values match very well with a previous calibration on the same apparatus performed in 2014.

4.1.3.Procedure

The testing was performed in accordance with ASTM 4015-07, and generally follows as: (1) sample preparation, (2) apparatus setup, (3) test operation, and (4) result calculation.

4.1.3.1. Sample Preparation

Two types of sample were used in the resonant column, remolded and undisturbed. Remolded samples were used for practice with the apparatus, as well as testing/validation of the suction control mechanism. A mold with dimensions of ~35.5 mm diameter and ~72 mm height was used (Fig. 4-8). In order to fit with the special suction control cap and pedestal, the soil was only remolded to a height of ~57 mm. Before soil was added and compacted, the mold walls were covered in a thin layer of petroleum jelly to prevent the soil from sticking and breaking off of the specimen when the mold is opened. At that point, roughly 100g of soil sieved through the #8 seive, then thoroughly mixed with 16g of water to simulate field water content, was added and compacted with a small hand tamper in four equal lifts to 55 – 57 mm height. The specimen could then be removed for installation into the apparatus.

For full-scale testing, undisturbed samples were extruded from clear plastic sleeves, which were used to capture and transport the samples in the field. A soil cylinder of ~80 mm was then cut and inserted into a frame for carving. The soil was then trimmed into a cylinder of 35 – 36 mm diameter. Once the specimen was removed from the frame, it was cut to the appropriate length for installation in the resonant column apparatus. The trimmings were saved for use in water content and Atterberg testing.

Figure 4-8: Sample mold for remolded specimens.

4.1.3.2. Apparatus Setup

The assembly of the testing apparatus is a very involved and difficult process that, if performed wrongly, could lead to specimen damage. Great care must be taken throughout the process to ensure soil integrity.

The first apparatus setup regime is to apply suction-saturation control. The specimen is set atop the pedestal and then topped with the cap. Once the specimen and cap are properly aligned, a rubber membrane is rolled around the sample from the top down. Once the membrane coveres the sample down to the bottom of the pedestal, rubber o-rings are applied around the membrane at the top and bottom cap. With the top cap, the rubber membrane must be placed low enough that it does not interfere with the ports for air pressure. The setup to this point is pictured in Figure 4-9.

Once the membrane and o-rings are securely in place, the ports to apply axis translation pressure can be applied. First, to ensure proper seal, white pipe tape is wrapped around the port threads. The elbow shaped ports are then installed, making sure they are just below horizontal facing the counterclockwise direction. The tubing can then be attached to the ports. The assembly to this points can be seen in Figure 4-10.

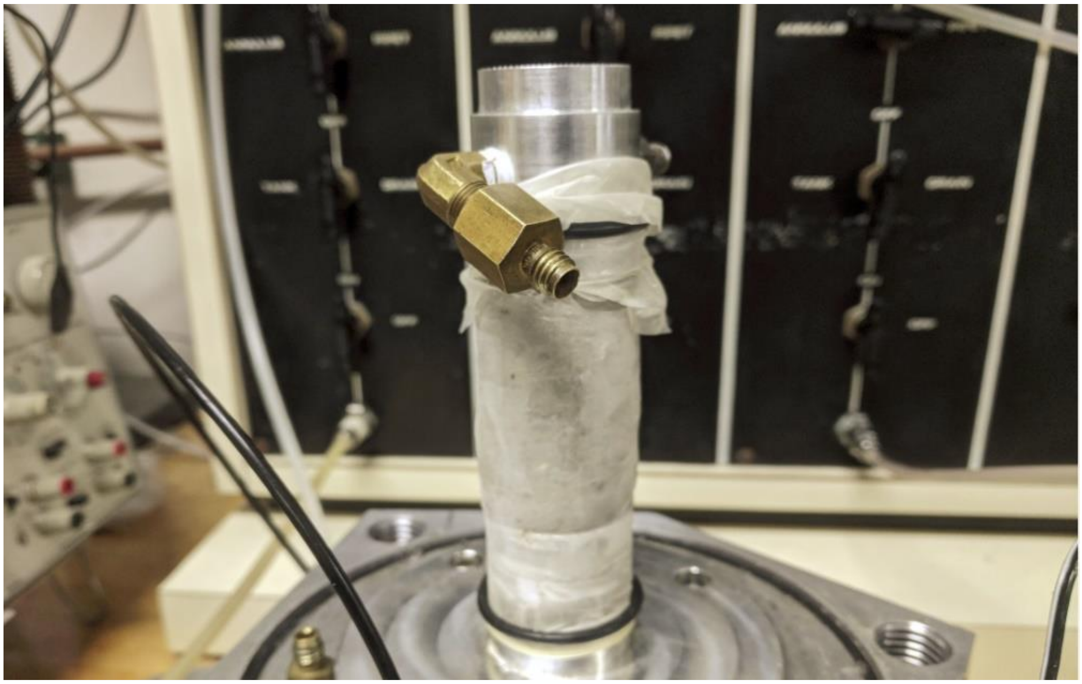

Figure 4-9: Soil specimen and platen assembly.

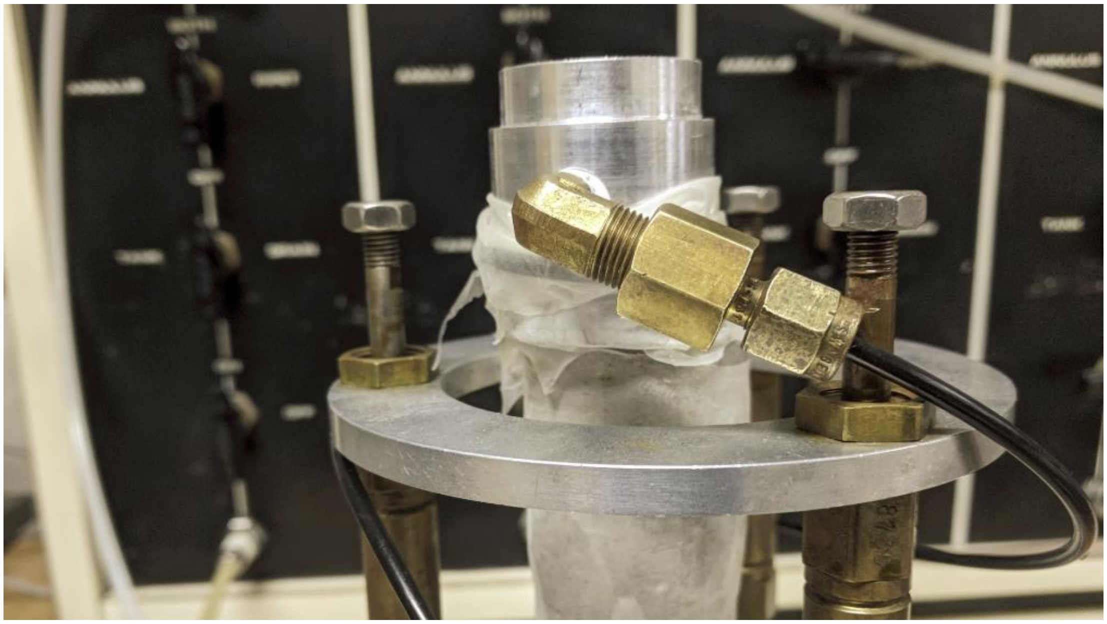

Figure 4-10: Top platen with air pressure ports connected.

The next stage is to assemble the frame itself. As mentioned, the oscillator must be countered by the pneumatic frame during assembly or counterbalance weight during testing. The pneumatic frame and pedestal ring should be installed during the tubing assembly outlined above. To neutralize the mass of the oscillator, about 290 kPa should applied to the frame. Once the pneumatic pistons have risen, the oscillator is gently placed atop the pedestal ring, taking care to be supporting the oscillator to prevent differential tilting/bending of the specimen. The small ring on the bottom of the oscillator should be lined up around the specimen's top cap and coupled by tightening the two bolts around the small ring. Once coupled, while supporting/balancing the oscillator, a clear acrylic chamber is added around the specimen and oscillator. Once a seal is made with the bottom o-ring, the frame cover is placed on top of the acrylic chamber. Finally, once all electrical plugs are connected, the apparatus is fully sealed by tightening the three bolts down over the cover. The counterbalance should then be assembled, with the weight added simultaneous to removing the pneumatic frame's pressure.

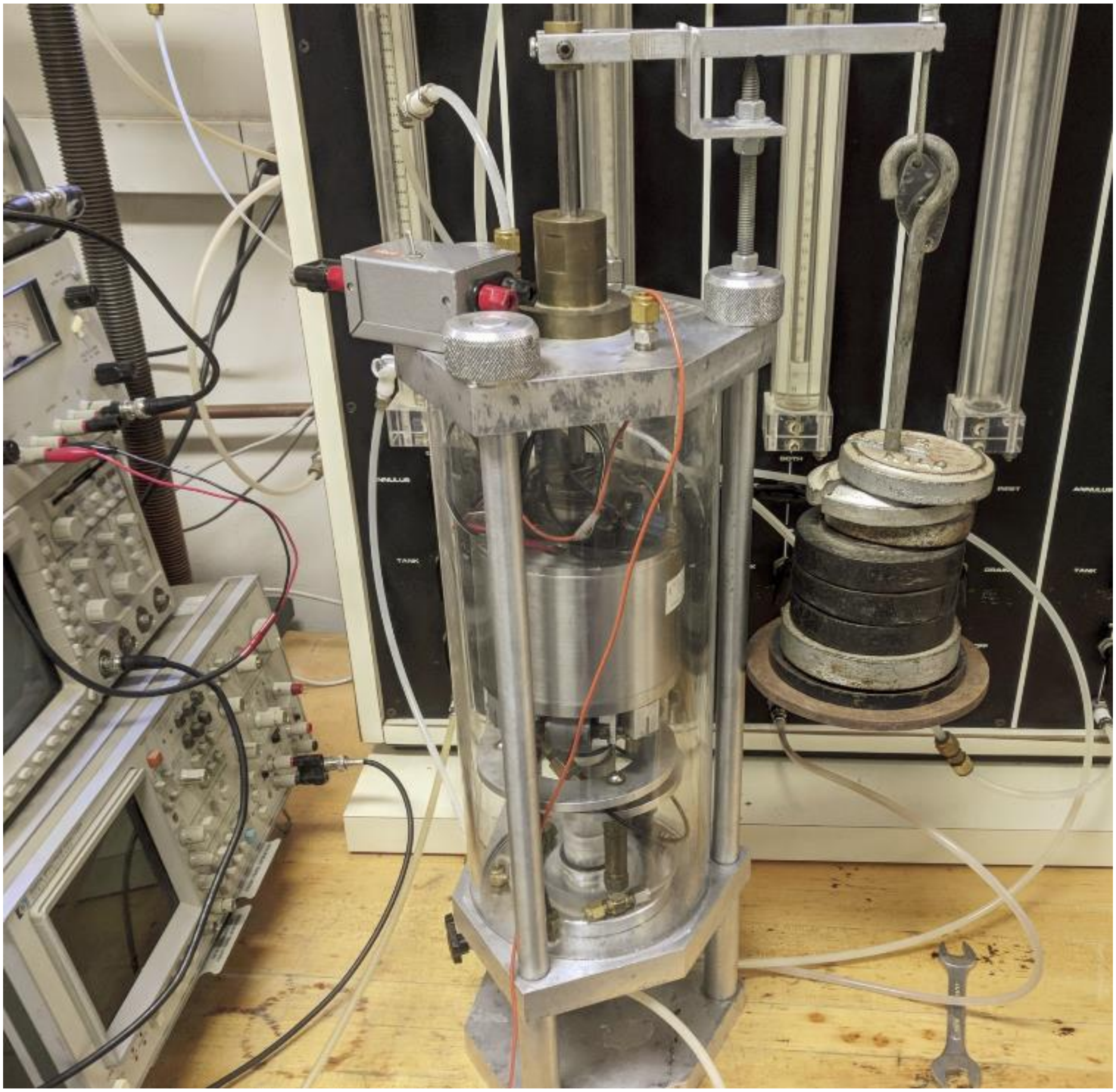

Figure 4-11: Completed resonant column setup.

4.1.3.3. Test Operation

The first step in testing is to saturate the sample. This is done by first applying a seating confining pressure of 25 kPa to maintain good contact between the soil and rubber membrane and prevent water flow around the specimen. Next, the backpressure reservoir is opened, and a pressure applied to increase speed of saturation. The air port connected to the top cap is kept open to allow displaced air to escape. Through a combination of reviews of similar studies and lab verification, it was determined that full saturation occurs in 36-48 hours. Samples were kept under saturation pressure for 48 hours, however, to ensure full saturation. Finally, before testing, the backpressure reservoir is closed and top cap air ports disconnected from the cap to allow unimpeded oscillation.

Once the saturation process is complete, the external resonant column wiring can be connected to the input amplifier and output amplifier. To begin testing, the signal amplitude was set to 15 mV, about the smallest amplitude that will yield a signal discernable from background vibrations. The signal is then set to sweep through a range of likely frequencies, typically 40 to 100 Hz. After allowing several sweep cycles to run (for ~2 min), the peak frequency and its amplitude are identified on the signal analyzer and recorded. This process is repeated for incrementally larger input amplitudes until the response signal begins to distort, indicating the strain limits of the test. During initial testing with remolded "dummy" samples, samples would fail along a lift interface if brought to max strain (~10^{-3} strain). For further testing, the data was plotted in Excel as testing occurred and tests were no longer run once the samples reached 1×10^{-4} to 5×10^{-4} strain. This proved to be effective at preventing failure and allowing specimens to be tested at multiple confining stresses before needing a new sample. For future testing, I recommend plotting the SMRC concurrent with testing to track the strain levels and monitor in real time that the test is running properly.

In addition to this thesis, a detailed operation manual was written for the resonant column that can be found in Appendix E or by speaking with Prof. James Tinjum or Prof. Dante Fratta.

4.1.3.4. Result Calculation

Calculation of the shear modulus, shear strain, and damping assumes a single degree of freedom (SDOF) system. The results of the resonant column test yield the values of voltage amplitude, frequency, and power spectrum or time decay. The process for converting test results to the required parameters is as follows:

First, the average shear strain must be determined via Equation 4-3.

$$\gamma = \frac{yD_s}{5S_a(2\pi f)^2 D_a H} \qquad [4\text{-}3]$$

$Where$:

$y = Accelerometer\ output$

$D_s = Specimen\ diameter$

$S_a = Accelerometer\ sensitivity$

$f = Resonant\ frequency$

$D_a = Distance\ from\ specimen\ center\ to\ accelerometer$

$H = Specimen\ height$

Accelerometer sensitivity was determined to be 1013 Mv/g. Furthermore, the ”5” in the denominator represents the ASTM D4015-07 recommended reduction factor for the cylinder’s “average” strain, since the strain magnitude varies with distance from the center, as discussed in Section 3.4.3.

Next, the shear modulus must be calculated from the resonant frequency. Richart *et al.* (1970) developed the following equations to model the system under resonant frequency:

$$\frac{I}{I_0} = FtanF \qquad [4\text{-}4]$$

$$F = \frac{2\pi f_r H}{v_s} \qquad [4\text{-}5]$$

$Where$:

$I = Rotational\ moment\ of\ inertia, specimen$

$I_0 = Rotational\ moment\ of\ inertia, oscillator$

$f_r = Resonant\ frequency$

$H = Specimen\ height$

$v_s = Shear\ wave\ velocity$

Substituting into the equation for shear modulus, the resulting Equation 4-6 is as follows:

$$G = \frac{\rho(2\pi H f_r)^2}{F^2} \qquad [4\text{-}6]$$

$Where$:

$\rho = Specimen\ density$

$F = Dimensionless\ factor$

F can be determined via the plot in Figure 4-12. However, to use the plot, T and P, additional dimensionless factors, must be determined by the following relationships.

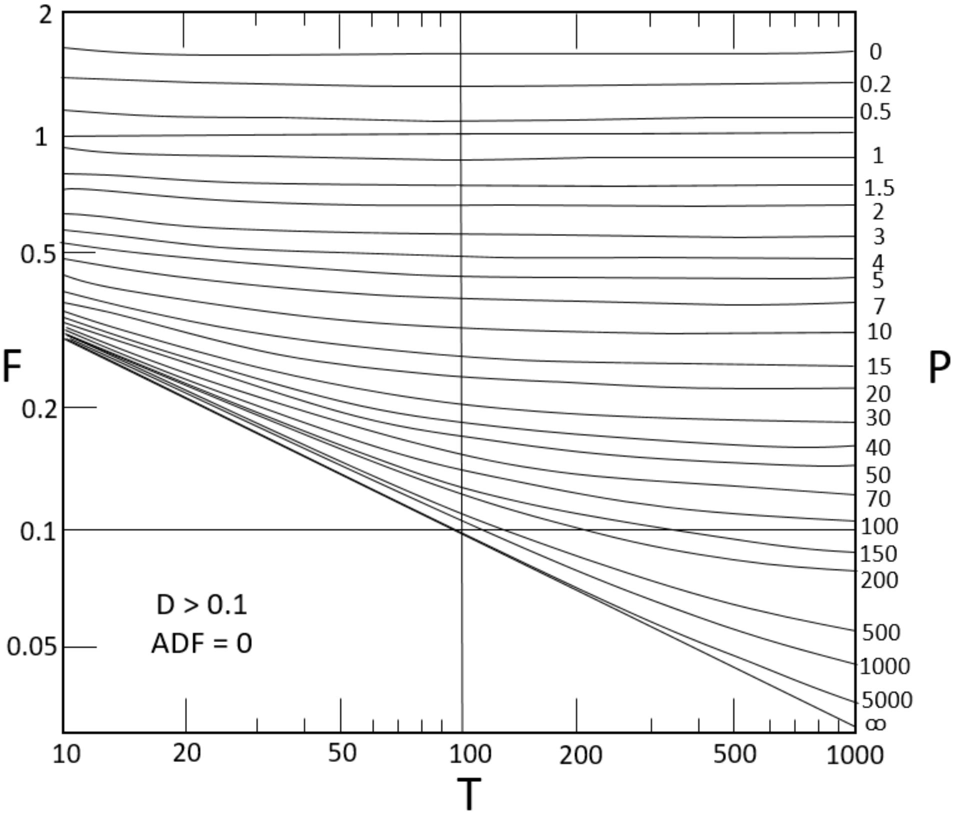

Figure 4-12: Chart adapted from ASTM D4015-07 for determining F.

$$T = \frac{J_A}{A}\left(1 - \left(\frac{f_0}{f}\right)^2\right) \qquad [4\text{-}7]$$

$Where$:

$J_A = Rotational\ inertia, oscillator$

$J = Rotational\ inertia, specimen$

$f = Specimen\ resonant\ frequency$

$f_0 = Apparatus\ resonant\ frequency$

For solid soil specimens, as were used in this study, Equation 4-8 can be used to calculate the specimen rotational inertia.

$$J = \frac{MD_S^2}{8} \qquad [4\text{-}9]$$

$Where$:

$M = Mass\ of\ specimen$

$D_s = Diameter\ of\ specimen$

Since the passive end (i.e. bottom pedestal) is assumed to be infinitely rigid relative to the specimen, P is assumed to be equal to infinity.

4.2. Cyclic Triaxial

4.2.1. Components of testing system

The cyclic triaxial apparatus is physically identical to a classic triaxial cell. The computer program used to control the load piston is the only major difference between a “static” triaxial cell and a “cyclic” triaxial cell. Similar to the resonant column, the bottom and top cap were modified to apply saturation-suction control on the specimen. This particular apparatus is load-controlled, though a strain-controlled apparatus is also possible.

4.2.1.1. Test Apparatus

There are several major components to the apparatus: the cell and loading device, data acquisition system, pressure supply, and axis translation control.

Contained within the main cell is the loading apparatus, consisting of a top and bottom platen. The bottom platen contains a high air entry (HAE) disc to apply a suction to the soil specimen. The top platen contains a sintered steel disc used to evenly distribute the axis translation pressure. The plastic cell is held in place by three metal rods that tighten to create a seal between the plastic cell and o-rings. Above the top platen is a load cell to measure the applied load from the load piston. An LVDT, used to measure displacement, is located outside the cell attached to the fixed frame. The end of the LVDT is set on a plate attached to the piston, which moves as load is applied. The bottom of the cell has five ports. One port applies confining pressure, two apply air pressure to the top (i.e. axis translation), and two apply backpressure/measure pore water pressure at the bottom of the specimen. A schematic of the cell can be seen in Figures 4-13 and 4-14.

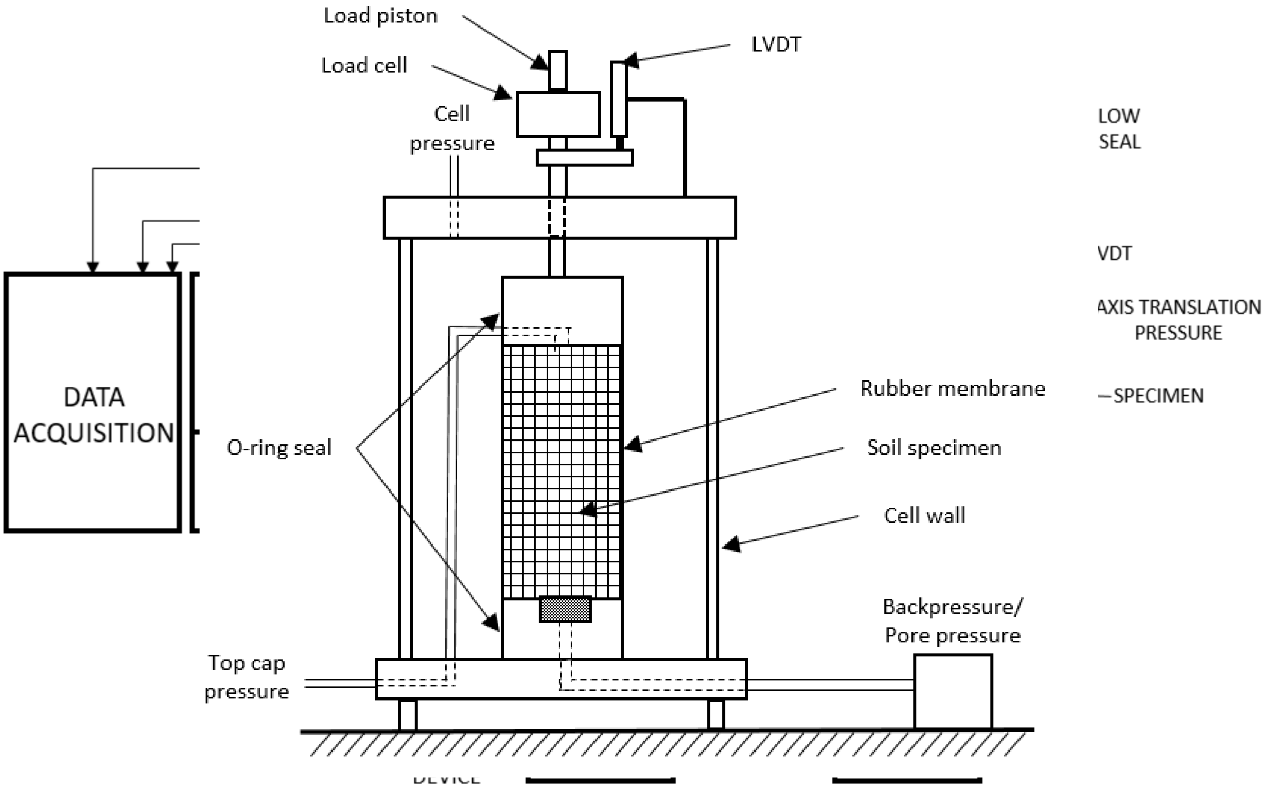

Figure 4-14: Close-up schematic of cyclic triaxial cell.

Figure 4-13: Cyclic triaxial apparatus schematic

The load piston is controlled via a computer program in which the loading amplitude is specified. For purposes of a WTG foundation, the sinusoidal loading frequency was set to 0.3 Hz. Backpressure, confining pressure, and top cap pressure are all controlled by a pressure board in which the mode of pressure (i.e. air or water) can be controlled. The backpressure is controlled by water, while the top cap and confining pressures are controlled by air.

4.2.2.Data Acquisition System

The entire system is computer controlled. A program was written in LabView© to control the test. Inputs into the computer are confining stress (σ_c), number of cycles (N), cyclic load (σ_{cyc}), and load offset ($\Delta\sigma$). Confining stress is required for the load piston to compensate for the upward net force of the pressure on the piston. Number of cycles and cyclic load are required to direct the program how long to test and at what load to oscillate at. The load offset is required to achieve one-way loading, as two-way loading leads to the piston lifting off of the specimen and slamming back down on it. As a result, $\Delta\sigma$ should be equal to $1\cdot\sigma_{cyc}$, so the net load oscillates between $2\cdot\sigma_{cyc}$ and 0.

As the test runs, the system measures three parameters. The LVDT supplies data on the deformation of the specimen. The load cell, which operates as a part of a feedback loop with the computer program, measures applied load. The load cell was calibrated before testing began to ensure accurate results. Finally, there is a pressure transducer that measures porewater pressure so that excess porewater pressure can be monitored. The system was set to measure at about 6.7 Hz for a loading period of about 3s, resulting in 20 data points per cycle.

4.2.3. System Calibration

Aside from standard calibration of the load cell and LVDT, system calibration was performed primarily through testing of rubber cylinders of a known modulus. Neoprene rubber rods were cut to length and tested as a soil sample would be. Figure 4-15 presents a typical result for a neoprene rod.

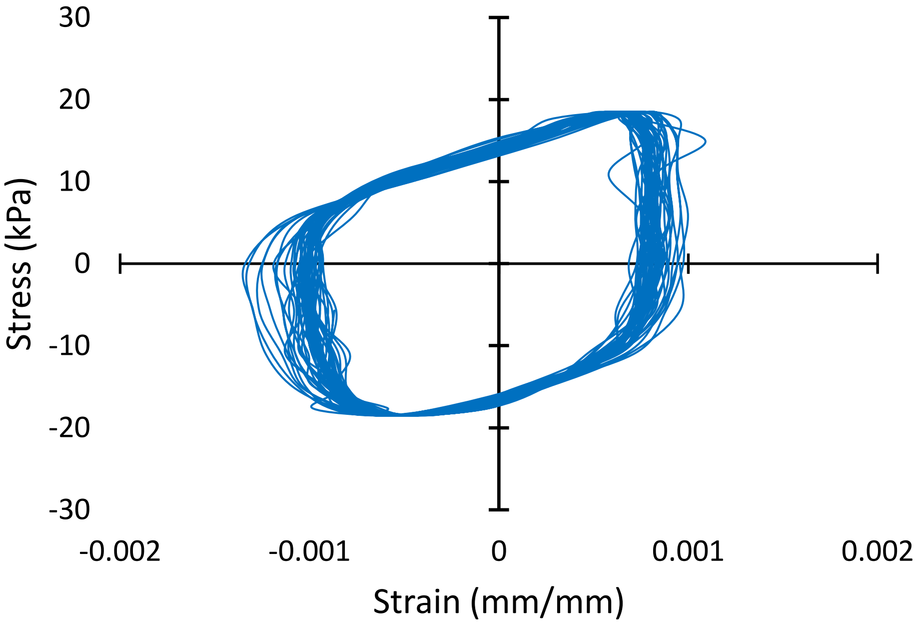

Figure 4-15: Hysteresis loop for a rubber test cylinder.

The shear modulus was measured to be 2.6 MPa, assuming a Poisson's ratio of 0.49. Neoprene has a Young's modulus of 1.5 to 2.5 MPa, depending on the blend (Cambridge 2003). The rubber rods used were a proprietary blend of primarily neoprene and a few other rubber compounds, so the actual value likely varies slightly from a raw neoprene. However, the measured value is very similar to expected values for neoprene blends.

4.2.4. Procedure

4.2.4.1. Sample Preparation

Sample preparation is identical to that of the resonant column. Samples were generally kept about the same length as the resonant column samples, but were at times longer if an impedance such as a piece of gravel would prevent trimming down to ~60mm.

4.2.4.2. Apparatus Setup

Similar to the resonant column, the setup begins with the application of a latex membrane that extends from the top platen over the soil specimen and to the bottom platen. The membrane is sealed on both platens by rubber o-rings. Before the plastic confining chamber is placed around the soil and platens, the air pressure tubes are connected to the top platen so axis translation pressure can be applied. Finally, as the top cover is placed on the chamber, the metal rod is screwed into the top platen. This rod is what connects the top platen to the load piston. Once the chamber is sealed, the apparatus is fully constructed.

4.2.4.3. Test Operation

A LabView program, developed by Ren (2015), was used to control the load applied to the soil cylinder. The parameter input screen required inputs of load amplitude (lbs), confining stress (psi), number of cycles, and maximum allowed deformation. Once the specimen was ready to be tested, progressively larger cyclic loads would be applied until either the specimen failed or the piston's maximum possible load was reached. The data was recorded in a text file, which could be transferred to Microsoft Excel or Matlab for data processing.

4.2.4.4. Result Calculation

Calculation was relatively simple. The load and deformation data was first converted to stress and strain, respectively, using the specimen's dimensions. A hysteresis loop, similar to the one seen in Fig.4-17, was then created for the test. The maximum stress and maximum strain were then recorded, which could be converted to Young's modulus by the following equation:

$$E = \frac{\sigma_{max}}{\varepsilon_{max}} \qquad [4\text{-}10]$$

Where:

$\sigma_{max} = Maximum\ cyclic\ stress$

$\varepsilon_{max} = Maximum\ cyclic\ strain$

This value could then be converted to the shear modulus (G) using Poisson's ratio (v):

$$G = \frac{E}{2(1+v)} \qquad [4\text{-}11]$$

Finally, the cyclic axial strain could be converted to cyclic shear strain by the following relationship:

$$\gamma_{cyc} = \frac{\varepsilon_{max}}{1+v} \qquad [4\text{-}12]$$

4.3. Hydraulic Control System

4.3.1. Hydraulic Control Apparatus

In this study, the saturation level of the specimen is controlled with the axis translation method via air pressure through the top platen. Though alternative methods have been used to control specimen saturation, such as the flow pump method used by Khosravi and McCartney (2011), the positive air pressure technique was selected due to its ease of use and abundance of reference literature from which to develop a design.

Axis translation allows direct control of the matric suction parameter ($u_a - u_w$), through air pressure applied through the top platen of both testing devices. With each specimen, backpressure is first applied to the HAE disc at the bottom of the specimen, saturating the specimen from the bottom up. Once saturation is achieved, the backpressure beneath the HAE disc is reduced to atmospheric pressure and air pressure through the top platen can be increased, resulting in a matric suction equal in magnitude to the positive air pressure applied to the top of the specimen. The HAE disc, when saturated, will not allow the passage of air, but water will flow freely until the specimen reaches an equilibrium saturation level. Once the pipette measuring water input and output has stopped rising, the specimen has reached the saturation level corresponding to the applied matric suction. Soil water characteristic curves were developed according to ASTM D6836-16 using the pressure chamber technique on undisturbed recovered sample soil to give context to the matric suction and apply the results to measured, in situ saturation levels.

4.3.2.System Testing

Before SMRC testing was performed, the saturation control mechanism was tested on remolded samples compacted to field density to ensure consistent results and establish typical imbibition and drainage times. To saturate a specimen, the latex membrane and pressure chamber were first sealed with rubber O-rings. Once the apparatus was successfully assembled, the chamber pressure was increased to 70 kPa, roughly equal to the in situ confining stress, as a seating confining stress. The lines connected to the HAE disc were then flushed of air with de-aired water. Water pressure was then increased to 35 kPa concurrent with a 35 kPa increase in confining pressure to maintain a 70 kPa effective stress within the specimen. The line connected to the top cap was opened to allow passage of displaced air as the specimen saturates. After a series of imbibition tests to saturate the sample, it was determined that full saturation from in situ moisture content occurs in 36-48 hours. Thus, a period of 48 hours was used for all specimens as the standard time of imbibition.

Once the saturation mechanism was confirmed to be functioning, the axis translation mechanism was tested to ensure consistent results. When the specimen was deemed fully saturated, the backpressure was reduced to atmospheric pressure, with the confining stress reduced back to 70 kPa. With the backpressure line remaining open to water flow, the air pressure through the top platen was increased to the desired matric suction magnitude. In the case of these preliminary tests, this pressure was 35 kPa. The confining pressure was increased by the same amount to maintain a constant 70 kPa net stress on the latex membrane. The specimen was allowed to drain until the pipette level remained constant. The compacted soil specimens drained to a consistent saturation, confirming a functioning hydraulic control system.

4.4. Experimental Variables

For full-scale testing, four suction-saturation conditions were tested: saturated, 25 kPa, 50 kPa, and 100 kPa. Furthermore, the variability of results with specimen location at the site would be assessed. Since the resonant column is non-destructive, the same specimen could be used for each level of matric suction. During cyclic triaxial testing, however, the specimen reaches, or nears, failure after each test. As a result, a new specimen must be trimmed, saturated, and drained at the given matric suction for each suction level tested. Resonant column testing began with the smallest signal amplitude that would yield readable results. The input voltage was progressively increased after each reading taken. Concurrent to testing, the points along the SMRC were plotted, and testing was halted once the shear strain approached 10^{-3}. Cyclic triaxial testing progressed from the smallest load the loading piston could impart until either the piston's maximum loading capability was reached, or the specimen failed.

5. MOMENT BASED ANALYSIS OF WTG FOUNDATION RESPONSE

5.1. Data Analysis

5.1.1. Tower Response to Wind Loading

A critical component of understanding the overall WTG system's response to wind events is to characterize the spectrum of overturning moments. For a five month period, tower moment was measured on an hour-averaged basis. Additionally, the component of the wind speed along the predominant wind direction (PWD) was calculated using wind data publicly available from a nearby airport. Trigonometric principles were used to break down the wind speed into its component parts, and the resulting wind speed magnitude along the PWD plotted against overturning moment (Fig. 5-1a and Fig. 5-1b), also calculated along the PWD. A positive wind speed represents a wind travelling along the PWD (i.e. from the SW) while a negative wind speed indicates that the wind component is travelling in the direction opposite the PWD (from the NE). A positive overturning moment indicates compression in TSG-1, while a negative moment indicates extension in TSG-1. Figure 5-1a shows this tower moment-wind relationship, with the overturning moment reaching a peak of approximately 14,000 kN·m, which is just over a quarter of the extreme overturning moment given by the load document (~50,000 kN·m). The data can also be plotted as a time-series. Figure 5-1b shows a three-week snapshot within the five-month measurement time, plotting overturning moment and wind speed component concurrently. It is apparent that the trend of each follows a distinctly similar path, reaching peaks and valleys at roughly the same time. The resulting correlation coefficient (R) of the data is 0.751, indicative of a strong positive correlation. Additionally, TSG-2, directly above TSG-1, trailed the curve for TSG-1, though it is not shown, as it cluttered the plot. Potential causes for error are the impacts of thermal gradients on the tower circumference due to preferential heating from sunlight, lag in the nacelle's yaw action lining up with wind changes, and the use of airport wind data a few kilometers from the site. Figure 3c shows the wind component plotted against the horizontal shear force, calculated using beam theory by taking the difference of the strain gauges stacked one meter apart, TSG-1 and TSG-2. Though the trend is less clear, with R equal to only 0.195, there is a general visual agreement between the shear force and wind speed. The calculation for shear force assumes a linear moment diagram, the gradient of which is the shear force. In reality, however, the moment distribution down the tower profile may not be linear, meaning that the measurement of such a small length of the tower may over-simplify reality.

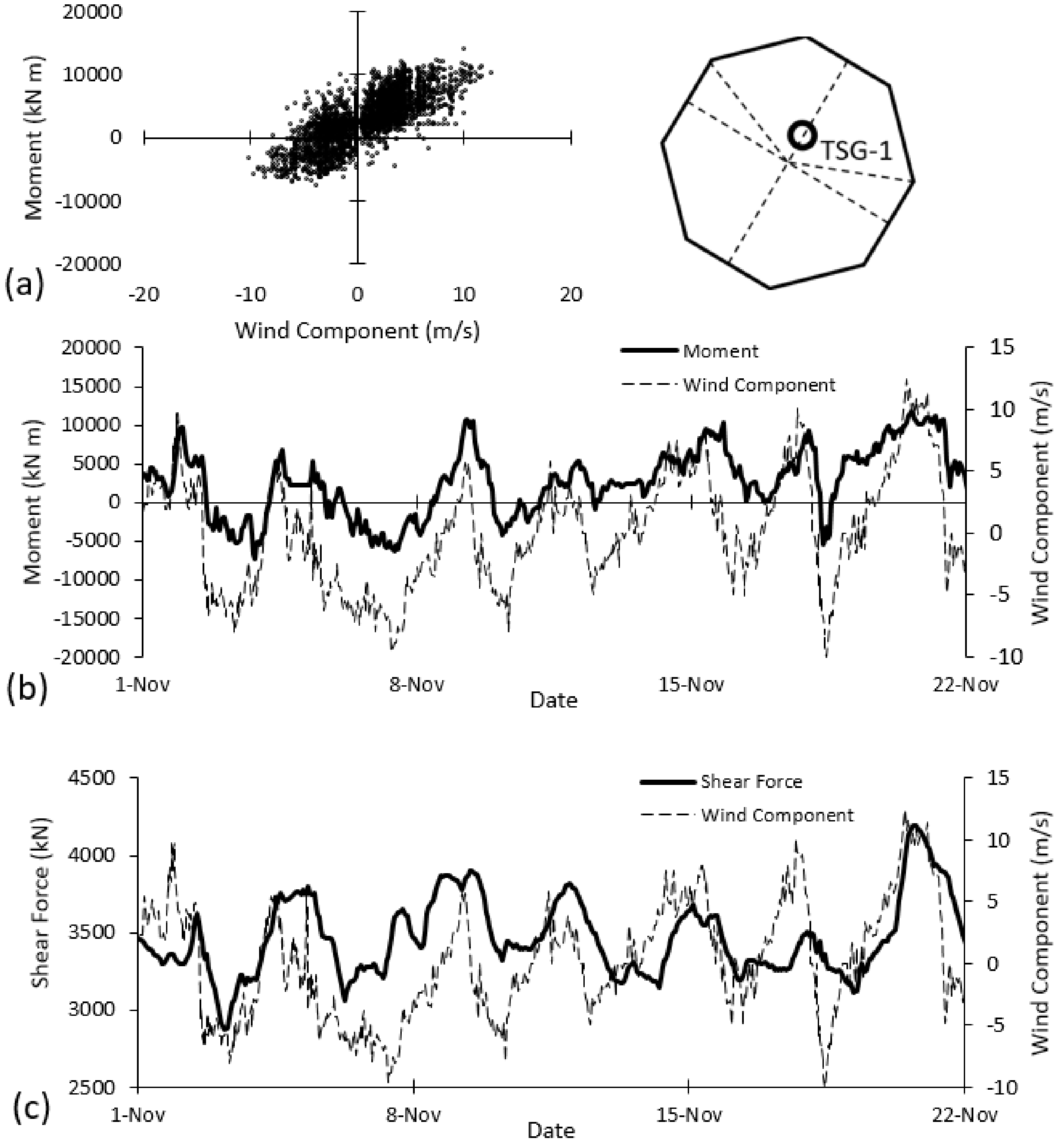

Figure 5-1: (a) Overturning moment vs. wind component along the PWD (b) overturning moment vs wind component over a three-week period and (c) shear force vs wind component over the same period.

Figure 5-2 also illustrates this relationship between wind and moment. However, the overall wind speed, regardless of direction, is plotted. Highlighted in boxes are periods during which the wind direction generally lines up with the PWD. The average wind direction for that period is indicated above each box. The spikes in overturning moment all coincide with wind events along the PWD. As expected, the results of these analyses point to a strong correlation between wind direction and overturning moment. Though the response appears generally linear in Fig. 5-1a, it is important to consider that at high wind speeds, such as during a one-, five-, or ten-year event, the response may no longer be linear and instead may flatten out, as the turbine will shut down and the blades will pitch back to minimize horizontal forces, and thus, tower moment. Over the ~20 year design life of a turbine, these extreme events will likely occur, however, none were able to be captured for this study.

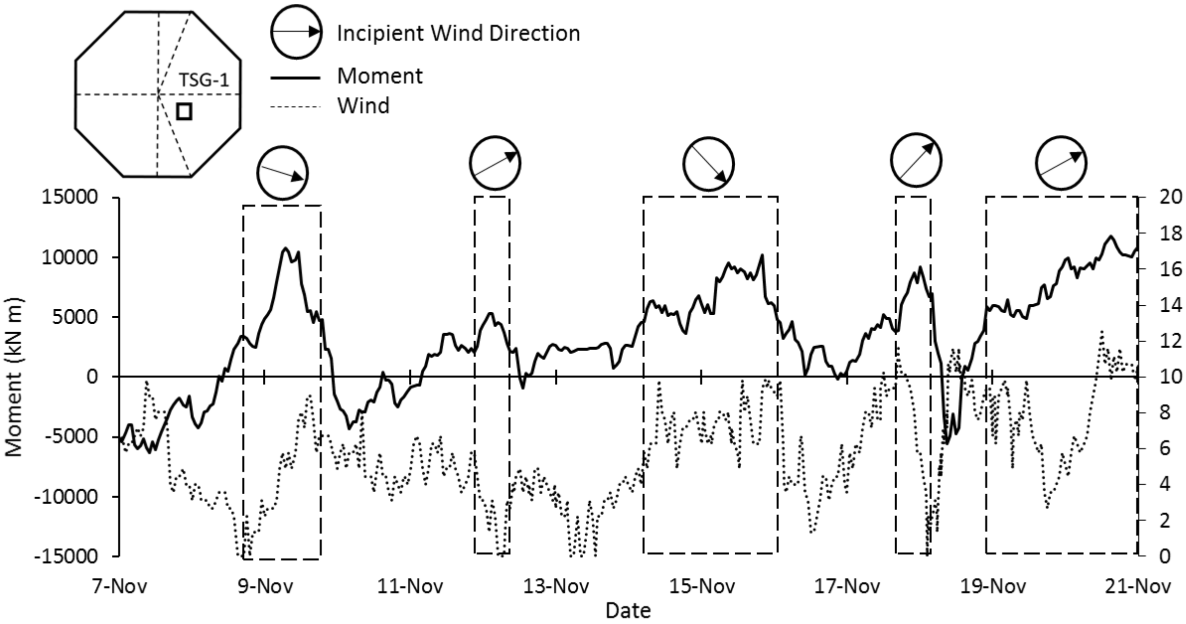

Figure 5-2: Tower moment along the PWD against wind speed. The boxes indicate periods during which the wind direction roughly lines up with the predominant wind direction.

5.1.2 Soil Response to Wind-Induced Tower Loads

With a correlation between overturning moment and wind speed established, the transfer of this horizontal wind load via tower moment to the underlying soil must be examined. Yilmaz (2014) established that both soil deformation and pressure correlate very well with wind. Subsequently, it stands to reason that overturning moment shares a similar relationship. To assess this, the overturning

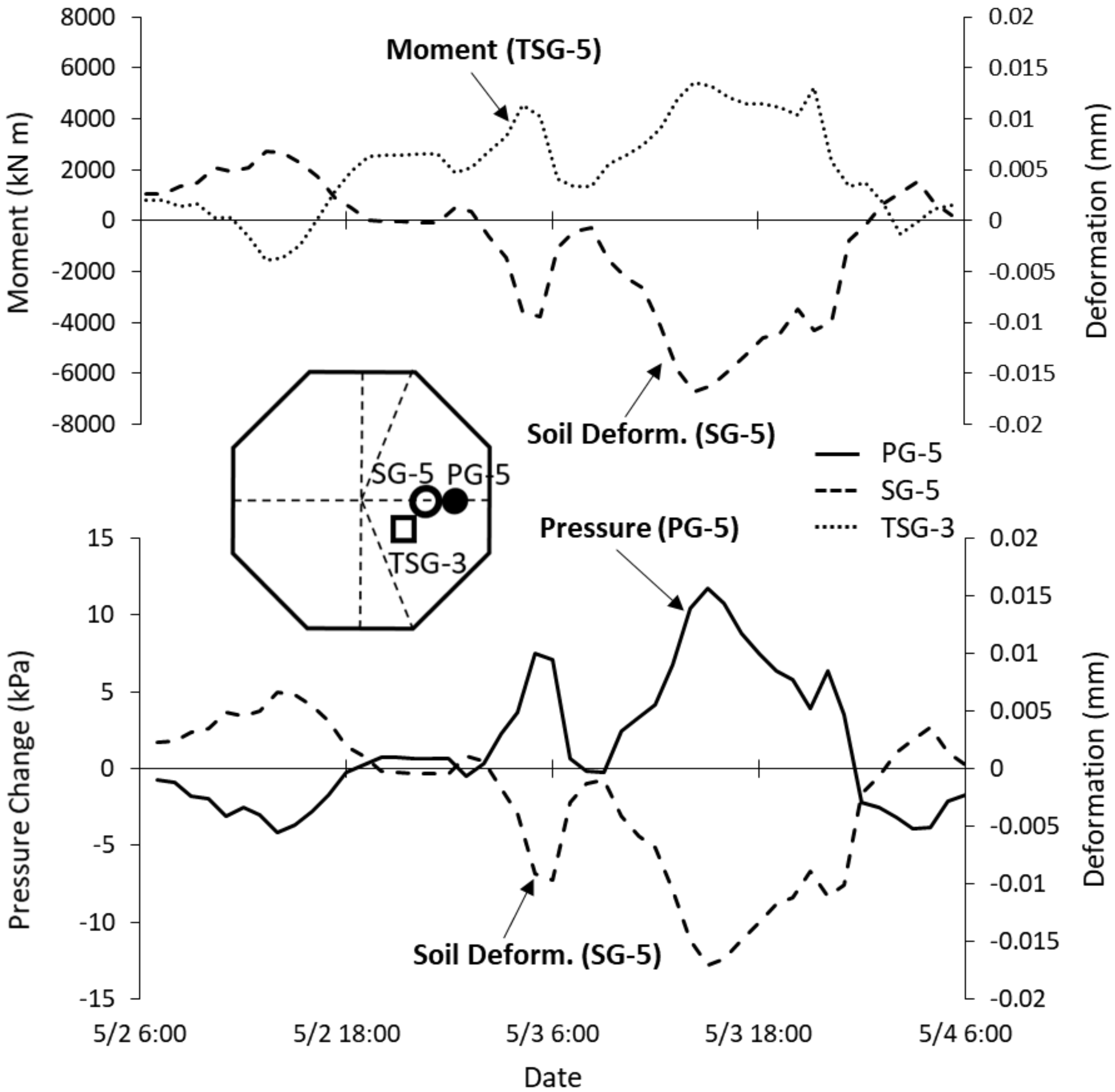

Figure 5-3: Temporal comparison between (a) overturning moment and soil deformation and (b) pressure change and soil deformation.

moment along the PWD was plotted on a time series with leeward soil deformation (Fig. 5-3a) using sensors at Site B.

The overturning moment and soil deformation have a distinct mirroring trend, where, as the overturning moment increases, the soil compresses on the windward side, and when the moment is negative, the soil compresses on the windward side. The correlation coefficient, R, between the pressure and soil strain is -0.960, indicating a very strong negative relationship between the two. Likewise, the leeward vertical pressure change from a static condition was plotted against the leeward soil deformation (Fig. 5-3b). As the vertical pressure increases, the soil compresses, as expected, with R equal to 0.928, again pointing to a very strong negative correlation. Though only two days of data are displayed, the trends depicted are typical beyond this small window. Moreover, the deformation and pressure change reach zero, or close to zero, at about the same time repeatedly throughout the time period analyzed, several examples of which can be seen in Fig. 5-3b, indicating a consistent and predictable stress-strain response. The overturning moment, however, does not line up quite as well with the null points of soil deformation, and appears to be registering ~2000 kN·m too high, consistent with the y-intercept of the plot in Fig. 5-1a. This amounts to roughly 5% of the manufacturer-given extreme overturning moment. This could be due to repeated loading of the strain gauge over 4+ years causing a plastic deformation that yields a higher moment reading during “static” conditions. Alternatively, this could be a result of incorrect initial readings of the tower strain gauges. When the gauges were installed, initial readings were taken as the "static” moment. However, even if the turbine were shut down during this measurement, there could have been a moment present that slightly skews the data. Nonetheless, the temporal patterns of each correspond very well, indicating a relatively predictable response.

To further visualize the soil’s response to the spectrum of overturning moments, hour-averaged pressure and moment measurements were calculated for a two-week period at Site A and directly plotted against each other. Figure 5-4 shows the results of this analysis for four PG’s along the PWD. Normalized pressure was plotted on the y-axis, which was calculated by dividing the pressure at a given moment by the “static” pressure, or pressure during a period of no wind, and thus, no overturning moment. Plotted with each is the "idealized" response for an assumed perfectly rigid footing. To determine this idealized response, an equation to calculate a triangular vertical load distribution from overturning moment was developed. This vertical load distribution was then integrated over the area of the footing, assumed circular for ease of calculation, to determine vertical pressure at varying distances from the center. It is first apparent that the edge PG's (Fig. 5-4a-b) respond quite similarly to the theoretical response. The inner PG's (Fig. 5-4c-d), however, respond with a larger slope than expected, suggesting the pressure distribution may be more complex than the idealized assumption. Furthermore, the responses appear to be linear, with little scatter, indicating a consistent and predictable response.

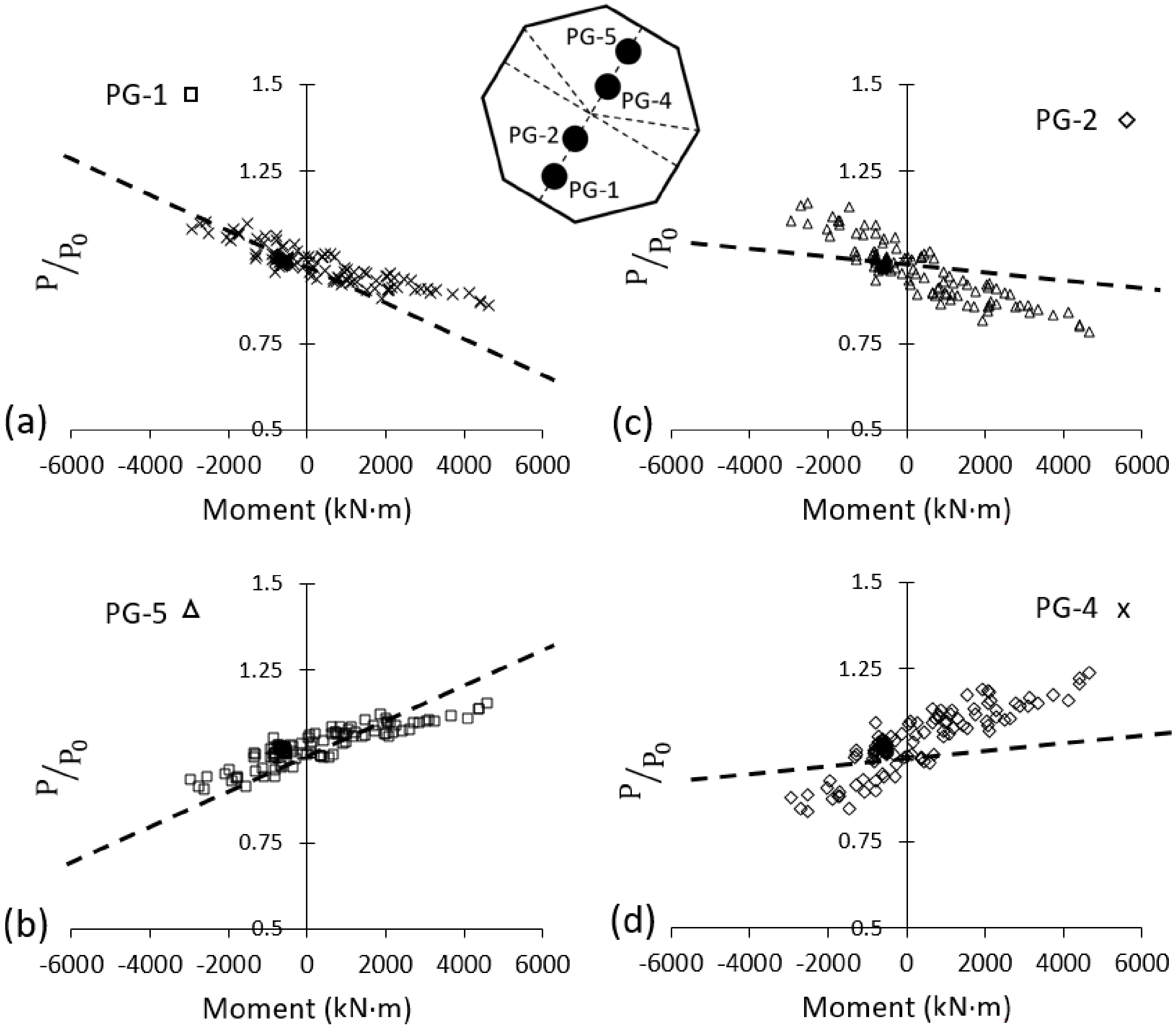

Figure 5-4: Normalized pressure vs. overturning moment at Site A along the PWD: (a) PG-1 (b) PG-5 (c) PG-2 and (d) PG-4. The dashed lines indicated the theoretical response of a rigid footing.

Figure 5-5 compares the results from both sites. Again, normalized pressure is used to minimize effects of slight differences in foundation geometry and static loads. Figures 5-5a and 5-5c shows the outer PG's, white Figure 5-5b and 5-5d shows the inner PG's. Most apparent is the near-identical responses of the inner PG's at both sites. Though Site B experiences a slightly larger range of moments, the slopes of each PG are remarkably similar. At Site A, PG-2 and PG-4 have slopes of -4.44·10-5 and -4.78·10-5, respectively, while their counterparts at Site B have slopes of -4.78·10-5 and -4.0·10-5.

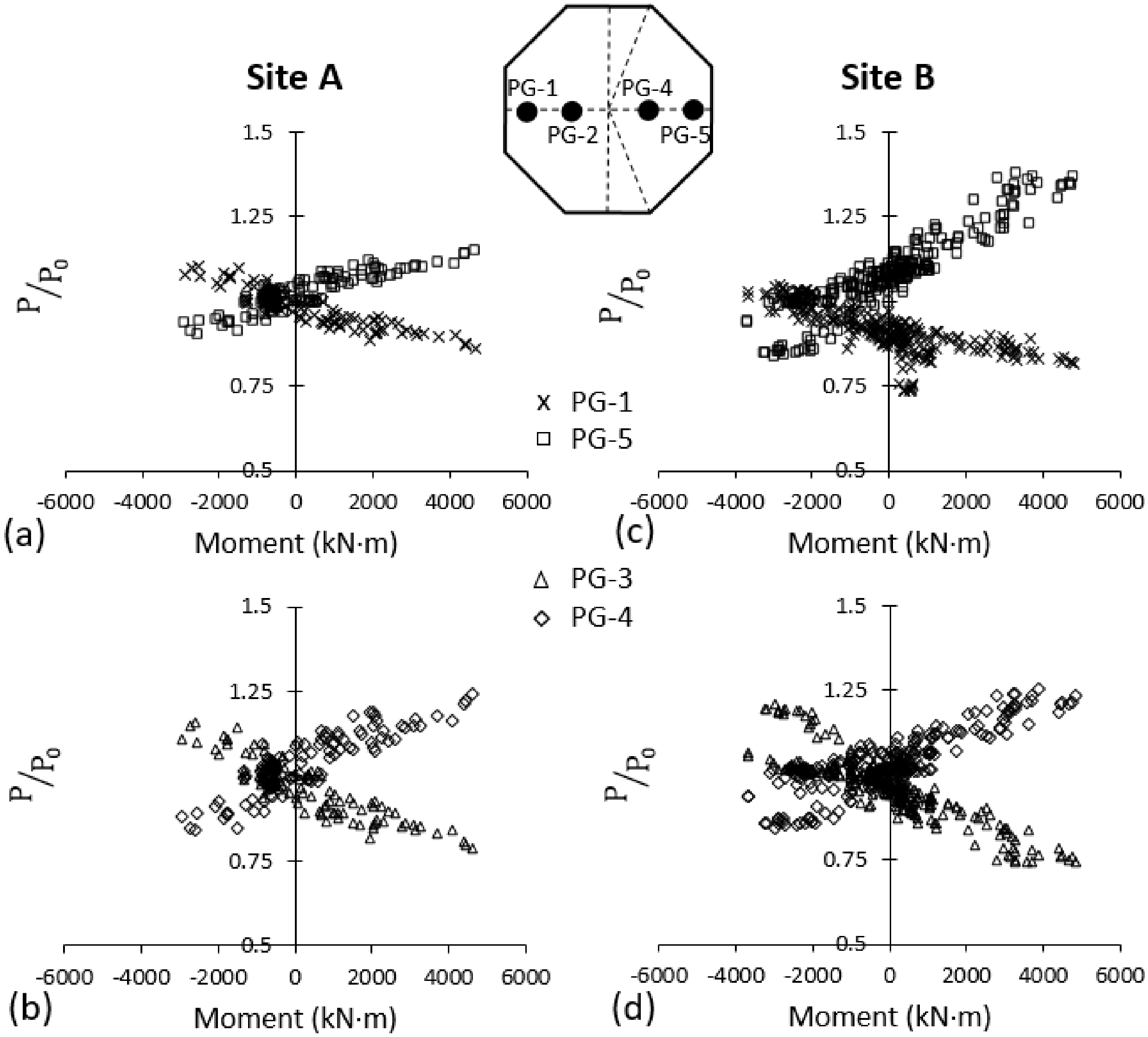

Figure 5-5: Comparison of normalized pressure responses at both sites along PWD: (a) Site A outer PG's (b) Site A inner PG's (c) Site B outer PG's and (c) Site B inner PG's.

Regarding the outer PG's, PG-1 at both sites respond quite similarly, with a slope of -2.91·10-5 at Site A and -2.75·10-5 at Site B. At Site B, PG-5 (slope = -5.78·10-5) has an elevated response to moment in comparison to Site A (slope = -2.92·10-5). Furthermore, the sensors at Site A do not exhibit the same scatter in pressure at negative overturning moments as are apparent at Site B, suggesting that the scatter at Site B may be an artifact of occasional instrument error or the datalogger occasionally mis-reading the signal rather than a result of the foundation's load transfer mechanism. The distinct similarity in pressure response, however, validates the observation of elevated pressure response compared to a theoretical response at the interior of the footing. A possible explanation of this phenomenon could be foundation flexibility, as the structure that is very wide and thin, so it may be overly-simplistic to assume a perfectly rigid footing. Finally, the response of two PG's that flank the PWD are compared in Fig. 5-6. Both PG's exhibit a similar response to overturning moment, though the sensor at Site A appears to have a non-linearity at high moments. Aside from the several non-linear points at Site A, both PG's exhibit a lesser response to the overturning moment than the PG's along the PWD, as would be expected.

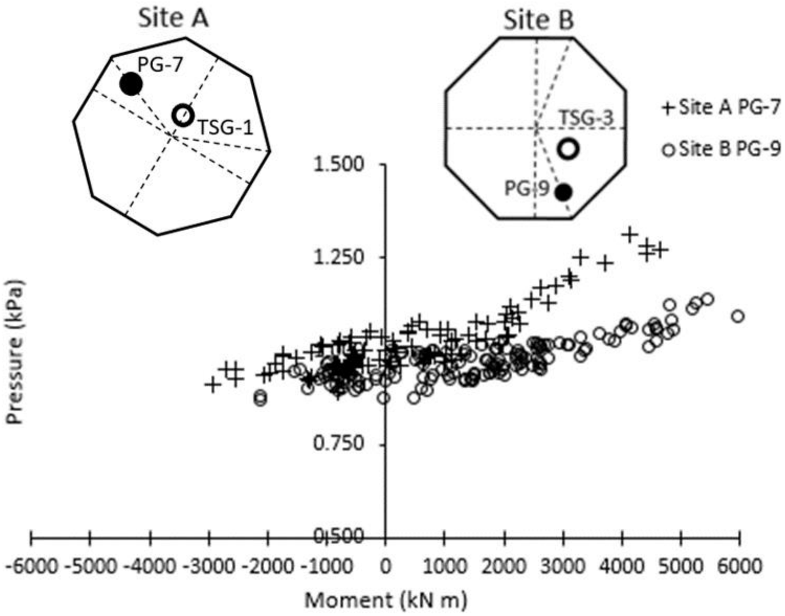

Figure 5-6: Normalized pressure vs. tower moment for a PG that flanks the PWD at each site.

5.1.3 Operational Stress-Strain Relationship

Figure 5-7 illustrates the strain and pressure response to moment at Site B. The deformation of SG-5, which corresponds to PG-5, also exhibits an elevated response to overturning moment, suggesting that the soil at the edge of the leeward side of the foundation may be more sensitive to load changes than the edge of the windward side. Since this does not occur at Site A, it appears this is a site-specific phenomenon. A possible explanation could be softer soil on the leeward side. Such a spatial variation in soil stiffness would result in higher deformation where soil is softer, and the elevated pressure response could be the result of a "bridging" phenomenon, where a significant difference in stiffness between the pressure cell and surrounding soil re-routes the load through the stiffer of the two materials. In this case, if the soil is softer, the pressure cell would be the stiffer medium, causing the induced loads

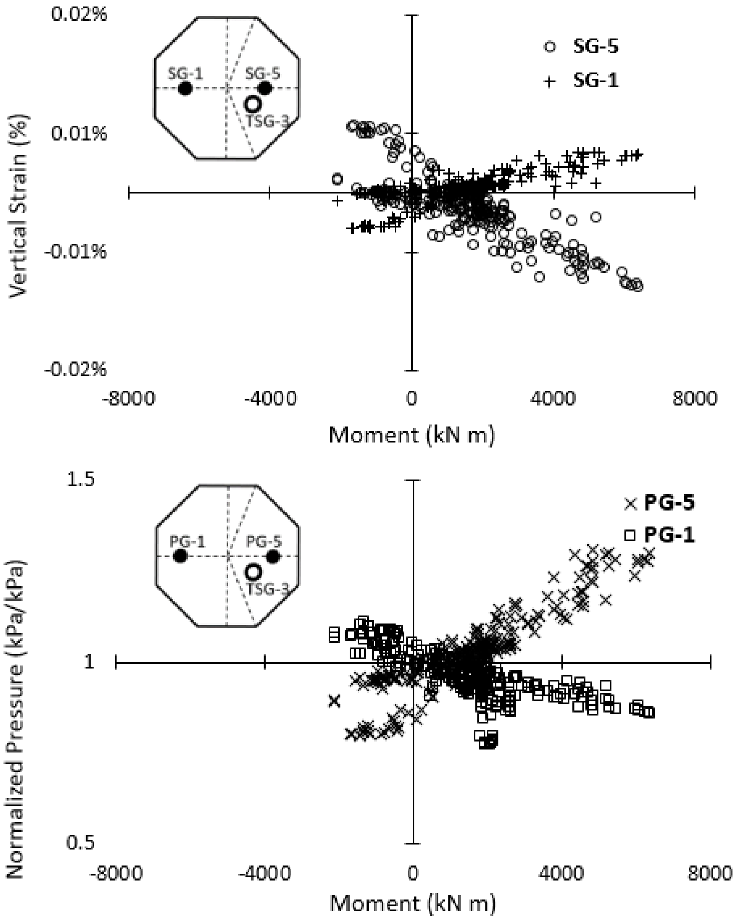

Figure 5-7: (a) Wind ward vs leeward SG relationship to overturning moment and (b) corresponding PG's vs overturning moment.

to preferentially flow through the pressure cell, resulting in a disproportionately higher response to transmitted vertical loads.

Finally, the stress-strain behavior of the soil was analyzed. At both sites, the normalized pressure was plotted against the strain. Figure 5-8 shows the results for the leeward side of the foundation (PG-5 and SG-5). Site A (Fig. 5-8a) shows a markedly steeper slope than Site B (Fig. 5-8b). The most likely explanation would be that the soil at Site A is stiffer than Site B. Though the boring logs for each site yielded nearly identical soils, the water content at each site could play a role in their stiffness, since a decrease in saturation is known to increase soils' stiffness. The water content of the foundation soil at Site A ranged from about 12% to 14%, while Site B's soil had slightly higher water contents from 13% to 19%. Furthermore, according to USGS historical data, the water table depth in the Site A region is

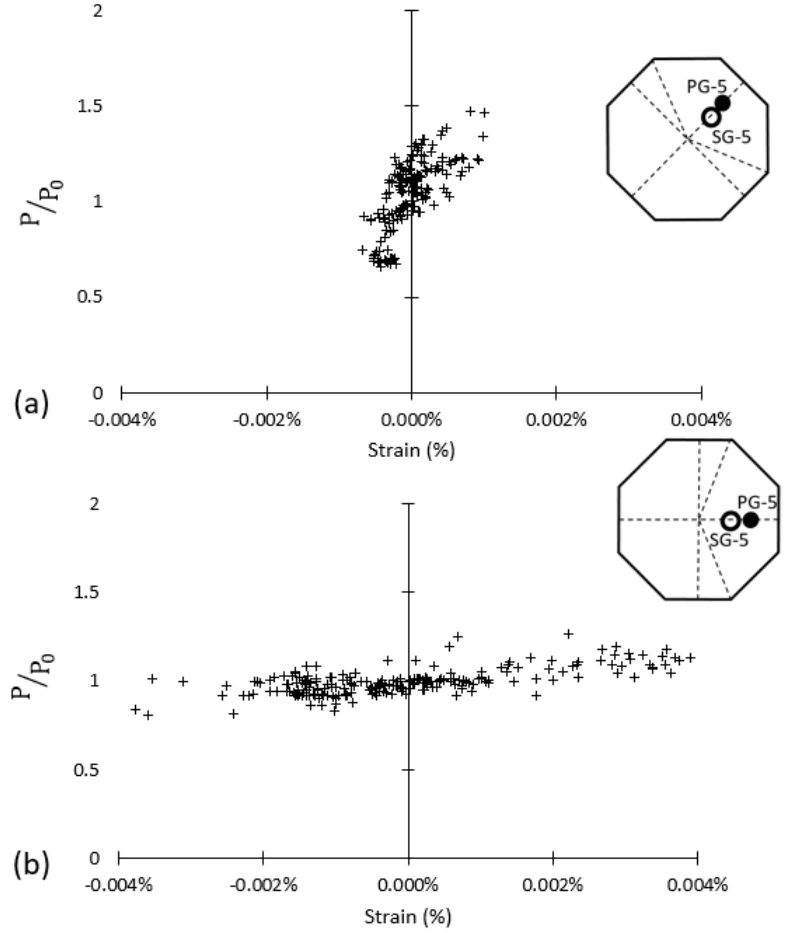

Figure 5-8: Soil strain versus normalized vertical pressure at (a) Site A and (b) Site B. The SG and PG used are adjacent and located on the leeward side of each foundation.

generally 30m or more below ground surface, whereas the water table in the Site B region is generally at around 10m depth, which could explain the lower water content, and subsequent stiffer soil, at Site A.

5.2 Design Implications

5.2.1 Harmonic Load Analysis

The results of this study have implications on design practices in three distinct ways: rotational stiffness calculation assumptions, pressure distribution for bearing capacity, and tower loads with regards to tower and anchor bolt design. Instrumentation results were compared to industry guidance, such as DNV/Risø (2002) and EuroCode 3 Chapter 9.

To assess the cyclic loads, an algorithm was used to calculate the magnitude of the cyclic moment and soil pressure. For each 4s cycle, the difference between the maximum strain and minimum strain was calculated and divided by two. The resulting value is the amplitude of the load cycle. The tower strain gauges in line with the PWD were used for the calculations, as they would represent the portion of the WTG experiencing the largest, most frequent loads, and can be considered the “worst case” at each site. Fig 5-9a shows the relationship between overturning moment and cyclic moment, which correlate well, as well as demonstrates that the cyclic moment varies throughout the life of the turbine and cannot be assumed to be a singular value. Based on the data recorded, the cyclic moment ranged from 0 kN·m to about 1,400 kN·m.

Furthermore, to validate the load transfer trends discussed in the Results section, the static vs. cyclic pressure was compared for PG-5 at Site B. Figure 5-9b displays the results for the same period as Fig. 5-9a, which exhibits a similar correlation, as well as follows a similar trend to, the tower moment, indicating the load transfer mechanism performs at both a macro- and micro-scale.

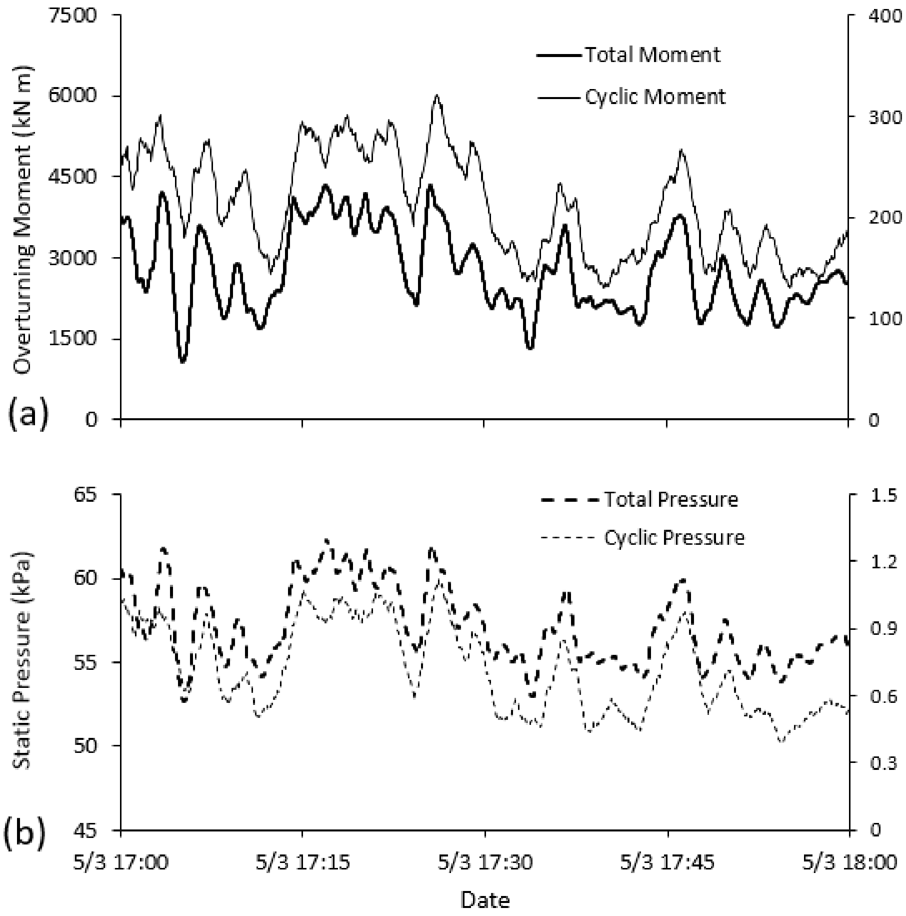

Figure 5-9: (a) Overturning moment and the cyclic moment amplitude at each point in time and (b) total average pressure with cyclic pressure amplitude at each point.

5.2.2 Foundation Soil Cyclic Shear Strain

The first major design implication relates to the rotational stiffness parameter. The controlling variable in the rotational stiffness calculation is the shear modulus, G. Since the foundation rocking induces dynamic loads in the foundation soil, however, the maximum shear modulus must be reduced by a reduction factor determined via a shear modulus reduction curve, which quantifies how the shear modulus of a soil degrades with increasing cyclic shear strain. In WTG design, the cyclic shear strain in the soil is assumed to be 0.1% (DNV/Risø 2002; ASCE/AWEA 2011), which significantly reduces the shear modulus for use in design calculations, typically by a factor of 0.2 to 0.45. Previous study, however, has suggested that this strain value is far too large (Yilmaz 2014). The maximum vertical strain measured by Yilmaz was about 0.007%, which corresponds to a shear strain of approximately

0.0055%. This value, however, represents the overall “static” deformation of the soil, as the strain gauges could only measure hour-averaged strain. Thus, the data neglects the cyclic component of the soil strain, though it does provide valuable insight into the overall stiffness of the soil. As discussed, however, the cyclic pressure and cyclic moment were able to be measured at high frequency, allowing analysis of their cyclic magnitudes. Soil strain was shown to have an approximately linear relationship with moment and pressure at the magnitudes measured (Fig. 5-7 and Fig. 5-8). Therefore, using the relationships established between soil strain, pressure and moment, in concert with measurements of cyclic pressure and cyclic moment, the cyclic shear strain could be back-calculated. Moreover, calculations in the opposite direction would reveal the approximate magnitude of cyclic moment required to induce 0.1% cyclic shear strain. Calculations were performed on data from Site B, as larger dataset was available, and Fig. 5-6 indicates the soil is less stiff than the soil at Site A, meaning the calculations would represent the weaker of the two sites.

For all calculations, the data from PG-5, TSG-3, and SG-5 were used, as they represent the leeward side of the turbine, which would experience the largest, and most frequent, cyclic loads. The required cyclic moment to induce 0.1% cyclic shear strain was calculated via two pathways. First, 0.1% cyclic shear strain was converted to cyclic vertical strain using an assumed Poisson’s ratio of 0.26 for unsaturated clay, which was then converted to cyclic moment with Fig 5-7a. The second path involved converting 0.1% cyclic shear strain to cyclic vertical strain and subsequently cyclic pressure with Fig 5-8b, which was converted to cyclic moment with Fig 5-4b. The resulting cyclic moments, found in the top two rows of Table 3, are both significantly higher than overturning moments, much less cyclic moments, that would be expected over the life of the turbine.

Conversely, two parameters were used to convert to maximum in situ vertical cyclic strain. The first calculation uses the maximum recorded cyclic moment, 1,400 kN·m, to calculate the cyclic vertical strain with Fig. 5-7a, which could then be converted from vertical to shear strain. The second parameter was the maximum recorded value for cyclic normalized pressure, 0.24, which was converted to cyclic moment with Fig. 5-5c, and then to cyclic vertical strain, and thus cyclic shear strain, with Fig. 5-7a.

The results are summarized in the final two rows of Table 3. Both methods yielded similar results of 0.0014% and 0.0021%, significantly lower than the assumed value of 0.1% and consistent with the magnitude of the results of previous research (Yilmaz 2014). Though this value will likely vary based on foundation subsurface conditions, foundation dimensions, and turbine size, it suggests a significant overestimation of in situ soil response, resulting in an unnecessarily over-conservative shear modulus reduction factor.

5.2.3 Soil-Structure Contact Pressure Distribution

Regarding the horizontal pressure distribution for bearing capacity calculations, DNV/Risø (2002) recommend an effective bearing area empirically derived from an idealized triangular pressure distribution that varies linearly across the diameter (Czerniak 1969). In this case, the pressure response nearer to the footing edge should be higher than the inner portion of the radius. Using Fig. 5-5 as a reference, the inner PG at three of the four pairs had a response 1.5-2 times that of the corresponding outer PG's. The lone exception is PG-5 and PG-4 at Site B, where PG-5 had a slightly stronger response than PG-4. Furthermore, if this relationship is carried to the PG's that flank the PWD, an identical response can be found, where the inner PG's have a response 1.5-2 times greater than the outer PG's. Altogether, these results suggest that the pressure distribution beneath the two WTG footings is non-uniform, with the peak pressure occurring somewhere in the middle of the footing radius.

5.2.4 Dynamic Tower Loads

Finally, the cyclic response of the tower was assessed for use in structural calculations, such as fatigue and tower vibration. DNV/Risø (2002) and EuroCode 3 Chapter 9 advise engineers to use a load spectrum to facilitate fatigue calculations. Additionally, DNV/Risø states that the stress distributions should follow an approximate Weibull distribution, similar to the wind speed profile. It was established in Fig. 5-1 that the tower moment and wind correlate well, so it stands to reason that the tower moment will also follow an approximate conventional Weibull distribution. To confirm this, however, a probability density distribution was created (Fig. 5-10a) for hour-averaged overturning moment data over the same five-month period as is used in Fig 5-1. A Weibull curve is plotted with the data points, confirming the assertion in DNV/Risø. Similarly, the cyclic moment data was plotted in a probability density function (Fig. 5-10b). Though this distribution also follows an approximate Weibull distribution, it has the shape of an exponential distribution, a special case of a Weibull curve. The tendency of the cyclic moment distribution towards smaller loads compared to the overturning moment, suggests that DNV/Risø (2002) is also correct in their assertion that stationary and operational conditions (i.e. smaller loads) dominate the fatigue load spectrum.

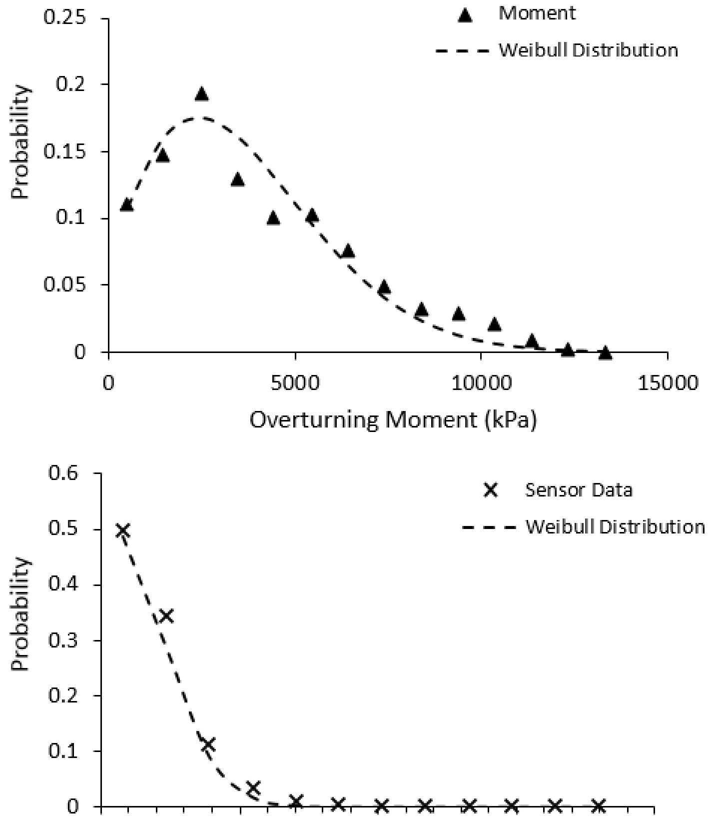

Figure 5-10: Probability distribution for (a) overturning moment and (b) cyclic moment. Plotted with each is a fitted Weibull distribution.

Next, a load spectrum was developed using each individual 4-second loading cycle during the two-week period. The loads were put into evenly-sized bins, and the size of each bin calculated. The data was then plotted (Fig. 5-11) based on the format of sample load spectrums given in DNV/Risø (2002) Section 4.4.1. and EuroCode 3 Chapter 9.

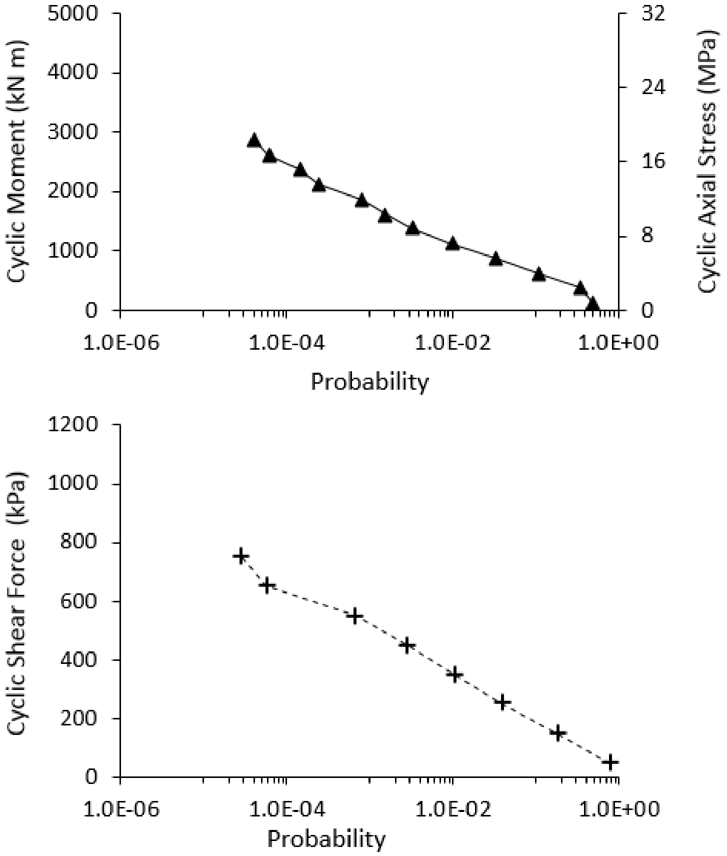

Figure 5-11: Load spectrums for (a) moment and corresponding axial stress and (b) shear force.

Figure 5-11a shows the cyclic axial stress, while Fig. 5-11b shows the cyclic shear force, calculated by finding the difference between the cyclic moments of the vertically stacked tower strain gauges. It is important to note, however, that this study's data was plotted with probability on the x-axis rather than total cycles, N, as industry guidance advises. A two-week window may not necessarily lend itself to extrapolating out to 20+ years of loading cycles, as it is unlikely that a ten, five, or even one-year wind event occurred during this period, which would induce even larger static and cyclic moments.

Additionally, as reported by Yilmaz (2014), large spikes in moment occur for several cycles immediately following a start-up and shut-down event, and this dataset may not include such events. However, the sample load spectrum given in DNV/Risø purports that a semilog load spectrum will be approximately linear, which is supported by the data plotted in Fig. 5-11. Being that the moment appears to follow the approximate Weibull distribution DNV/Risø recommends, it may be reasonable to assume one of two possibilities: that this trend continues, maintaining a near-linear semi-log relationship on the load spectrum at high loads, or that the slope may actually begin to flatten at high loads, as turbines will pitch the blades at extremely high wind speeds to minimize overturning moment. Nonetheless, the data suggests that, during normal, operational conditions, the distribution of cyclic loads follows an approximately linear semi-log trend. This data can be used in several ways, whether it be determining the fatigue loads in the anchor bolts or tower structure, calculating cyclic deformation (i.e. stiffness) of the anchor bolts/base joint, and assessing the vibration of the tower itself.

5.3 Conclusions

In this study, the operational tower loads and foundation soil response was investigated with direct measurements by field instrumentation. Tower moment and shear force were found to be correlated with wind speed, with magnitudes within expected design values. Furthermore, the moment along the predominant wind direction (PWD) was found to spike when the wind direction coincided with the PWD. When overturning moment was compared to the soil deformation and vertical pressure, the three mirrored each other extremely well, indicating a predictable, consistent load transfer. The overturning moment and pressure along the PWD also proved to have a nearly linear relationship. When normalized to the static, zero wind-load vertical pressure, the pressure responses at the two sites were nearly identical. The windward and leeward pressure gauges also nearly perfectly mirrored each other, indicating that the windward uplift was roughly balanced by the leeward pressure spike. Interestingly, the response of the inner pressure gauges was greater than the outer pressure gauges, suggesting that the load distribution is more complex than design engineers commonly assume. The soil strain response also compared similarly to the overturning moment, resulting in a nearly linear relationship.

Furthermore, when plotted versus pressure, the stress-strain response also proved to be nearly linear, with Site A being the stiffer of the two responses. Finally, the harmonic analysis of the tower and soil pressure response revealed that the amplitude of the cyclic moment was about an order of magnitude less than the overall overturning moment, and that the cyclic pressure amplitude was nearly two orders of magnitude less than the static pressure. These cyclic measurements, when correlated to cyclic shear strain, resulted in a maximum shear strain two orders of magnitude less than the industry standard assumption of 0.1%. When placed into a probability distribution, the moment distributions followed approximate Weibull distributions, with the cyclic moment tending towards static and operational conditions, while the overall overturning moment resembled the general Weibull distribution of wind speed. The cyclic moment and cyclic shear force distributions also yielded a nearly linear load spectrum, similar to the example given in DNV/Risø (2002). Altogether, when considered within the framework of WTG foundation design, the conclusions of this study point to an overall lack of understanding of the fundamental soil response mechanisms beneath a WTG, and should be considered in the overall design to improve reliability and efficiency.

6 SUCTION CONTROLLED DYNAMIC LAB TESTING

6.1 Method Development

6.1.1 Specimen Preparation

To determine the effects of matric suction on the shape and magnitude on a SMRC for undisturbed soil, specimens were taken directly adjacent to each other from the plastic liner, with care taken to ensure changes in material (i.e., brown clay to gray clay) were not present within or between specimens in each set. Once an intact, un-fractured section of soil was selected for use, the length needed for trimming was extruded. Then, the sections were carefully trimmed down to 35-36 mm diameter. To ensure consistency, the diameter along the length of each specimen was measured repeatedly with calipers and altered until all measurements along the specimen length were between 35 and 36 mm. Once the required diameter was reached, the length of the specimen was trimmed to 56-58 mm and leveled on each end.

6.1.2 Hydraulic Control Testing

Before SMRC testing was performed, the saturation control mechanism was tested on remolded samples compacted to field density to ensure consistent results and establish typical imbibition and drainage times. To saturate a specimen, the latex membrane and pressure chamber were first sealed with rubber O-rings. Once the apparatus was successfully assembled, the chamber pressure was increased to 70 kPa, roughly equal to the in situ confining stress, as a seating confining stress. The lines connected to the HAE disc were then flushed of air with de-aired water. Water pressure was then increased to 35 kPa concurrent with a 35 kPa increase in confining pressure to maintain a 70 kPa effective stress within the specimen. The line connected to the top cap was opened to allow passage of displaced air as the specimen saturates. After a series of imbibition tests to saturate the sample, it was determined that full saturation from in situ moisture content occurs in 24-36 hours. Thus, a period of 36 hours was used for all specimens as the standard time of imbibition.

Once the saturation mechanism was confirmed to be functioning, the axis translation mechanism was tested to ensure consistent results. When the specimen was deemed fully saturated, the backpressure was reduced to atmospheric pressure, with the confining stress reduced back to 70 kPa. With the backpressure line remaining open to water flow, the air pressure through the top platen was increased to the desired matric suction magnitude. In the case of these preliminary tests, this pressure was 35 kPa. The confining pressure was increased by the same amount to maintain a constant 70 kPa net stress on the latex membrane. The specimen was allowed to drain until the pipette level remained constant. The compacted soil specimens drained to a consistent saturation, confirming a functioning hydraulic control system.

Soil water characteristic curves (SWCC's) for the site soil can be seen in Fig. 6-1.

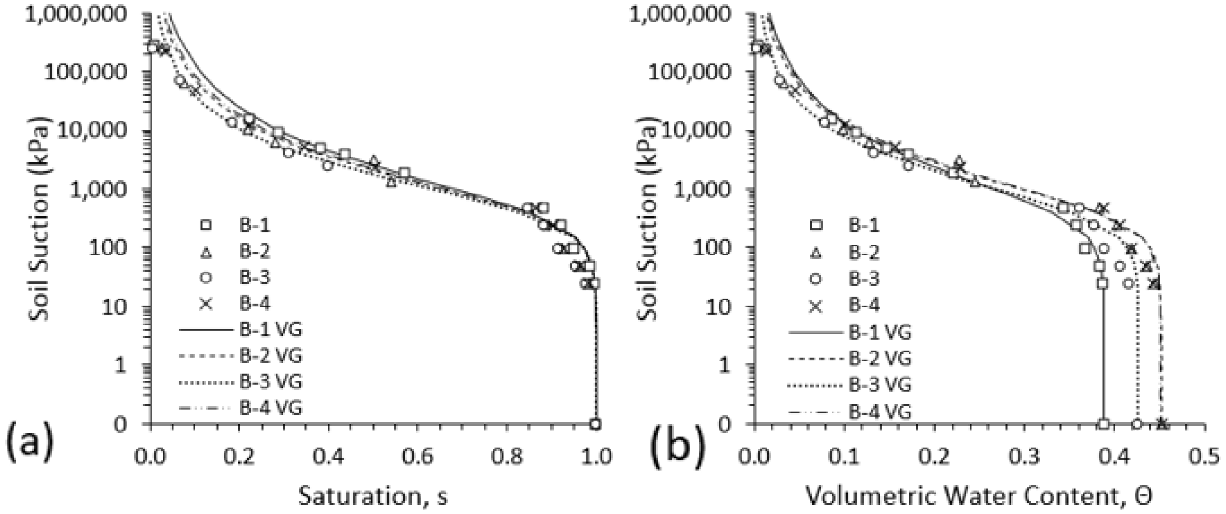

Figure 6-1: Soil water characteristic curves for the site soil based on (a) saturation and (b) volumetric water content. Van Genuchten fits are plotted for each.

6.1.3 Testing Parameters

For full-scale testing, four matric suction conditions were tested: saturated, 25 kPa, 50 kPa, and 100 kPa. Since the resonant column is non-destructive, the same specimen could be used for each level of matric suction. During cyclic triaxial testing, however, the specimen reaches, or nears, failure after each test. As a result, a new specimen must be trimmed, saturated, and drained at the given matric suction for each suction level tested. Resonant column testing began with the smallest signal amplitude that would yield readable results. The input voltage was progressively increased after each reading taken. Concurrent to testing, the points along the SMRC were plotted, and testing was halted once the shear strain approached 10^{-3}. Cyclic triaxial testing progressed from the smallest load the loading piston could impart until either the piston's maximum loading capability was reached, or the specimen failed.

6.2 Results

An example of a SMRC for two soil specimens is shown in Fig. 6-2. Figure 6-2a shows the results for a soil taken from boring B-1 at a depth of roughly 5m below ground surface. Figure 6-2b shows the response of a soil from boring B-3 at a depth of approximately 5m below ground surface. A clear trend of increasing shear modulus with increasing soil suction is present.

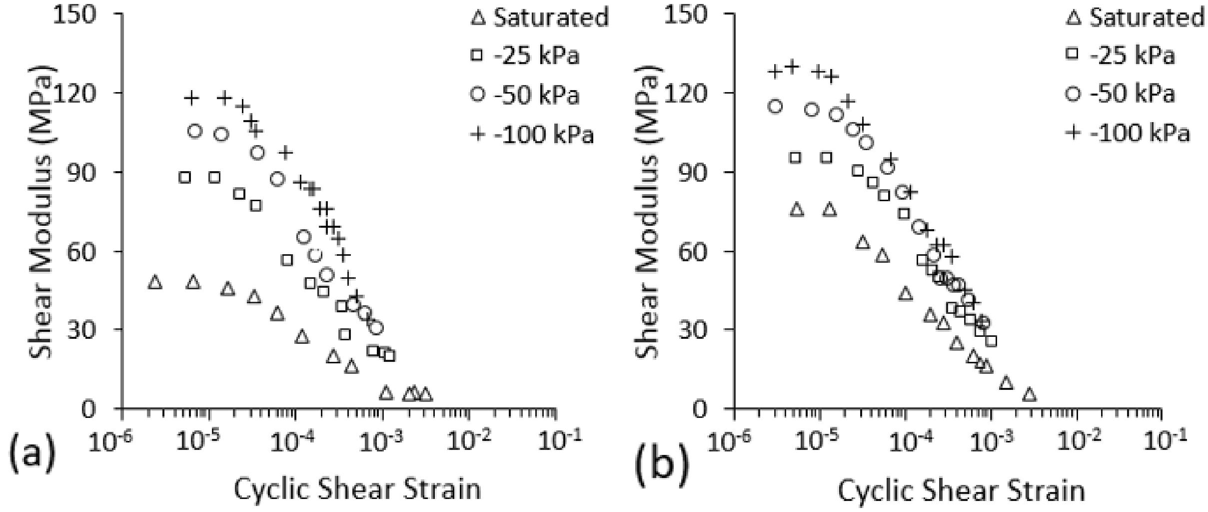

Figure 6-2: Typical SMRC's for the site soil. (a) B-1 at 5m depth and (b) B-3 at 5m depth.

Moreover, this increase exists at all strain magnitudes measured. The merging of resonant column and cyclic triaxial data was generally successful and smooth, though issues did arise. For example, since cyclic triaxial testing is destructive, new specimens had to be made for each suction level. Due to inherent heterogeneity in the soil profile, the responses, even between specimens only several centimeters apart in the profile, occasionally did not line up as well with the resonant column data. Figure 6-2b illustrates this phenomenon, where the points at ψ = 100 kPa begins to cross the points at ψ = 50 kPa as the SMRC approached 10^{-3} cyclic strain. Moreover, at ~$3\cdot10^{-4}$ strain, the cyclic triaxial results at ψ = 50 kPa appear to intersect the resonant column data for ψ = 25 kPa. Such deviations, however, were expected prior to testing due to the aforementioned inherent heterogeneity. The SMRC's in Fig. 6-2a, on the other hand, lined up quite well, with the saturated, 25 kPa, and 50 kPa curves continuing from resonant column to cyclic triaxial smoothly, though the cyclic triaxial portion of the curve for ψ = 100 kPa appears to cross the data for ψ = 50 kPa. Only one specimen, from boring B-2 at 5m depth, resulted in resonant column and cyclic triaxial curves that were too incongruent to justify use.

The main utility in a SMRC lies in its ability to depict a soil's response at various strain levels. Figure 6-3 illustrates this by plotting the shear modulus at each matric suction level for three different strain magnitudes. The data is taken from the SMRC for boring B-1 at 5m depth (Fig. 6-3a) and boring B-3 at 5m depth (Fig. 6-3b).

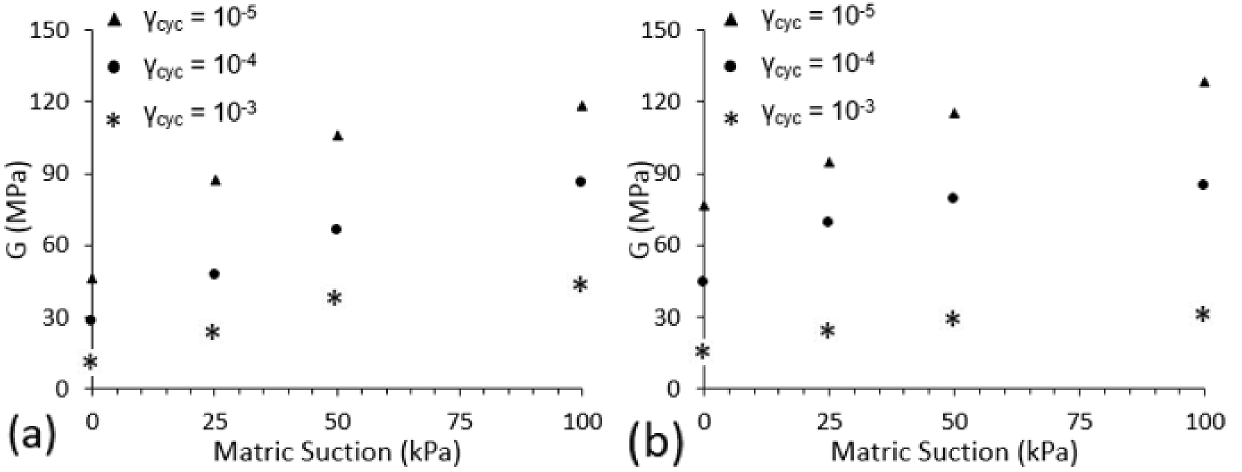

Figure 6-3: Shear modulus response at incremental matric suctions for three strain levels in (a) B-1 at 5m depth and (b) B-3 at 5m depth.

A strain of 10^{-5} represents the small strain shear modulus, G_0, while 10^{-4} and 10^{-3} represent intermediate and large strains, respectively. The data shows that, as strain increases, the effects of suction appear to diminish, as the slope begins to flatten between points. For B-1, at 10^{-5} strain, the spread of measured stiffness values is roughly 72 MPa, while at 10^{-3} strain, the spread is about 33 MPa. Similarly, the small strain and large strain ranges for specimen B-3 are about 52 MPa and 16 MPa, respectively. Figures 6-4a and 6-4b shows the same stiffness data, however the matric suction was converted to equivalent saturation based on the SWCC's in Figure 6-1.

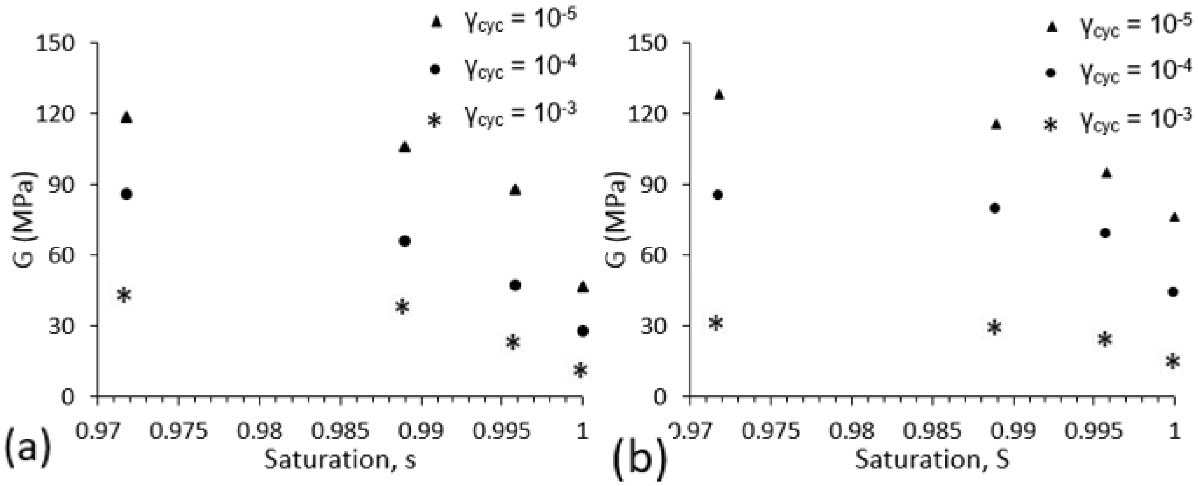

Figure 6-4: Shear modulus response vs. saturation for three strain levels in (a) B-1 at 5m and (b) B-3 at 5m depth.

SMRC's can also be normalized by dividing the shear modulus at each measured strain by G_0. The resulting normalized parameter is also known as the shear modulus reduction factor, and is useful for estimating a reduced shear modulus when only the G_0 is available. The normalized curves suggest that the overall stiffness-strain relationship is not sensitive to saturation. The specimens generally fell along the same curve. Figure 6-5 show typical results for the soils tested. Though the curves were not identical, no discernible or regular pattern emerged specimen to specimen. When plotted against typical SMRC curves for various soil types, the specimens generally fall around the sand or lean clay region (Fig. 6-6). As the site's low plasticity clay contains sand and gravel throughout, this trend is consistent with expectations. It

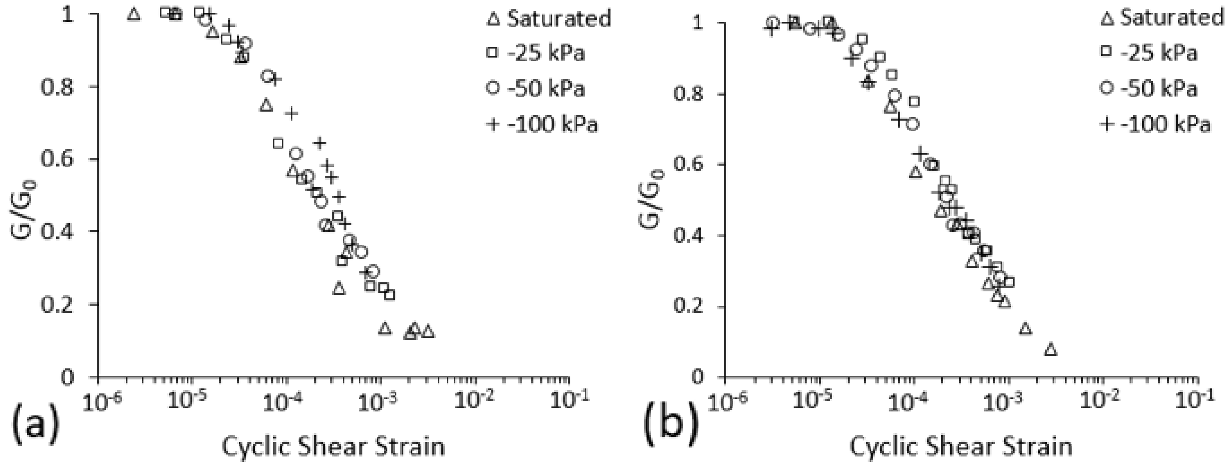

Figure 6-5: Normalized shear modulus reduction curves for specimens at (a) B-1 at 5m depth and (b) B-3 at 5m depth.

does appear the curves do tend towards the sand/gravel portion of the curve, suggesting that the presence of sand in gravel, even in small quantities, can have a non-negligible effect on the shape of the curve.

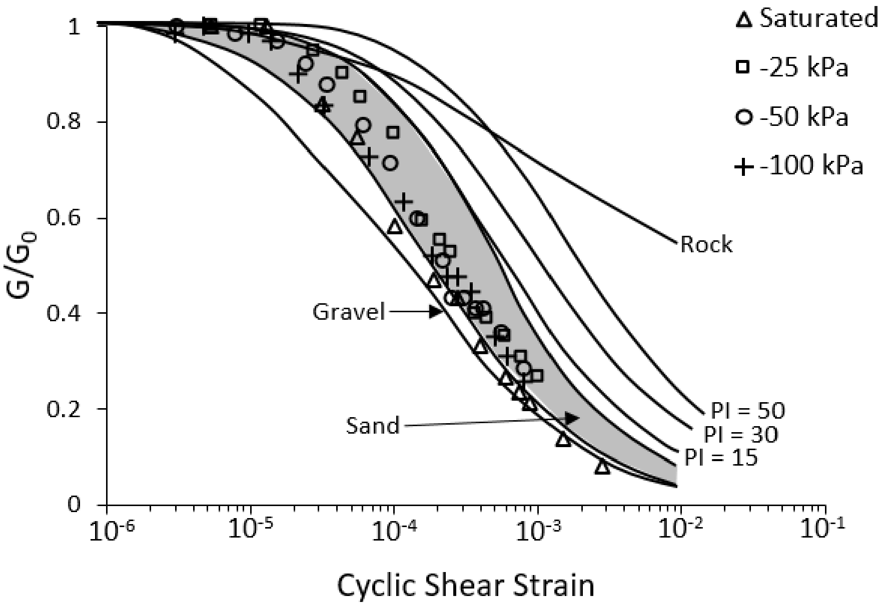

Figure 6-6: Normalized SMRC from site soil vs typical curves for various soil types (after Sykora et al 1992, Vucetic & Dobry 1991).

To illustrate the full spectrum of specimen values, Fig. 6-7 shows the effects of matric suction on the shear modulus at the same three strain levels as in Fig. 6-7. In this case, however, the three strain levels are split up so that the results of each specimen tested can be displayed. Figure 6-7a, 6-7b and 6-7c represent strains of 10^{-5}, 10^{-4}, and 10^{-3}, respectively. The shape of each specimen's curve remains similar, though the magnitude of each varies, creating an envelope of possible soil stiffness' at the site. As mentioned previously, some crossover within specimen curves occurs at large strain, where the stiffness at 100 kPa matric suction, for example, may be equal to, and in one case, less than the stiffness at 50 kPa suction. Again, the effects of matric suction appear to diminish with increasing strain consistently among tests.

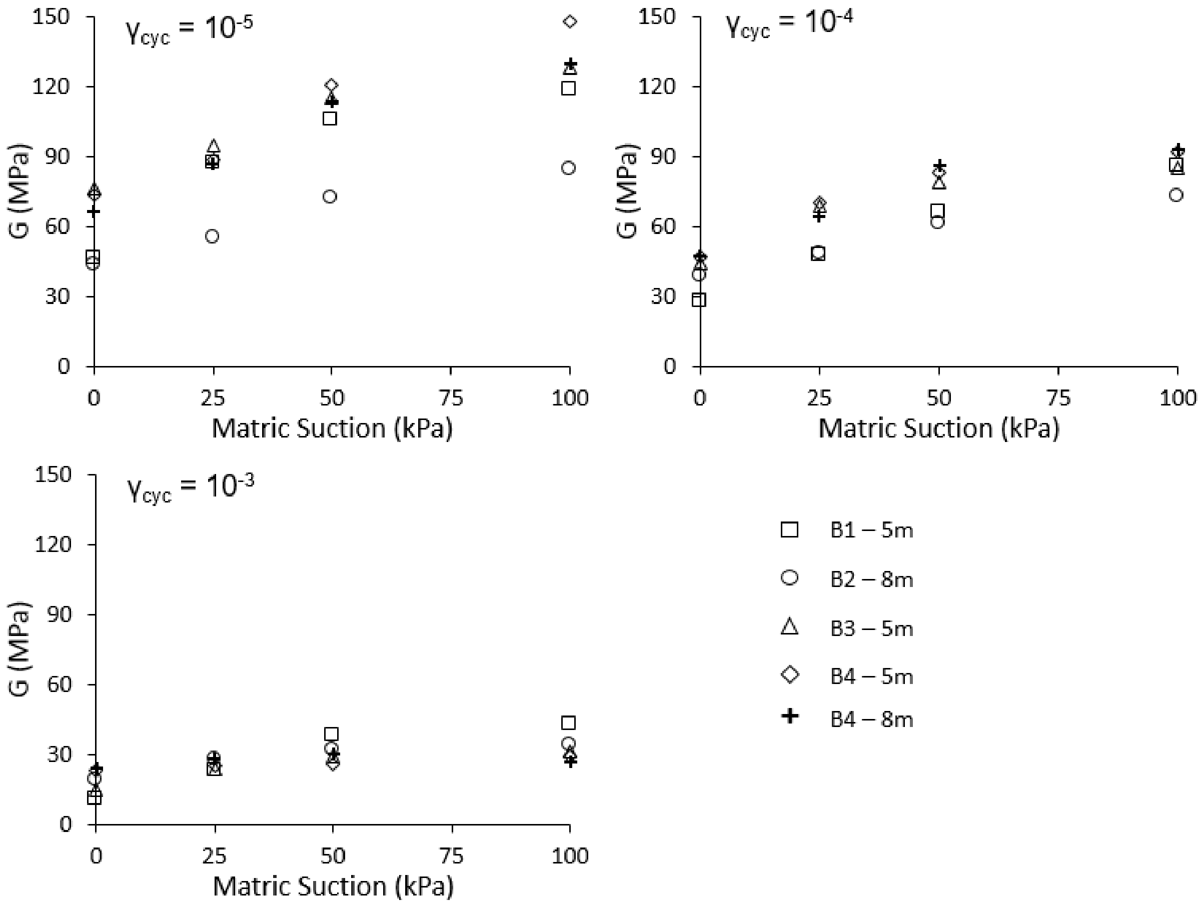

Figure 6-7: Stiffness vs matric suction response for each specimen tested at (a) $10^{-}{}_{5}$ *(b)* 10^{-4} *(c)* 10^{-3} *strain.*

6.3 Conclusions and Discussion

As a method for developing shear modulus reduction curves over a full spectrum of cyclic strains, the use of resonant column and cyclic triaxial was generally successful. The majority of datasets were able to be reasonably merged into one cohesive curve. Some combinations of the two methods, however, did not overlap well, or, in some cases, crossed over into curves of specimens at lower suction. This was expected prior to testing, as two specimens, no matter how close together in the soil profile, will not be perfectly identical and will vary in their response due to vertical and horizontal spatial variations in the depositional environment and load history. In addition, the differences in specimen loading during each test could impact the response, potentially affecting the marriage of the two datasets. Resonant column testing directly measures shear through the propagation of shear waves through the soil cylinder, while the cyclic triaxial test indirectly measures shear response by measuring the compressional response of the cylinder, which is then correlated to the shear modulus via Poisson's ratio. The stress path each method induces in the specimen is fundamentally different, meaning the methods are not completely analogous and may illicit different responses.

The application of matric suction to the two approaches proved to be effective overall in affecting the stiffness response. The method worked better with the resonant column, as it is non-destructive, so the suction could be progressively increased without changing the specimen out. Thus, the results of the resonant column are likely more representative of the true response of the soil to changes in saturation. Conversely, the need to change cyclic triaxial soil cylinders for each suction level resulted in less consistent results. Small changes in soil composition and void ratio from specimen-to-specimen could affect the suction-saturation response, potentially altering the stiffness response among cylinders. Overall, however, the hydraulic control system was effective, repeatable, and yielded reasonable results. Regarding the specimens' response, the effects of matric suction consistently diminished with increasing strain. This is likely due to the breaking of menisci between soil particles. These menisci create a capillarity effect due to the surface tension of water, which pulls the particles together, increasing the overall effective stress of the soil block. As soil particles begin to move relative to one another, ultimately separating during high dynamic strain events, the menisci will break, eliminating the capillary effects, and thus effective stress, within the soil skeleton (Bozkurt et al. 2017).

The variation in response across the site was significant, with $G_{0,sat}$ varying from 43 to 76 MPa. Based on the boring logs, the site subsurface was reported as very uniform. The use of undisturbed soil, however, showed that, though the site appeared uniform, the laboratory tested soil stiffness distribution did not necessarily follow the same trend. Small strain shear moduli across the four matric suction levels applied for all specimens tested can be seen in Fig. 6-8. The presence of gravel could, however, have an impact on specimens as small as those used in testing. When trimming samples, 1.0-1.5cm diameter pieces of gravel would occasionally impede the trimming process, making the specimen unusable. If, for instance, a large piece fell perfectly within the soil cylinder and was thus undetectable, the specimen would be tested with a large piece of gravel inside. Conversely, an adjacent specimen used for the same SMRC might have had

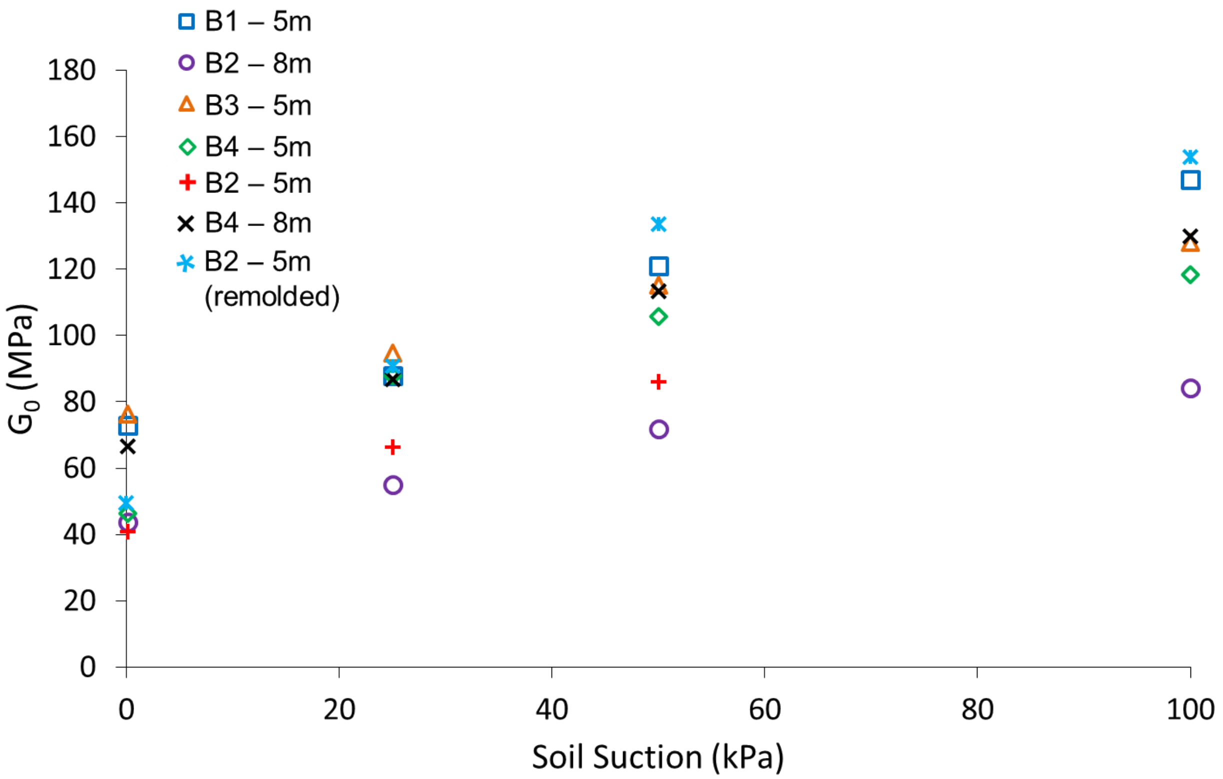

Fig. 6-8: Summary of small-strain shear modulus response to matric suction for all specimens tested.

little to no gravel at all, even though both specimens would be treated as identical volumes of soil. Even for specimens only centimeters apart in the profile, the presence of gravel in one cylinder and not the other could produce discrepant, unrepresentative results, when in reality, the response of the larger soil block would likely be somewhere in between the two. Nonetheless, the results presented in this study underscore the viability of this methodology for characterizing the dynamic response of unsaturated soils over multiple strain regimes. Though the normalized SMRC's appear generally unaffected by saturation, the overall variation in magnitude of the shear modulus with decreasing saturation can be utilized in systems such as shallow foundations under dynamic loading (i.e. wind turbine generators) and geotechnical systems in earthquake-prone areas.

7 WTG SITE SOIL PROFILE CHARACTERIZATION

7.1 Data Analysis

7.1.1 Models

Three models were used to estimate the stiffness profile of the site soil. The models and their inputs are summarized in Table 7-1.

Table 7-1: Summary of stiffness models.

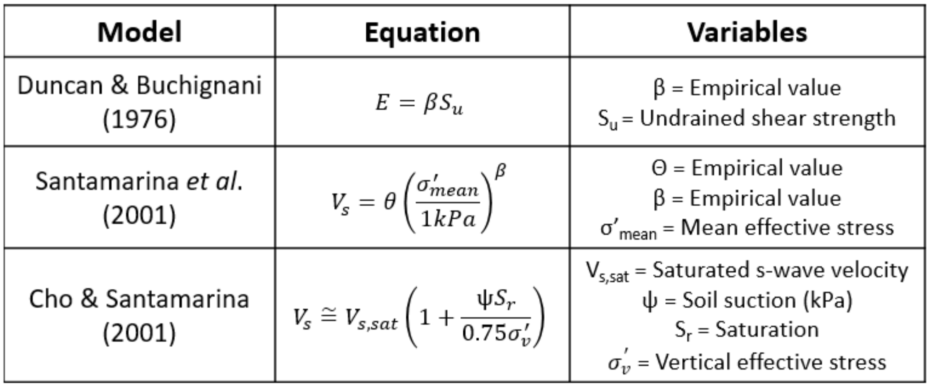

Model	Equation	Variables
Duncan & Buchignani (1976)	$E = \beta S_u$	β = Empirical value S_u = Undrained shear strength
Santamarina *et al.* (2001)	$V_s = \theta \left(\frac{\sigma'_{mean}}{1kPa} \right)^{\beta}$	Θ = Empirical value β = Empirical value σ'_{mean} = Mean effective stress
Cho & Santamarina (2001)	$V_s \cong V_{s,sat} \left(1 + \frac{\psi S_r}{0.75 \sigma'_v} \right)$	$V_{s,sat}$ = Saturated s-wave velocity ψ = Soil suction (kPa) S_r = Saturation σ'_v = Vertical effective stress

Duncan and Buchignani (1976) provide a simple model (Model 1) for determination of a fine-grained soil's Young's modulus, E, via the undrained shear strength, where β is an empirically derived parameter that is a function of the soils plasticity index (PI) and overconsolidation ratio (OCR). Due to the many uncertainties in the problem, as well as complexity in soil behavior, there is quite a large spread for a given soil. For the WTG site soil, where the PI is between 12 and 15, the range of β is 600 to 1500 for normally consolidated soil. As OCR increases, both the upper and lower bounds decrease, resulting in a lower value of β. Though the difference between the bounds of β decreases as OCR increases, the envelope still indicates significant uncertainty in the model. Such uncertainty would logically push engineers to be more conservative, yielding potentially overconservative, and thus overly expensive, designs.

This model, however, was used to develop envelopes for the soil's stiffness based on undrained shear strength values determined via pocket penetrometer and SPT correlations, seen in Fig 7-1. The maximum stiffness calculated was 264 MPa, while the minimum was found to be 30 MPa. Within a single s_u measurement, the largest difference in modelled stiffness was in B2 at a depth of 3.66m, where the envelope spanned 106 to 264 MPa. Furthermore, the general trend of the stiffness in the top 7.32m in both borings is similar, with the profile reaching a peak stiffness around 3m and immediately degrading with depth.

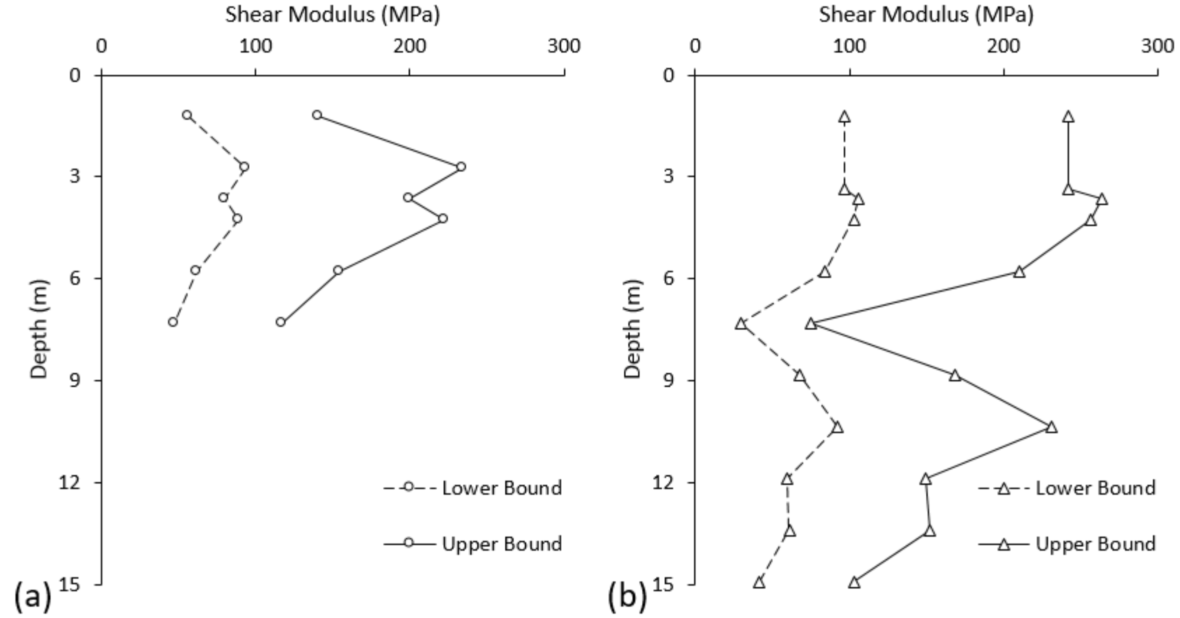

Figure 7-1: Stiffness profile based on undrained shear strength derived from SPT blow counts for (a) boring to 7.5m and (b) boring to 15 at Site A.

The next model (Model 2), given by Santamarina *et al*. (2001), considers the soil's unit weight and two empirical parameters, β and Θ. The β parameter is a function of soil type, and can be determined via a plot of Θ vs. β, where ranges of β for various soil types are given. In the case of the stiff, overconsolidated clay at the WTG site, β would be roughly between 0.15 and 0.10. Using a measured soil density of 2125 kg/m^3, two profiles were plotted with the equation from Table 7-1, one for each bound of β (Fig. 7-2).

As illustrated in the profile, the effects of β affect the overall slope of the profile. In fact, the average stiffness of the profiles is 167.3 and 165.9 MPa for β values of 0.15 and 0.10, respectively. Furthermore, the difference in stiffness at the top of the profile, roughly 18 MPa, is approximately equal to the stiffness difference at the bottom. This method results in smooth, simple profiles that requires only basic knowledge

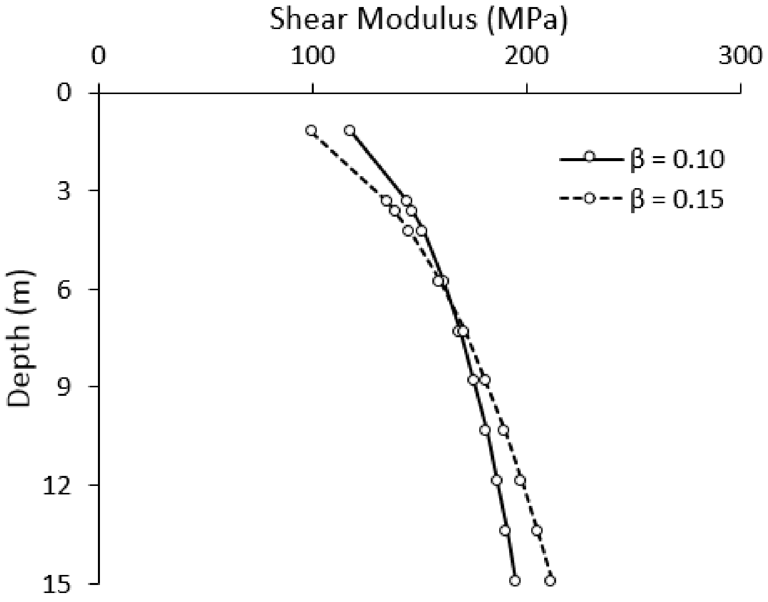

Figure 7-2: Stiffness profile model for Site A.

of the soil's geotechnical parameters. However, this model does not take into account variabilities in the soil other than density that may affect stiffness.

The final model (Model 3) examined was developed by Cho and Santamarina (2001) and considers the effects of soil saturation. Based on soil water characteristic curves (SWCC's) (ASTM D6936-16) developed for the site soil (Fig 6-1), the approximate soil suction could be estimated based on water content, a profile of which was provided in the boring logs. The void ratio varied between 0.3884 and 0.4519 for the specimens tested. Since void ratio was not measured at each depth, a range of saturation levels was calculated based on the range of void ratios, which were then converted to soil suctions based on the SWCC's. The model also considers the vertical effective stress and β parameter as a part of a correction factor that is multiplied by the saturated shear wave velocity. Figure 7-3 illustrates the stiffness profiles based on the model for the measured upper and lower bounds of void ratio. Most apparent is the increase in stiffness and variability predicted by this model compared to Santamarina *et al*. (2001). The stiffness increases the most at the top of the profiles, where the soil would theoretically be the least saturated. The profiles then continue in a nearly vertical direction, reaching a minimum of 211.8 and a maximum of 297.8

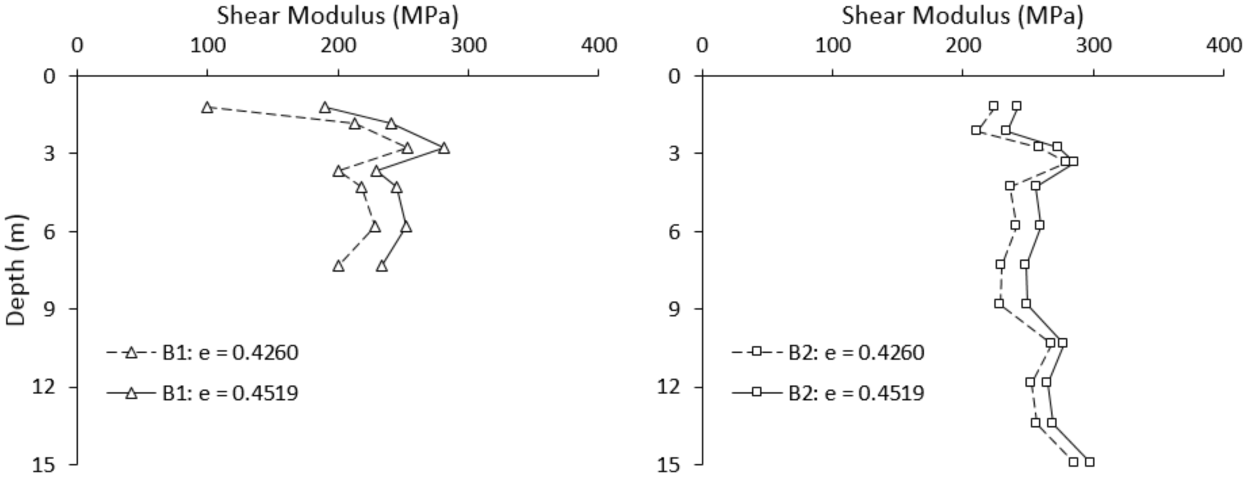

Figure 7-3: Stiffness profile considering unsaturated conditions for the borings to (a) 7.5m and (b) 15m at Site A.

MPa at 2.1m and 15m depths, respectively. The profiles exhibit localized peaks at depths of approximately 2.75-3.4m and 10m, while local minimums occur at depths of 7.3-8.8m and 12-13.5m. The upper and lower bounds have average G values of 263.1 and 247.7, respectively.

Figure 7-4 directly compares the results of the three models. The spread of Model 1 is clearly the largest, covering a span of up to about 160 MPa, whereas the other two only span a maximum of 20 MPa at a given depth. Models 1 and 2, however, cover a similar range overall, averaging 133 MPa and 166 MPa along the entire profile. Model 3, on the other hand, averages 255 MPa. Interestingly, the profile based on undrained shear strength and soil saturation share a similar trend along the profile, suggesting that SPT blow counts do capture stiffness changes to some degree. Both reach local maximums around 3m and 10m, while sharing decreases in stiffness from 3-8m and 10-14m. With regards to model overlap, the only significant overlap occurs between Model 1 and Model 2, though it should be noted that the large spread of Model 1 likely contributes to this. Furthermore, when comparing Models 2 and 3, the effects of depth (i.e. increasing effective stress) appear to be at least partially negated by the saturation profile.

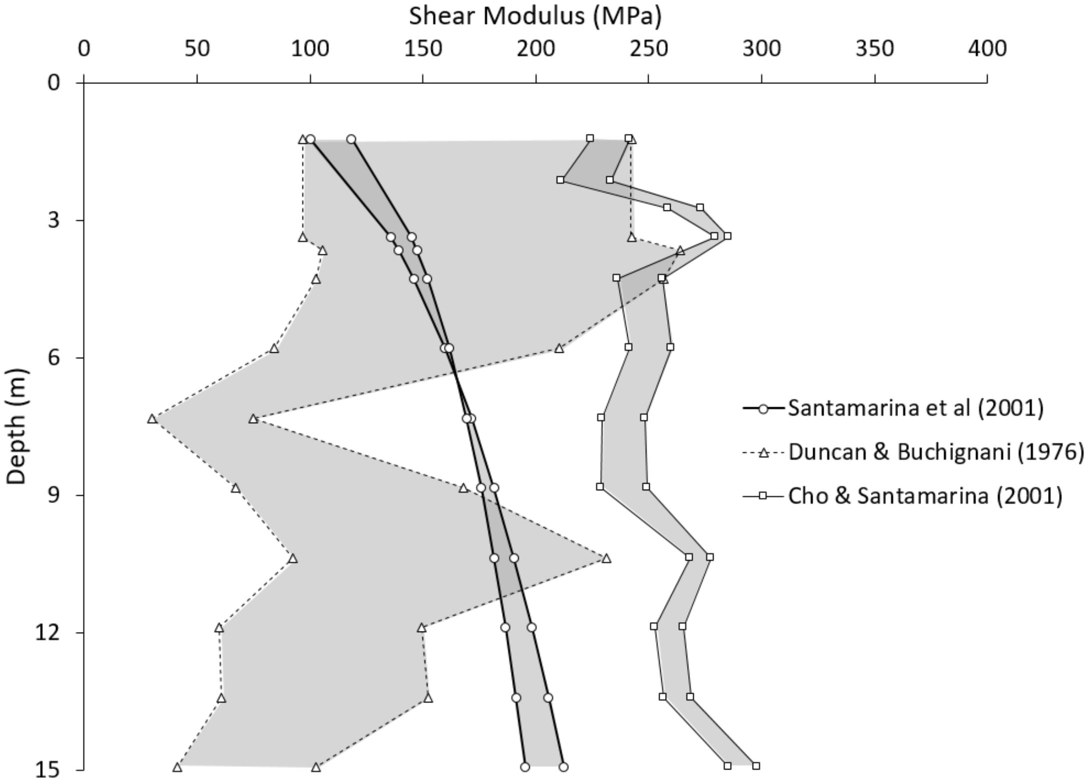

Figure 7-4: Combination of all three model results, with the envelopes for each shaded.

7.1.2 Laboratory Results

Resonant column and cyclic triaxial tests were used to measure soil stiffness in a controlled laboratory setting. The range of maximum shear moduli (G_0), was found to be approximately 43-76 MPa at 70 kPa confining stress, the approximate confining stress immediately beneath the WTG foundation. When normalized by G_0, the shear modulus reduction curves (SMRC) generally follow the same trend, with the exception of the soil at 8m depth from B2, which is shifted to the upper right. The general scatter, even with an extremely uniform site soil, may be due to variations in the sand and gravel content across the site. The boring logs, as well as the additional borings advanced post-construction, indicated seams of increased sand and gravel, which would affect the shape of the SMRC's.

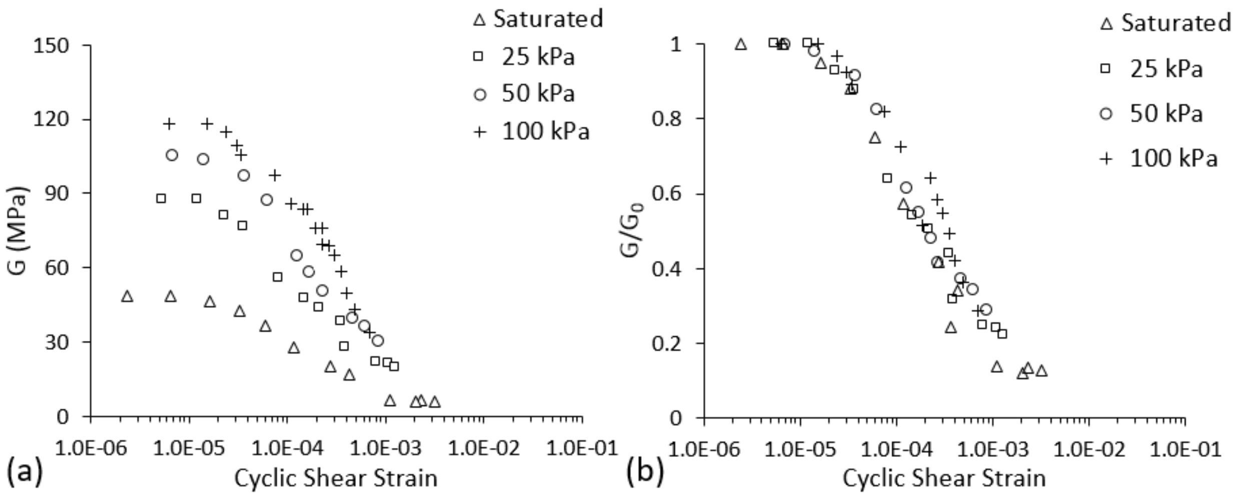

Figure 7-5: (a) raw SMRC and (b) normalized SMRC for a specimen tested at matric suctions of 0, 25, 50, and 100 kPa.

The specimens were also tested at soil suction levels of 25, 50, and 100 kPa. An example of a suction-controlled SMRC can be seen in Figure 7-5a. The soil shows a clear increase in stiffness with increasing suction (i.e. decreasing saturation) at all strain magnitudes measured. Furthermore, this increase in stiffness diminishes with strain, though the normalized SMRC (Fig 7-5b) indicates that the suction has no discernible impact on the shear modulus reduction factor (G/G_0). Figure 7-6a illustrates the effect of soil suction on G_0 for the specimens tested. The results showed that, at 100 kPa soil suction, the soil stiffness reached 84 to 147 MPa, roughly doubling G_0 from saturated conditions. Moreover, the data showed that the gains in stiffness with soil suction decreased as soil suction increased. The data was then normalized by dividing G_0

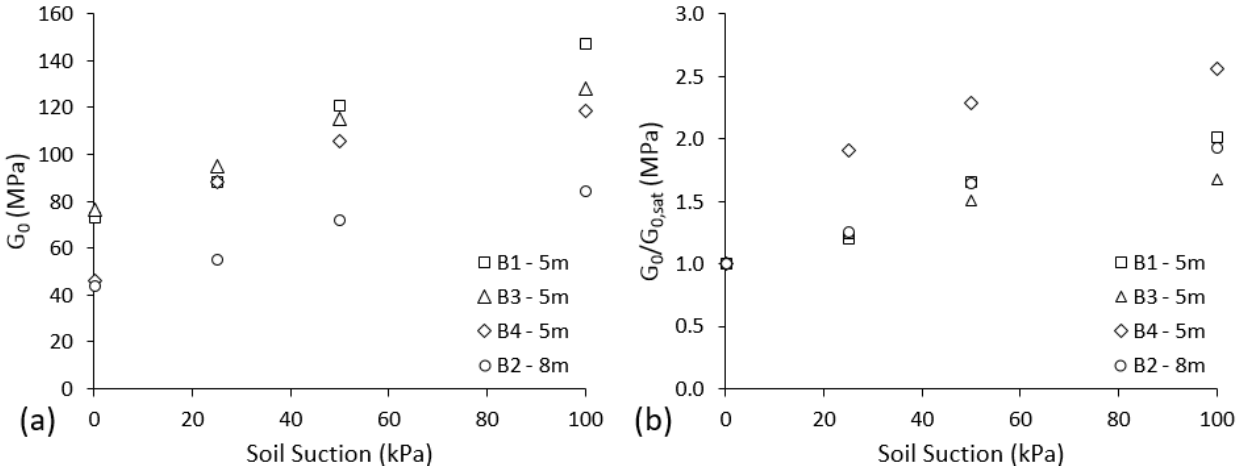

Figure 7-6: Effects of matric suction on G_0 for (a) raw shear modulus and (b) G_0 divided by G_0 at saturation.

at each suction level by G_0 at soil saturation (Fig 7-6b). The data again showed a spread in results. For example, at 100 kPa suction, the measured stiffness ranged from 1.67 to 2.56 times the saturated G_0.

7.1.3 Shear Modulus Envelope

Using the data from one of the thermal dissipation sensors, TDS-1, the *in situ* water content (Θ) directly below the footing could be assessed. During a six month period in 2017, moisture content readings were taken every hour, allowing a time series of water content to be created (Fig. 7-7). The sensors revealed a clear seasonal trend, where moisture content reaches a peak of 0.4531 in November. The minimum recorded value occurred in minimum of 0.4515 in August. Since the void ratio where the sensors were placed is unknown, assumptions from measurements at other site locations were made. Based on the SWCC's for the site soil (Fig. 6-1), the data would theoretically only be valid for the case where the void ratio is 0.4519, as the volumetric water content cannot be greater than the void ratio. In this case, the lowest measured Θ corresponds to a saturation of approximately 99.91%. According to the SWCC van Genuchten fit, the equivalent suction at this saturation level is 43 kPa. The maximum measured Θ corresponds to the saturated condition. Figure 7-8 demonstrates the envelope of shear moduli based on the variation in soil location and

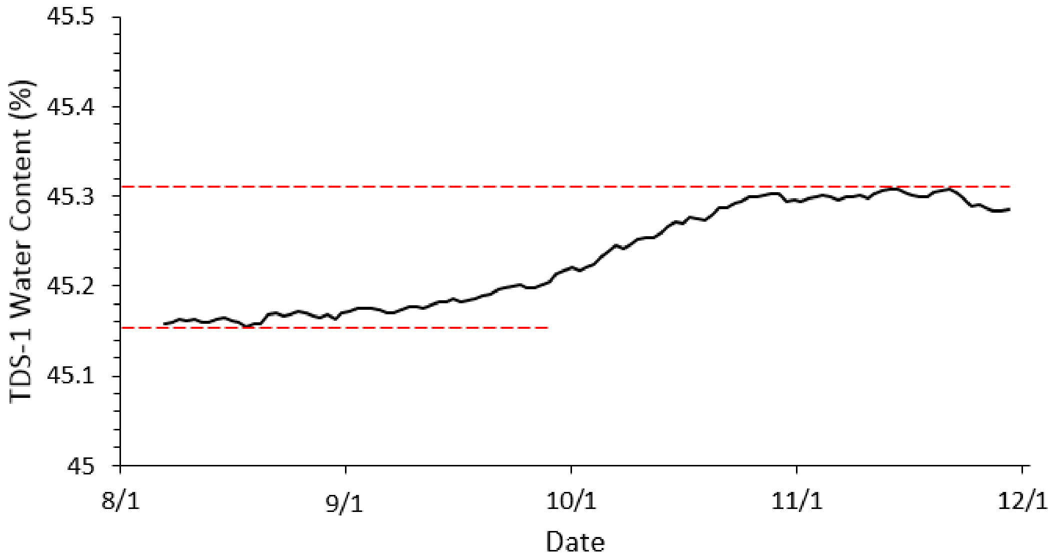

Figure 7-7: Time series of 12-hour averaged volumetric water content data for TDS-1 at Site A.

measured soil suction. The stiffness ranged from approximately 43 MPa to 115 MPa for specimens tested at a confining stress of 70 kPa, approximately the confining stress at TDS-1.

7.2 Discussion

Each of the three models used resulted in an envelope with some degree of uncertainty. Model 1, though simple to calculate using data from SPT blow counts and pocket penetrometer testing, yielded a spread where the lower bound of stiffness was 2.5 times smaller than the upper bound stiffness. Such uncertainty would undoubtedly call for significant conservatism. Model 2, on the other hand, proved relatively consistent within the parameters used. Moreover, the two profiles had roughly the same average stiffness over the depth of investigation. The model, however, is highly idealized and produces a smooth curve that does not necessarily capture inherent heterogeneity in the soil. Lastly, Model 3 has a spread similar to Model 2, while considering the effects of soil suction due to unsaturated conditions. As alluded to previously, this model depicts similar trends to Model 1, suggesting some correlation between SPT results and water content. Model 3, however, has significantly less uncertainty in the spread. For more accurate results, however, *in situ* soil suction would have to be monitored via instrumentation or undisturbed samples

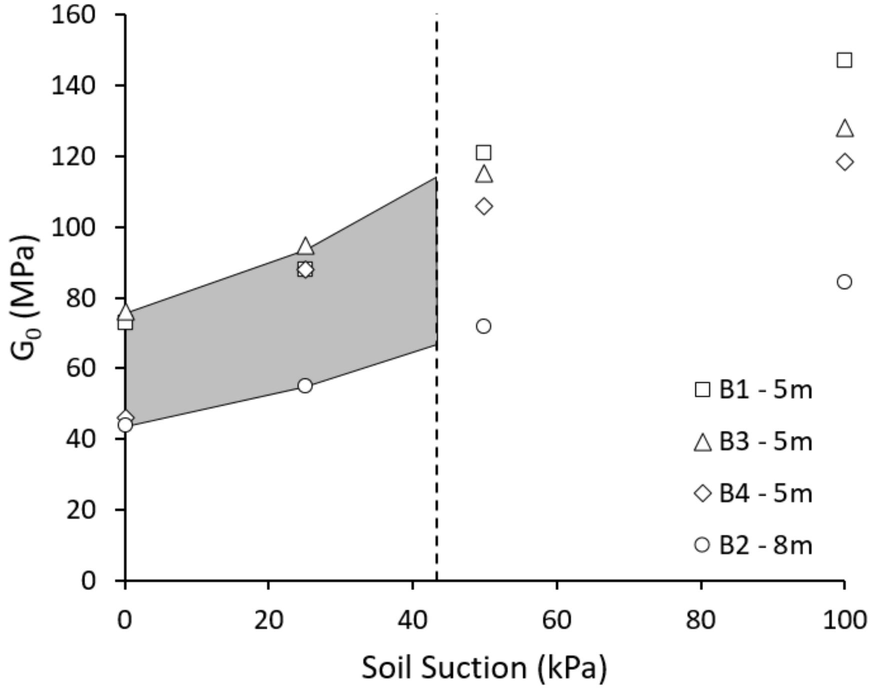

Figure 7-8: Shear modulus envelope for Site A soil immediately below foundation based on measured water content values.

used to calculate saturation and develop SWCC's. Such instruments and lab testing can be costly and time consuming. Moreover, the fluctuation in water content would need to be monitored long-term to determine the wettest, and thus least stiff, conditions.

When comparing the lab data and models, it is apparent that Model 3 significantly overestimates the soil stiffness. The results of Model 1 line up relatively well with the range the envelope in Fig. 7-9 covers. At 5m and 8m depth, where all specimens were taken from, Model 1 ranges from roughly 50-100 MPa, nearly identical to the lab testing. However, this may be coincidental, as Model 1 varies considerably with depth. Model 2 appears to overestimate the stiffness, though not as much as Model 3. Since Model 2 is highly idealized, it was expected that the value would likely not match perfectly.

7.3 Conclusions

Overall, the models' performance varied. Though Model 1 appeared to match well with lab values, the overall uncertainty associated with the model is not ideal. As a result, an engineer using this model would likely have to use the more conservative value. Model 2 performed worse that Model 2 in that it did not overlap with lab results. On the other hand, the spread was much smaller and undrained shear strength values are not needed. If such geotechnical parameters do not exist for a given soil, this Model may be useful as a rough starting point, however, it should be used with caution, as it does not account for profile heterogeneity. Finally, Model 3 performed the worst of the three Models compared to lab values. Though the model can account for changes in the soil conditions, the values were far too high. Moreover, the saturation level and soil suction along the profile can be difficult to measure and predict long-term. Thus, an engineer in practice would likely have to assume the more conservative case of soil saturation, rendering Model 3 useless.

8 REFERENCES

Adekunte, A. O., Gavin, K., & Casey, B. 2009. Comparison of monitored wind turbine foundation behaviour with design predictions. In *Sustainable Energy Ireland*.

Araya, S. C. 1979. *Design of Structures and Foundations for Vibrating Machines*. Houston, TX: Gulf Publishing Co.

ASCE/AWEA. 2011. *Recommended Practice for Compliance of Large Land-Based Wind Turbine Support Structures*. American Wind Energy Association, (Washington, DC) and American Society of Civil Engineers (Reston, VA).

ASTM D698. 2012. *Standard Test Methods for Laboratory Compaction Characteristics of Soil Using Standard Effort*. ASTM International, West Conshohocken, PA. www.astm.org

ASTM D1557. 2015. *Standard Test Methods for Laboratory Compaction Characteristics of Soil Using Modified Effort*. ASTM International, West Conshohocken, PA. www.astm.org

ASTM D2407. 2017. *Standard Practice for Classification of Soils for Engineering Purposes (Unified Soil Classification System)*. ASTM International, West Conshohocken, PA. www.astm.org

ASTM D3999M-11e1. 2013. *Standard Test Methods for the Determination of the Modulus and Damping Properties of Soils Using the Cyclic Triaxial Apparatus*. ASTM International, West Conshohocken, PA. www.astm.org

ASTM D4015-15e1. 2017. *Standard Test Methods for Modulus and Damping of Soils by Fixed-Base Resonant Column Devices*. ASTM International, West Conshohocken, PA.

ASTM D4318. 2017. *Standard Test Methods for Liquid Limit, Plastic Limit, and Plasticity Index of Soils*. ASTM International, West Conshohocken, PA. www.astm.org. ASTM International, West Conshohocken, PA. www.astm.org

ASTM D6836-16. 2016. *Standard Test Methods for Determination of the Soil Water Characteristic Curve for Desorption Using Hanging Column, Pressure Extractor, Chilled Mirror Hygrometer, or Centrifuge*. ASTM International, West Conshohocken, PA. www.astm.org

ASTM D6913. 2004. *Standard Test Methods for Particle-Size Distribution (Gradation) of Soils Using Sieve Analysis*. ASTM International, West Conshohocken, PA. www.astm.org.

ASTM D7263. 2009. *Standard Test Methods for Laboratory Determination of Density (Unit Weight) of Soil Specimens*. ASTM International, West Conshohocken, PA. www.astm.org

Biglari, M., d'Onofrio, A., Mancuso, C., Shafiee, A., Jafari, M.K. 2010. "Small Strain Behavior of Unsaturated Plastic Material in Suction Control RCTS Test." *Unsat Soils*. 1. 33 – 38.

Biglari, M., Jafari, M.K., Shafiee, A., Mancuso, C., d'Onofrio, A. 2011. "Shear Modulus and Damping Ratio of Unsaturated Kaolin Measured by New Suction-Controlled Cyclic Triaxial Device" *Geotech Testing J*. 34(5). 525 – 536.

Biglari, M., & Ashayeri, I. 2012. An empirical model for shear modulus and damping ratio of unsaturated soils. In *5th Asia-Pacific Conference on Unsaturated Soils*. Pataya, Thailand.

Borowicka, H. 1943. Uber ausmittig belastete, starre Platten auf elastisch-isotropem Untergrund. *Ingenieur-Archiv, 1*, 1–8.

Boussinesq, J. 1885. Application des potentiels a l'etude de l'equilibre et du mouvement des solides elastiques. *Memoire Suive de Notes Etendues Sur Divers Points de Physique-Mathematique Ed d'Analyse*.

Bowles, J. E. 1982. *Foundation Analysis and Design*. McGraw-Hill.

Bozkurt, M.G., Likos, W.J., Fratta, D.O. 2017. "Capillary forces between equally sized moving glad beads: an experimental study." *Canadian Geotech J*. 54: 1300-1309.

Cambridge University. 2003. *Materials Data Book*. Cambridge University Engineering Department, Cambridge, UK.

Cavallaro, A., Grasso, S., Maugeri, M. 2006. "Dynamic Clay Soils Behaviour by Different in Situ and Laboratory Tests." Presented at the *Geotechnical Symposium - Soil Stress-Strain Behavior: Measurement, Modeling and Analysis*. Rome, Italy. March 16-17, 2006.

Cho, G.C., Santamarina, J.C. 2001. "Unsaturated particulate materials – particle-level studies." *J Geotech Geoenv Eng.* 127(1), pp 84-96.

Cho, G., Dodds, J., & Santamarina, C. J. 2006. Particle Shape effects on Packing Density, Stiffness, and Strength: Natural and Crushed Sands. *Journal of Geotechnical and Geoenvironmental Engineering*, *132*(5), 591–602.

Clayton, C. R. I., Priest, J. A., Bui, M., Zervos, A., & Kim, S. 2009. The Stokoe resonant column apparatus: effects of stiffness, mass and specimen fixity. *Geotechnique*, *59*(5), 429–437.

Coduto, D., Yeung, M. R., & Kitch, W. A. 2010. *Geotechnical Engineering: Principles and Practices* (2nd ed.). Prentice-Hall.

Czerniak, E. 1969. Foundation Design Guide for Stacks and Towers. *Hydrocarbon Processing*, *June*, 95–114.

Diaz-Rodriguez, J. A., & Lopez-Molina, J. A. 2008. Strain Thresholds in Soil Dynamics. In *14th Wolrd Conference on Earthquake Engineering*. Beijing, China.

Det Norske Veritas (DNV/Risø). 2002. *Guidelines for Design of Wind Turbines* (2nd ed.). Copenhagen, Denmark: Det Norske Veritas & Risø National Laboratory.

Dong, Y. Lu, N., MCartney, J. 2018. "Scaling Shear Modulus from Small to Finite Strain for Unsaturated Soils*." J Geotech Geoenv Eng*. 144(2): 04017110.

Drnevich, V. P., Hardin, B. O., & Shippy, D. 1978. *Modulus and Damping of Soils by the Resonant-Column Method*. *STP35673S Dynamic Geotechnical Testing*. West Conshohocken, PA.

Duncan, J.M., Buchignani, A.L. 1976. *An Engineering Manual for Settlement Studies*. Dept. of Civil Engineering, U. California-Berkeley.

El Mohtar, C.S., Drnevich, V.P., Santagata, M., Bobet, A. 2013. "Combined Resonant Column and Cyclic Triaxial Tests for Measuring Undrained Shear Modulus Reduction of Sand With Plastic Fines." *Geotechnical Testing Journal*. 36(4). 1-9.

EN 1993-1-9 (EuroCode). 2005. (English): Eurocode 3: Design of steel structures - Part 1-9: Fatigue. European Committee for Standardization, Brussels, Belgium.

Elsabee, F., & Murray, J. P. 1977. *Dynamic Behavior of Embedded Foundations*. *R77-33*. Cambridge, MA.

Gazetas, G., Tassoulas, J.L., Dobry, R., O'Rourke, M.J. 1985. "Elastic settlement of arbitrarily shaped foundations embedded in half-space." *Geotechnique*. 35(2), 339-346.

Geokon Instruction Manual, Model 3500, 3510, 3515, 3600 Earth Pressure Cells. Geokon Inc., New Hampshire, USA.

Geokon Instruction Manual, Model 4430 VW Deformation Meter. Geokon Inc., New Hampshire, USA.

Ghayoomi, M., Suprunenko, G., Mirshekari, M. 2017. "Cyclic Triaxial Test to Measure Strain-Dependent Shear Modulus of Unsaturated Soil." *Int'l J Geomech*. 17(9). 04017043.

Hadjian, A. H., & Luco, J. E. 1977. On the Importance of Layering on the Impedance Functions. In *6th World Conderence on Earthquake Engineering* (pp. 1675–1680). New Delhi, India.

Hardin, B. O., & Drnevich, V. P. 1972. Shear modulus and damping in soils: measurement and parameter effects. *ASCE Journal of Soil Mechanics Foundation Division*, *98*(SM6), 603–624.

Hardin, K. O., Vincent, I., Drnevich, P., Wang, J., & Clay, E. 1994. Resonant Column Testing at Pressures up to 3.5 MPa. *Geotechnical Testing II*, *ASTM 1213*, 222–233.

Hoyos, L., Suescun-Florez, E., Puppala, A. 2015. "Stiffness of Intermediate Unsaturated Soil from Simultaneous Suction-Controlled Resonant Column and Bender Element Testing." *Eng. Geology*. 188. 10–28.

International Electrotechnical Commision, (IEC). 2005. *IEC 61400-1 International Standard: Wind Turbines - Part 1: Design Requirements*. Geneva, Switezerland.

Intergovernmental Panel on Climate Change (IPCC). 2012. *Renewable Energy Sources and Climate Change Mitigation: Special Report of the Intergovernmental Panel on Climate Change*. Cambridge University Press, Inc. NY.

Ishimoto, M., & Iida, K. 1937. Determination of elastic constants of soils by means of vibration methods, Part 2. Modulus of rigidity and Poisson's ratio. *Bulletin of Earthquake Research Institute*, *15*, 67–85.

Kausel, E. 1974. *Forced vibrations of circular foundations on layered media*. Massachusetts Institute of Technology.

Khosravi, A., Salam, S., McCartney, J., & Dadashi, A. 2016. Suction-Induced Hardening Effects on the Shear modulus of Unsaturated Silt. *International Journal of Geomechanics*, *16*(6), 1–10.

Khosravi, A., & Mccartney, J. S. 2011. Resonant Column Test for Unsaturated Soils With Suction – Saturation Control, *34*(6), 730–739.

Kramer, S. L. 1996. *Geotechnical Earthquake Engineering*. Upper Saddle River, NJ: Prentice-Hall.

Lade, P. V. 1977. Elasto-plastic stress-strain theory for cohesionless soil with curved yield surfaces. *International Journal of Solids and Structures, 13*(11), 1019–1035.

Lang, P. 2012. *SENSITIVITY OF SHALLOW WIND TURBINE FOUNDATION DESIGN AND SOIL RESPONSE TO GEOTECHNICAL VARIANCE WITH CONSTRUCTION COST IMPLICATIONS*. University of Wisconsin - Madison.

Lockwood, J., Chase, M., McRory, T. (2016) “Higher Wind Towers on the Rise.” *Concrete International*. August, 2016, pp 29-32.

Madaschi, A., Gajo, A., Molinari, M., Zonta, D. 2016. “Characterization of the Dynamic Behavior of Shallow Foundations with Full-Scale Dynamic Tests.” *J Geotech Geoenviron Eng*. 14(7): 04016026.

Mancuso, C., Vassallo, R., d’Onofrio, A. 2002. “Small Strain Behavior of a Silty Sand in Controlled-Suction Resonant Column – Torsional Shear Tests.” *Can Geotech J*. 39. 22-31.

Meyerhof, G. G. 1953. The bearing capacity of foundations under eccentric and inclined loads. In *Third International Conference on Soil Mechanics and Foundation. Organizing Committee ICOSOMEF* (pp. 440–445).

Morgan, K., & Ntambakwa, E. 2008. Wind Turbine Foundation Behavior and Design Considerations. In *AWEA WINDPOWER Conference* (pp. 1–14). Houston.

Murthy, V. N. S. 2003. *Geotechnical engineering: principles and practices of soil mechanics and foundation engineering*. New York, NY.

Ng, C. W. W., & Xu, J. 2012. Effects of current suction ratio and recent suction history on small-strain behaviour of an unsaturated soil. *Canadian Geotechnical Journal*, (49), 226–243. https://doi.org/10.1139/T11-097

Ntambakwa, E. (2009). “Seismic Forces for Wind Turbine Foundations.” Presentation given at *WINDPOWER 2009*. Chicago, IL.

Prakash, S. 1981. *Soil Dynamics*. Shamsher Prakash Foundation, Rolla, MO, USA.

Porter, H. C. 1946. Elastic-Limit Basis for Designing Highway Substructures in Clay Soil. *Engineering News-Record*, 92–93.

Richart, F. E., Hall, J. R., & Woods, R. D. 1970. *Vibrations of Soils and Foundations*. Englewood Cliffs, NJ: Prentice-Hall, Inc.

Holtz, R., Kovacs, W. 1986. An Introduction to Geotechnical Engineering. *Engineering Geology*. https://doi.org/10.1016/0013-7952(86)90005-0

Santamarina, C. J. 2003. Soil Behavior at the Microscale: Particle Forces. In *Soil Behavior and Soft Ground Construction*.

Santamarina, C. J., Klein, A., & Fam, M. A. 2001. *Soils and waves: Particulate materials behavior, characterization and process monitoring*. Chichester, UK: John Wiley & Sons.

Savidis, S.A., Vrettos, C. Richter, T. 1993. “Resonant Column and Cyclic Triaxial Testing of Tailing Dam Material.” *Soil Dyn and Earthq Eng*. 3. 291-298.

Schmertmann, J. H. 1970. Static cone to compute static settlement over sand. *ASCE Journal of Soil Mechanics Foundation Division Foundations Division*, *96*(3), 1011–1043.

Stanislav, L. 2004. The Effect of Density and Water Content upon the Dynamic Properties of Reconstituted Moraine Samples in the Small Strain Range. *Academic Open Internet Journal*, *11*.

Sykora, D. W., Wahl, R. E., & Wallace, D. C. 1992. *USACE geotechnical earthquake engineering software*. Washington, D.C.

Tinjum, J. M., & Christensen, R. W. 2011. Site investigation, characterization and assessment for wind turbine design and construction. *Wind Enery Systems*, (December 2011), 28–45. https://doi.org/http://dx.doi.org/10.1533/9780857090638.1.28

Tinjum, J. M., & Lang, P. 2012. Wind Energy Geotechnics. *GeoStrata*, (February), 18–26.

Vucetic, M., & Dobry, R. 1991. Effect of soil plasticity on cyclic response. *Journal of Geotechnical Engineering*, *117*(1), 89–107.

Wood, D. M. 1991. *Soil Behaviour and Critical State Soil Mechanics* (1st ed.). Cambridge University Press.

Wu, S., Gray, D., & Richart, F. E. 1984. No TitleCapillary Effects on dynamic Modulus of Sands and Silts. *Journal of Geotechnical Engineering*, *110*(9), 1188–1203.

Yilmaz, M. 2014. *Foundation soil response to wind turbine generator loading*. University of Wisconsin - Madison.

Yilmaz, M., Schubert, S., Tinjum, J. M., & Fratta, D. 2014. Foundation soil response to wind turbine generator loading. *Geo-Congress 2014 Technical Papers: Geo-Characterization and Modeling for Sustainability*, 1493–1502.

9 APPENDIX A – SITE A GEOTECHNICAL INFORMATION

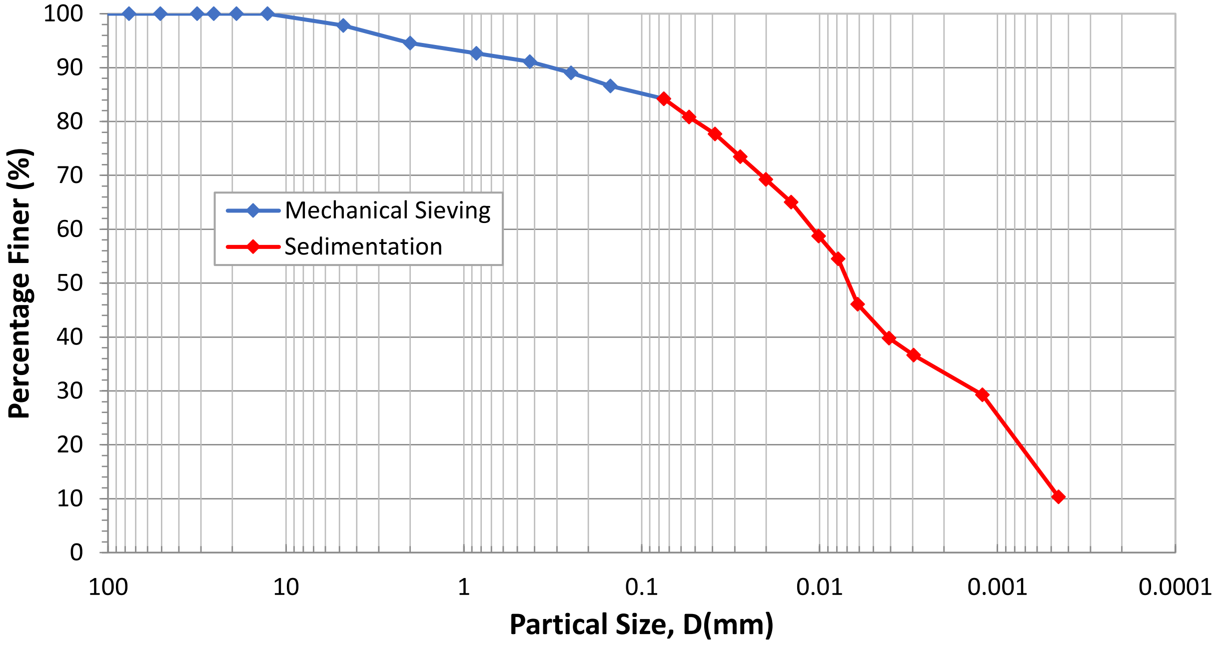

B-2: 2.75-4.25m

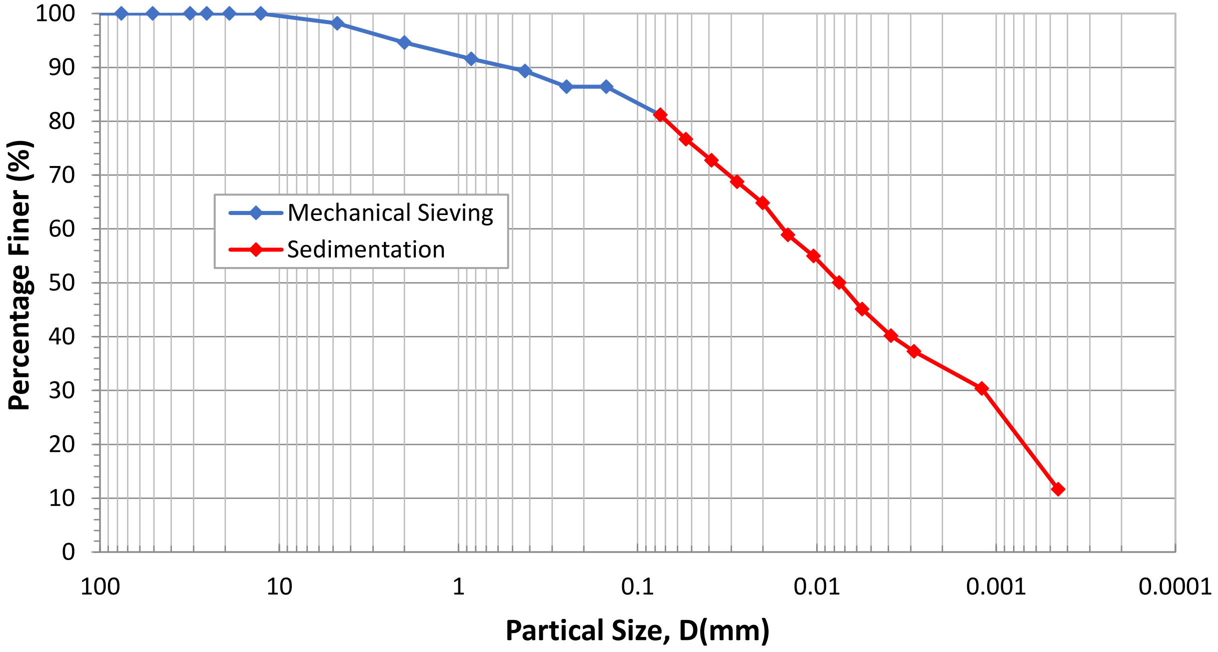

B-3: 2.75-4.25m

Figure A-1: Particle size distributions for soil retrieved in 2017 site visit.

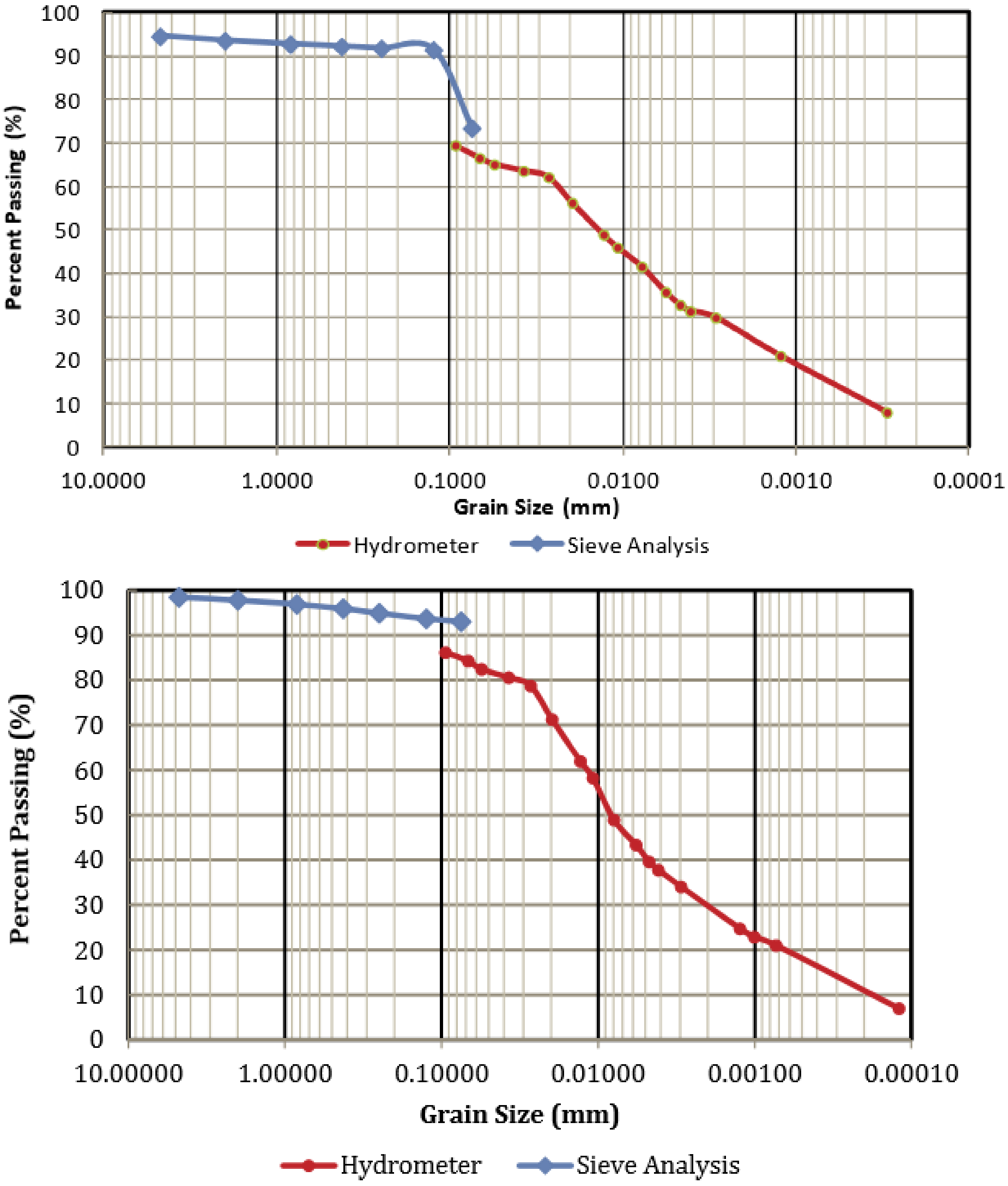

Figure A-2: Particle size distribution for shallow (top) and deep (bottom) soil (Schubert 2013).

Table A-1: Sieve results for B-2: 2.75-4.25m

Sieve No.	Sieve Opening	Weight Retained on Each Sieve	Percent Retained on Each Sieve	Cumulative Percent Retained	Percent Finer
4	4.75	8.34	2.19	2.19	97.81
10	2.00	12.42	3.26	5.46	94.54
20	0.85	7.20	1.89	7.35	92.65
40	0.425	5.95	1.56	8.91	91.09
60	0.250	7.93	2.08	11.00	89.00
100	0.150	9.07	2.38	13.38	86.62
200	0.075	9.17	2.41	15.79	84.21
Sieve Pan	--	320.40	84.21	100	0

Table A-2: Sieve results for B-3: 2.75-4.25m

Sieve No.	Sieve Opening	Weight Retained on Each Sieve	Percent Retained on Each Sieve	Cumulative Percent Retained	Percent Finer
4	4.75	4.88	1.85	1.85	98.15
10	2.00	9.42	3.57	5.42	94.58
20	0.85	7.84	2.97	8.40	91.60
40	0.425	5.96	2.26	10.66	89.34
60	0.250	7.67	2.91	13.57	86.43
100	0.150	0.06	0.02	13.59	86.41
200	0.075	13.81	5.24	18.83	81.17
Sieve Pan	--	214.05	71.17	100	0

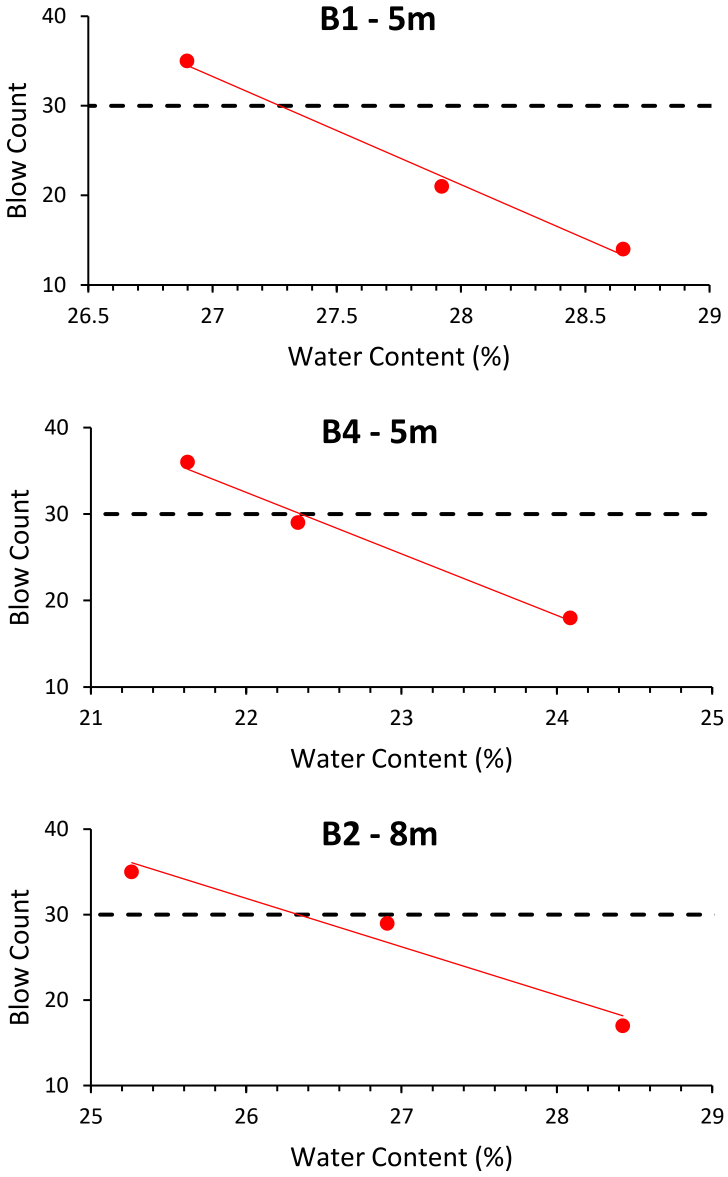

Figure A-3: Sample Liquid Limit results for Site A.

Tale A-3: Miscellaneous measurements for specimens tested via Resonant column and Cyclic Triaxial.

Boring	Depth	W	Θ	PI	e
--	(m)	(%)	(%)	--	--
B-1	5	13.5	35.8	12.6	0.3884
B-2	8	13.7	36.3	11.1	0.4519
	5	16	42.4	9.2	
B-3	5	13.5	35.8	8.9	0.4261
B-4	5	14.1	37.4	7.4	0.4511
	8	14.6	38.7	8.2	0.3620

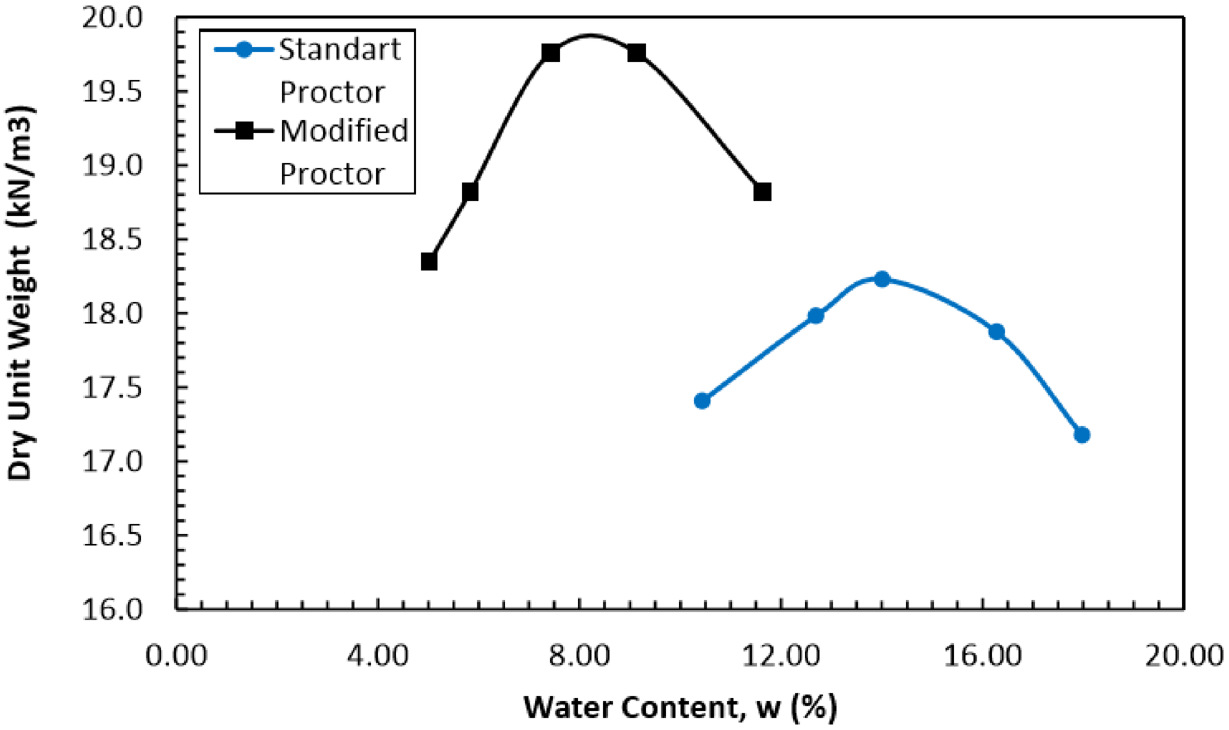

Figure A-4: Compaction curve for shallow site soil (Yilmaz 2014).

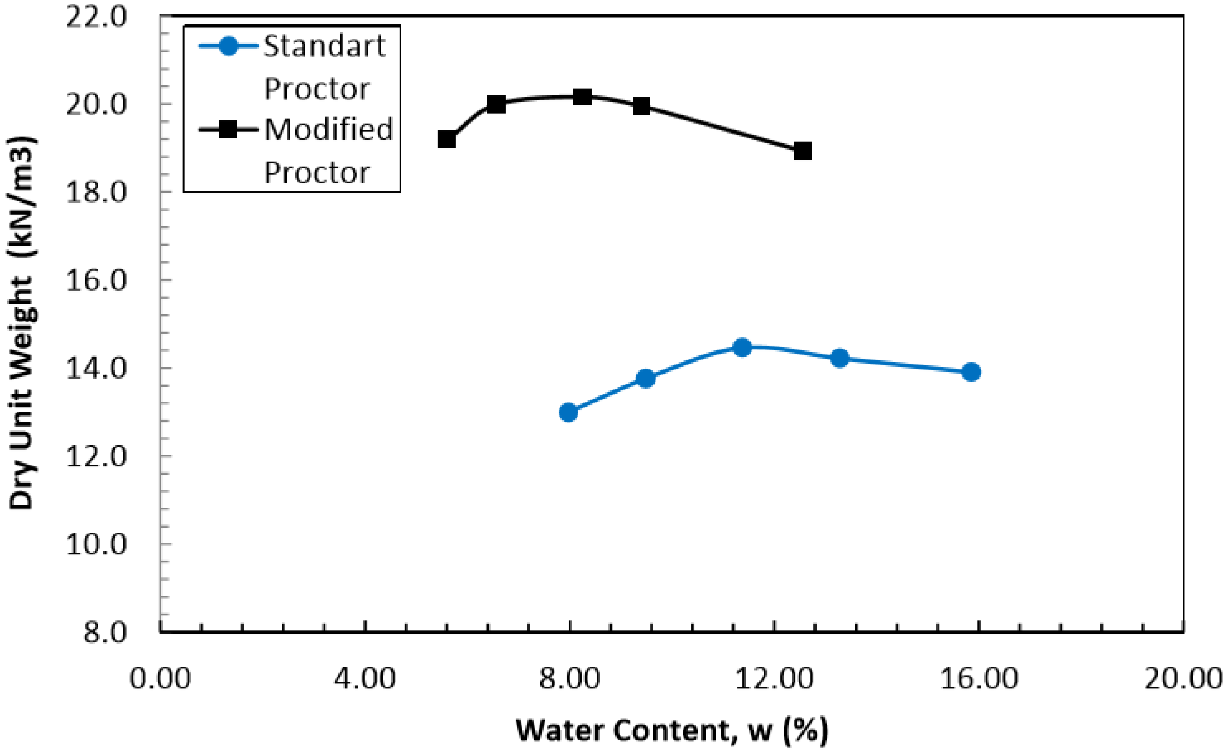

Figure A-5: Compaction curve for deep soil (Yilmaz 2014).

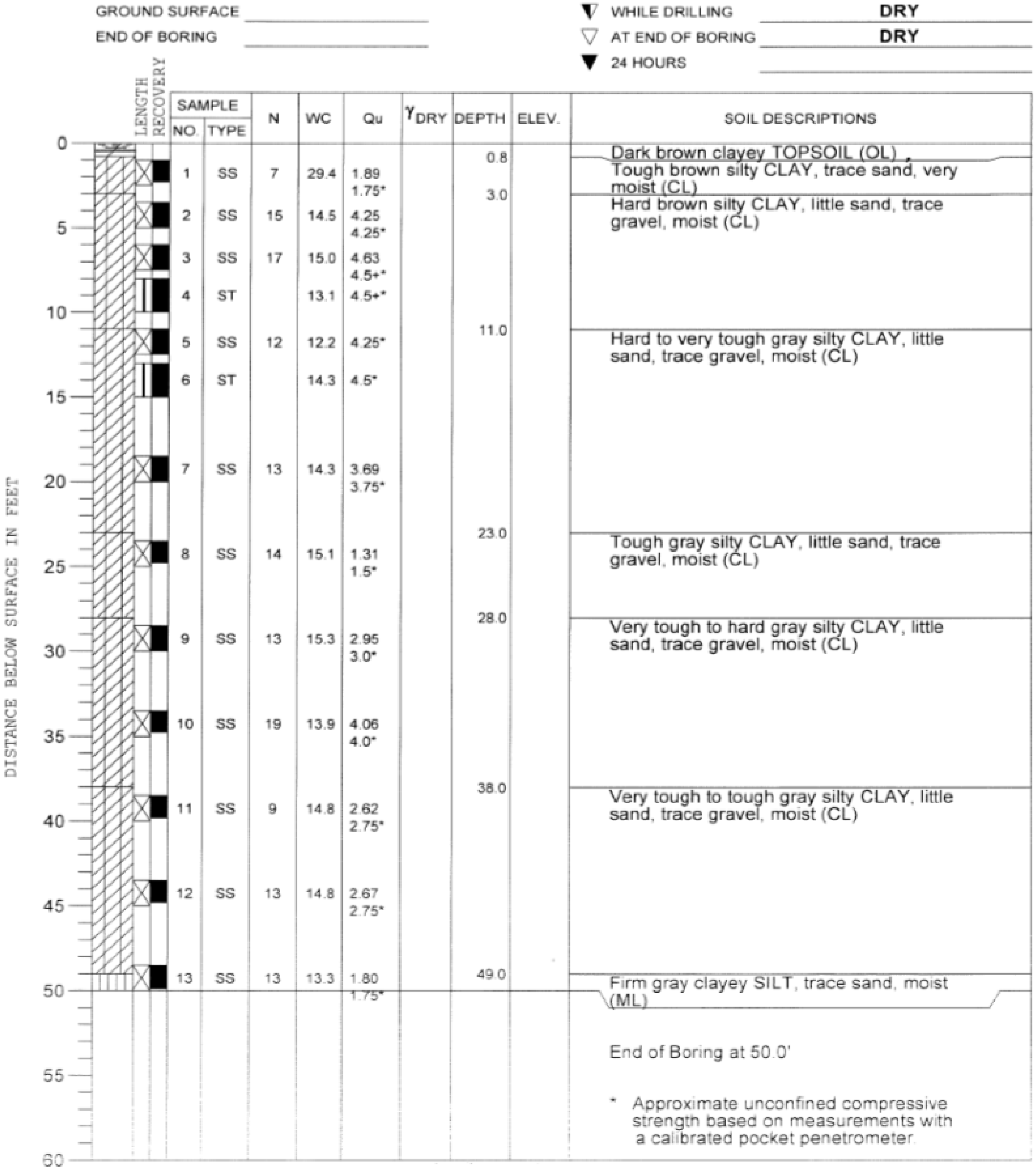

GROUND SURFACE ____________
END OF BORING ____________

▼ WHILE DRILLING **DRY**
▽ AT END OF BORING **DRY**
▼ 24 HOURS ____________

SAMPLE NO.	SAMPLE TYPE	N	WC	Qu	γDRY	DEPTH	ELEV.	SOIL DESCRIPTIONS
						0.8		Dark brown clayey TOPSOIL (OL)
1	SS	7	29.4	1.89 1.75*		3.0		Tough brown silty CLAY, trace sand, very moist (CL)
2	SS	15	14.5	4.25 4.25*				Hard brown silty CLAY, little sand, trace gravel, moist (CL)
3	SS	17	15.0	4.63 4.5+*				
4	ST		13.1	4.5+*				
						11.0		
5	SS	12	12.2	4.25*				Hard to very tough gray silty CLAY, little sand, trace gravel, moist (CL)
6	ST		14.3	4.5*				
7	SS	13	14.3	3.69 3.75*				
						23.0		
8	SS	14	15.1	1.31 1.5*				Tough gray silty CLAY, little sand, trace gravel, moist (CL)
						28.0		
9	SS	13	15.3	2.95 3.0*				Very tough to hard gray silty CLAY, little sand, trace gravel, moist (CL)
10	SS	19	13.9	4.06 4.0*				
						38.0		
11	SS	9	14.8	2.62 2.75*				Very tough to tough gray silty CLAY, little sand, trace gravel, moist (CL)
12	SS	13	14.8	2.67 2.75*				
						49.0		
13	SS	13	13.3	1.80 1.75*				Firm gray clayey SILT, trace sand, moist (ML)

End of Boring at 50.0'

* Approximate unconfined compressive strength based on measurements with a calibrated pocket penetrometer.

Figure A-6: Soil boring to 15m.

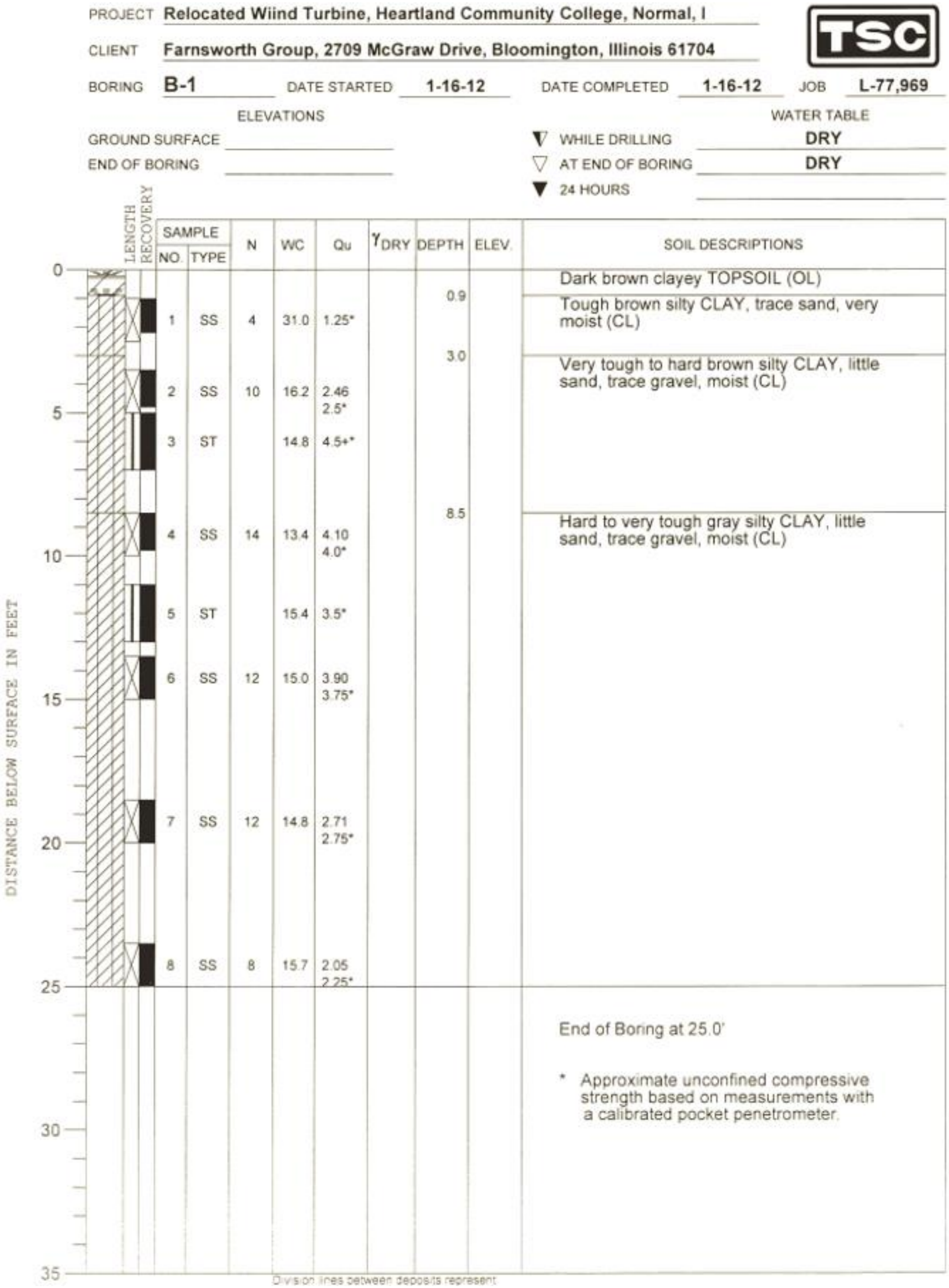

PROJECT **Relocated Wiind Turbine, Heartland Community College, Normal, I**

CLIENT **Farnsworth Group, 2709 McGraw Drive, Bloomington, Illinois 61704**

BORING **B-1** DATE STARTED **1-16-12** DATE COMPLETED **1-16-12** JOB **L-77,969**

ELEVATIONS		WATER TABLE	
GROUND SURFACE		▼ WHILE DRILLING	**DRY**
END OF BORING		▽ AT END OF BORING	**DRY**
		▼ 24 HOURS	

SAMPLE NO.	SAMPLE TYPE	N	WC	Qu	γ_{DRY}	DEPTH	ELEV.	SOIL DESCRIPTIONS
								Dark brown clayey TOPSOIL (OL)
						0.9		Tough brown silty CLAY, trace sand, very moist (CL)
1	SS	4	31.0	1.25*				
						3.0		Very tough to hard brown silty CLAY, little sand, trace gravel, moist (CL)
2	SS	10	16.2	2.46 2.5*				
3	ST		14.8	4.5+*				
						8.5		Hard to very tough gray silty CLAY, little sand, trace gravel, moist (CL)
4	SS	14	13.4	4.10 4.0*				
5	ST		15.4	3.5*				
6	SS	12	15.0	3.90 3.75*				
7	SS	12	14.8	2.71 2.75*				
8	SS	8	15.7	2.05 2.25*				
								End of Boring at 25.0'
								* Approximate unconfined compressive strength based on measurements with a calibrated pocket penetrometer.

Division lines between deposits represent

Figure A-7: Soil boring to 7.5m.

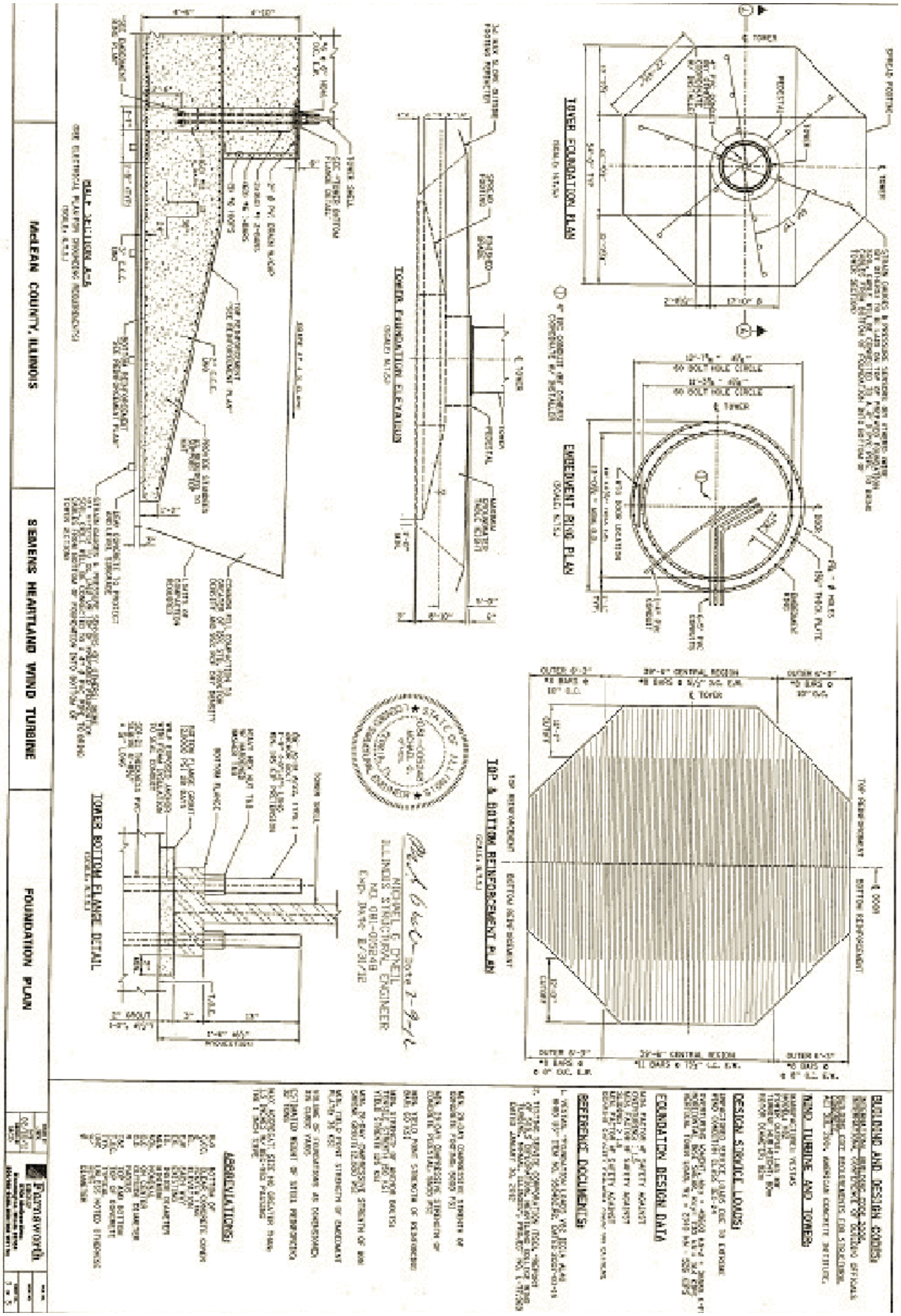

Figure A-8: Site A foundation geometry.

10 APPENDIX B – SITE B GEOTECHNICAL INFORMATION

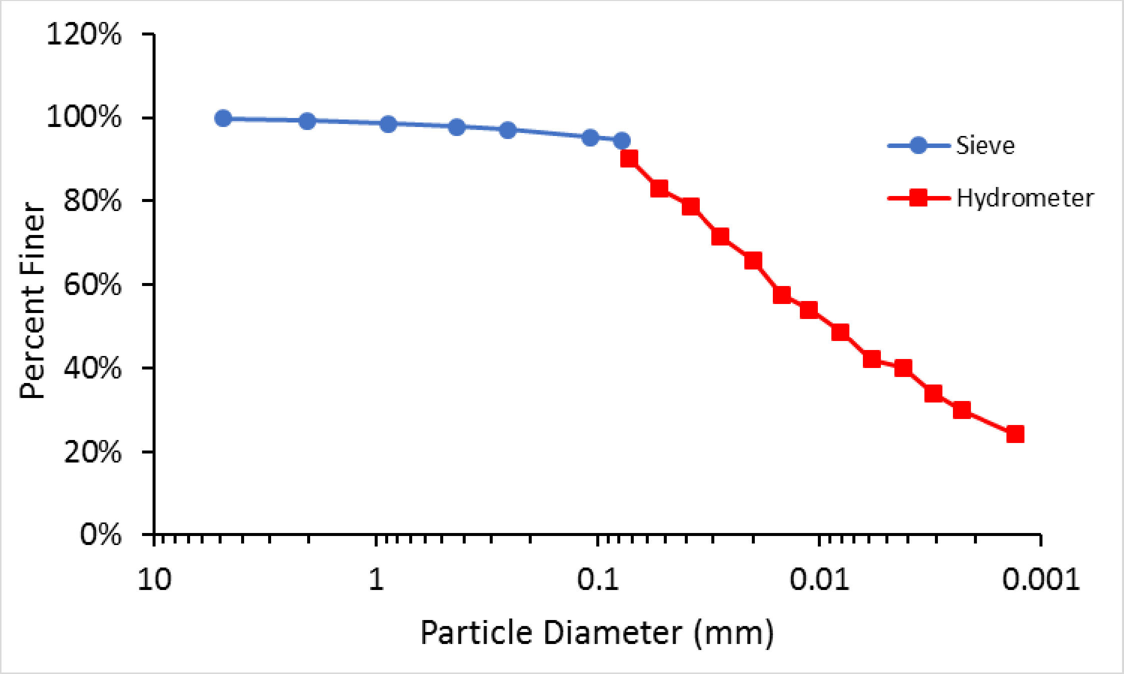

Figure B-1: Particle size distribution for sample W5B1 (Yilmaz 2014).

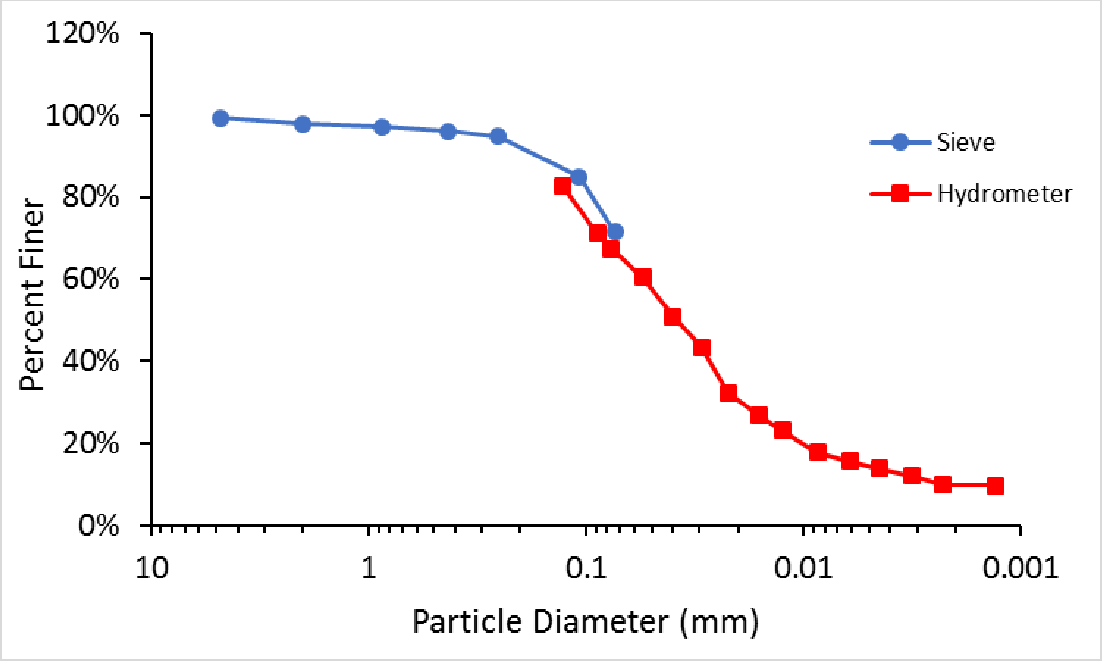

Figure B-2: Particle size distribution for sample E1A1 (Yilmaz 2014).

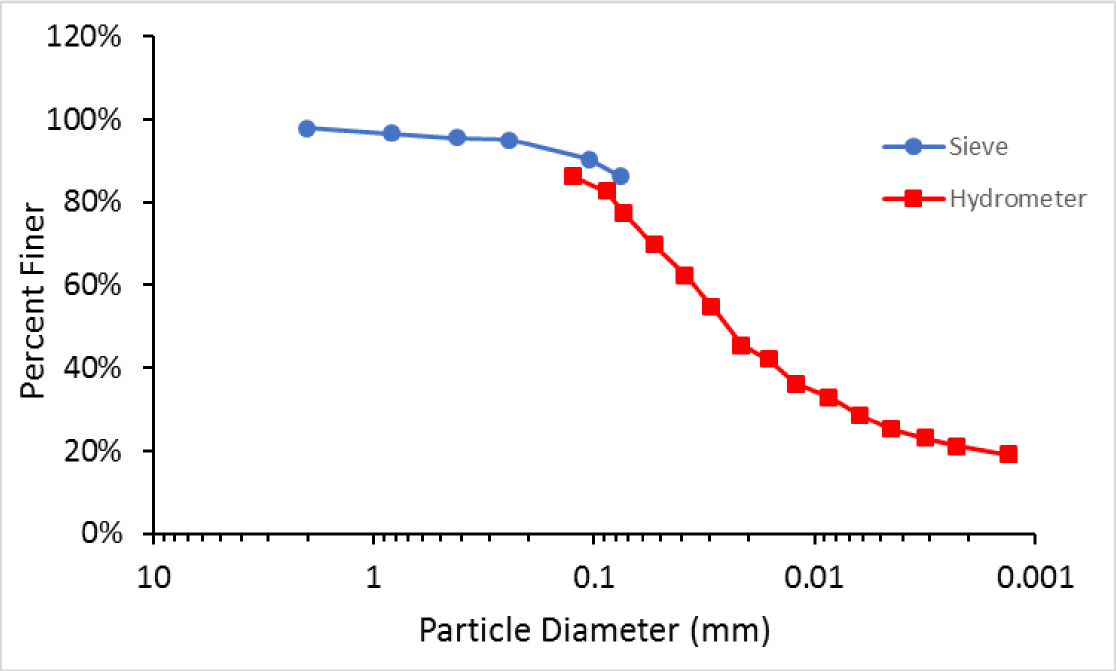

Figure B-3: Particle size distribution for sample E3A2 (Yilmaz 2014).

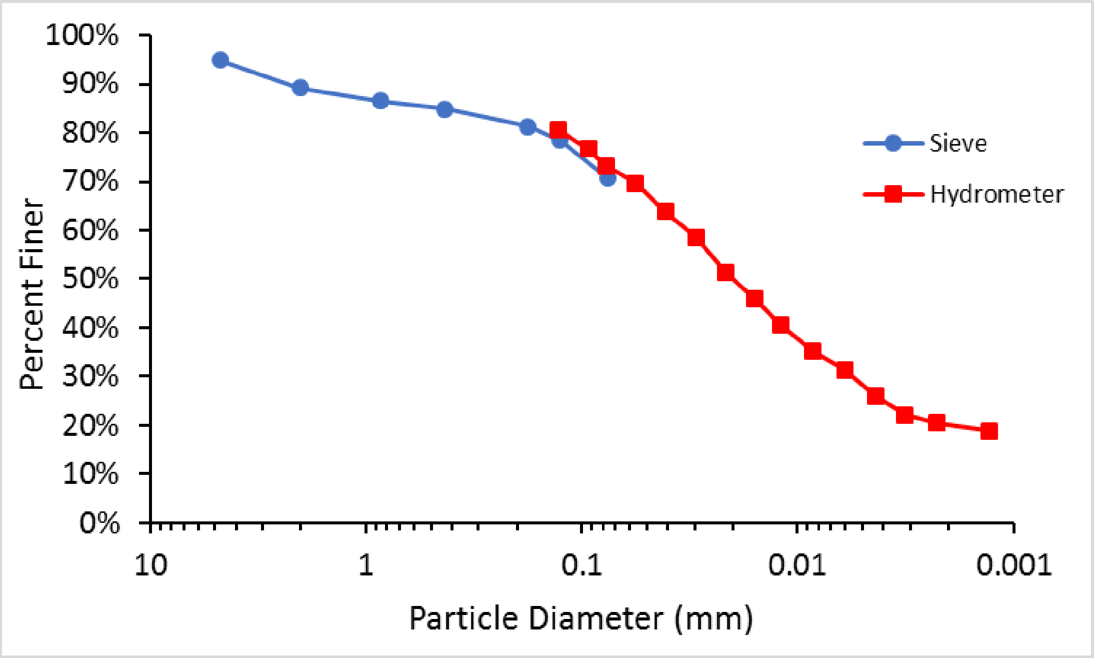

Figure B-4: Particle size distribution for sample SG-3 Top (Yilmaz 2014).

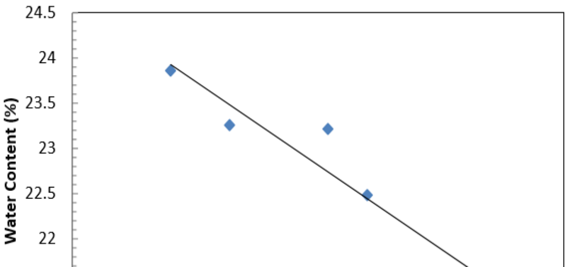

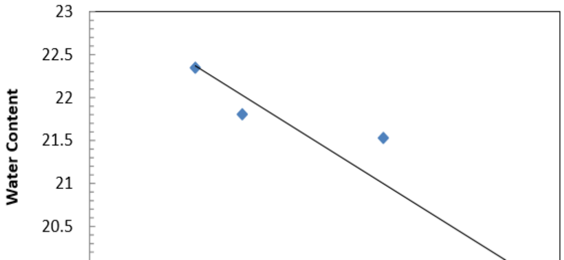

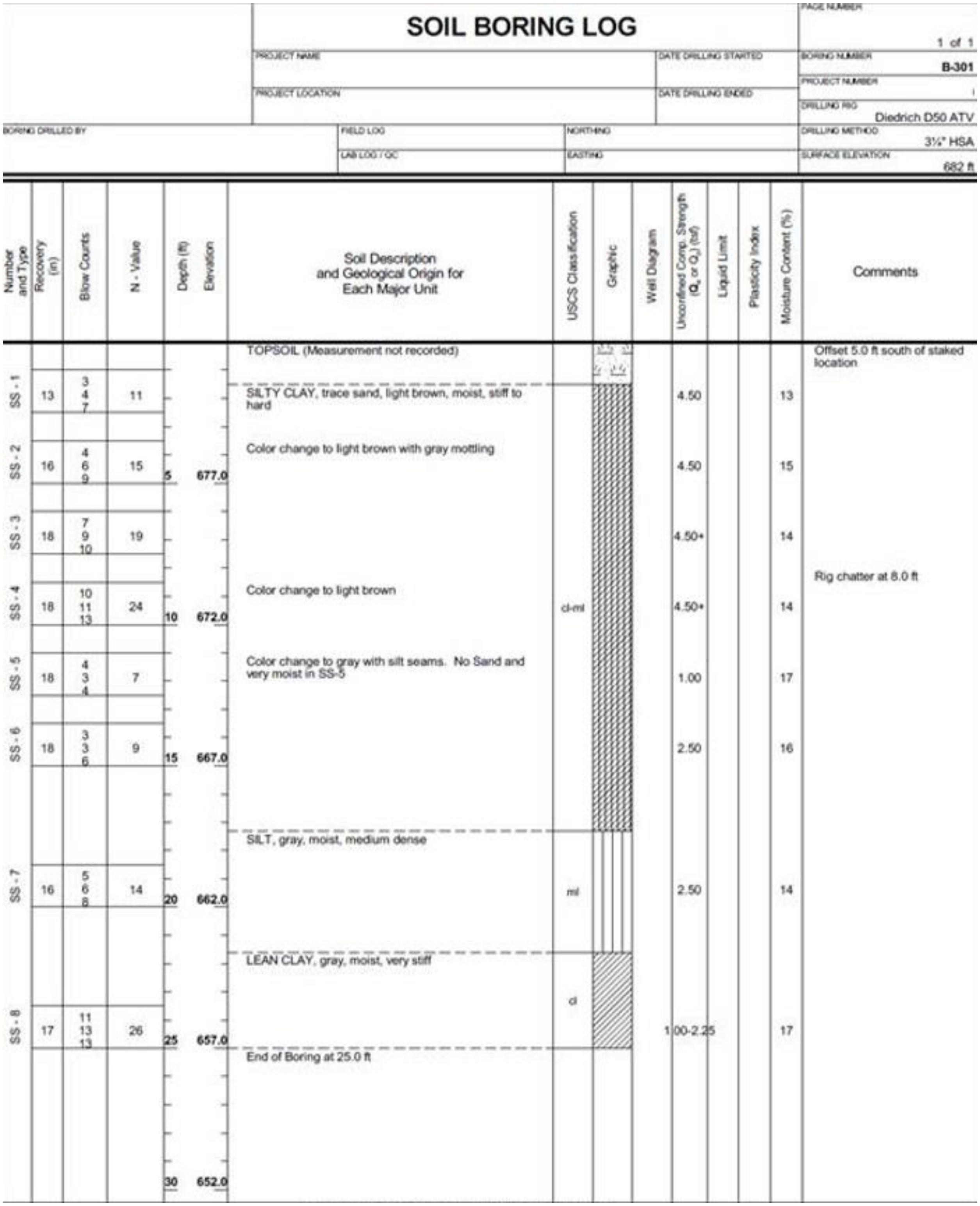

SOIL BORING LOG

PAGE NUMBER 1 of 1
PROJECT NAME
DATE DRILLING STARTED
BORING NUMBER B-301
PROJECT NUMBER
PROJECT LOCATION
DATE DRILLING ENDED
DRILLING RIG Diedrich D50 ATV
BORING DRILLED BY
FIELD LOG
NORTHING
DRILLING METHOD 3¼" HSA
LAB LOG / QC
EASTING
SURFACE ELEVATION 682 ft

Number and Type	Recovery (in)	Blow Counts	N - Value	Depth (ft)	Elevation	Soil Description and Geological Origin for Each Major Unit	USCS Classification	Graphic	Well Diagram	Unconfined Comp. Strength (Q_u or Q_p) (tsf)	Liquid Limit	Plasticity Index	Moisture Content (%)	Comments
						TOPSOIL (Measurement not recorded)								Offset 5.0 ft south of staked location
SS - 1	13	3 4 7	11			SILTY CLAY, trace sand, light brown, moist, stiff to hard				4.50			13	
SS - 2	16	4 6 9	15	5	677.0	Color change to light brown with gray mottling				4.50			15	
SS - 3	18	7 9 10	19							4.50+			14	
SS - 4	18	10 11 13	24	10	672.0	Color change to light brown	cl-ml			4.50+			14	Rig chatter at 8.0 ft
SS - 5	18	4 3 4	7			Color change to gray with silt seams. No Sand and very moist in SS-5				1.00			17	
SS - 6	18	3 3 6	9	15	667.0					2.50			16	
						SILT, gray, moist, medium dense								
SS - 7	16	5 6 8	14	20	662.0		ml			2.50			14	
						LEAN CLAY, gray, moist, very stiff	cl							
SS - 8	17	11 13 13	26	25	657.0					1.00-2.25			17	
						End of Boring at 25.0 ft								
				30	652.0									

Figure B-6: Boring log at Site B.

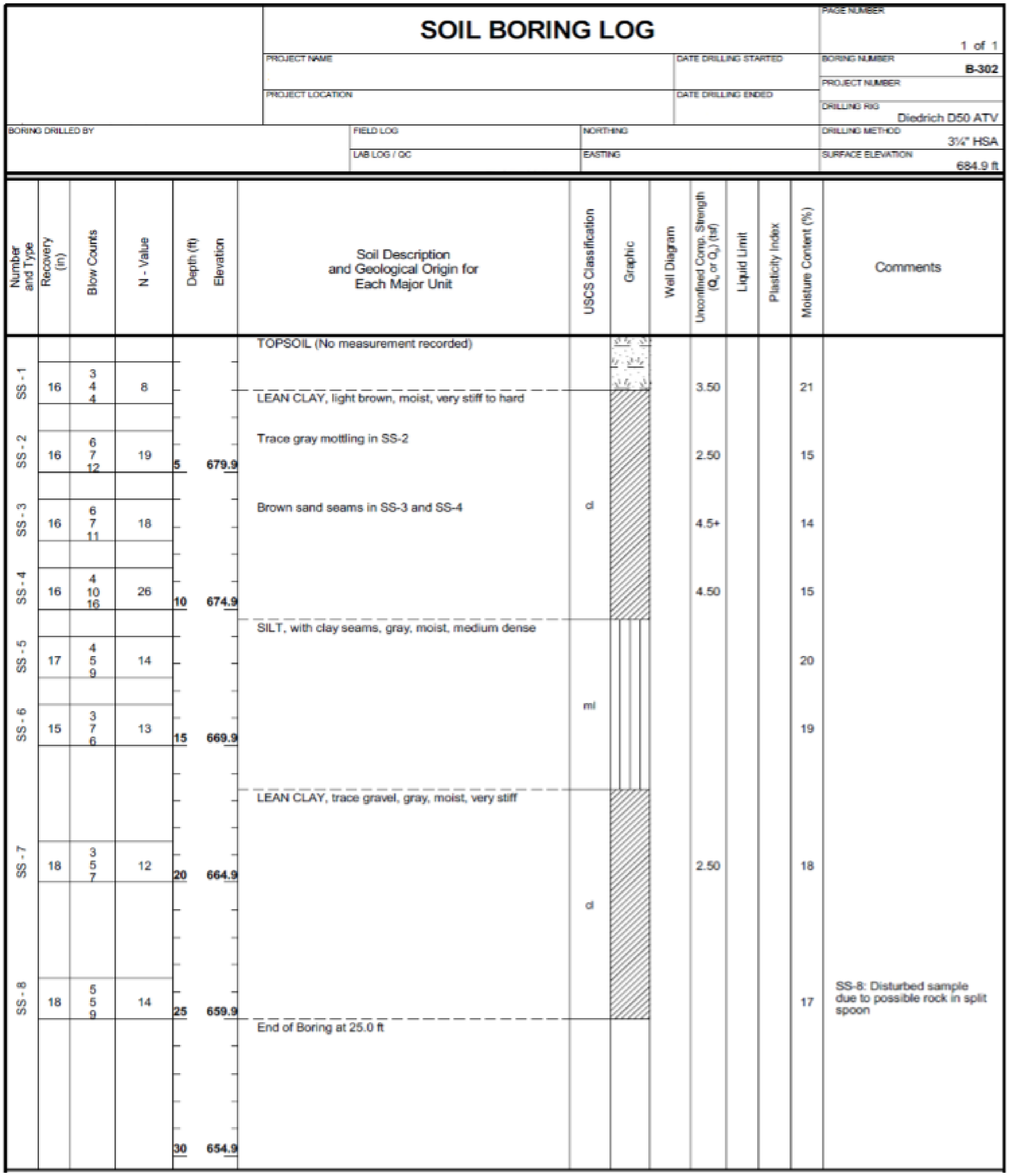

SOIL BORING LOG

PROJECT NAME	DATE DRILLING STARTED	PAGE NUMBER	1 of 1
		BORING NUMBER	B-302
PROJECT LOCATION	DATE DRILLING ENDED	PROJECT NUMBER	
		DRILLING RIG	Diedrich D50 ATV
BORING DRILLED BY	FIELD LOG	NORTHING	DRILLING METHOD: 3¼" HSA
	LAB LOG / QC	EASTING	SURFACE ELEVATION: 684.9 ft

Number and Type	Recovery (in)	Blow Counts	N - Value	Depth (ft)	Elevation	Soil Description and Geological Origin for Each Major Unit	USCS Classification	Graphic	Well Diagram	Unconfined Comp. Strength (Q_u or Q_p) (tsf)	Liquid Limit	Plasticity Index	Moisture Content (%)	Comments
						TOPSOIL (No measurement recorded)								
SS - 1	16	3 4 4	8							3.50			21	
						LEAN CLAY, light brown, moist, very stiff to hard								
						Trace gray mottling in SS-2								
SS - 2	16	6 7 12	19	5	679.9					2.50			15	
						Brown sand seams in SS-3 and SS-4	cl							
SS - 3	16	6 7 11	18							4.5+			14	
SS - 4	16	4 10 16	26	10	674.9					4.50			15	
						SILT, with clay seams, gray, moist, medium dense								
SS - 5	17	4 5 9	14										20	
							ml							
SS - 6	15	3 7 6	13	15	669.9								19	
						LEAN CLAY, trace gravel, gray, moist, very stiff								
SS - 7	18	3 5 7	12	20	664.9					2.50			18	
							cl							
SS - 8	18	5 5 9	14	25	659.9								17	SS-8: Disturbed sample due to possible rock in split spoon
						End of Boring at 25.0 ft								
				30	654.9									

Figure B-7: Boring log for Site B.

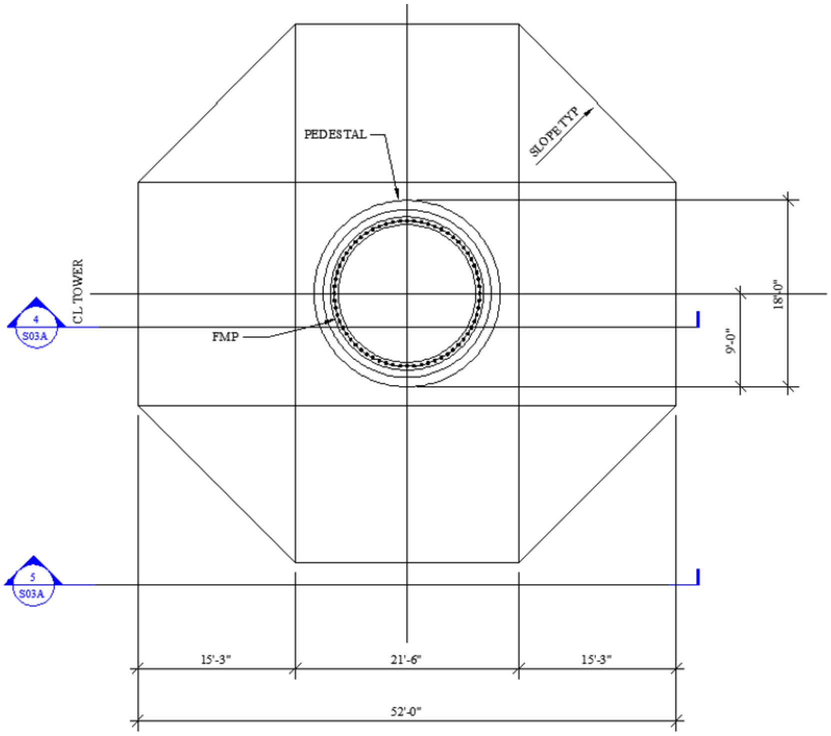

Figure B-8: Plan view of Site B footing.

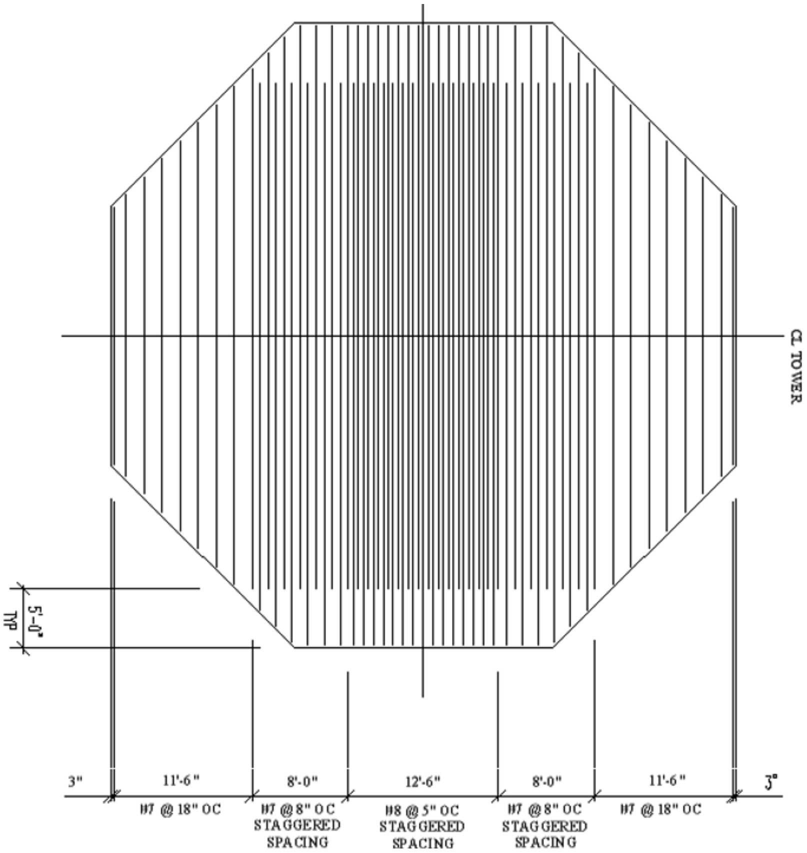

Figure B-9: Plan view of bottom mat reinforcing plan.

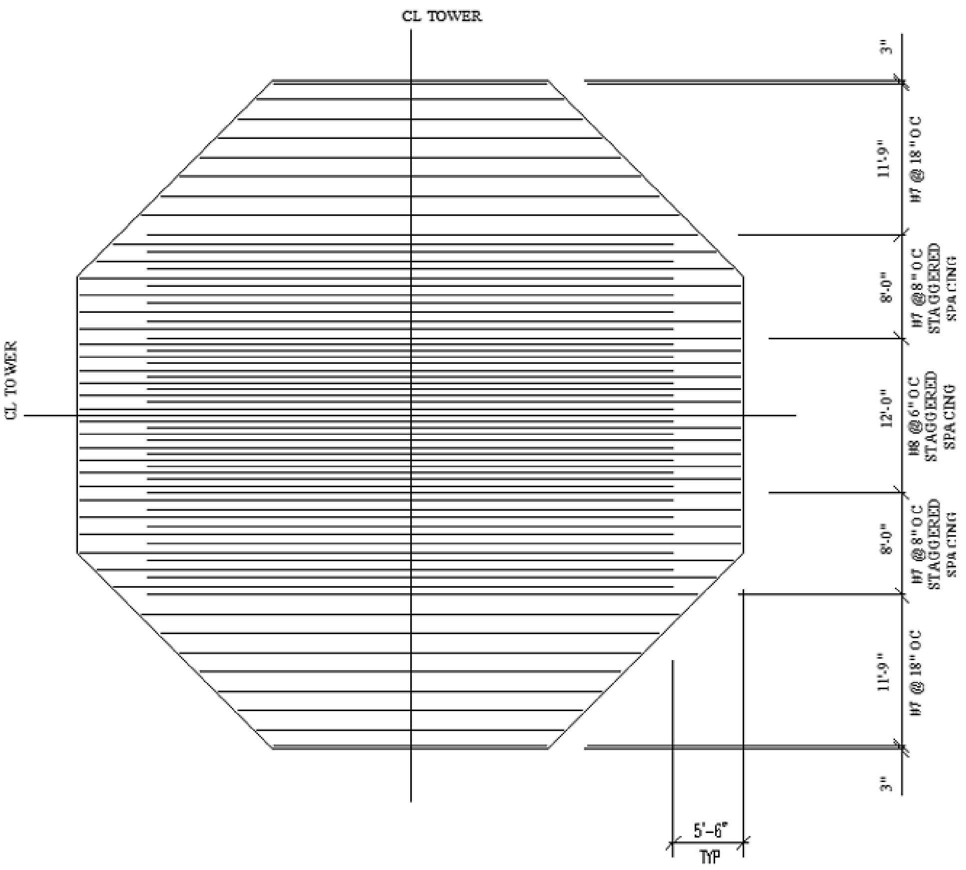

Figure B-10: Plan view of top mat reinforcing plan.

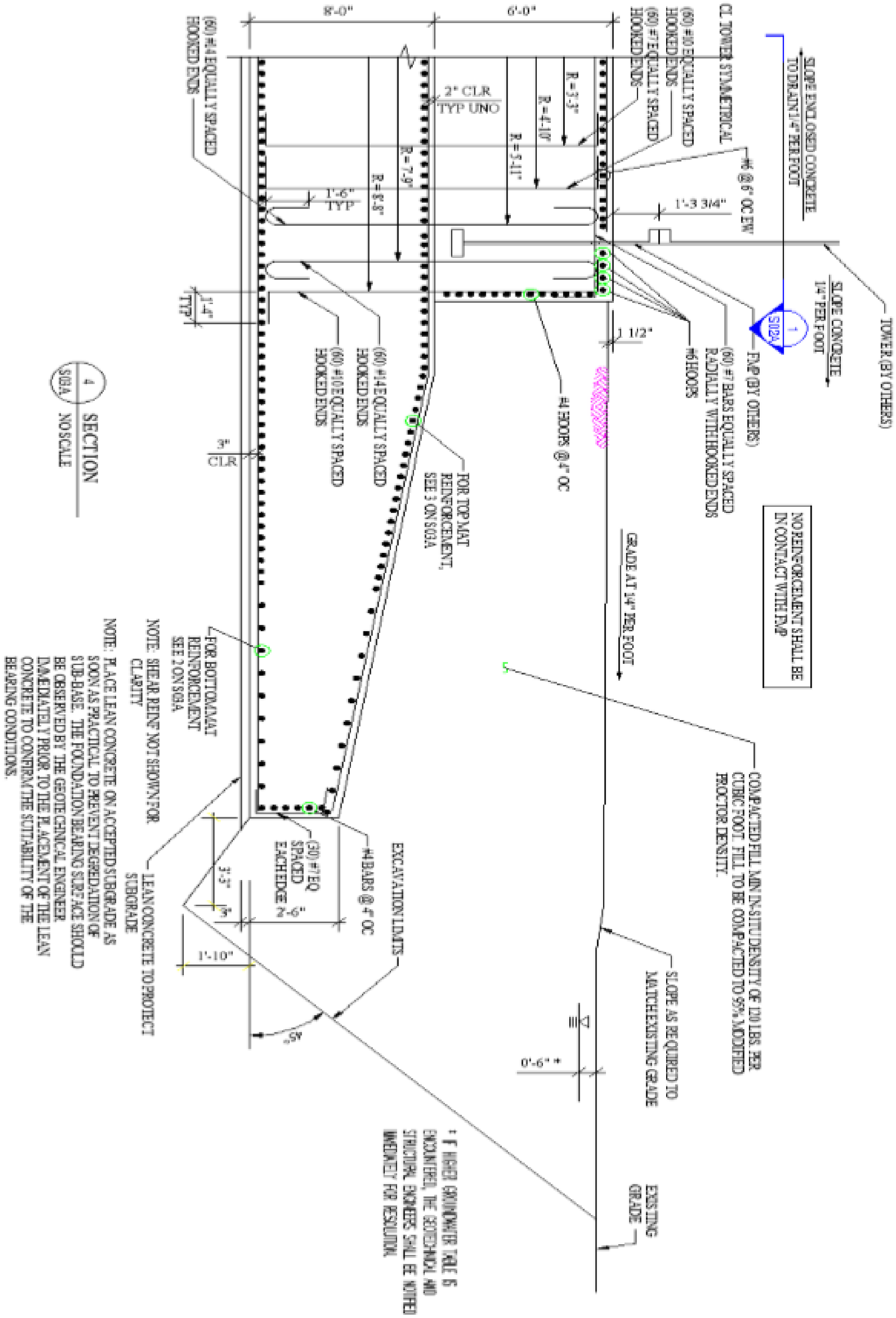

Figure B-11: Foundation cross section.

11 APPENDIX C – INSTRUMENTATION CALIBRATION AND DATA REDUCTION

Table C-1: Site A Pressure Gauge readings.

Sensor Name	Initial Reading	Gage Factor (kPa/V)
PG-1	0.166	50.0
PG-2	0.153	50.0
PG-3	0.151	50.0
PG-4	0.134	50.0
PG-5	0.113	50.0
PG-6	0.145	50.0
PG-7	0.148	50.0
PG-8	0.139	50.0
PG-9	0.143	50.0

Table C-2: Site B Pressure Gauge readings.

Sensor Name	Initial Reading	Gage Factor (kPa/V)
PG-1	0.129	49.92
PG-2	0.171	50.10
PG-3	0.110	49.92
PG-4	0.176	50.01
PG-5	0.165	49.93
PG-6	0.149	49.92
PG-7	0.186	49.91
PG-8	0.208	49.84
PG-9	0.217	49.86

Table C-3: Site A Soil Deformation Gage readings.

Sensor Name	Linear Gage Factor (mm/digit)	Initial Reading (Digits)	Temperature (^{0}C)
SG-1	0.002399	4492.994	5.64
SG-2	0.002401	4491.230	6.13
SG-3	0.002408	4509.069	6.18
SG-4	0.002407	4499.185	8.03
SG-5	0.002410	4481.587	7.09
SG-6	0.002407	4502.386	7.02
SG-7	0.002411	4503.225	7.91
SG-8	0.002400	4501.222	9.89
SG-9	0.002395	4489.089	5.82
SG-10	0.002408	4500.953	4.10

Table C-4: Site B Soil Deformation Gage readings.

Sensor Name	Linear Gage Factor (mm/digit)	Initial Reading (Digits)	Temperature (^{0}C)
SG-1	0.002327	4763.792	16.3
SG-2	0.002775	4693.475	18.8
SG-3	0.002336	4550.996	19.4
SG-4	0.002327	4775.694	21.0
SG-5	0.002327	4560.589	18.3
SG-6	0.002766	4556.993	19.2
SG-7	0.002332	4561.185	17.7
SG-8	0.002320	4546.017	17.4
SG-9	0.002337	4715.983	19.5
SG-10	0.002408	4640.187	20.2

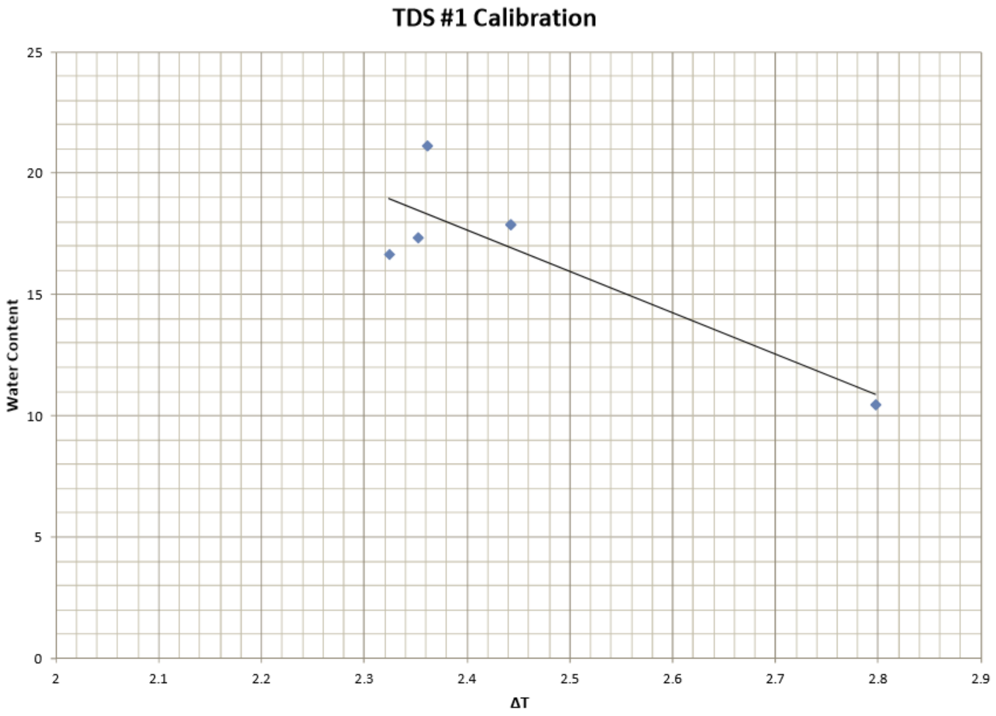

Figure C-1: Calibration curve for TDS-1 (Schubert 2013).

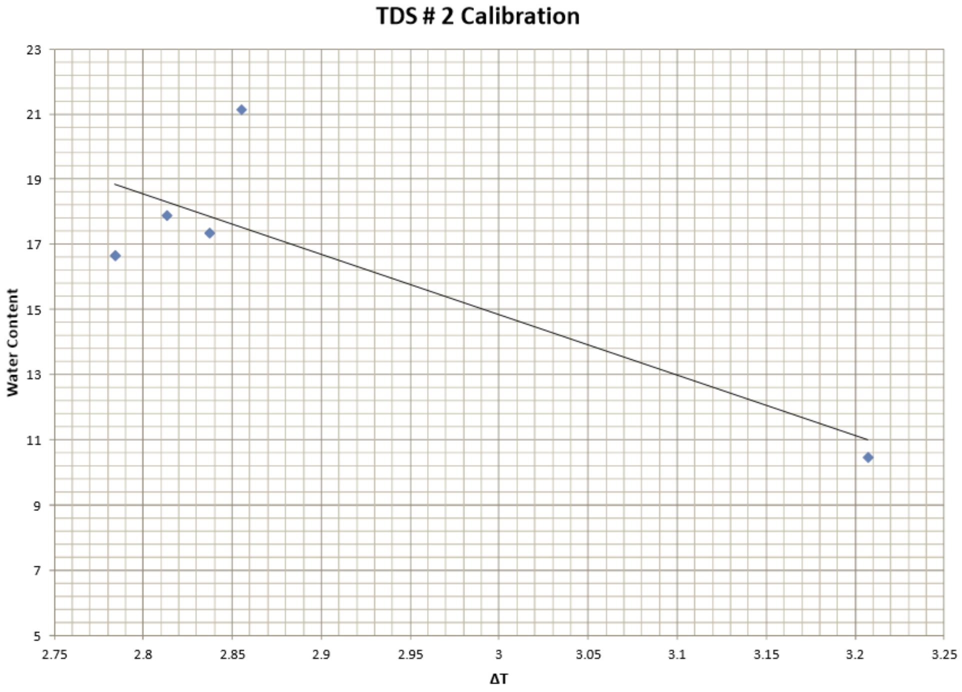

Figure C-2: Calibration curve for TDS-2 (Schubert 2013).

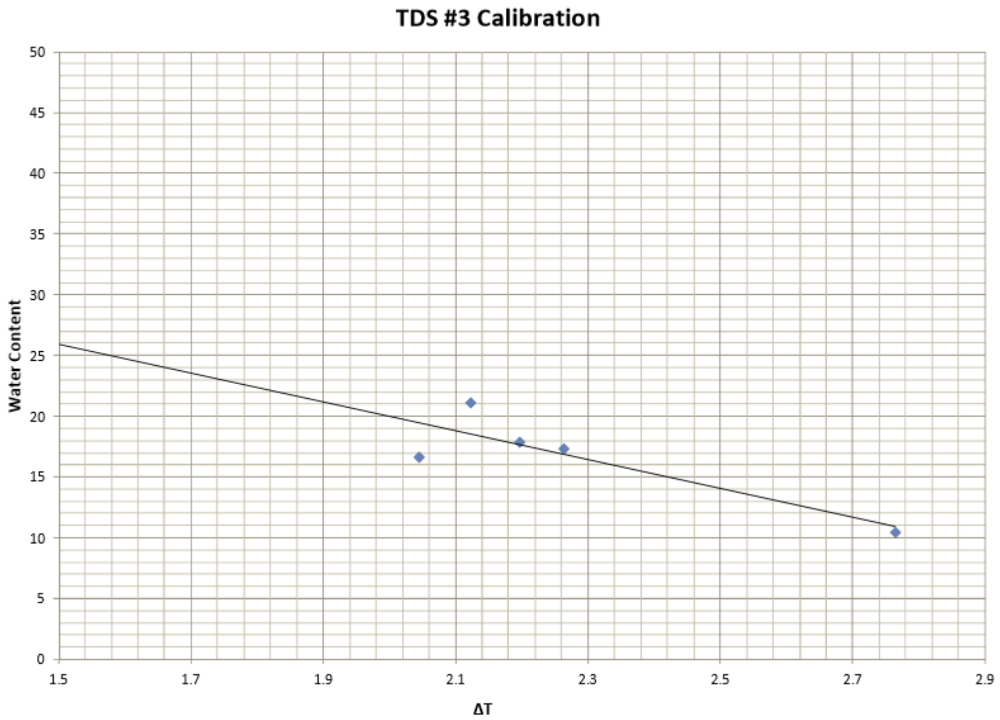

Figure C-3: Calibration curve for TDS-3 (Schubert 2013).

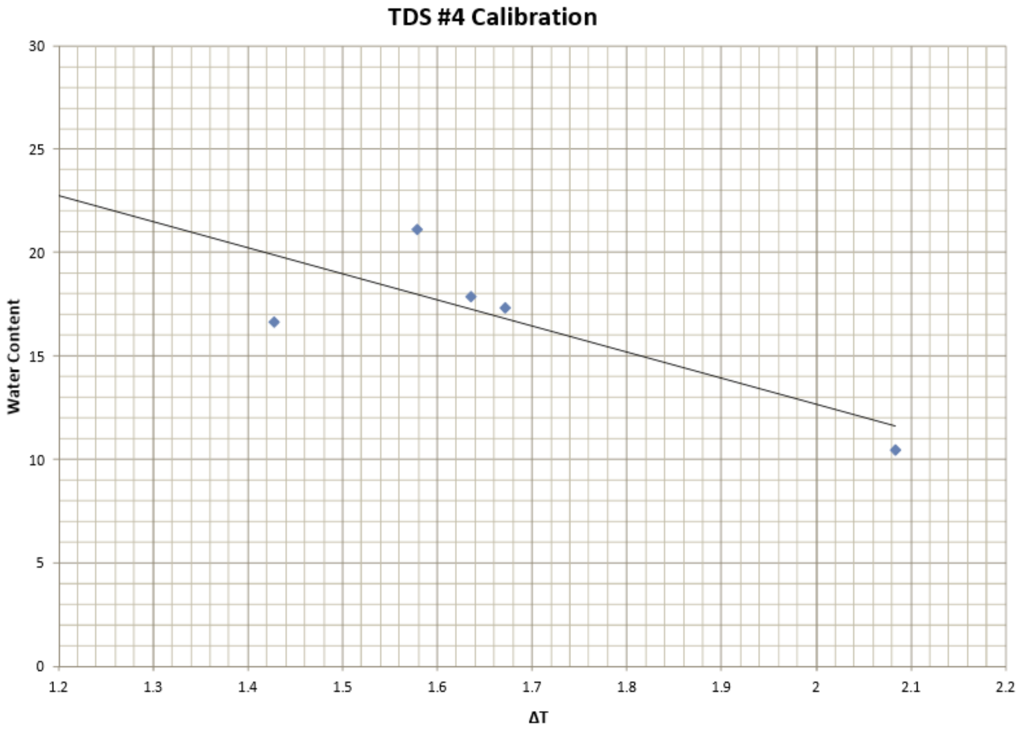

Figure C-4: Calibration curve for TDS-4 (Schubert 2013).

12 APPENDIX D – RESONANT COLUMN OPERATION MANUAL

University of Wisconsin – Madison

Resonant Column Operation Manual

Civil & Environmental Engineering/Geological Engineering

Christopher Enos

TABLE OF CONTENTS

12.1 Background

The resonant column apparatus is used to measure dynamic soil response at low strain levels (<0.01%) in a non-destructive manner (Drnevich 1978), utilizing torsional motion to impart shear waves into the soil. By propagating a swept of a range of excitement frequencies, the resonant frequency of the system can be determined by measuring the peak amplitude response of the soil. The resonant frequency can then be used to calculate the shear modulus of the soil using the theory of elastic wave propagation (Richart 1970). First developed by Ishimoto & Iida (1937), the concept has been applied in various iterations and developments, with the most common being the Hardin type and Stokoe type, which apply unique boundary conditions to achieve desired results.

The Hardin type utilizes a *fixed-free* boundary condition, where the bottom of the specimen is fixed to a bottom platen, while the top of the cylinder is attached to a top platen and heavy, freely rotating oscillator controlled by a magnet-coil system. The high mass of the oscillator is necessary to apply sufficient shear strain to the specimen, and must be counterbalanced to control deviatoric stress (Richart 1970). In this study, a Hardin-type resonant column is used, with the operation and components described in further detail later in this thesis. The Stokoe type utilizes a *free-free* (Menq & Stokoe 2003) or *fixed-free* condition to apply sufficient shear strain. Stokoe type resonant columns have the advantage over Hardin types in that they can apply a larger torque and are generally easier to assemble and operate. As shown in Figure 2-17, the bottom of the specimen is, again, fixed to the bottom platen, while the top is connected to a top platen that is rotated by a magnet-coil system that is fixed to the resonant column apparatus. Stokoe's method, after extended refinement and development, was adopted as a testing standard by ASTM (ASTM 4015-07). This manual outlines the operation of UW Madison's Hardin-type resonant column.

12.2 Components

Various components will be listed below with a numbered image for each category. The four major groups are: resonant column apparatus, electronics, pressure board, and tools.

12.3 Resonant Column

1. Metal frame
2. Pressure chamber
3. Heavy oscillator
4. Bottom platen
5. Top platen
6. Top cover
7. 3 threaded rods
8. 3 large nuts
9. Counterweight system
10. O-rings

11. Electromagnetic motor power cable
12. Axis translation pressure line
13. Epoxy-sealed elbow fitting
14. Open elbow fitting

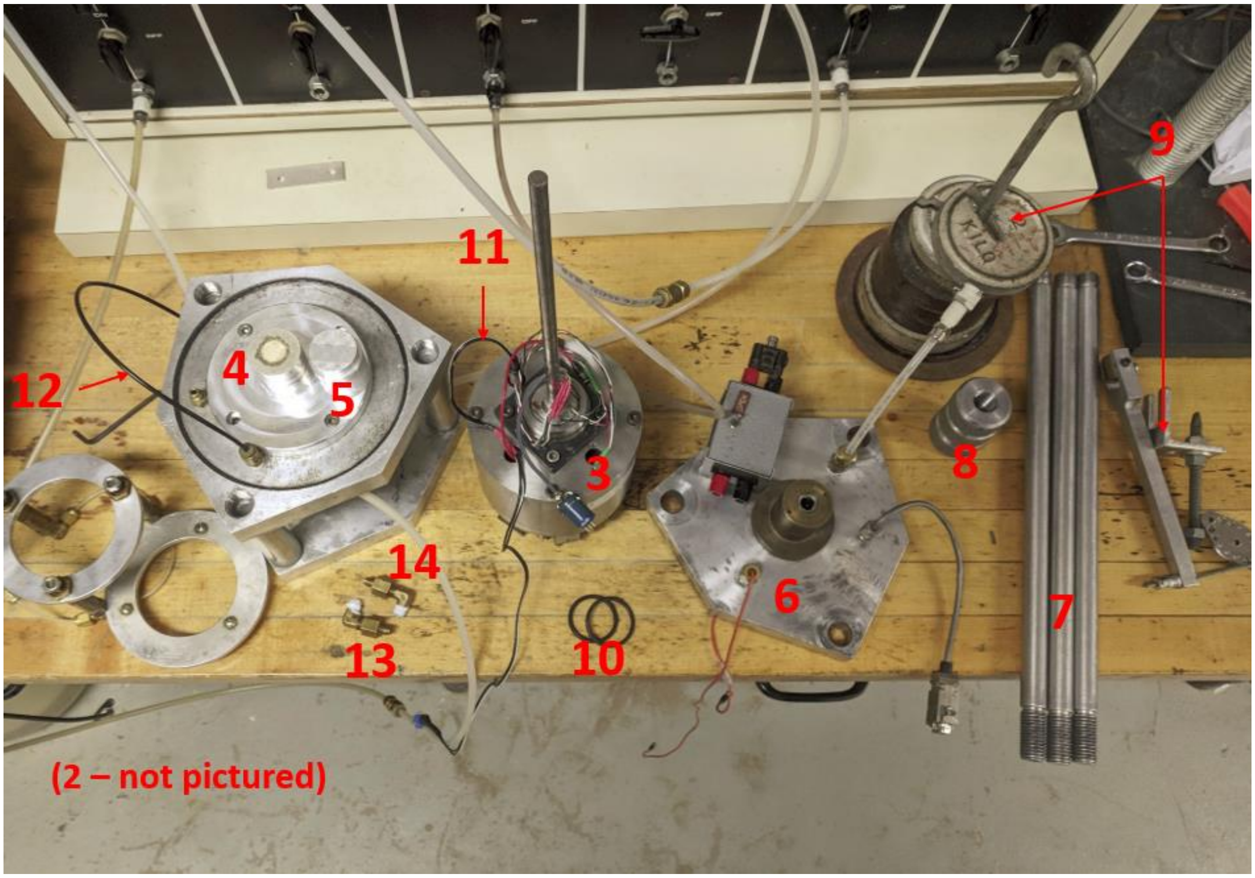

Figure 2.1: Resonant column apparatus components.

12.4 Electronics

Signal generator – 1
Signal conditioner – 2
Power amplifier – 3
Digital oscilloscope – 4
Spectrum analyzer – 5

12.5 Cables

Signal generator → Signal conditioner
Signal generator → Digital oscilloscope
Signal conditioner → Resonant column

Power amplifier → Spectrum analyzer/Digital oscilloscope

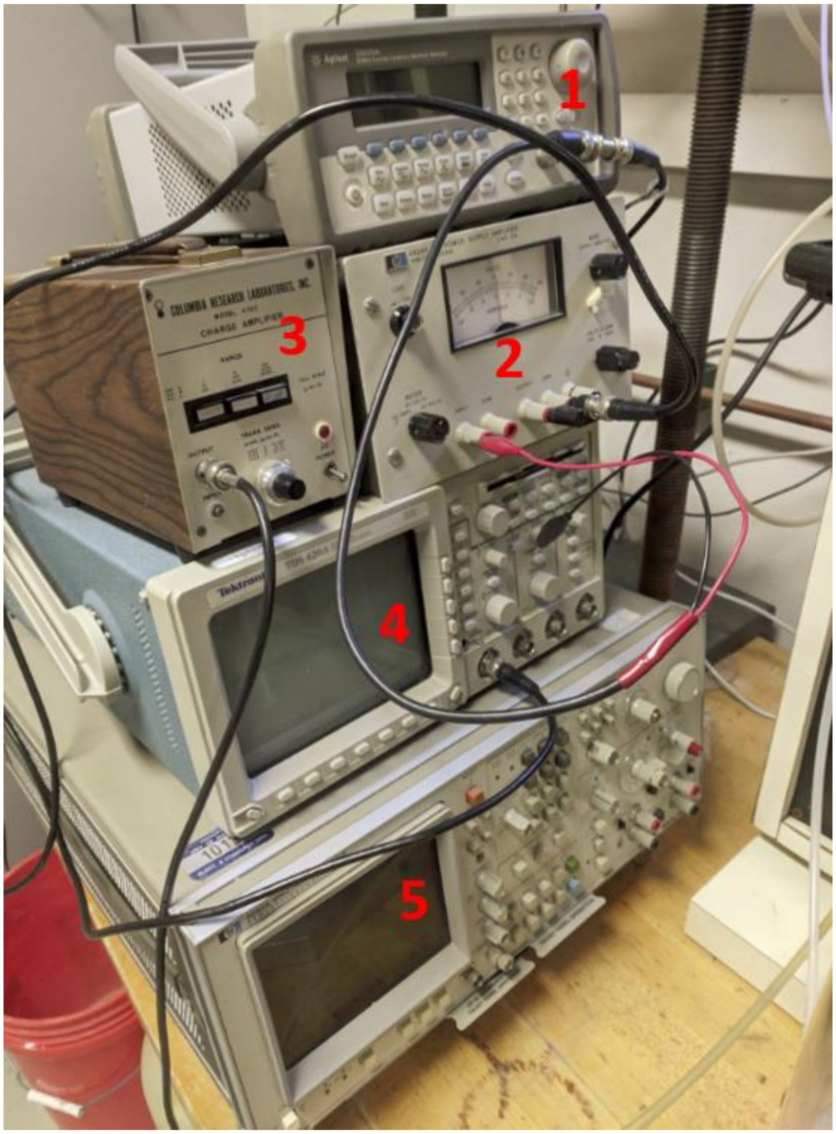

Figure 2.2: Electronic components.

12.5.1 Pressure Board

1. 2 Backpressure water reservoirs
2. Confining pressure/hydraulic jack air pressure

3. Axis translation air pressure

Figure 2.3: Typical pressure board. Any port may be used for the above purposes.

12.5.2 Tools

1. Allen wrenched
    a. (size 1)
    b. 4.5mm
2. Wrenches
    a. 11mm
    b. 14mm
    c. 16mm
3. Silicone grease
4. Pipe seal tape
5. Flathead screwdriver
6. Adjustable pliers/wrench
7. Safety glasses

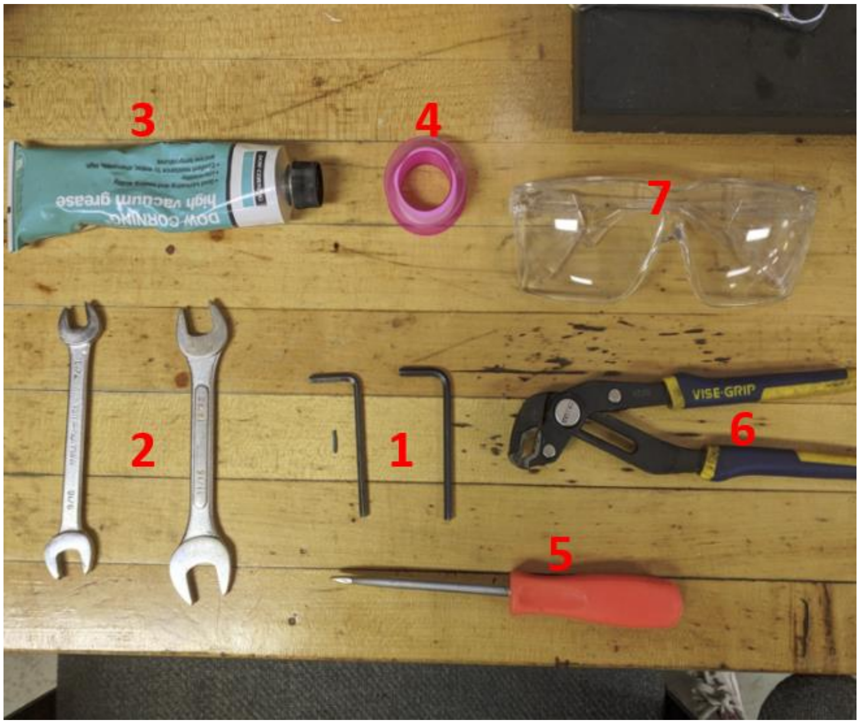

Figure 2.4: Tools for setup of apparatus.

12.6 Apparatus Assembly

At this point, the apparatus should be disassembled as pictured below:

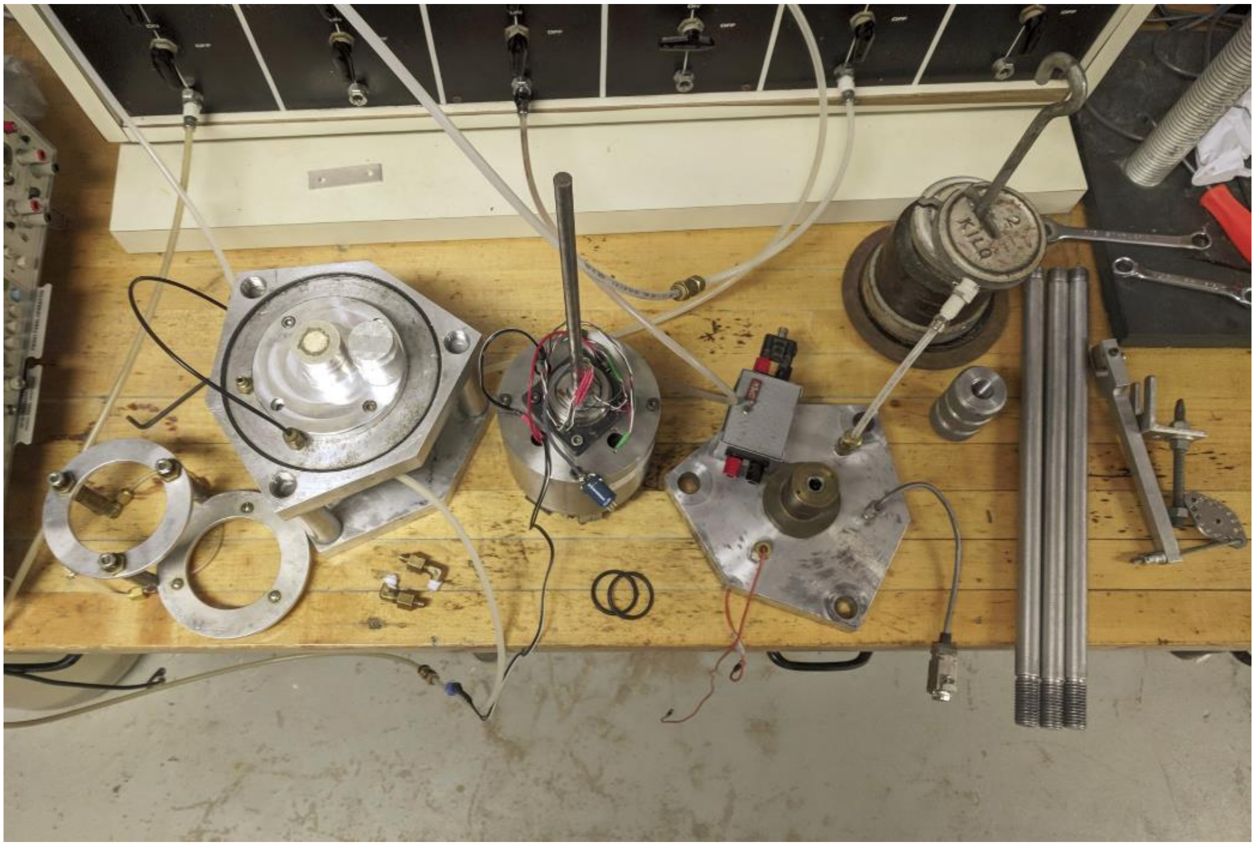

Figure 3.1: Disassembled resonant column.

The first step is to install the specimen. First, place an O-ring around the bottom platen pedestal pushed to the base of the pedestal. Before moving further, ensure the high air entry (HAE) ceramic disc is saturated and allows the flow of water by increasing the backpressure to ~30 kPa and watching for water droplets to begin forming on the HAE disc. If water does not propagate through the disc, an air bubble may have formed beneath the disc. To solve this, flush the system of air by pushing water back and forth between the two connected reservoirs through the bottom platen. Once air bubbles stop rising in the reservoirs, the system should be flushed. Once flow is confirmed, place the soil specimen on top of the pedestal, ensuring no debris is preventing coupling between the soil and platen.

Before installing the top platen, place the latex membrane around the platen on the table and place an O-ring around the membrane and platen, taking care to ensure an even seal and not rip the membrane. Cut out the top of the membrane so you can roll it down over the O-ring. Your setup should look like this:

Figure 2.2: Top and bottom platen with O-rings and membrane prepped.

Place the top platen on top of the specimen. Roll the membrane down around the specimen and as far down the bottom platen as it can go. Again, carefully roll the O-ring on the pedestal up over the bottom of the membrane, taking care to ensure a good seal. Your setup should now look like this.

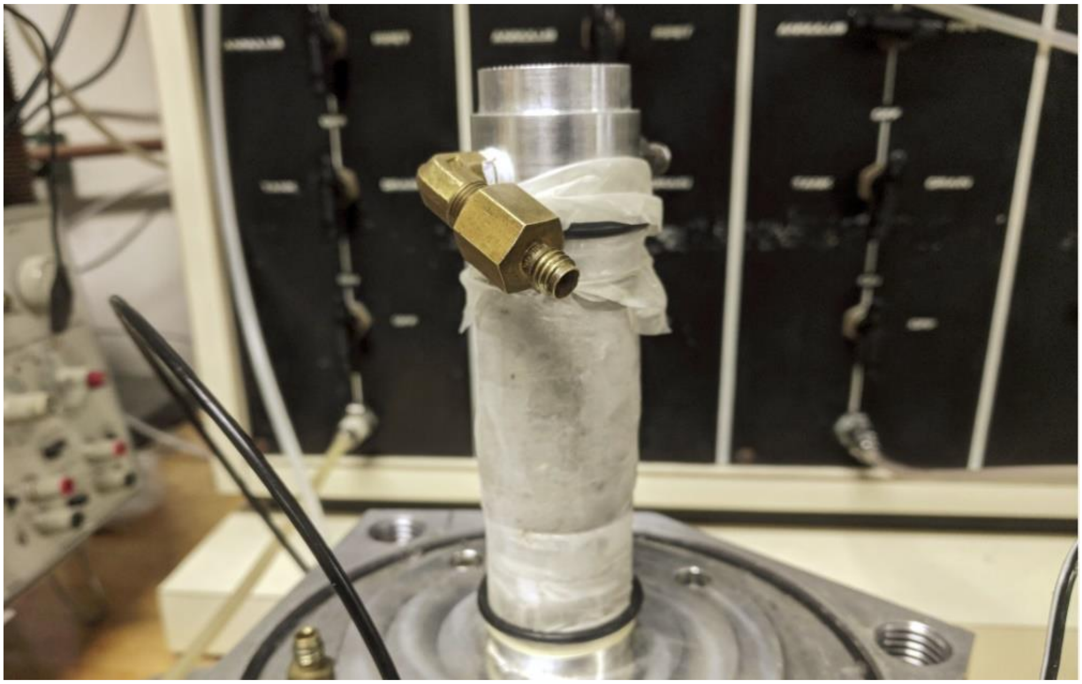

Figure 2.3: Specimen and membrane assembly.

Next, the axis translation mechanism must be set up. Screw both the sealed and open elbow fittings into the top platen. It is important to install both elbow fittings to maintain symmetry and an even weight distribution for accurate results. Pipe sealing tape can be used to ensure the system is air-tight**. Be careful not to screw the fittings on too tight, as they are made of brass and can damage the aluminum threads**. To clear both rings of the hydraulic jack, the elbow fittings should be left at an angle like the one below.

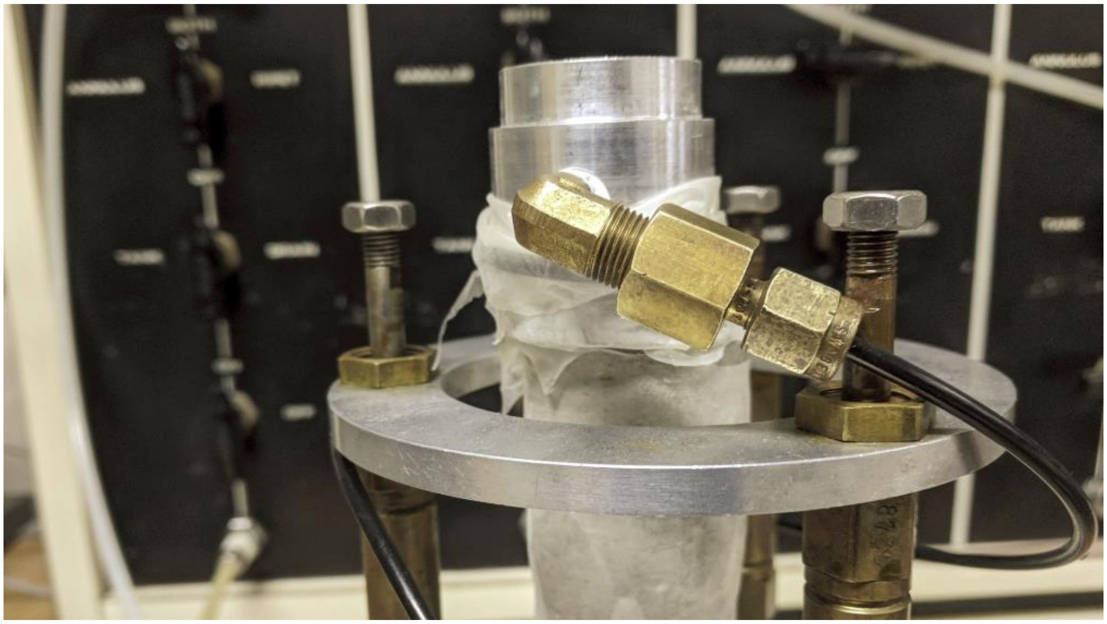

Figure 2.4: Axis translation line installation.

Before hooking up the air-line to the open fitting, place the pneumatic jack over the specimen and screw it to the air valve. Then, the axis translation line can be connected and the jack pedestal ring can be placed on the jack. Screw in the three threaded rods. Your setup should look like this:

This stage in the assembly is difficult, delicate, and the most dangerous part of assembly. **Improper care can result in destruction of the specimen or damage to the oscillator. It is best to use another person to help with this stage, especially when first learning.** Though the majority of tests I ran were by myself, I occasionally used a helper for ~5 minutes to make this step easier. Increase the pressure on the jack to 275 – 300 kPa (40 – 43 psi). This is enough to support most of the weight of the oscillator, but will let it lower down over the top platen. Once all three pistons are extended, carefully place the oscillator on the pedestal, doing your best to center the circular clamp over the top platen. While supporting/balancing the oscillator, slightly lift and slide it until the circular clamp slides over the top cap. Lower the oscillator until it is flush with the top platen lip and, while supporting the oscillator, use the Allen wrench to tighten ***both*** of the clamp’s bolts to secure the oscillator with the top platen. Then, while supporting the oscillator from the lower half, use your other hand to place the acrylic chamber over the oscillator. As the chamber reaches your supporting hand, use the chamber to balance the oscillator and move the supporting hand to the metal rod sticking out the top of the oscillator to balance it. Lower the chamber all the way down and ensure it is firmly sealed to the O-ring. At this point, it is pretty safe to let go of the oscillator. Your setup should look like this:

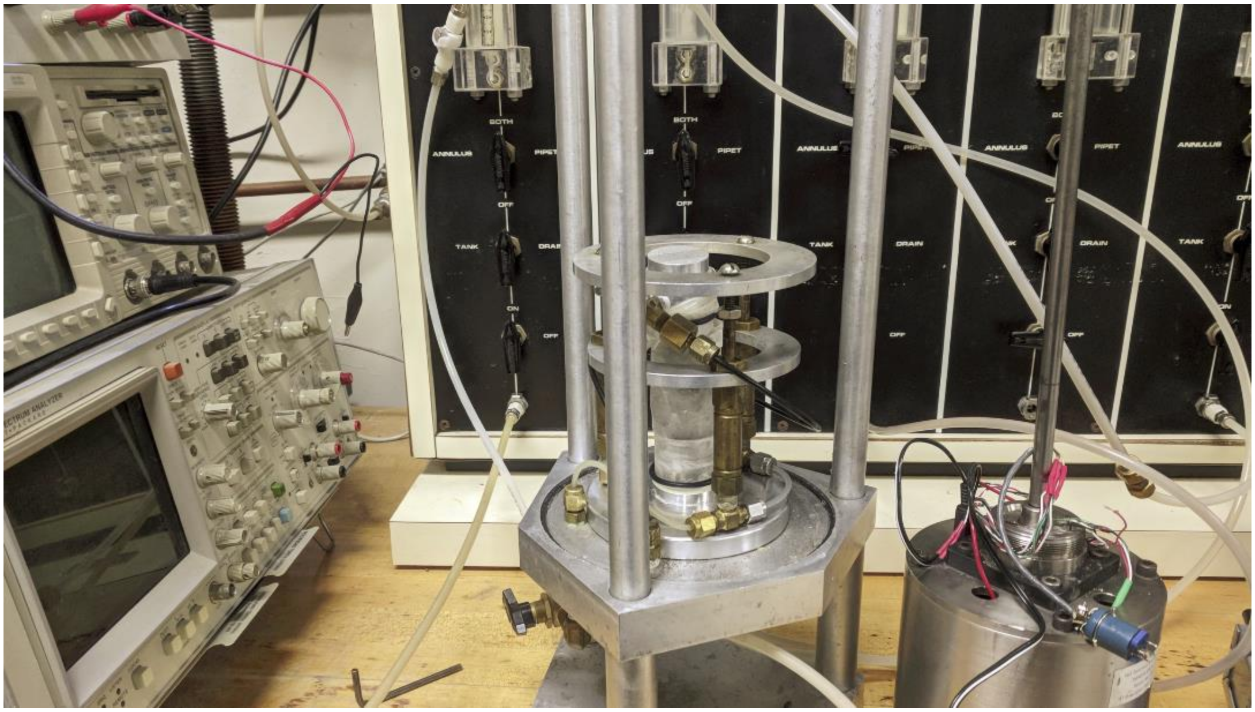

Figure 2.5: Threaded rod installation.

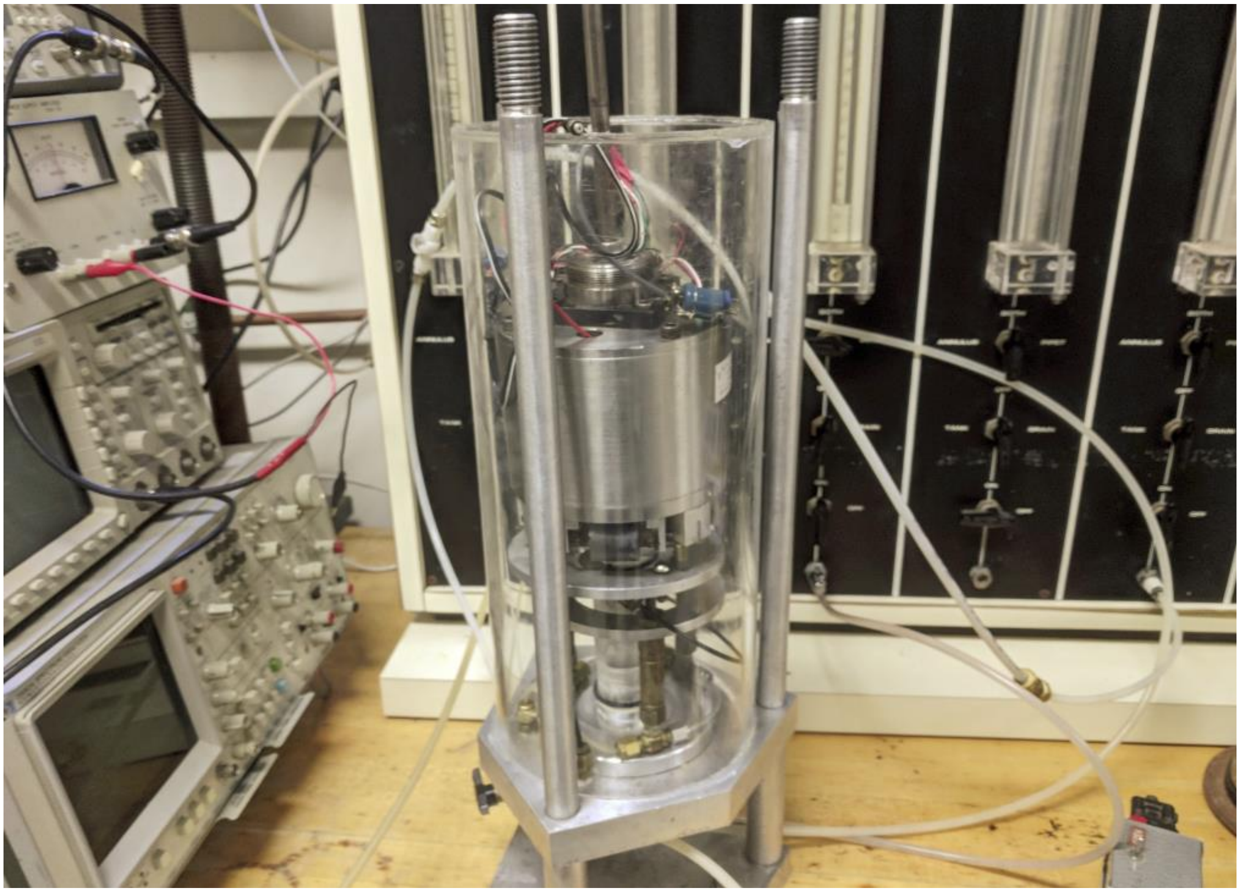

Figure 2.6: Oscillator and pressure chamber assembly.

Slide the top cover over the metal rod and down over the pressure chamber. Rest it on the top of the threaded rods and plug in the power cord, strain gauge cord, and connect the orange accelerometer cables. Slide it down the threaded rods and again ensure a good seal between the O-ring and chamber. Screw the large nuts over the threaded rods and tighten until you feel confident it is airtight. Your setup should look like this:

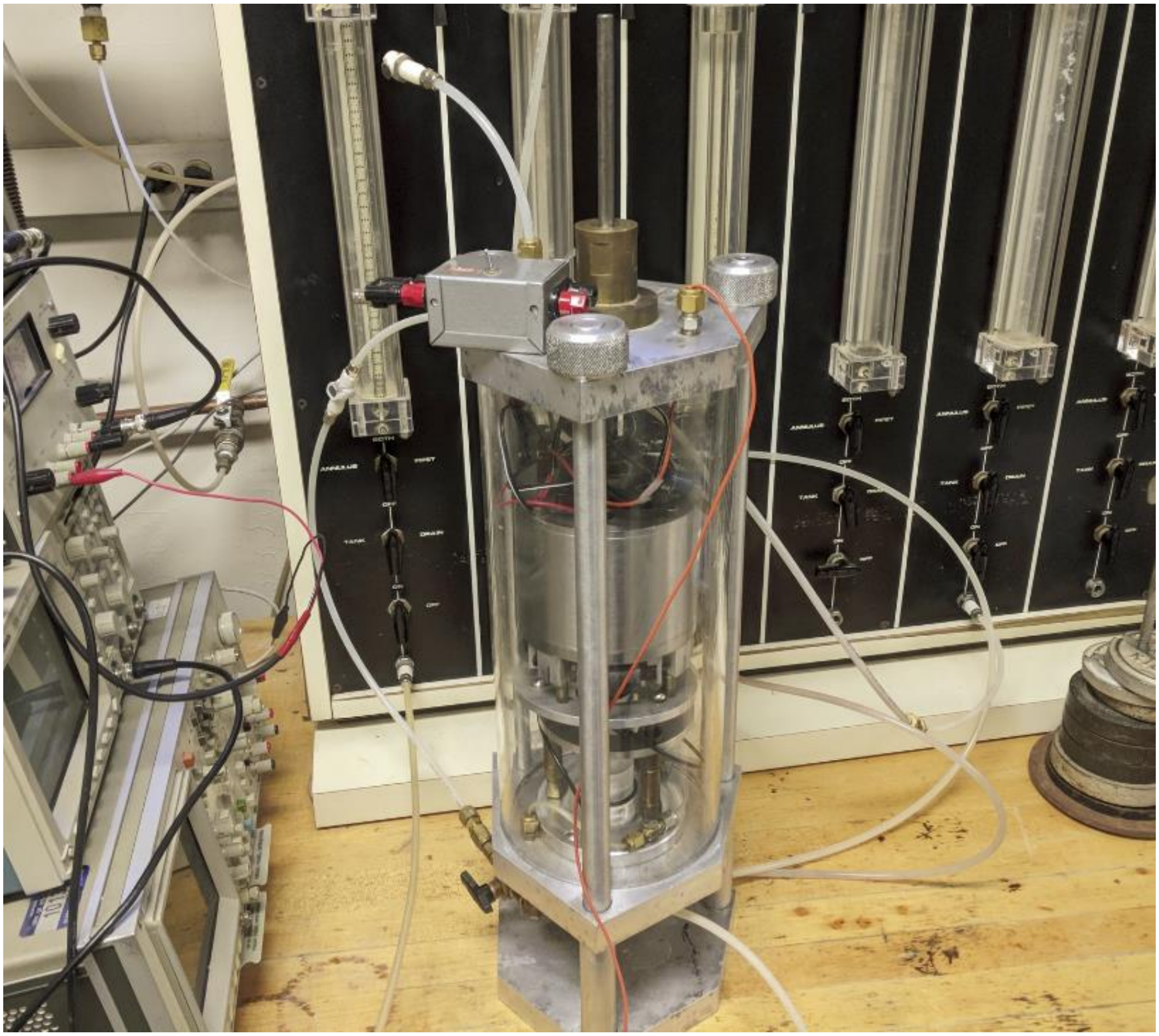

Figure 2.7: Top cover installation.

Now, it’s time to assemble the counterbalance. Screw the fulcrum into the hollow threaded rod. Then, place the lever arm over the metal rod and inside the “U” shape of the fulcrum. Make sure the hook is facing down, and screw the lever to the metal rod. Be careful not to tighten it too hard, as the thread can be stripped, or bolt damaged by pressing it too hard against the metal rod. Your setup should look like this:

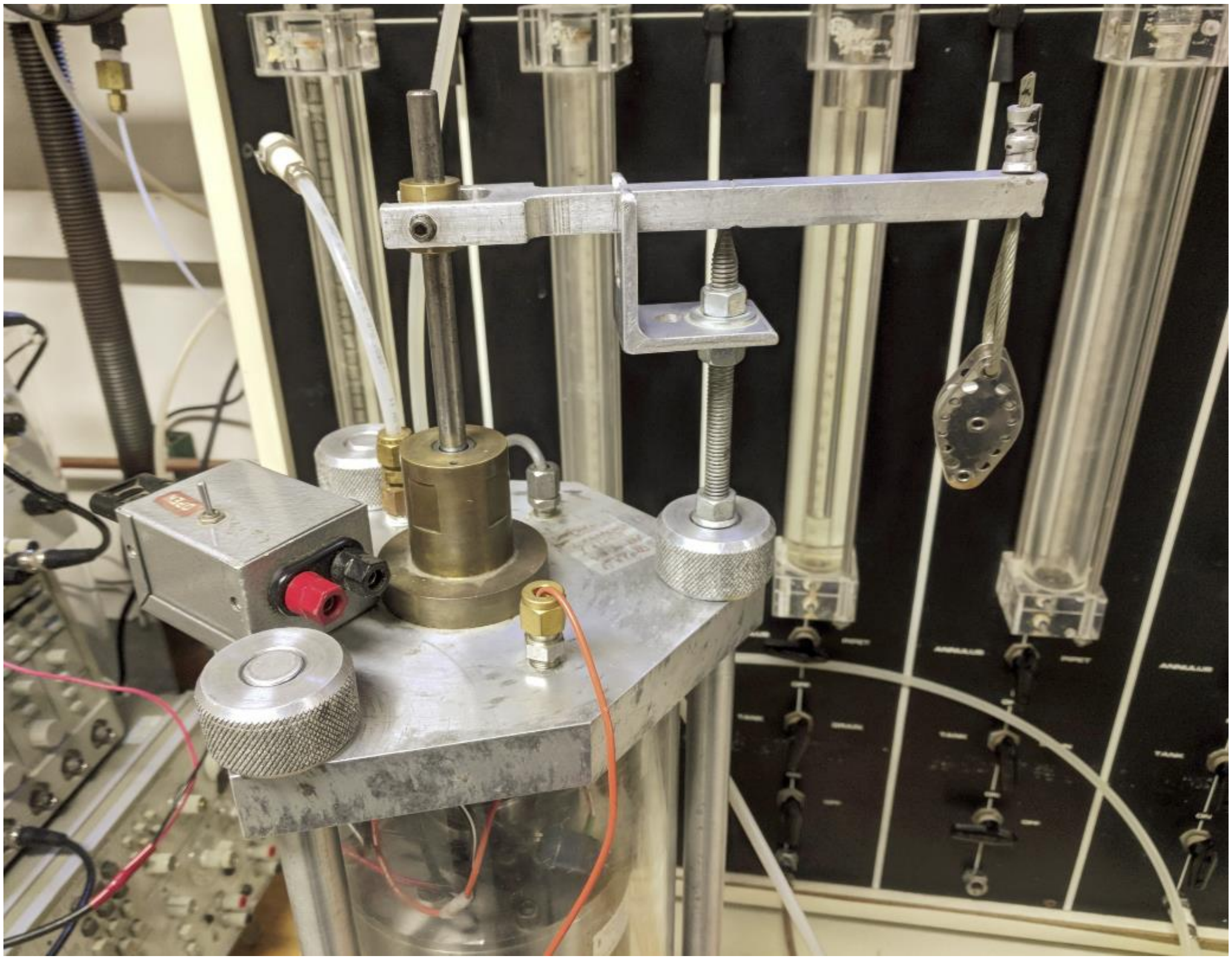

Figure 2.8: Counterbalance assembly.

To counterbalance the oscillator, take the counterbalance platform with the requisite weight and bring the hook over the lever arm hook. **The following steps must be done at the same time to prevent specimen damage**. As you flip the jack valve shut, lower the weight onto the lever arm hook. This will transfer the weight without adding excess deviatoric stress on the soil. Your setup is now complete and should look like this:

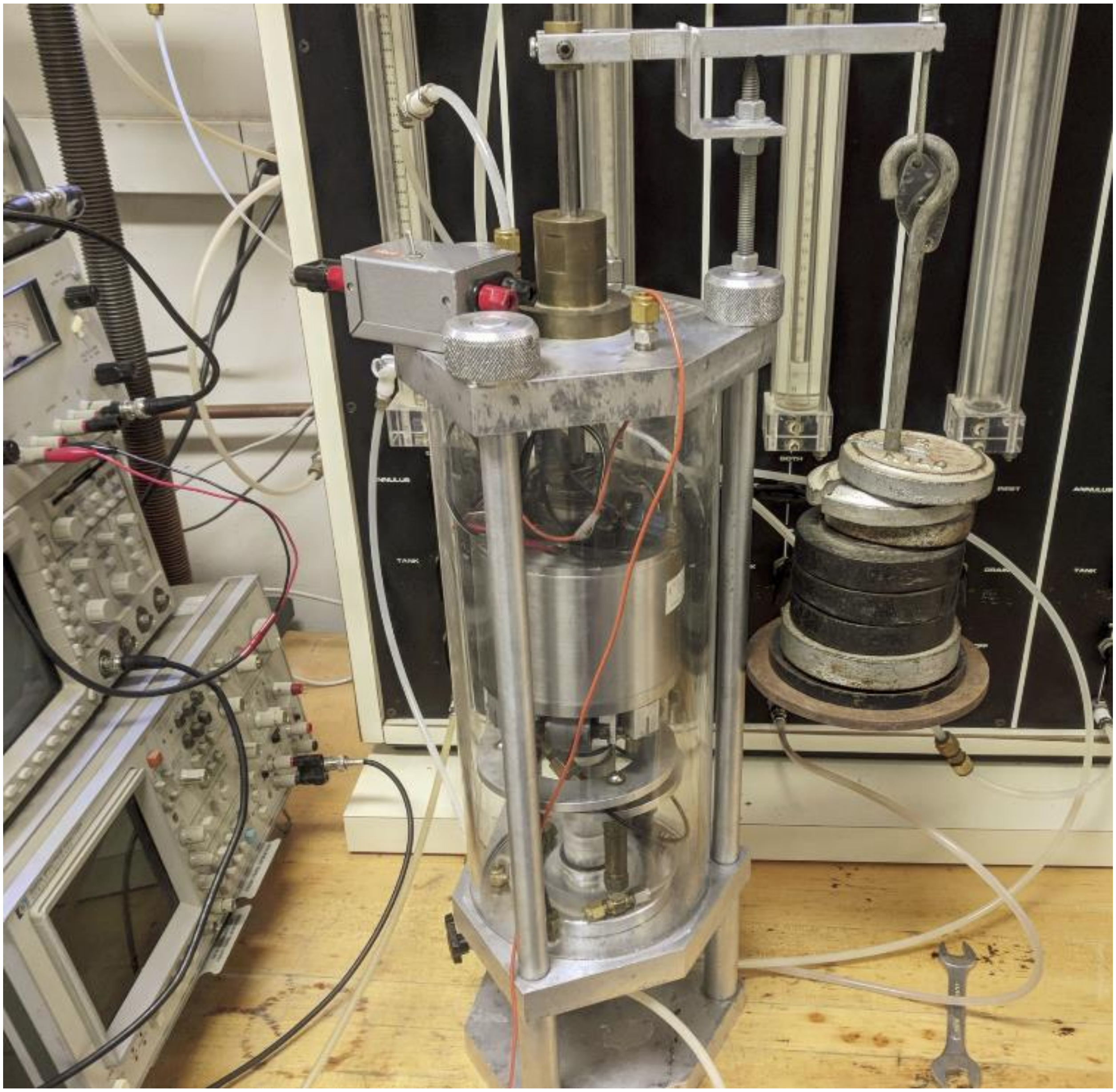

Figure 2.9: Completed assembly of resonant column apparatus,

Troubleshooting for common issues:

- If, after applying confining pressure, there is a leak, you can unscrew the nuts from the threaded rods and pullup the top cover without removing the counterbalance system. Rest the cover on top of the rods and you can add vacuum grease to the top of the chamber or lift the chamber and add it to the bottom O-ring. The seal must be ***complete,*** or the confining pressure will be too low due to air leakage. Also, if there is debris on the ends of the chamber or on the O-rings, this can cause a leak, so be sure the surfaces are clear of debris such as dirt and dust.
    - Air can also leak through the hole where the metal rod protrudes through the top cover. This is likely due to vacuum grease not filling the cracks. I was able to fix this usually by quickly applying very high confining pressure (~ 25 psi) to push vacuum grease into the openings. Alternatively, more grease can be applied to the hollow rods within the hole.
- If the pneumatic jack pedestal ring is on contact with the elbow fitting, it is either due to the sample being too long or the jack not being centered with the specimen. If the jack is centered, there should be plenty of clearance for both fittings. I tested a sample with a fitting touching the ring and not touching the ring, and my results were essentially the same, so, as long as the impedance is not significant, it shouldn't be a huge deal. If it is, you will need to disassemble the resonant column and re-center the jack, which will include supporting and moving the oscillator to keep it centered on the specimen. This is best done with assistance. The sample can be taken out and shortened as well, but do not shorten it too much, or it will contact the jack frame and affect the results.
- If the membrane does not quickly tighten over the specimen with confining stress, it is either due to a leak in the axis translation line that is allowing confining pressure to enter the inside of the membrane, lack of ventilation from the top platen, or a leak in the pressure chamber releasing confining pressure. First, ensure that the axis translation line is allowed to vent, as air cannot escape the inside of the membrane if it is closed to air flow. This can be fixed by disassembling the resonant column and tightening the fittings and adding pipe sealing tape. If there is a leak in the confining stress, see previous point on fixing leaks.

12.7 Hydraulic System Control

For hydraulic control, there are four ports on the resonant column apparatus that must be used in addition to the pneumatic jack port. First, there are two ports on the bottom of the bottom platen that are saturated with water and used for backpressure. Then, attached to the axis translation lines, there is a port on the bottom of the metal frame that is connected to an air pressure port. Finally, on top of the top cover, there is a port for application of confining stress via air pressure. The seals on these should be airtight and not allow *any* leakage of air or water. The pipe sealing tape can be used to seal these connections.

The water and air pressure are controlled by a pressure board. There are several throughout the many soils labs. This manual uses a pressure board in the basement lab of the CAE building (1410 Engineering

Dr.), but the principles hold for any pressure board. Just make sure you understand the operation of the pressure board before using it. This manual will assume you understand how to operate the pressure boards. If you are unsure of how to operate the board, ask the lab manager, a professor, or a grad student who knows how to use one. The resonant column requires four (4) ports in a pressure board. Two will contain a water reservoir and two will be air only.

For the water ports, start by filling one burette ¾ full of water and another ¼ full. Connect the ports to the lines attached to the bottom of the bottom platen. Saturate the lines by running pressurized water from the ¾ filled port to the other through the lines until the other burette is ¾ full. This will get rid of any air bubbles caught in the system. Alternate until bubbles no longer rise through the burettes during flow. In the end, you should have one burette ¾ full and one ¼ full. If the levels have fallen significantly due to displaced air, add water to roughly these levels. The ¾ full burette will be the one in which you apply pressure. Turn both ports to the "off" position for the time being.

There is no real prep for the air pressure ports besides emptying them of water. To achieve this, turn the port to the "drain" position and apply pressure. This will push water out of the lines into the bucket beneath the board. Let the lines flow until only air blows out of the drain line. You can also test this by inserting an open-ended line to the port in front and applying air pressure. If only air flows through, the line is devoid of water.

The locations of the water vs air ports does not matter (i.e. the water burettes do not need to be next to each other). If each port works and is properly prepared, you are ready to operate the hydraulic controls. **The following sections assume the apparatus has been fully assembled and ready for testing.**

12.7.1 Saturation

Since you verified the HAE disc allows water flow during apparatus assembly, the system is ready to saturate a specimen.

First, open the port for the ¾ full burette and leave the ¼ full port closed. The reservoir should still be set to apply water pressure to both the annulus and pipette for now. Since water pressure is being applied and the effective stress must be maintained, the confining pressure must be increased an amount equal to the water pressure. I typically saturated the specimen with 25 kPa of water pressure. As a result, the confining stress was concurrently increased by 25 kPa. As soon as water pressure is applied, switch the port to apply pressure only to the pipette within the larger annulus. This will allow easier reading of water volume change, since the total volume added to the specimen will be equal to the change in level between the annulus and pipette. As a backup, record the initial reading on the pipette. **Make sure the port connected to the line leading to the top platen is set to "vent" and turned "on" so that the water can displace the air within the specimen**. The specimen should now be saturating. Check on the specimen periodically and make sure the pipette water level continues to decrease. For the stiff CL samples I used, saturation took 36 hours, but if your soil is significantly different, you should test run several samples and determine a reliable saturation time. Once saturation is complete, lower the water pressure to zero and return the confining pressure to its original value.

By the time saturation has finished, there has likely been an excess of water that flows through the specimen and evaporates once it reaches the top platen and vent. The final pipette reading should not be taken as the amount of water added to the specimen. It is used at this stage to ensure constant flow of water. It will later be used to measure changes in water content during the axis translation process.

12.7.2 Axis Translation

After testing a saturated specimen, it's time to de-saturate the specimen. You should have set matric suction levels you will use for every sample. For example, I tested each specimen at 25 kPa, 50 kPa, 100 kPa, and 200 kPa.

First, make sure the water port you used to saturate the specimen with is still set to “on”. Additionally, there should be **zero** pressure applied to the port. Essentially, nothing on this port changes from the saturation stage other than reducing water pressure to zero (i.e. atmospheric). **Next, switch the axis translation port from “vent” to “pressure”. THIS IS CRUCIAL AND FAILING TO DO SO WILL NOT APPLY AIR PRESSURE TO YOUR SPECIMEN**.

Finally, at whichever matric suction you desire, apply an air pressure of equal magnitude to this port. Concurrent to this, you should increase the confining pressure an equal amount so the net stress on the soil remains the same. If you fail to do this, the confining stress will be incorrect and results will not be valid. Additionally, at pressures higher than your confining pressure, the latex membrane will expand with air and explode inside the chamber (yes…this happened to me). Make sure you write down the level of the pipette, as the increase from this level will indicate the change in water content/saturation.

The system has equilibrated once the water level no longer changes. This can be very difficult at lower matric suctions, but, through a combination of pipette monitoring and moisture content of dummy samples at various time intervals, I found that equilibration consistently occurred at 36 hours. Again, this will vary with your specimen, so be sure to calibrate this number for your soil. Be sure to reduce the axis translation pressure to zero, as well as reducing the confining pressure an equal amount prior to testing.

12.8 Electronics Setup

As outlined in the equipment section, there are five components of the electronics setup. This section will detail the connection and general operation of each. Some of the components will differ and as a result, operation will differ, so the guidelines should be tailored to your equipment.

12.8.1 Signal Generator

To produce excitation in the coils driving the electromagnetic motor, an Agilent 33220A 20 MHz Function/Arbitrary Waveform Generator (below) was used. Several signal options are available with this device, including sine, square, ramp, pulse, and noise. For the purposes of this study, a sine signal was chosen, as directed by the ASTM standard. Signals ranging from 0 to 20 MHz can be used, as well as amplitudes from 6 mV_{RMS} to 7.3 mV_{RMS}. The frequency can be controlled manually or set to “sweep” through a set range.

Figure 5.1: Signal generator

12.8.2 Signal Amplification

Due to the relatively small input from the signal generator and output voltage from the accelerometer, an amplifier and signal conditioner were used to better measure/control the input and response. For the excitation signal, an HP 6824A DC Power Supply Amplifier (below – left) was used as a signal conditioner. For the accelerometer output, a Columbia Research Laboratory Model 4102 Charge Amplifier (below – right) was used. Confirmation of the amplification level was used by measuring the output of the amplifier versus the output of the signal generator with the digital oscilloscope. This confirmation was performed throughout the study to ensure the amplification had not drifted or been changed over time.

Figure 5.2: Signal conditioner (left) and power amplifier (right).

Accurate measurement of the *accelerometer amplifier* if vital to accurate measurement of shear strain. The resonant frequency will be the same regardless of amplification, however, the shear strain is dependent on the accelerometer output’s amplitude.

12.8.3 Spectrum Analyzer

To plot the response curve for the accelerometer, a, HP 3582A Spectrum Analyzer (below) was used. The device should be set to plot in the frequency domain, with the amplitude of the signal plotted on the y-axis, from which the resonant frequency and amplitude were recorded. The resolution, range, and sensitivity can be controlled via the control panel on the right of the screen. The spectrum analyzer can measure voltages ranging from 1 μV to 40 V. As the signal analyzer sweeps through a range of frequencies, the spectrum analyzer, using a Fourier transform, records peak voltage at each frequency. Several sweeps are needed to fully develop the plot, as the sampling frequency cannot capture each frequency with only one pass.

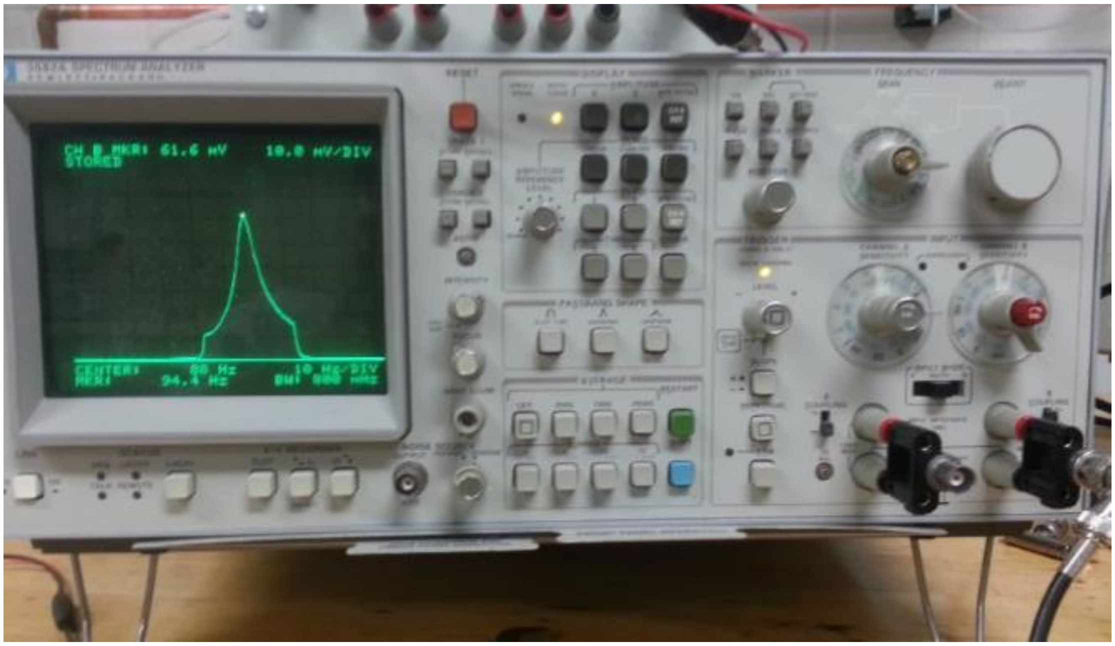

Figure 5.3: Spectrum analyzer.

To set the spectrum analyzer up to record peak amplitude at each frequency, set the control panel *exactly* as outlined below by ensuring buttons in *red* are pushed in.

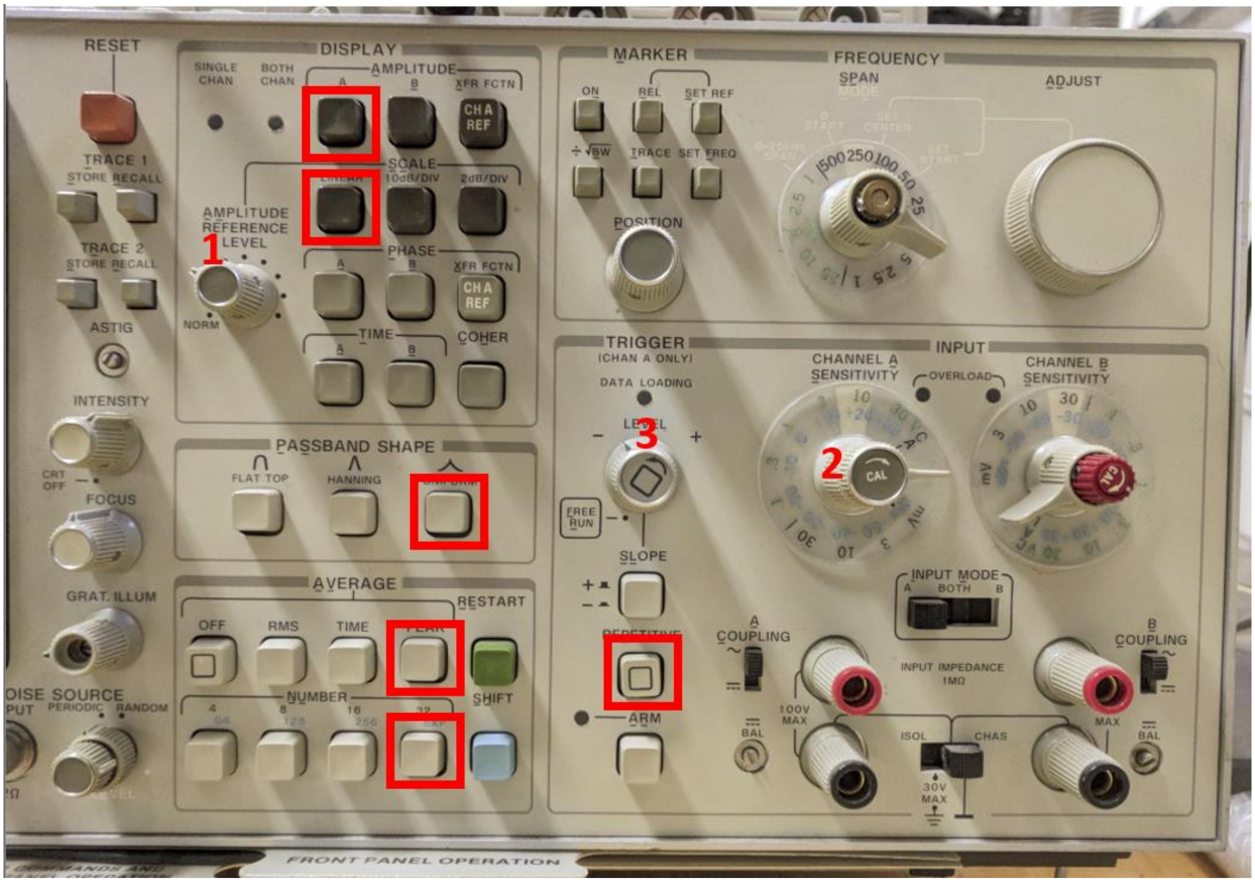

Figure 5.4: Spectrum analyzer setup.

12.8.4 Digital Oscilloscope

A digital oscilloscope was used to analyze the input and output signals for the accelerometer, oscillator, and both amplifiers. The electrical signal appears as a time series on the display, with the horizontal and vertical scales able to be altered to avoid clipping. Additionally, the oscilloscope can measure various properties of the signal, such as frequency and amplitude. This function was primarily used to periodically validate the spectrum analyzer output and visualize the frequency sweep and signal generator amplitude.

The oscilloscope is pictured below. In a pinch, if the spectrum analyzer does not work or is unavailable, it can be used to find peak amplitude and resonant frequency, but the process is cumbersome and more time consuming.

Figure 5.5: Digital oscilloscope.

12.9 System Calibration

Calibration of the system requires two main components: apparatus resonant frequency and the rotational inertia of the oscillator. First, the resonant frequency of the apparatus should be found by essentially running a test without a sample present. Using the counterbalance, the oscillator is suspended inside the chamber, and a range of frequencies swept, resulting in a peak amplitude at 24 Hz. Thus, the resonant frequency of the system was determined to be 24 Hz. A student who ran this calibration in 2013 found the resonant frequency to be 23 Hz. Since the spectrum analyzer measures in 1 Hz increments, the true resonant frequency is likely about 23.5 Hz. Run this calibration test to verify the apparatus is working correctly before beginning your testing program.

Second, the rotational inertia of the oscillator has to be determined to properly calculate the soil's resonant frequency. The following equation can be used to relate resonant frequency and rotational inertia:

$$J = \frac{k}{(2\pi f)^2} \qquad [6\text{-}1]$$

$Where;$

$J = Rotational\ moment\ of\ inertia$
$k = Torsional\ stiffness$
$f = Resonant\ frequency$

Due to the complicated shape of the oscillator and varying densities of the components' materials, numerical calculation of the rotational moment of inertia is impractical. However, Equation 6-1 can be solved by measuring the resonant frequency of a material with a known stiffness. The lab has three PVC rods of varying diameter and constant shear modulus (1 GPa) to be used as calibration rods. The shear modulus used for the PVC is an approximation by the manufacturer, and if a more accurate value is needed, the calibration rods themselves must be calibrated. However, the 1 GPa approximation should yield usable results. The equation that relates the resonant frequency of a known specimen to the rotational inertia of the oscillator is as follows:

$$J_{Osc} = \frac{\pi d^4 G}{32 l} \qquad [6\text{-}2]$$

$Where:$

$G = Shear\ modulus\ of\ specimen$
$l = Length\ of\ specimen$
$d = diameter\ of\ specimen$

The procedure begins with installing the PVC rod in the chamber in place of the top platen, bottom platen, and soil. The signal generator is then set to sweep through a range of likely frequencies, with the peak amplitude representing the resonant mode. Then, using equation 6-2, the oscillator's rotational inertia could be determined. Table 6-1 summarizes results from a 2017 study. Figure 6-1 illustrates the results for each calibration rod from tests performed in 2014 and 2017.

Table 6.1: Resonant column calibration results.

Column	Diameter	Length	Resonant Frequency	Torsional Stiffness	Rotational Inertia
--	mm	mm	Hz	N·m	kg·m^2

Large	35.1	129.1	206	1154.2	0.000698
Medium	24.8	129.1	109	287.7	0.000645
Small	15.0	129.1	47	38.5	0.000597

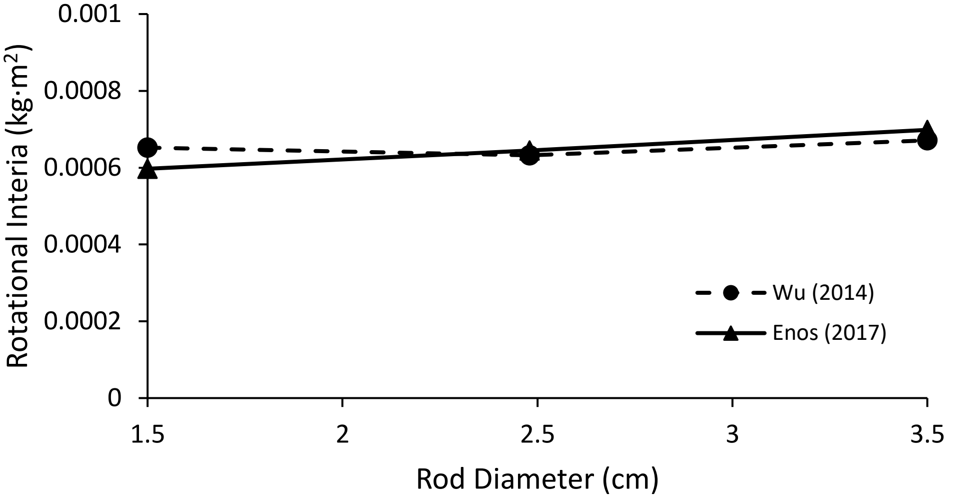

Figure 6-1: Oscillator rotational inertia calibration results

The calibration rods yielded very similar results, averaging out to about 0.000647 kg·m^2, with the deviation of the minimum and maximum values being within 8% of the average. Furthermore, the measured values match very well with a previous calibration on the same apparatus performed in 2014. **Verify that you yield the same results before your testing program.**

12.10 Test Operation

Once the saturation or suction equilibration process is complete, the external resonant column wiring can be connected to the input signal conditioner, set to amplify the signal by 2x, and output amplifier, set to amplify by 100x. The input amplification is less important, as this can be adjusted and does not affect any calculations. The only condition is that the amplitude reaches a level that can apply a strain of 10^{-3} to the specimen. The output amplification must be well controlled and accurate to ensure proper calculation of shear strain. The switch atop the resonant cover should be switched off for the time being. To begin testing, the signal amplitude should be set to 25 mV, about the smallest amplitude that will yield a signal discernable from background vibrations. Additionally, the signal generator should be set to sweep a likely range of frequencies. Generally, this is between 40 and 100 Hz, though the saturation level, soil type, confining stress, and density can result in a resonant mode lower or higher than this range.

Once you are prepared to take measurements, flip the switch on the cover to the on position. At this low amplitude, you **will not** be able to visibly see oscillation. Push the green “Restart” button and immediately hold the blue button directly below it. The blue button allows measurement for an indefinite measurement period. After allowing several sweep cycles to run (for ~2 min), the peak frequency and its amplitude are identified on the signal analyzer by moving the marker to the highest point on the plot. Record the resonant frequency and the signal amplitude, as shown in the figure below.

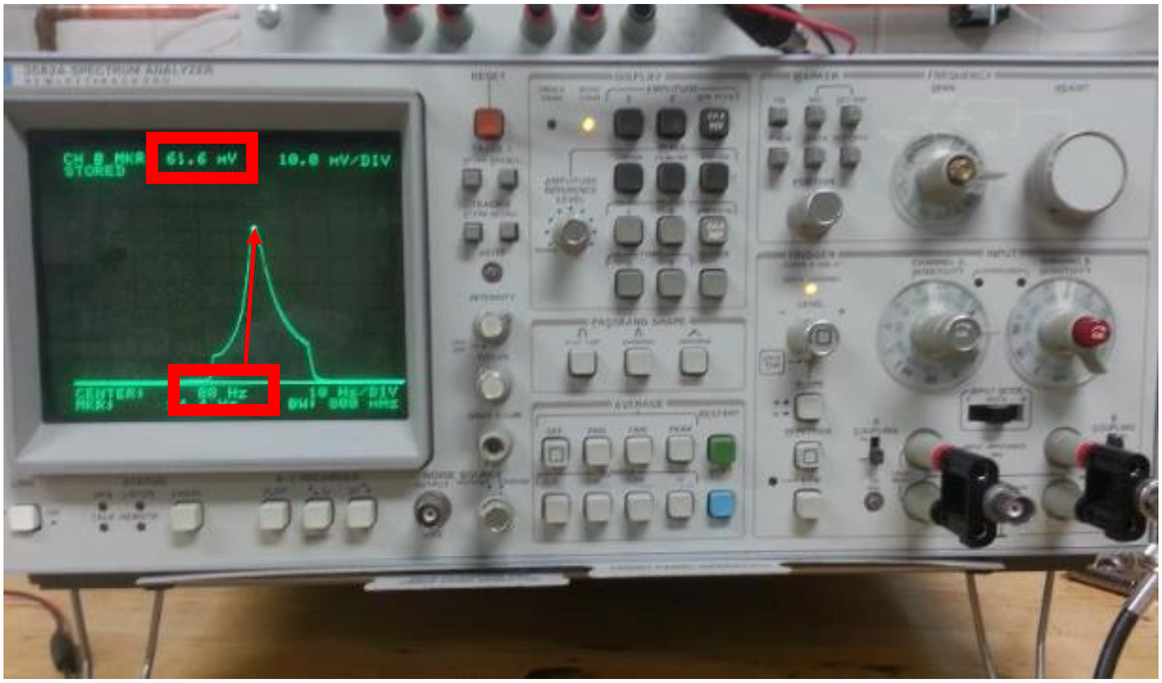

If the curve is too small and difficult to see, or too large and off the screen, adjust the “Amplitude Reference Level” knob (Fig. 5.4 – labelled 1) just to the right of the screen to change the scale of the y-axis. This **does not** adjust sensitivity of the sensor, just the scale of the y-axis. If the signal is not registering, it is likely too low to be detected, so the sensitivity of the spectrum analyzer must be raised. Alternatively, if the signal is too strong and overloading the sensor, the sensitivity must be lowered. This is done by adjusting the knob directly above the left input port (Fig. 5.4 – labelled 2). Rotating it clockwise raises the sensitivity, and rotating it counterclockwise lowers the sensitivity. Adjust it until the trigger light consistently flashes yellow during data collection, which indicates incoming data is being read.

The “Trigger” knob (Fig. 5.4 – labelled 3) to the left of the sensitivity knob can also be adjusted, though it rarely, if ever, needed adjustment once a good spot was found at about the 315° position. Ultimately, there is no surefire method to adjusting these knobs, and it takes practice and patience. The best thing to do is to run dummy tests on extra soil to get a feel for how to adjust these knobs.

This process is repeated for incrementally larger input amplitudes until the shear strain reaches about 10^{-3}. It is best to plot the shear modulus reduction curve in an Excel template concurrent to testing so that you will know when the strain limit is reached. Typical input voltages were of 25, 50, 100, 250, 500, 750, 1000, 1500, 2000, 2500, and 3000 mV. This varied specimen to specimen, and using the Excel template was helpful in determining the intervals. For example, if a soil was particularly stiff, larger intervals were used to reach the requisite strain than in a softer soil.

Of particular note is that during initial testing with remolded “dummy” specimens, the cylinders would fail along a lift interface if brought near max strain (~10^{-3} strain), so care should be taken to rough up the lift surface before the next lift added to maximize coupling. When the lifts were well coupled, this issue did not occur.

12.11 Data Reduction

Calculation of the shear modulus, shear strain, and damping assumes a single degree of freedom (SDOF) system. The results of the resonant column test yield the values of voltage amplitude, frequency, and power spectrum or time decay. The process for converting test results to the required parameters is as follows:

First, the average shear strain must be determined via Equation 8-1.

$$\gamma = \frac{yD_s}{5S_a(2\pi f)^2 D_a H} \qquad [8\text{-}1]$$

$Where$:

$y = Accelerometer\ output\ amplitude$
$D_s = Specimen\ diameter$
$S_a = Accelerometer\ sensitivity$
$f = Resonant\ frequency$
$D_a = Distance\ from\ specimen\ center\ to\ accelerometer\ (0.035m)$
$H = Specimen\ height$

Accelerometer sensitivity was determined to be 101.3 mV/g with the output amplifier set to 100x. Furthermore, the ”5” in the denominator represents the ASTM D4015-07 recommended reduction factor for the cylinder’s “average” strain, since the strain magnitude varies with distance from the center.

Next, the shear modulus must be calculated from the resonant frequency. Richart (1975) developed the following equations to model the system under resonant frequency:

$$\frac{I}{I_0} = FtanF \qquad [4\text{-}4]$$

$$F = \frac{2\pi f_r H}{v_s} \qquad [8\text{-}2]$$

$Where$:

$I = Rotational\ moment\ of\ inertia, specimen$
$I_0 = Rotational\ moment\ of\ inertia, oscillator$
$f_r = Resonant\ frequency$
$H = Specimen\ height$

$v_s = Shear\ wave\ velocity$

Substituting into the equation for shear modulus, the resulting Equation 8-3 is as follows:

$$G = \frac{\rho(2\pi H f_r)^2}{F^2} \qquad [8\text{-}3]$$

$Where$:

$\rho = Specimen\ density$
$F = Dimensionless\ factor$

F can be determined via the plot in Figure 8-1. However, to use the plot, T and P, additional dimensionless factors, must be determined by the following relationships.

$$T = \frac{J_A}{A}\left(1 - \left(\frac{f_0}{f}\right)^2\right) \qquad [8\text{-}4]$$

$Where$:

$J_A = Rotational\ inertia, oscillator$
$J = Rotational\ inertia, specimen$
$f = Specimen\ resonant\ frequency$
$f_0 = Apparatus\ resonant\ frequency$

For solid soil specimens, as were used in this study, Equation 8-5 can be used to calculate the specimen rotational inertia.

$$J = \frac{MD_s^2}{8} \qquad [8\text{-}5]$$

$Where$:

$M = Mass\ of\ specimen$
$D_s = Diameter\ of\ specimen$

Since the passive end (i.e. bottom pedestal) is assumed to be infinitely rigid relative to the specimen, P is assumed to be equal to infinity.

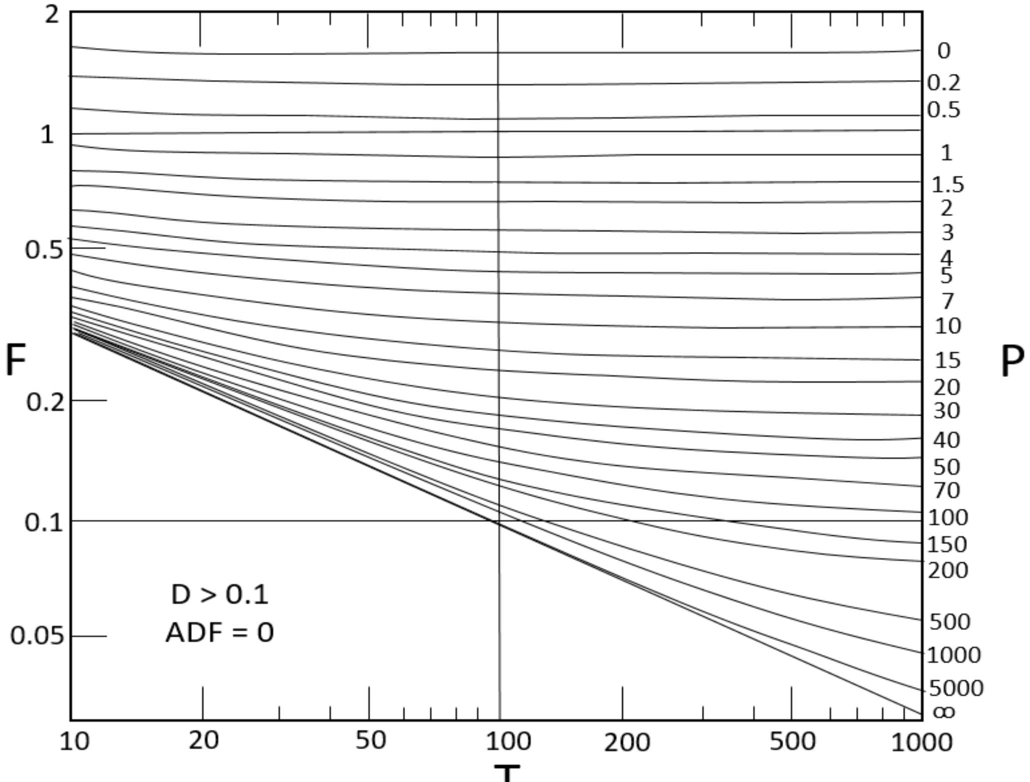

13 APPENDIX E – SUCTION-SATURATION CONTROL COMPONENTS

Figure E-1: Resonant column bottom platen without HAE disc.

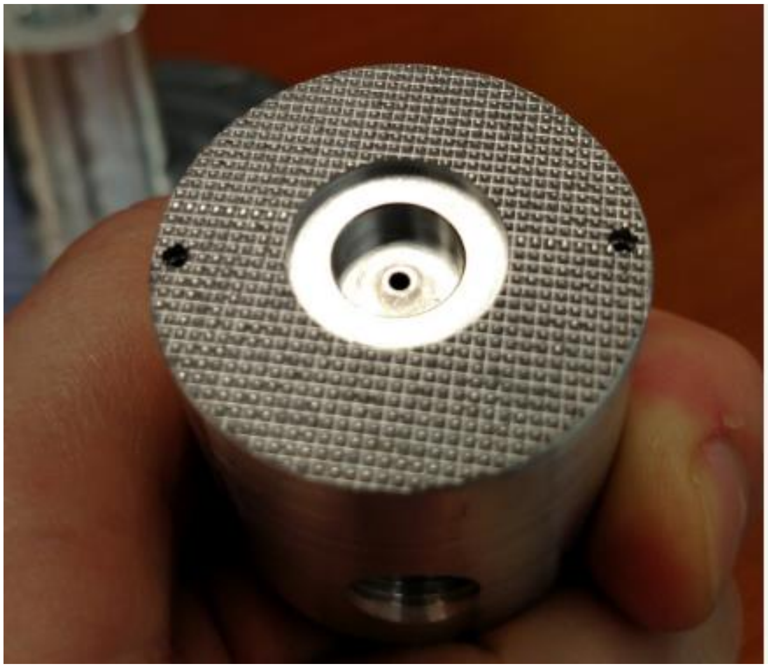

Figure E-2: Resonant column top platen without sintered disc.

Figure E-3: Resonant column suction control components.

Figure E-4: Cyclic triaxial bottom platen with HAE disc.

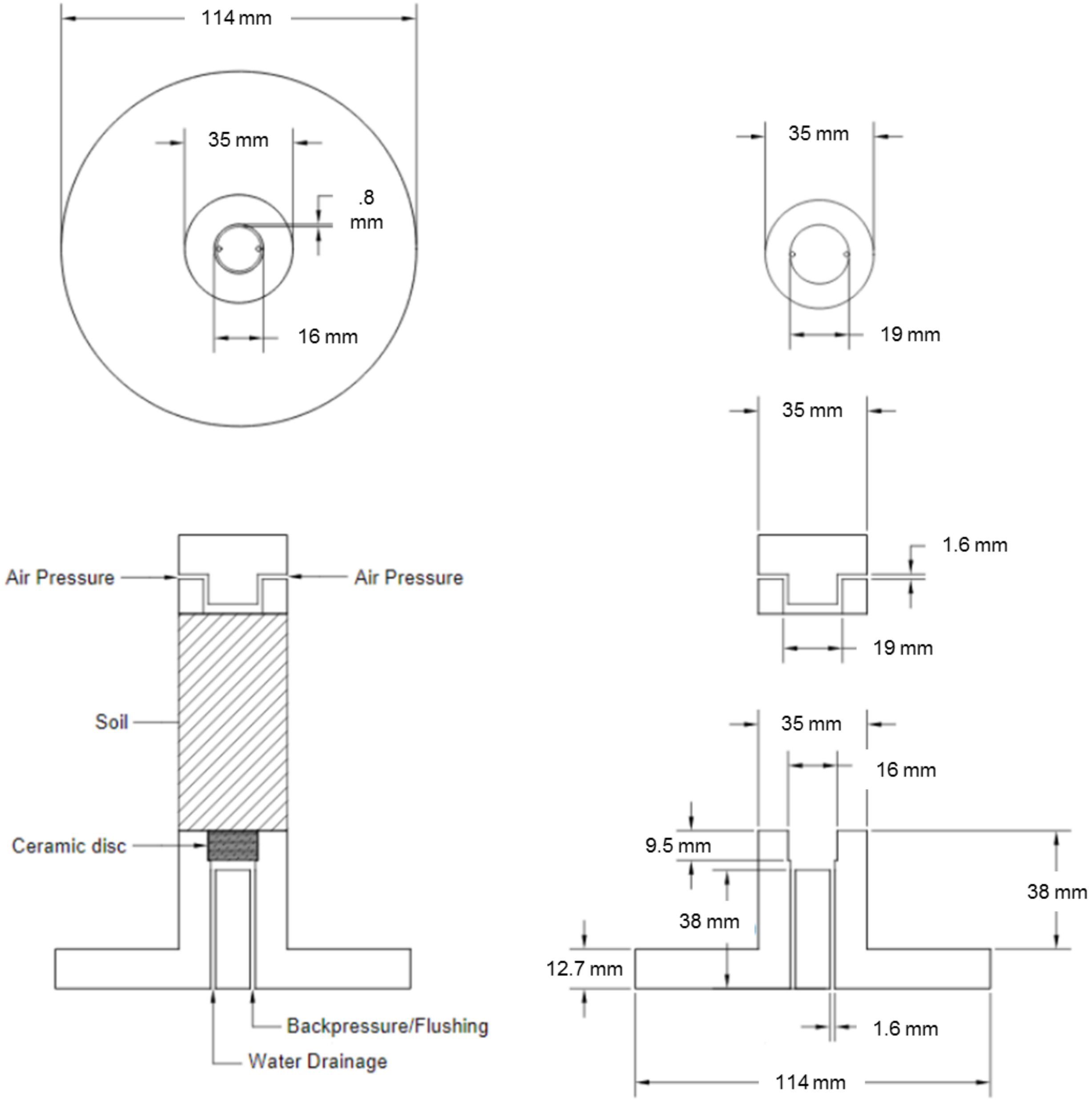

Figure E-5: Design for resonant column top platen and bottom pedestal.

14 APPENDIX F – WTG FOUNDATION DESIGN WHITEPAPERS

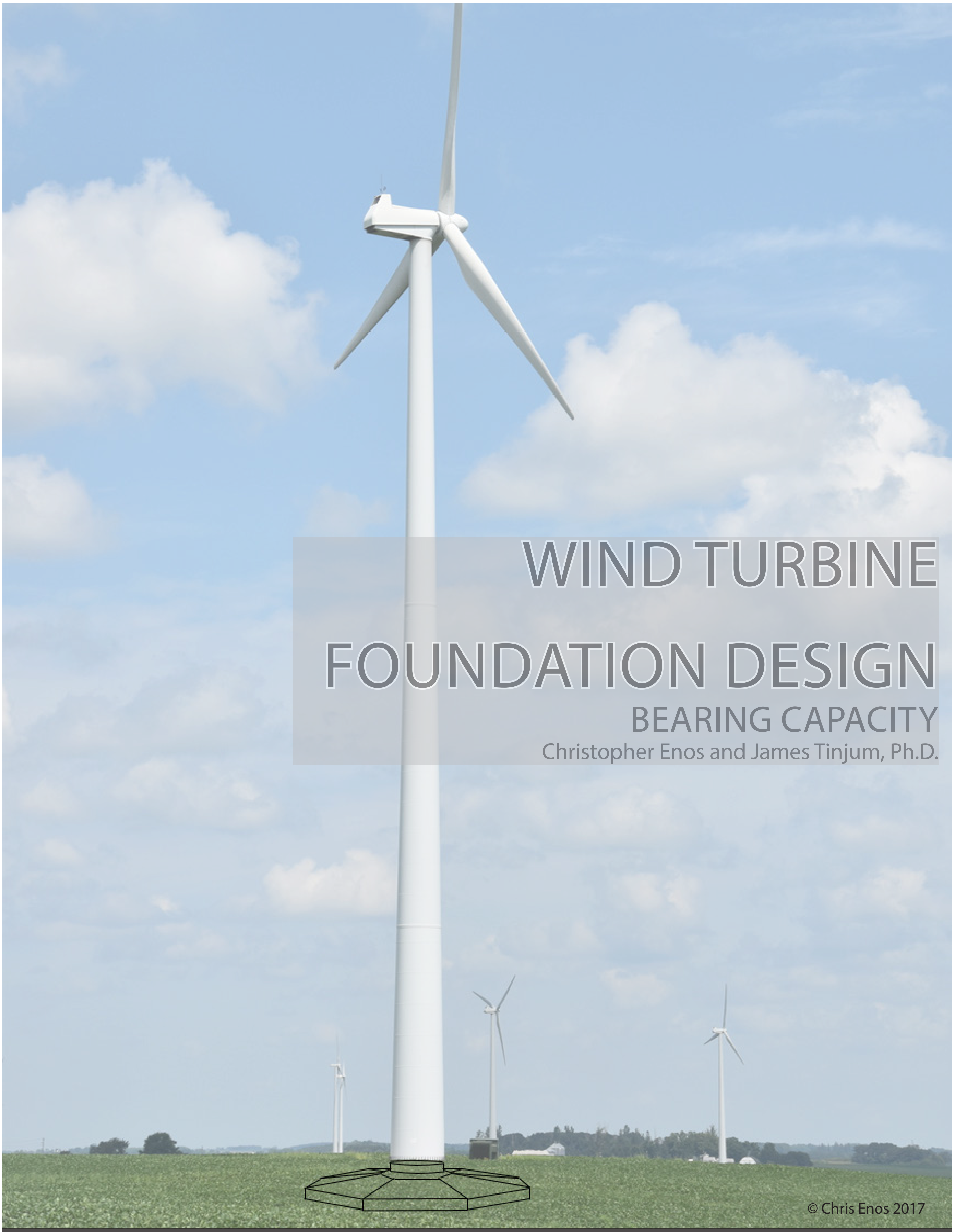

WIND TURBINE FOUNDATION DESIGN

BEARING CAPACITY

Christopher Enos and James Tinjum, Ph.D.

JAMES TINJUM, PH.D UNIVERSITY OF WISCONSIN-MADISON


© James Tinjum 2017

"...optimization of foundation design will be crucial in reducing costs to facilitate the growth of the industry."

WITH THE GROWING DEMAND for wind energy the need for larger, more powerful turbines grows with it. As capacity grows, however, so does the cost of each turbine, with the foundation accounting for about 25% of the overall cost (Lang 2012). As such, optimization of foundation design will be crucial in reducing costs to facilitate the growth of the industry.

Shallow, on-shore wind turbine generator (WTG) systems are typically founded on massive gravity-based footings, which support temporally and spatially varying vertical, horizontal, and overturning forces due to changing wind loads. As rated capacity increases, the magnitude of overturning moments increases, requiring larger foundations to accommodate rotational stiffness, bearing capacity, and overturning requirements.

Bearing capacity, in particular is a parameter that can have potentially immense consequences. Lang (2012) found that, as the allowable bearing capacity decreases, the required foundation size increases exponentially. Understanding the fundamental principles of bearing capacity and its application to the unique loads of a WTG system is key to optimizing efficiency of design.

This paper focuses on the theory and application of bearing capacity to shallow, on-shore wind turbine foundation systems. First, the discussion will focus on the fundamental concepts relating to bearing capacity. Then, current design practices will be discussed, as well as some state-of-the-art research that can be used to further develop mechanistically correct models and design procedures.

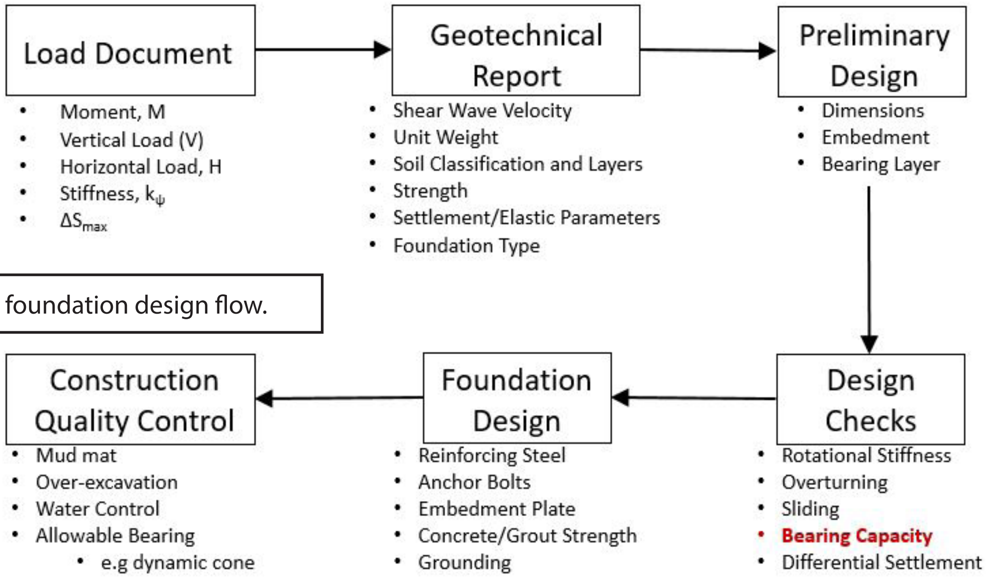

Fig. 1: General WTG foundation design flow.

BEARING CAPACITY

> “...the unique, dynamic loads imparted on WTG foundations complicates the [bearing capacity] problem.”

Like all other foundation systems, the bearing capacity is a key design parameter that often controls the design. This is no different in wind turbine generator (WTG) foundations, however, the unique, dynamic loads imparted on WTG foundations complicates the problem.

At its core, this problem centers around the balance between induced ground pressure and allowable bearing capacity. Since the soil itself has a relatively set bearing capacity (soil improvement methods aside), the balance must be altered by reducing the induced ground pressure, typically by increasing the area of the footing.

Bearing capacity failure falls under the category of a catastrophic, as opposed to a serviceability failure, where the foundation fails beyond repair or continued use.

Fig. 2: WTG foundation during construction (© James Tinjum)

Within the WTG general design flow (Fig. 1), this step falls within the design check component. Proper assessment of the soil’s breaing capacity, however, is relient upon the geotechnical report step. Furthermore, the induced ground pressure is calculated via data given in the Load Document.

BEARING CAPACITY MECHANICS

Bearing capacity, being such a large part of geotechnical engineering, has been refined and researched throughly over the years. However, it is still an imperfect analysis, as it comes with some assumptions and limitations.

One key assumption is that the soil in question is linear elastic - perfectly plastic. In other words, the soil behaves as a perfectly linear elastic material until a threshold stress, at which point it behaves perfectly plastic. Futhermore, though spatial variation in soil properties can be taken into account, the true variability and complexity of a volume of soil cannot be fully incorporated, resulting in a simplification of the soil and its properties.

Bearing capacity failure occurs when the ultimate gross bearing capacity is reached, shifting the soil into critical state. A commonly used schematic for bearing capacity mechanics in a strip footing can be seen in Fig. 3. In this model, the wedge of soil pushes down into the ground, forcing the flanking soil out along a slip plane. For circular footings, such as a WTG foundation, this wedge becomes a cone shape, pushing soil out in 360 degrees.

As the load increases to failure, the buildup of unrecoverable plastic soil strains causes the soil mass to break free, causing a pileup next to the footing.

Determination of the allowable bearing capacity utilizes a concept called limit equilibrium, which boils down to calculating a force or moment balance. Limit equilibrium follows three basic steps. First, a plausible failure surface si selected. Next, the forces acting on the system must be determined. Finally, using statics principles, equilibrium equations must be developed, with the active forces resisted by the friction along the slip plane and weight of the soil mass.

Each plausible failure surface will yield different results for maximum allowable load. The smallest value is deemed as the limiting load, and controls the design. The resisting forces can be increased by strain-harding soils, adding overburden, or using ground improvement techniques.

> “Bearing capacity failure occurs when the ultimate gross bearing capacity is reached, shifting the soil into critical state...as the load increases to failure, the buildup of unrecoverable plastic soil strains causes the soil mass to break free...”

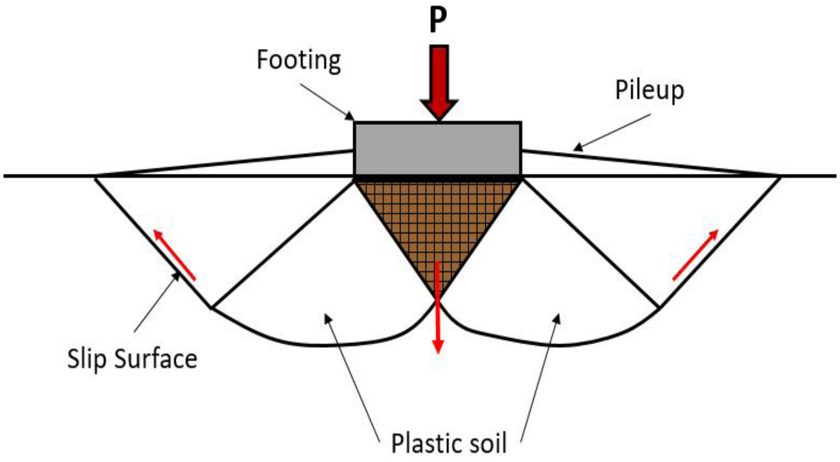

Fig. 3: Illustration of the bearing capacity mechanism of a strip footing (adapted from Budhu 2007)

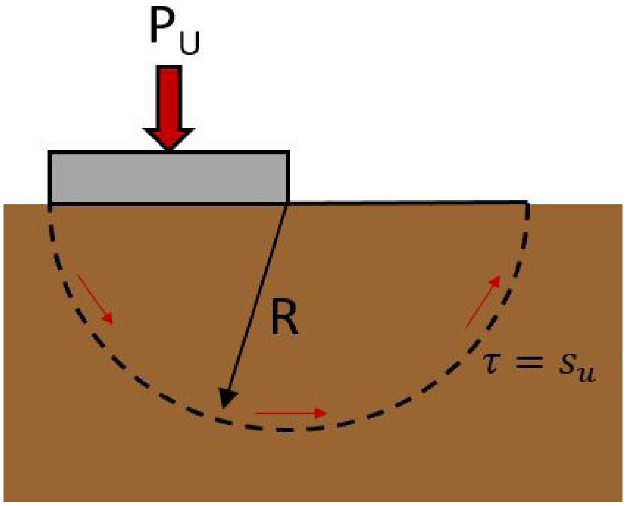

Fig. 4: Limit equilibrium example (Budhu 2007)

Take the example above in Fig. 4. In this scenario, we have a simple strip footing resting atop a volume of soil. The failure surface for this calculation is the half-circle, with a radius (R) equal to the width of the footing, marked by a dashed line.

The ultimate load is P_U, acting upon the center of the footing of unit area of R m^2/m. We will assume this analysis is an total stress analysis (TSA), so our shear strength (τ) along the failure surface is equal to s_U, the undrained shear strength.

To solve for the value of P_U, simply solve a moment balance about the bottom right corner of the footing using the principles of statics:

$$\Sigma M = P_U \cdot (B/2) - s_U B\pi \cdot B = 0$$

Solutions such as this can be performed for any footing type and any shaped plausible failure surface, where the lowest value of P_U will control the overall bearing capacity. Moreover, the bearing capacity must be adressed for both drained and undrained soil conditions in fine-grained soils, as the allowable bearing capacity can vary considerably between the two.

Both fine- and coarse-grained soils must be analyzed using an effective stress analysis for the long term condition. Mechanically, this assessment takes into account the state of stress once the porewater pressure has dissipated. The shear strength parameter in this case is the friction angle, Φ.

A total stress analysis is required for analyzing the short-term, undrained conditions of the soil, hence it is only applicable to fine grained soils, as coarse-grained soils drain much more quickly and pore pressure dissipates. As used in the limit equilibrium example, the controlling parameter is the undrained shear strength, s_U.

Each analysis, however, requires several correction factors to account for variables such as foundation dimensions/shape, inclination, Terzaghi's bearing capacity factor, and overburden. The solutions for each of these factors can be found in any standard textbook on foundation design.

The final stage determines the factor of safety of the analysis via the following equation:

$$FS_{BC} = q_{ult}/q_{applied}$$

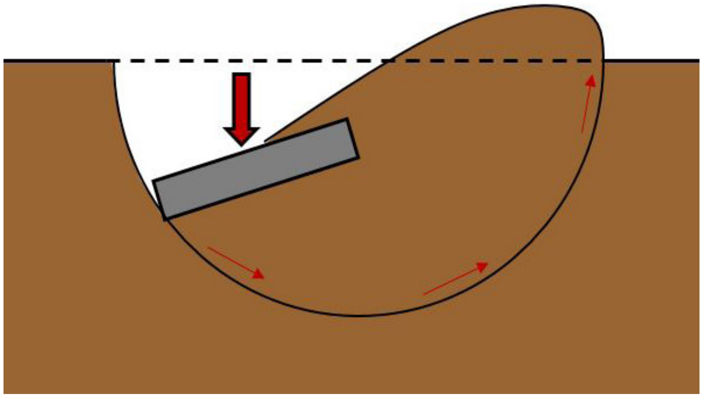

Fig. 5: Example of bearing capacity generalized shear failure (Coduto *et al*. 2016)

APPLICATION TO WTG SYSTEMS

WTG foundations are subject to a unique loading environment due to high horizontal forces and moments relative to the weight of the system. This presents a complex problem to geotechnical engineers, as the load can no longer be assumed to act uniformaly across the area of the footing. Furthermore, the moment doesn't just shift the static vertical load towards the leeward side, it adds vertical load to the leeward side in addition to the existing static load.

Several conceptual models can be used to approximate the load distribution as illustrated in Fig 6.

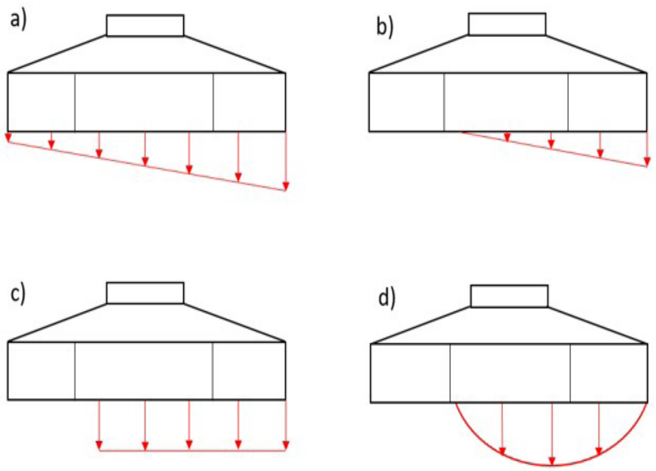

Fig. 6: Load distribution models (a) linear across diameter (b) triangle along effective area (c) uniform along effective area and (d) circular along effective area

Each of these models has their own strengths and weaknesses. For the purposes of conventional bearing capacity, it is easiest to reduce the load distribution to a uniform load along an effective bearing area. Though this is not necessarily mechanistically correct, it allows engineers to quickly assess bearing capacity for projects where there may be 100+ foundations to design.

DNV/Riso (2002) instructs engineers to develop an effective bearing area that acts eccentric to the center of the foundation:

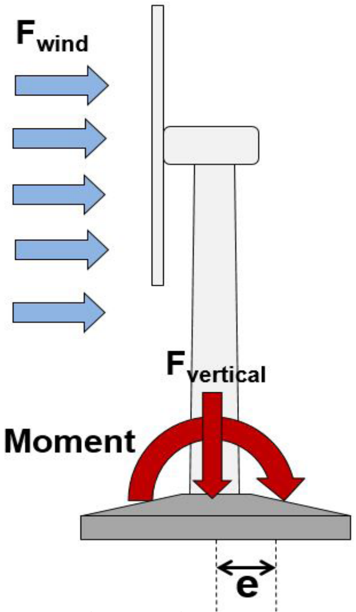

Fig. 7: Loading of a WTG foundation (Zen 2016)

For simplification, the octagonal footing is assumed to be circular. An ellipsoid area is then calculated to represent the area that uniformly bears the entirety of the turbine's vertical load. This ellipse is then converted into an equivalent rectangle shape to facilitate bearing capacity calculation.

In addition to conventional bearing capacity analysis, the design check requires that the vertical force not act outside the middle third of the foundation. The eccentricity can be calculated via the following equation:

$$e = M_{OT}/F_V$$

where M_{OT} is the extreme overturning moment and F_V is the vertical load given by the Load Document.

The following page will go through the calculation process to determine the effective bearing area to calculate the bearing capacity factor of safety.

SAMPLE CALCULATION

Step 1: Calculate the effective ellipse area:

$$A_{\text{eff}} = 2\left[R^2 \arccos\left(\frac{e}{R}\right) - e\sqrt{R^2 - e^2}\right]$$

where R and e are the foundation radius and eccentricity, as shown in Fig 8.

Step 2: Calculate the major axes of the ellipse:

$$l_e = 2R\sqrt{1-\left(1-\frac{b}{2R}\right)^2}$$

$$b_e = 2(R-e)$$

Step 3: Convert the major ellipse axes to the dimensions of an equivalent rectangle:

$$l_{eff} = \sqrt{A_{eff}\frac{l_e}{b_e}} \quad and \quad b_{eff} = \frac{l_{eff}}{l_e} b_e$$

Step 4: Calculate the effective bearing area for the rectangle shaped bearing zone:

$$A_{\text{eff}} = b_{\text{eff}} \times l_{\text{eff}}$$

This area can then be assumed to bear the vertical load uniformly across its area. With the equivalent area and applied ground pressure set, the next step would be to assess the ultimate bearing capacity of the soil. For this example, we will use a total stress analysis.

$$q_{ult} = S_U N_C S_C i_C + P_0$$

where:

P_0 = effective overburden pressure
N_C = pi + 2
S_C = shape factor

$$= 1 + 0.2(b_{eff}/l_{eff})$$

i_C = inclination factor

$$= 0.5 + 0.5(1 - H_{design}/(A_{eff}S_U))^{1/2}$$

H_{design} = horizontal design load (Load Doc)

Finally, using the equation for factor of safety given on page 4, the foundation dimensions can be evaluated for their effectiveness.

The use of these equations is an iterative process, with the radius increased or decreased until it matches the design requirement given by the load document.

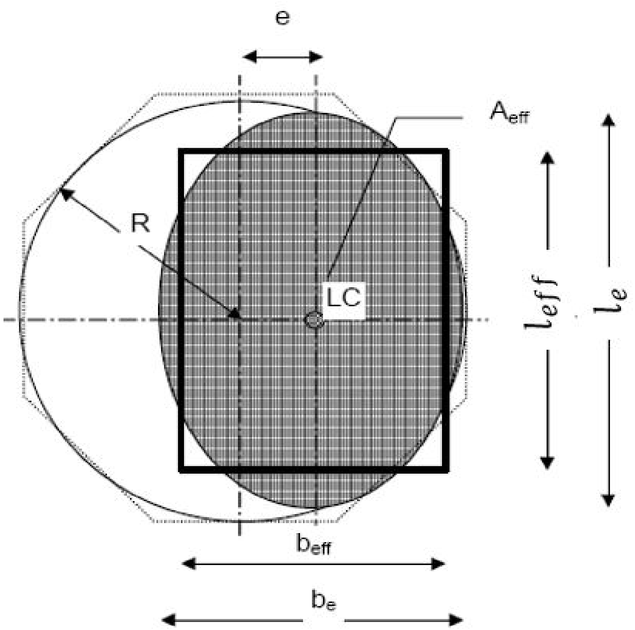

Fig. 7: Effective bearing area for WTG design (*DNV/Riso* 2002)

CURRENT RESEARCH

Current research efforts regarding foundation bearing capacity and load distribution has involved field work and in situ data acquisition, as well as WTG foundation sensitivity analyses. Efforts are ongoing, with additional work in modelling and foundation instrumentation in the works.

An analysis performed by Paul Lang in 2012 examined the sensitivity of foundation dimensions to variations in allowable bearing capacity for several WTG actual projects. Fig 8 shows the results for three of the sites.

Most apparent is the inverse exponential relationship between bearing capacity and foundation radius, making construction on relatively weak soils cost prohibitive. Since the soil's bearing capacity cannot be improved outside of costly ground improvement techniques, a potential pathway to reducing foundation size would be the development and implementation of more mechanistically correct, and thus, less conservative design methods. Such a leap in design methods could allow previously untenable sites to become viable for WTG construction.

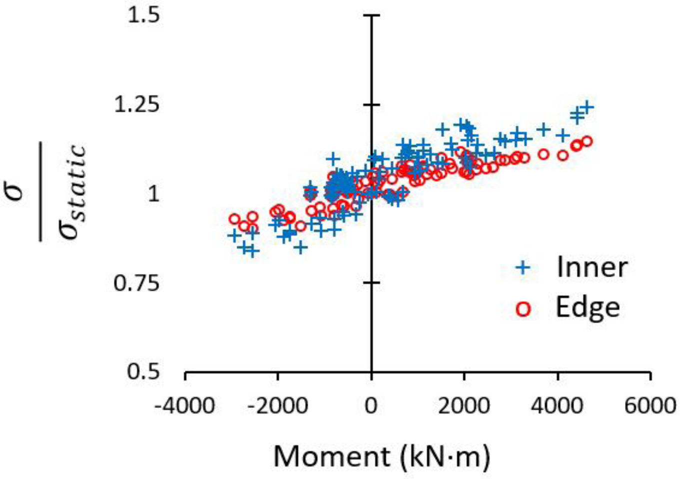

Fig. 7: Foundation soil pressure sensitivity to moment (Enos 2018)

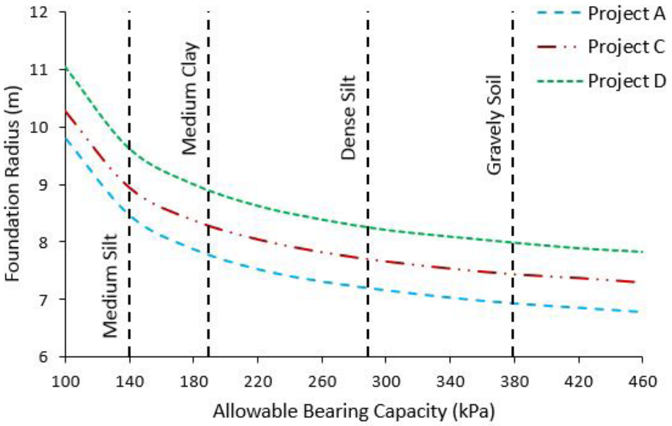

Fig. 8: Foundation radius sensitivity to allowable bearing capacity (Lang 2012)

Figure 7 shows results of pressure and tower moment monitoring in the soil below an 8m radius WTG foundation. The hourly average pressure was divided by the static (i.e. zero wind load) pressure and plotted vs. the corresponding hourly average induced tower moment.

A positive moment indicates the moment is inducing a compressive pressure on the measured side, while a negative moment indicates an "uplifting" pressure. The inner and edge pressures were measured 2.85 and 6.1 meters from the footing center, respectively.

The results at two sites exhibit similar results, though only one site is shown, indicating that the peak pressure occurs somewhere in the *middle* of the footing radius as opposed to the edge, suggesting a more complex load distribution with a small er eccentricity than is typically assumed.

Gathering and analysis of data is ongoing, with potential future efforts including finite element modelling and additional foundation instrumentation.

© James Tinjum 2017

IN SUMMARY

In this paper, we have reviewed the fundamentals of bearing capacity, discussed its application to WTG systems, and exhibited ongoing research efforts to advance our understanding of the mechanisms behind WTG foundation loading.

Wind energy is a rapidly advancing and growing technology in an industry where demand will only grow. Staying on the cutting edge of all aspect of design, including the geotechnical component, is a necessity to continue decreasing costs and building safer turbines. As turbine sizes grow larger and technological advances continue, foundation design must keep pace to accomodate increasingly unique and extreme loads.

REFERENCES

Budhu, M. 2016. *Soil Mechanics and Foundations*. 3rd ed. New York: Wiley, 2016. Print.

Coduto, P., Kitch, W., Yeung, M.R. 2016. *Foundation Design Principles and Practices*. 3rd ed. Upper Saddle River, New Jersey: Pearson, 2016. Print.

Det Norske Veritas (DNV), 2002. Guidelines for Design of Wind Turbines. Risø National Laboratory, Copenhagen.

Enos, C. 2018. "Insert Thesis title" MS Thesis, Univ. wisconsin-Madison, Madison, WI, USA.

Lang, P.J. 2012. "Sensitivity of shallow wind turbine foundation design and soil response to geotechnical variance with construction cost implications." Thesis, University of Wisconsin-Madison, Madison, WI.

Wu, Z. 2014. "Measuring dynamic properties of wind turbine foundation soil in resonant column - issues and challenges." MS Thesis, Univ. Wisconsin-Madison, Madison, WI

Yilmaz, M. 2014. "Foundation soil response to wind turbine generator loading." MS Thesis, Univ. Wisconsin-Madison, Madison, WI.

Zen, W. 2015. "Numerical Modeling of Pressure Distribution of Wind Turbine Generator Foundation on Lean Clay." Independent Study Report, University of Wisconsin – Madison, Madison, WI, USA.

WIND TURBINE FOUNDATION DESIGN

SOIL STIFFNESS

Christopher Enos and James Tinjum, Ph.D.

JAMES TINJUM, PH.D
UNIVERSITY OF WISCONSIN-MADISON

WITH THE GROWING DEMAND for wind energy the need for larger, more powerful turbines grows with it. As capacity grows, however, so does the cost of each turbine, with the foundation accounting for about 25% of the overall cost (Lang 2012). As such, optimization of foundation design will be crucial in reducing costs to facilitate the growth of the industry.

Shallow, on-shore wind turbine generator (WTG) systems are typically founded on massive gravity-based footings, which support temporally and spatially varying vertical, horizontal, and overturning forces due to changing wind loads. As rated capacity increases, the magnitude of overturning moments increases, requiring larger foundations to accommodate rotational stiffness, bearing capacity, and overturning requirements.

> The foundation accounts for about 25% of a wind turbine's overall cost.

One key parameter of significance is the rotational stiffness, kψ, of the WTG system. In soft soil with a shear modulus of about 29 MPa or less, rotational stiffness often controls the overall foundation design (Lang 2012). Calculation of rotational stiffness is a complex, multi-step problem that ultimately relies on accurate geotechnical data and design assumptions.

In conjunction with other papers, we aim to introduce the problem, break down the process into its component parts, and explain the methodology. Specifically, this paper focuses on the determination and use of soil stiffness as it pertains to rotational stiffness. In addition, aspects of current research will be included, aiming to disseminate state-of-the-art results into practice.

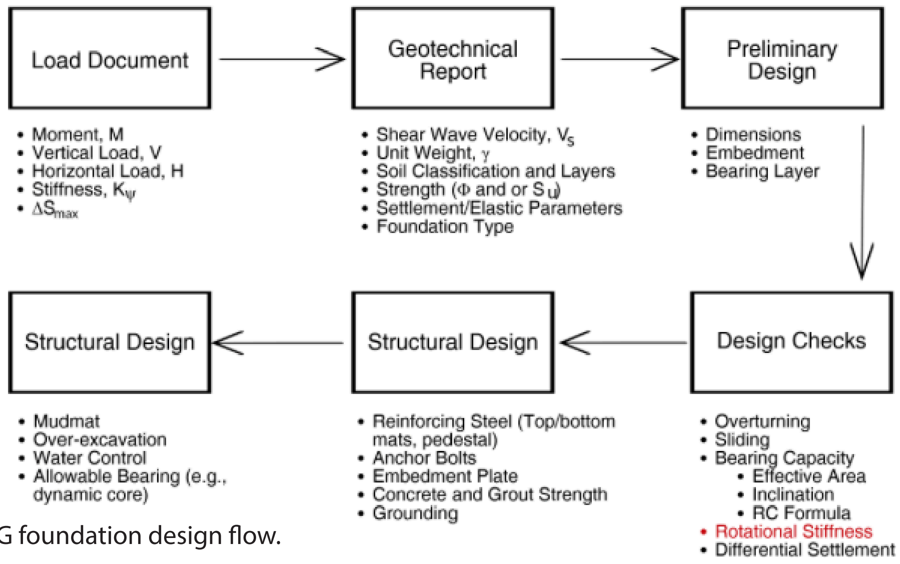

Fig. 1: General WTG foundation design flow.

ROTATIONAL STIFFNESS

> "The foundation cost is one of the largest cost items in wind-farm construction, ranging from \$10M to \$20M per project or project phase. Even a 10% reduction in cost due to design efficiency and better understanding of the soil behavior and the soil-structure interaction can translate from \$1M to \$2M per site/project."
>
> -Mohamed Nofal
> RES Americas

A key step in the design process for a WTG foundation is the system's rotational stiffness parameter, kψ. Being essentially a lever arm supported on one end, the tower will continuously rock back-and-forth at its natural frequency (Fig. 2). Excessive rocking risks serviceability and potentially structural failure.

The formula for rotational stiffness is a corollary to Hooke's Law of Elasticity, and is used to determine the foundation radius. This design check depends heavily on the shear modulus, G, which in turn depends heavily on the cyclic shear strain:

$$K_\varphi = \frac{8GR^3}{3(1-v)}$$

Further refinement and correction of this formula is necessary, however, for use with a WTG foundation.

© Chris Enos 2017

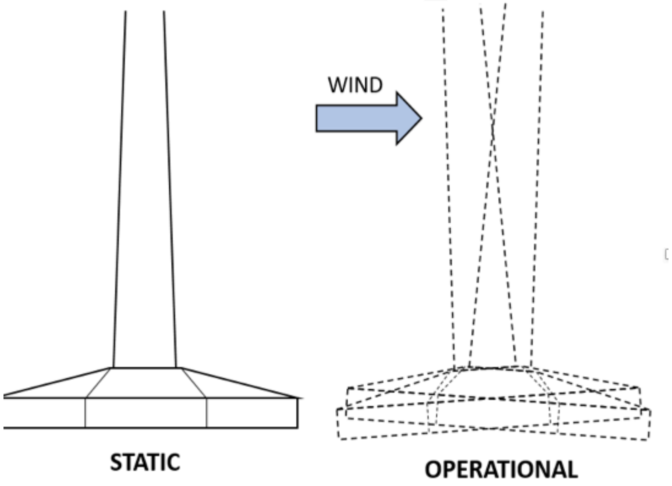

Fig. 2: Illustration of a rocking WTG.

Within the WTG general design flow (Fig. 1), this step falls within the design check component. The determination of G, however, falls within the geotechnical report phase, as G is a soil material property that impacts many components of WTG geotechnical design.

SHEAR MODULUS

The shear modulus, G, of a material is a measure of it's resistance to forces perpendicular to axial loads (i.e. shear forces). The shear modulus is assumed to be elastic, and acts as the spring constant in Hooke's Law of Elasticity:

$$F = -k\Delta x$$

where F is the applied force, k is the spring constant, and x is the displacement. Shear modulus is a function of many parameters, including saturation/water content, void ratio, effective stress, and soil minerology. Though models exist to predict G, it is generally determined via direct methods such as seismic analysis or conversion of Young's modulus, E. Though damping, a measure of a material's ability to disspate energy, is also an important aspect of dynamic characterization of a soil, it is implicitly included in the models used in WTG design check equations.

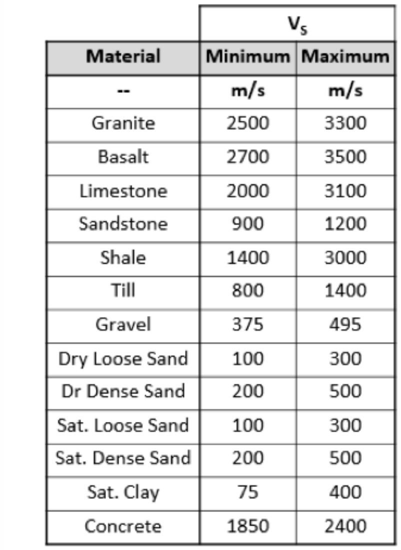

	V_S	
Material	**Minimum**	**Maximum**
--	**m/s**	**m/s**
Granite	2500	3300
Basalt	2700	3500
Limestone	2000	3100
Sandstone	900	1200
Shale	1400	3000
Till	800	1400
Gravel	375	495
Dry Loose Sand	100	300
Dr Dense Sand	200	500
Sat. Loose Sand	100	300
Sat. Dense Sand	200	500
Sat. Clay	75	400
Concrete	1850	2400

Table1: Typical V_s values for various soil types (Tinjum and Christensen 2010).

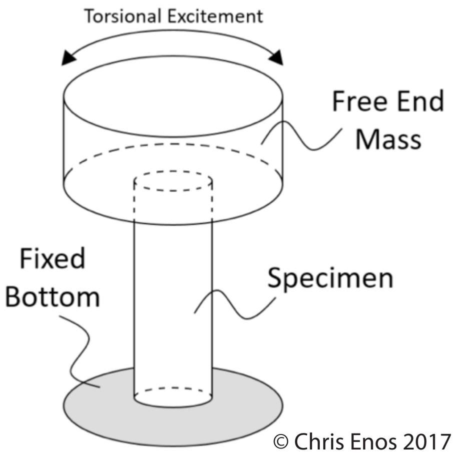

© Chris Enos 2017

Fig. 3: Simple resonant column schematic

Measurement of Vs provides in situ modulus, and can be performed during the geotechnical investigation. With Vs known, G can be calculated via the following equation:

$$G_0 = \rho V_s^2$$

Where ρ is the soil density and G0 is the small-strain shear modulus. Typical values can be found in Table 1.
A resonant column (Fig. 3) and cyclic triaxial apparatus can also be used to measure shear modulus and its relationship with strain. A resonant column applies an oscillating torsional shear force to the soil, while the cyclic triaxial cell applies a cyclic axial load to the soil. In conjunction with one another, they can be used to characterize the soil's shear response over a broad spectrum of shear strain magnitudes.

Once the shear modulus has been determined, the role of cyclic strain must be accounted for.

There are two primary methods to directly measure the shear modulus: shear wave velocity (V_s) and dynamic lab testing.

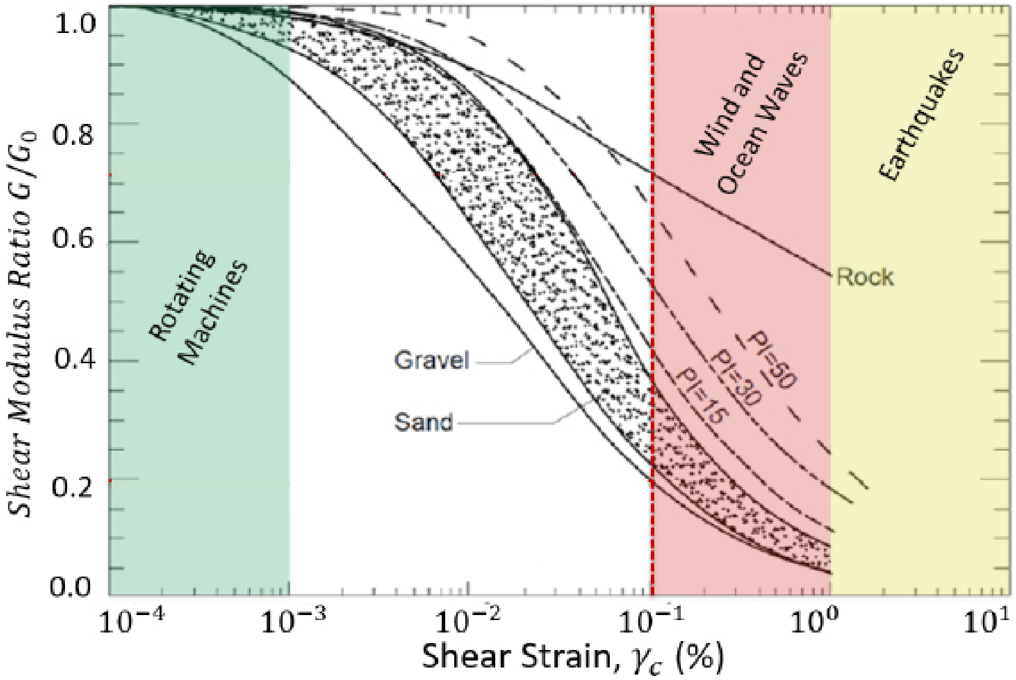

Fig. 4: Shear modulus reduction curves for various soil types (Tinjum and Christensen 2011).

For fine-grained soils at small strains (< 10-3%), inter-particle forces play the dominant role in the dynamic properties of the soil and the shear modulus retains a nearly linear relationship with strain (Vucetic & Dobry 1991; Diaz-Rodriguez & Lopez-Molina 2008). At higher strains, the soil fabric degrades due to relative slippage of particles; which is a function of effective stress, void ratio, and particle shape (Santamarina et al. 2001; Santamarina 2003; Cho et al. 2006; Diaz-Rodriguez & Lopez-Molina 2008). This slippage causes a re-structuring of the soil skeleton and a non-linear shear modulus reduction.

This reduction in shear modulus is characterized by a shear modulus reduction curve (SMRC). A general SMRC for various soil types is shown in Figure 4.

The resonant column and cyclic triaxial methods, discussed previously, produce a SMRC for a given soil. The y-axis can indicate either the actual shear modulus or the shear modulus reduction factor, which is multiplied by G_0.

To use the chart, simply find the cyclic shear strain experienced by the soil, draw a line vertically up to the soil description that best suits the site soil, and draw a horizontal line over to the y-axis. The resulting decimal should then be multiplied by G_0, to determine G, which should be used in the rotational stiffness design calculations.

Accurate representation of in situ shear strain is crucial to accurate G0 reduction, especially in the middle of the plot, where the curve is steepest. In WTG geotechnical design, the cyclic shear strain is assumed to be 10-1% (DNV/Risø 2007). Industry guidance, however, supplies no justification or citations regarding this number.

CURRENT RESEARCH

Current research efforts regarding soil stiffness as it pertains to WTG foundations include resonant column and cyclic triaxial testing of WTG site soil from different depths and locations at the site to develop SMRC's at varying confining stress (σ_c) and matric suction (ψ) levels.

Testing of foundation soil at several confining stresses yielded a clear increase in G_0 as σc increased (Fig 5a). However, when data was normalized to plot the reduction factor on the y-axis, the resulting SMRC's were nearly identical (Fig 5b).

Interestingly, increasing the confining stress from 25 kPa to 100 kPa, roughly the increased σc from adding a WTG, roughly doubled the shear modulus, resulting in a much stronger soil than would have been assessed during investigation. Accounting for such an increase in σc, and thus effective stress, could have significant ramifications on soil parameters used in design check calculations.

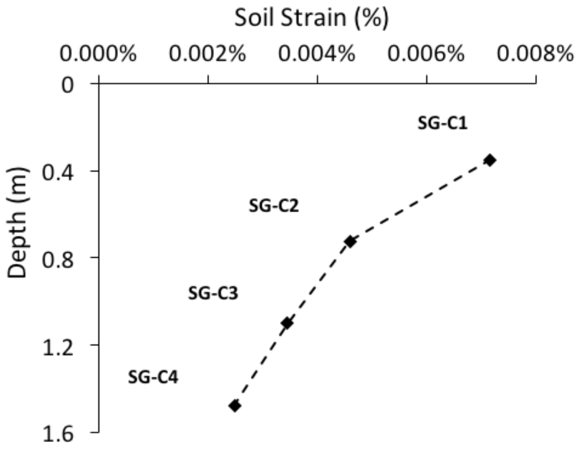

Fig. 6: Soil strain with depth under a WTG (Yilmaz 2015).

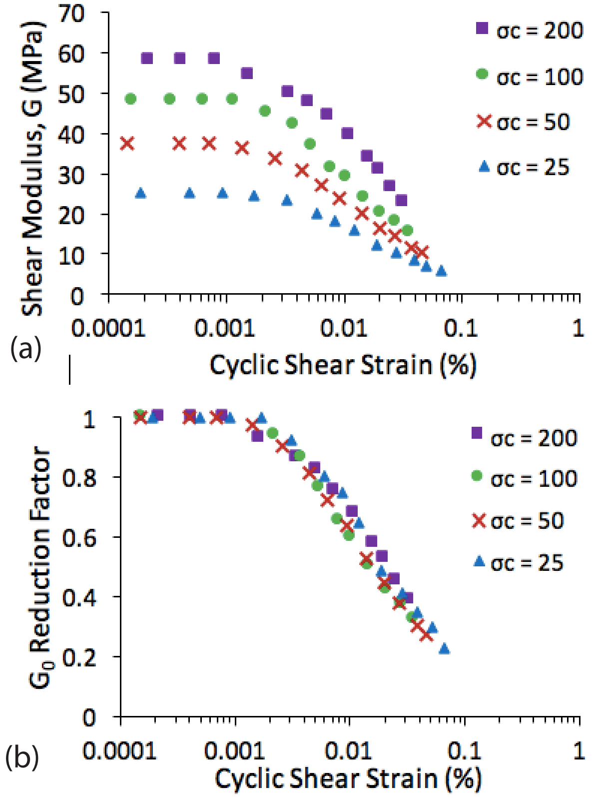

Fig. 5: (a) raw and (b) normalized SMRC's for site soil (Wu 2015)

Furthermore, in situ measurements of soil strain underneath two WTG foundations in the Midwest have revealed smaller strains than industry guidance instructs engineers to assume. The largest axial strain measured was 0.007% (Fig 6).

Such a stark difference in assumed and measured strain suggests an overly-conservative design procedure. Whether the over-performance of the foundation is due to stiffer than expected soil or mechanistically incorrect design models, continued data analysis and, eventually, additional instrumentation of WTG's in a variety of soil conditions is necessary to give engineers the cutting-edge tools they need to design the most cost-efficient foundation possible.

IN SUMMARY

Wind energy is a rapidly advancing and growing technology in an industry where demand will only grow. Staying on the cutting edge of all aspect of design, including the geotechnical component, is a necessity to continue decreasing costs and building safer turbines.

Accurate characterization and implementation of soil stiffness is key to a properly designed foundation. Thorough understanding of the mechanisms and implications of material properties such as shear modulus give engineers the tools necessary to best help their clients.

Though current methods and models are far from perfect, continued study on WTG foundations in various soil conditions in different wind climates will develop design practices into state-of-the-art, mechanistically correct guidance.

© James Tinjum 2017

REFERENCES:

Det Norske Veritas (DNV), 2002. Guidelines for Design of Wind Turbines. Risø National Laboratory, Copenhagen, Denmark.

Cho, G., Dodds, J. and Santamarina, J.C., "Particle Shape Effects on Packing Density, Stiffness, and Strength: Natural and Crushed Sands," J Geotech Geoenv Eng, 132(5), 2006, 591–602.

Diaz-Rodriguez, J.A. and Lopez-Molina, J.A., "Strain Thresholds in Soil Dynamics," presented at the 14th World Conf on Earthq Eng, Beijing, China, October 12-17, 2005.

Lang, P.J. 2012. "Sensitivity of shallow wind turbine foundation design and soil response to geotechnical variance with construction cost implications." Thesis, University of Wisconsin-Madison, Madison, WI.

Santamarina, C. J., "Soil Behavior at the Microscale: Particle Forces," presented at the Symposium on Soil Behavior and Soft Ground Construction, Massachusetts Institute of Technology, Boston, MA, October 5-6, 2001..

Tinjum, J. M., and Christensen, R. W. (2010). "Site investigation, characterization and assessment for wind turbine design and construction." In Wind Energy Systems, edited by John D. Sorensen and Jens N. Sorensen, 26-45. Woodhead Publishing.

Vucetic, M., and Dobry, R., "Effect of Soil Plasticity on Cyclic Response," J Geotech Eng, 117(1), 1991, 89–107.

Wu, Z. (2014). "Measuring dynamic properties of wind turbine foundation soil in resonant column - issues and challenges." MS Thesis, Univ. Wisconsin-Madison, Madison, WI

Yilmaz, M. (2014). "Foundation soil response to wind turbine generator loading." MS Thesis, Univ. Wisconsin-Madison, Madison, WI..

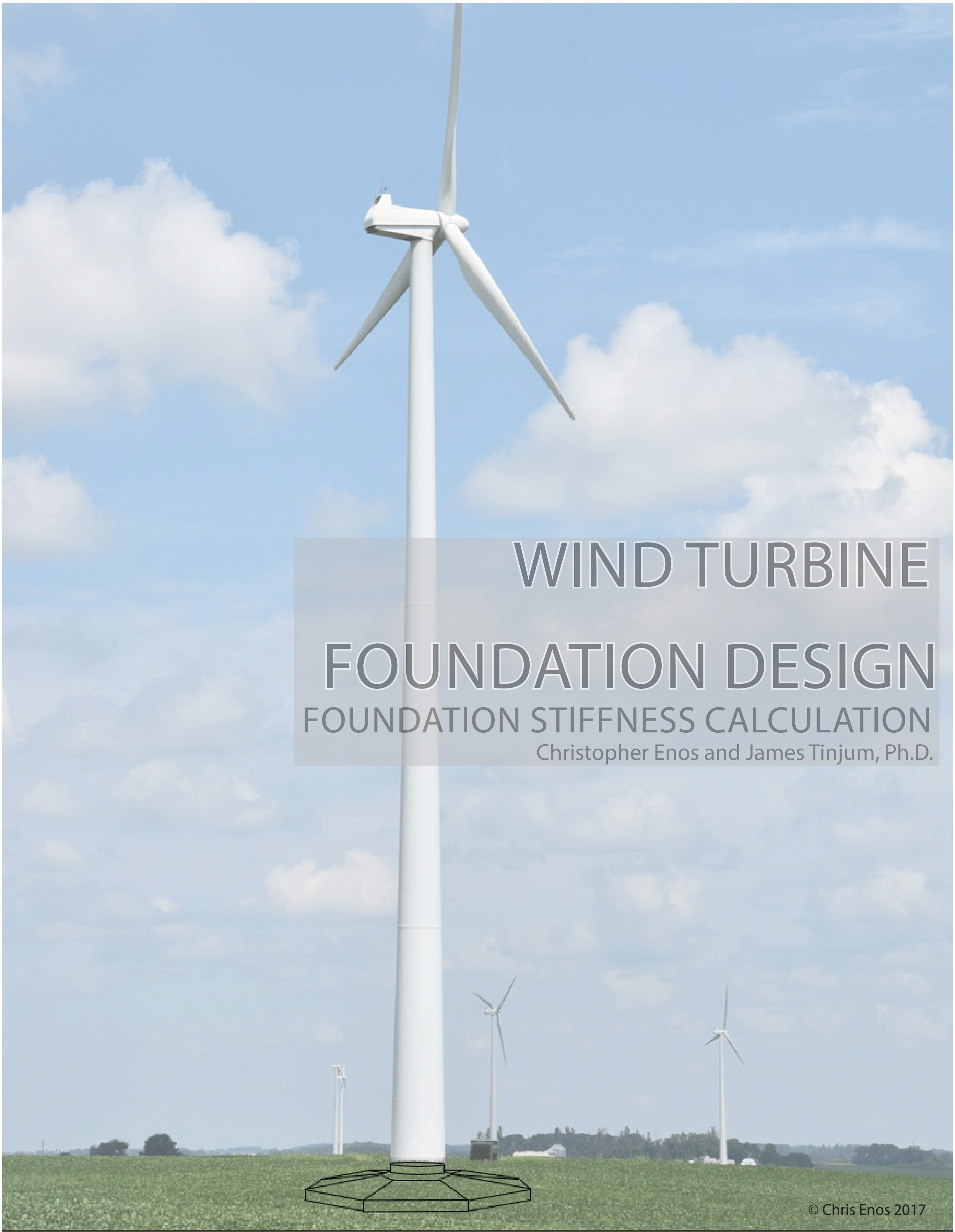

WIND TURBINE FOUNDATION DESIGN

FOUNDATION STIFFNESS CALCULATION

Christopher Enos and James Tinjum, Ph.D.

JAMES TINJUM, PH.D UNIVERSITY OF WISCONSIN-MADISON


© James Tinjum 2017

WITH THE GROWING DEMAND for wind energy the need for larger, more powerful turbines grows with it. As capacity grows, however, so does the cost of each turbine, with the foundation accounting for about 25% of the overall cost (Lang 2012). As such, optimization of foundation design will be crucial in reducing costs to facilitate the growth of the industry.

Shallow, on-shore wind turbine generator (WTG) systems are typically founded on massive gravity-based footings, which support temporally and spatially varying vertical, horizontal, and overturning forces due to changing wind loads. As rated capacity increases, the magnitude of overturning moments increases, requiring larger foundations to accommodate rotational stiffness, bearing capacity, and overturning requirements.

The foundation accounts for about 25% of a wind turbine's overall cost.

One key parameter of significance is the rotational stiffness, kψ, of the WTG system. In soft soil with a shear modulus of about 29 MPa or less, rotational stiffness often controls the overall foundation design (Lang 2012). Calculation of rotational stiffness is a complex, multi-step problem that ultimately relies on accurate geotechnical data and design assumptions.

In conjunction with other papers, we aim to introduce the problem, break down the process into its component parts, and explain the methodology. Specifically, this paper focuses on the basic theory, development of, and use of rotational stiffness design check calculations. In addition, aspects of current research will be included, aiming to disseminate state-of-the-art results into practice.

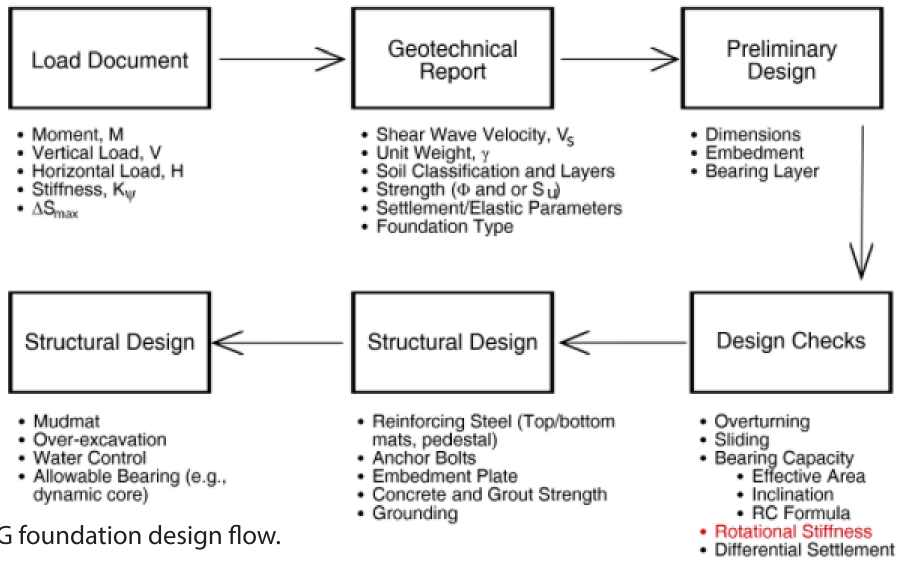

Fig. 1: General WTG foundation design flow.

ROTATIONAL STIFFNESS

> "The foundation cost is one of the largest cost items in wind-farm construction, ranging from \$10M to \$20M per project or project phase. Even a 10% reduction in cost due to design efficiency and better understanding of the soil behavior and the soil-structure interaction can translate from \$1M to \$2M per site/project."
>
> -Mohamed Nofal
> RES Americas

A key step in the design process for a WTG foundation is the system's rotational stiffness parameter, $k\psi$. Being essentially a lever arm supported on one end, the tower will continuously rock back-and-forth at its natural frequency (Fig. 2). Excessive rocking risks serviceability and potentially structural failure.

The formula for rotational stiffness is a corollary to Hooke's Law of Elasticity, and is used to determine the foundation radius. This design check depends heavily on the shear modulus, G, which in turn depends heavily on the cyclic shear strain:

$$K_{\varphi} = \frac{8GR^3}{3(1-\nu)}$$

Further refinement and correction of this formula is necessary, however, for use with a WTG foundation.

© Chris Enos 2017

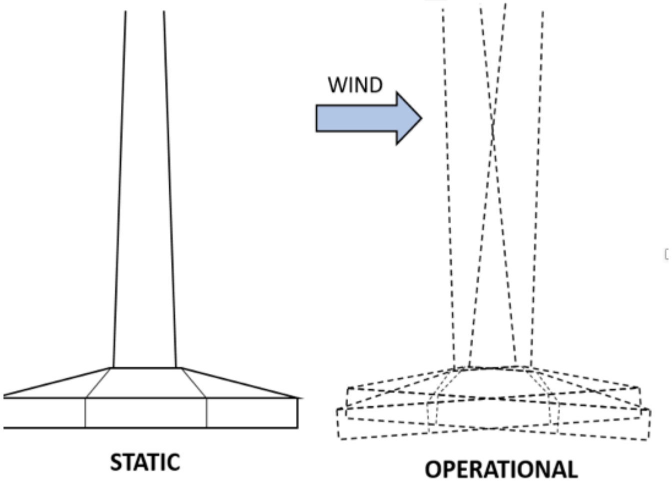

Fig. 2: Illustration of a rocking WTG.

Within the WTG general design flow (Fig. 1), this step falls within the design check component. The determination of G, however, falls within the geotechnical report phase, as G is a soil material property that impacts many components of WTG geotechnical design.

ELASTIC HALFSPACE

Calculation of foundation stiffness fundamentally lies in the assumption that the footing lies on what is known as an elastic halfspace (Fig.3). An elastic halfspace is not a unique to foundation engineering. It is a concept widely used in materials science and engineering as an idealized model for the behavior of a medium

Elastic halfspace theory relies on the four principle assumptions that the medium, in this case soil is perfectly linear elastic, homogenous, isotropic, and semi-infinite. These assumptions are highly idealized, and as such in general require conservative application.

Boussinesq's closed form solution (Fig. 4) to a vertical stress distribution is the most commonly known derivation of elastic halfspace theory to geotechnical and civil engineers alike. In 1943, Hubert Borowicka further derived elastic halfspace theory and the base equation for rotational stiffness of a circular footing.

It is important to mind soil's inherent violations of the assumptions of an elastic halfspace. For example, soils are layered media, violating the assumptions of isotropy and homogeneity. Beyond that, though soil exhibits nearly elastic properties at very small strains, elasticity and linearity begin to fall apart as strain increases. The geotechnical investigation will be a key tool to guide your understanding and use of these assumptions as they apply to your design.

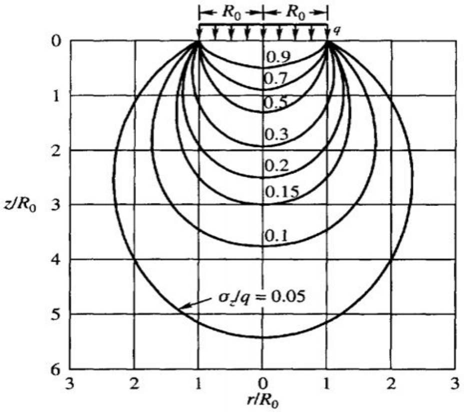

Fig. 4: Boussinesq's solution to a vertical stress distribution (Murthy 2003).

> It is important to mind soil's inherent violations of the assumptions of an elastic halfspace...the geotechnical investigation will be a key tool to guide your understanding and use of these assumptions as they apply to your design.

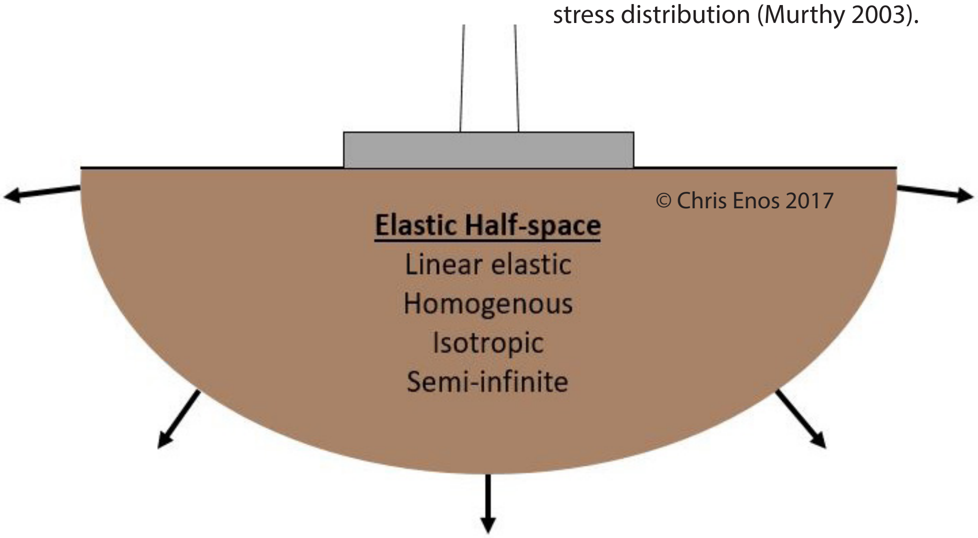

© Chris Enos 2017

Fig. 3: Illustration of a footing sitting atop an elastic halfspace.

On stratum over bedrock	On two unique strata	Embedded in stratum over bedrock
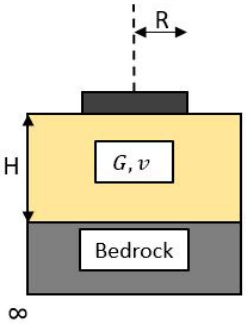	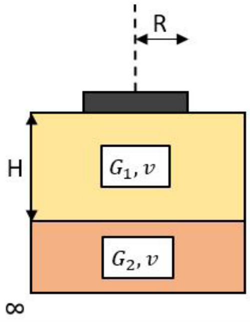	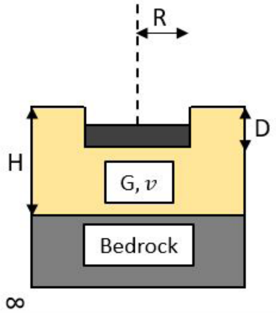
$K_V = \frac{4GR}{1-v}\left(1+1.28\frac{R}{H}\right)$	$K_V = \frac{4G_1R}{1-v}\frac{\left(1+1.28\frac{R}{H}\right)}{\left(1+1.28\frac{R}{H}\frac{G_1}{G_2}\right)}$	$K_V = \frac{4GR}{1-v}\left(1+1.28\frac{R}{H}\right)\left(1+\frac{D}{2R}\right)\left(1+\left(0.85-0.28\frac{D}{R}\right)\right)\left(\frac{D/H}{1-D/H}\right)$
$K_H = \frac{4GR}{1-v}\left(1+1.28\frac{R}{H}\right)$	$K_H = \frac{8G_1R}{1-v}\frac{\left(1+\frac{R}{2H}\right)}{\left(1+\frac{R}{2H}\frac{G_1}{G_2}\right)}$	$K_H = \frac{8GR}{1-v}\left(1+\frac{R}{2H}\right)\left(1+\frac{2}{3}\frac{D}{R}\right)\left(1+\frac{5}{4}\frac{D}{H}\right)$
$K_R = \frac{8GR^3}{3(1-v)}\left(1+\frac{R}{6H}\right)$	$K_R = \frac{8G_1R^3}{3(1-v)}\frac{\left(1+\frac{R}{6H}\right)}{\left(1+\frac{R}{6H}\frac{G_1}{G_2}\right)}$	$K_R = \frac{8GR^3}{3(1-v)}\left(1+\frac{R}{6H}\right)\left(1+2\frac{D}{R}\right)\left(1+0.7\frac{D}{H}\right)$

Fig. 5: Formulas for vertical, horizontal, and rotational stiffness for three soil scenarios (DNV/Riso). 2007)

As alluded to previously, there are corrections to the base equation for rotational stiffness available for several site conditions. The corrections are empirically derived formulas developed in the 1970's as a result of three separate modelling studies. The equations are given above in Figure 5.

Equations are given for three types of stiffness: horizontal (K_H), vertical (K_V), and rocking/rotational (K_R). Horizontal stiffness refers to the horizontal translational oscillating motion of the footing. Similarly, vertical stiffness refers to the vertical translational oscillation of the footihng. Though these two conditions rarely, if ever, control over rotational stiffness, they are given for reference.

The first condition is a footing resting atop a soil stratum over bedrock at some depth, H. This set of equations was developed by Elsabee and Morray in 1977. In this case, the bedrock is assumed to be rigid.

The next set of equations describes a site in which the footing is resting atop a soil stratum of finite depth over a 2nd stratum of an assumed infinite depth. This was developed by Hadjian and Luco in 1977. The rotational stiffness equation is valid for $1 \leq H/R \leq 5$.

Finally, the third condition, and the most complex, describes a footing embedded in a soil stratum of depth H atop a bedrock layer. This study was developed by Eduardo Kausel in 1972. This set of equations is valid for $D/R < 2$ and $D/H < 1\backslash 2$. Again, the bedrock is assumed to be rigid.

The use of these equations is an iterative process, with the radius increased or decreased until it matches the design requirement given by the load document. In the case of the third condition, the embedment depth may also be changed until the requirement is met.

SAMPLE CALCULATION

Step 1: Select appropriate approach. In this case, we will use case 3: a footing embedded in soil above bedrock.

$$K_R = \frac{8GR^3}{3(1-v)}\left(1+\frac{R}{6H}\right)\left(1+\frac{D}{2R}\right)\left(1+0.7\frac{D}{H}\right)$$

Step 2: Estimate Poisson's ratio based on soil profile. For a poorly graded sand, we'll use 0.35.

Step 3: Determine shear wave velocity from the soil profile. Use an effective zone of half of the diameter. In this case, the shear wave velocity, V_S, is 150 m/s, or 492 ft/s, for the 24 ft of soil.

Step 4: Calculate G_{max} using VS and soil density.

$$G_{max} = \rho V_S^2 = \frac{\gamma}{g} V_S^2$$

$$G_{max} = \frac{115\ pcf}{32.2\frac{ft}{s^2}} * \left(492\frac{ft}{s}\right) = 864.5\ ksf$$

Step 5: Determine modulus reduction based on 0.1% shear strain and soil type.

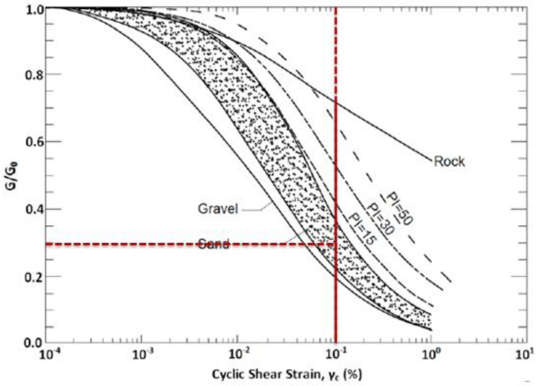

$$\frac{G}{G_{max}} = 0.3$$

$$G = 864.5\ ksf * 0.3 = 259.4\ ksf$$

Step 6: Enter parameters into stiffness equation from Step 1.

G = 259.4 ksf
R = 24.0 ft
v = 0.35
H = 200 ft
D = 8.0 ft

$$K_R = \frac{8(259.4\ ksf)(24.0\ ft)^2}{3(1-0.35)}\left(1+\frac{24.0\ ft}{6(200\ ft)}\right)\left(1+0.7\frac{8.0\ ft}{200\ ft}\right)$$

$$K_R = 25{,}705{,}412\ \frac{kip * ft}{rad}\ or\ 34.9\frac{GN * m}{rad}$$

Step 7: Does the available rotational stiffness meet the design requirements?

$$34.9\frac{GN * m}{rad} > 34\frac{GN * m}{rad}$$

Yes, the stiffness is sufficient!

Step 8: Determine maximum outer edge displacement.

$$K_R = \frac{M}{\theta}$$

Where:
M = Applied moment
Θ = Rotation [rad]

$$\theta = \frac{M}{K_R} = \frac{45{,}000\ ft * kips}{25{,}705{,}412\ {kip * ft}/{rad}}$$
$$= 0.001751\ rad$$

$$Disp_V = R\sin\theta = 24\ ft * \sin(0.001751\ rad)$$

$$Disp_V = 0.042\ ft\ or\ 0.504\ in$$

The use of these equations is an iterative process, with the radius increased or decreased until it matches the design requirement given by the load document.

CURRENT RESEARCH

Current research efforts regarding foundation stiffness has ranged from field work and in situ data acquisition to laboratory work and WTG foundation sensitivity analyses. Efforts are ongoing, with additional work in modelling and foundation instrumentation in the works.

A study performed by Paul Lang in 2012 examined the sensitivity of foundation dimensions to variations in field conditions. The study looked at many design parameters for a WTG foundation, including rotational stiffness. The load document and geotechnical data for several actual sites were used to perform the analysis.

Figure 6 shows the impact of the shear modulus reduction factor on footing radius, while Figure 7 shows its sensitivity with shear wave velocity. Each of these plots ultimately represent the soil stiffness in one way or another, showing just how crucial proper shear modulus characterization is to the overall design. In reality, the foundation radius will not reach 5-6 m if the input soil stiffness is increased, but the radius can be decreased to a point where rotational stiffness no longer controls the design.

From a laboratory perspective, through dynamic soil testing of WTG site soil via a resonant column, results have shown a clear increase in shear modulus with confining stress. If the shear modulus is determined before the turbine is constructed, the additional confinement (~70 kPa) could nearly double the soil's shear modulus based on the SMRC's in Figure 8. The implications of doubling the soil's stiffness are significant and can markedly change the foundation's rotational stiffness.

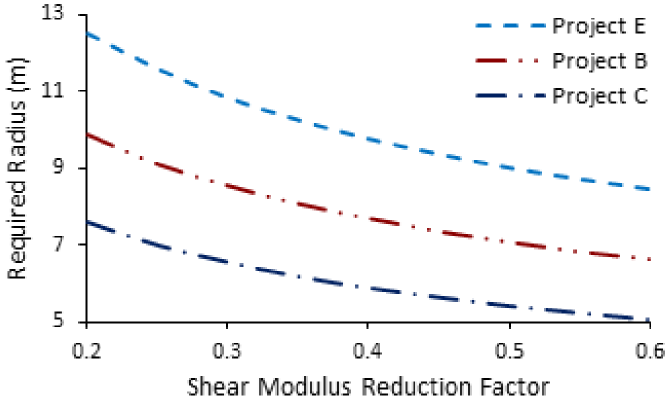

Fig. 6: Foundation radius sensitivity to shear modulus reduction (Lang 2012)

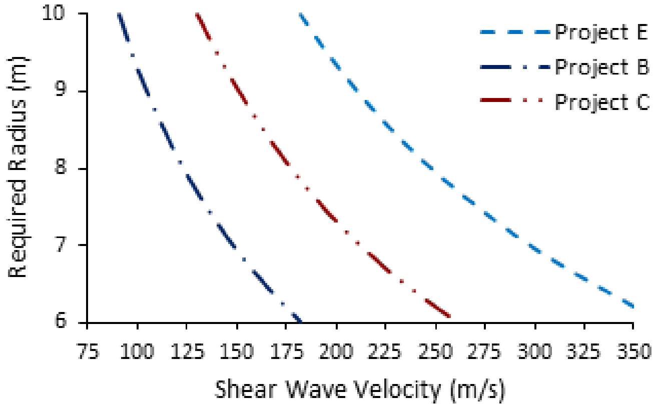

Fig. 7: Foundation radius sensitivity to shear wave velocity (Lang 2012)

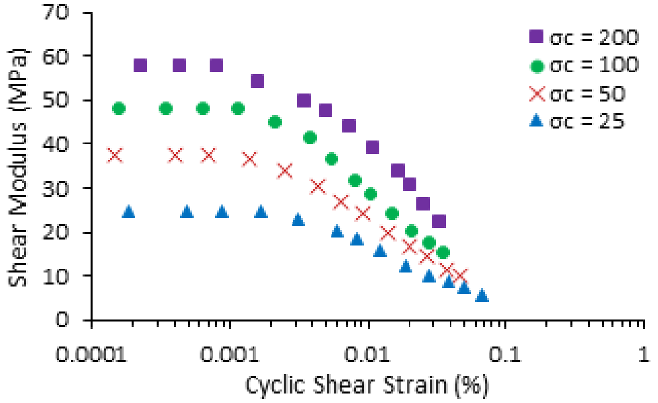

Fig. 9: Shear modulus reduction curves for a site soil at four confining stresses (Wu 2015).

IN SUMMARY

© James Tinjum 2017

Wind energy is a rapidly advancing and growing technology in an industry where demand will only grow. Staying on the cutting edge of all aspect of design, including the geotechnical component, is a necessity to continue decreasing costs and building safer turbines.

Well defined subsurface conditions and accurate use of key design assumptions are vital to properly implementing the rotational stiffness parameter.

Well-defined soil and site conditions, as well as meticulous calculation, will lead to not only a more cost efficient design, but a safer, more effective design.

Though current methods and models are far from perfect, continued study on WTG foundations in various soil conditions in different wind climates will develop design practices into state-of-the-art, mechanistically correct guidance.

REFERENCES

Borowicka, H. (1943). "Uber ausmittig belastete starre Platten elastischisotropem Untergrund." Ingenieur-Archiv. 1:1-8

Det Norske Veritas (DNV), 2002. Guidelines for Design of Wind Turbines. Risø National Laboratory, Copenhagen.

Elsabee, F., Murray, J.P. (1977). "Dynamic Behavior of Embedded Foundations." Research Rep. R77-33, MIT.

Hadjian, A.H., Luco, J.E. (1977). "On the Importance of Layering on Impedance Functions." Paper part of proceedings of 6th World Conference on Earthquake Engineering, New Delhi, India. pp 1675 – 1680.

Kausel, E. (1972). "Forced Vibrations of Circular Foundations on Layered Media." Dissertation, Massachusetts Institute of Technology, Cambridge, MA, USA.

Lang, P.J. 2012. "Sensitivity of shallow wind turbine foundation design and soil response to geotechnical variance with construction cost implications." Thesis, University of Wisconsin-Madison, Madison, WI.

Murthy, V. *Geotechnical Engineering: Principles and Practices of Soil Mechanics and Foundation Engineering.* New York, NY: Marcel Dekker, 2003.

Tinjum, J. M., and Christensen, R. W. (2010). "Site investigation, characterization and assessment for wind turbine design and construction." In Wind Energy Systems, edited by John D. Sorensen and Jens N. Sorensen, 26-45. Woodhead Publishing.

Wu, Z. (2014). "Measuring dynamic properties of wind turbine foundation soil in resonant column - issues and challenges." MS Thesis, Univ. Wisconsin-Madison, Madison, WI Yilmaz, M. (2014). "Foundation soil response to wind turbine generator loading." MS Thesis, Univ. Wisconsin-Madison, Madison, WI.